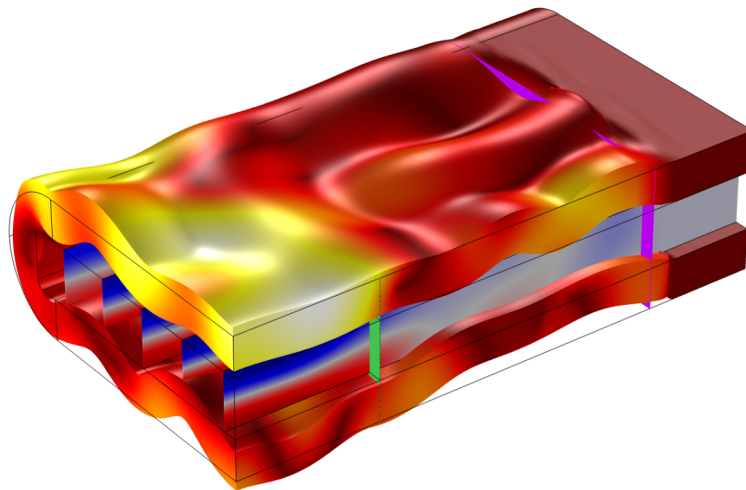


Ph.D. Thesis

Effective modelling of acoustofluidic devices



Mikkel Wennemoes Hvitfeld Ley

Supervisor: Professor Henrik Bruus

Department of Physics
Technical University of Denmark

August 14, 2017

Cover illustration: Illustration of the solid displacement field and fluid pressure in a mm-size liquid-filled glass capillary actuated by ultrasound.

Effective modelling of acoustofluidic devices

Copyright © 2017 Mikkel Wennemoes Hvitfeld Ley All Rights Reserved
Typeset using L^AT_EX

<http://www.fysik.dtu.dk/microfluidics>

Abstract

In this thesis work we develop three models for involved systems in the field of microscale acoustofluidics. Because of the complexity of the systems studied, the aim of the Ph.d. project has been to make simplified and effective descriptions of these systems, capturing the most essential behaviour of the system, as opposed to making detailed calculations of idealised cases.

The effective models developed in this thesis concerns: 1) hydrodynamic particle-particle interactions in dense microparticle suspensions, 2) the acoustic field in mm-sized liquid-filled glass capillaries used for acoustic trapping, and 3) acoustic streaming patterns in the devices considered in model 2).

1) We derive an effective model for numerical studies of hydrodynamic particle-particle interactions in microfluidic high-concentration suspensions. A suspension of microparticles placed in a microfluidic channel and influenced by an external force, is described by a continuous particle-concentration field coupled to the continuity and Navier–Stokes equation for the solution. The hydrodynamic interactions are accounted for through the concentration dependence of the suspension viscosity, of the single-particle mobility, and of the momentum transfer between the particles and the suspension.

2) We derive a full 3D numerical model for the coupled acoustic fields in mm-sized water-filled glass capillaries, calculating pressure field in the liquid coupled to the displacement field of the glass channel, taking into account mixed standing and travelling waves as well as absorption. We model the connective tubing at the outlets, either as being free reflecting surfaces or perfect absorbers of outgoing acoustic waves, and we make an effective description of the mechanical actuation of the attached piezoelectric transducer.

3) Using the model for the acoustic field in glass capillary devices derived in 2), we make an effective model for calculating the acoustic streaming velocity in 3D. To do this, we use recent analytical results that allows calculation of the acoustic streaming field resulting from channel-wall oscillations in any direction, with significantly lower computational power requirements compared to previous methods, enabling full 3D calculations.

Resumé

I denne afhandling udvikler vi tre modeller for avancerede systemer indenfor mikroskala akustoffluidik. Grundet kompleksiteten af de valgte systemer, har målet i dette Ph.D.-projekt været at udvikle simplificerede og effektive beskrivelser af disse systemer, der fanger essensen af systemernes opførsel, i kontrast til udvikling af detaljerede modeller for idealiserede systemer. De effektive modeller udviklet i denne afhandling omhandler: 1) hydrodynamiske partikel-partikel vekselvirkninger i højkonzentrations mikropartikel-opslæmninger i mikrokanaler, 2) akustiske felter i mm-størrelse væskefyldte glas kapillarrør, anvendt som en akustisk fælde, og 3) udregning af akustiske strømningsfelter for glas-kapillarrør-systemet fra model 2).

1) Vi udvikler en numerisk effektiv model for hydrodynamiske partikel-partikel vekselvirkninger i højkonzentrations mikropartikel-opslæmninger. En højkonzentrations opslæmning placeres i en mikrokanal, hvor mikropartiklerne udsættes for eksterne kræfter. Partiklerne beskrives som et kontinuums-konzentrationsfelt der kobles til kontinuitets- og Navier–Stokes ligningen for partikel-opslæmningen. De hydrodynamiske vekselvirkningers koncentrationsafhængighed beskrives gennem en effektiv viskositet, en effektiv én-partikel mobilitet, og impulsoverførsel mellem partikler og væske.

2) Vi udvikler en numerisk model i fuld 3D for de akustiske felter i mm-størrelse væskefyldte glas-kapillarrør. Vi beregner det akustiske tryk-felt i væsken, samt de mekaniske forskydninger i glasset, og der tages højde for blandingen af stående og rejsesende bølger, samt absorption. Vi modellerer slangerne forbundet til kanalen som enten frie reflekterende overflader, eller som perfekt absorberede udgående bølger, og den mekaniske aktivering fra den piezoelektriske aktuator beskrives med en effektiv model.

3) Som en udvidelse af model 2), udvikler vi en effektiv model for beregning af den akustiske strømning i 3D i glas-kapillarrør som beskrevet i 2). Dette realiseres ved at anvende nye analytiske resultater der tillader beregning af det akustiske strømningsfelt som resultat af de vibrerende kanalvægge i kapillarrøret. Denne metode sænker den nødvendige regnekraft markant i forhold til tidligere beregningsmetoder, hvilket muliggør beregninger i fuld 3D.

Preface

This thesis is submitted as partial fulfilment of the prerequisites for obtaining the degree of Doctor of Philosophy (Ph.D.) at the Technical University of Denmark (DTU). The project was financed partly by a grant from Lund University, Sweden and partly by the Technical University of Denmark, and was carried out at the Department of Physics, DTU, over a three year period from August 2014 to August 2017. The project was supervised by professor Henrik Bruus, leader of the Theoretical Microfluidics Group (TMF) at the Department of Physics.

As an important research collaboration and source of very valuable input and sparring, I have visited and collaborated with the research group led by Professor Thomas Laurell at department of biomedical engineering at Lund University, Sweden. Especially, I would like to thank Carl Johannesson, Mikael Evander and Thomas Laurell for a fruitful collaboration and many interesting discussions, as this has proved an invaluable part of making relevant and useful theoretical contributions to the field of acoustofluidics.

As part of my studies I visited the group of professor Jürg Dual at the Federal Institute of Technology, Zürich, Switzerland, from August 28, 2016 to December 22, 2016.

Firstly, I would like to thank my supervisor Henrik Bruus for his competent supervision and mentorship over the past five years, always wanting us, his students, to understand, and perform to the best of our ability. I am thankful to Henrik for being given the opportunity to be part of TMF these years, and to his ability to attract ambitious and intelligent students, to have as wonderful colleagues and friends. I am both proud and happy to have been a part of that. Additionally, I would like to thank past and present members of the group: Rune Barnkob, Peter Muller Tribler, Christoffer Nielsen, Rayisa Moiseyenko, Fabio Garofalo, Nils Refstrup Skob, and Jacob Søberg. Last, and most importantly I want to express my deep gratitude and respect to my colleague, office-buddy, and close friend Jonas Tobias Karlsen, for always being there for me, professionally as well as personally. This journey would not have been the same without you.

Secondly, I would like to thank professor Jürg Dual and his group at ETH for welcoming me during my visit in the fall 2016, for being warm, including, and creating an open and friendly lab-atmosphere. Furthermore, I would to thank my friend and Ph.D. student Seraina Dual at for helping me settle in at my research visit in Zürich, both professionally and especially socially.

I would like to thank all my friends in the danish swing dancing community, because dancing has been a much needed outlet and respite away from the computer and the equations. Having you and dancing in my life during my Ph.D. studies have been vital in

the weekly renewal of the energy needed to finish what at times can seem like a Sisyphean-task.

I would also like to thank my close friends Andreas, Johannes, Hjalte and Jens for being a much needed social base in the past many years, and for enabling me in creating a healthy work-life balance during my studies.

Finally, I would like to thank my parents Susan and Poul-Henning, and my brothers Tjalfe and Julius for always believing in me, and for being proud of my achievements at times when I fail to appreciate them myself.

Kongens Lyngby, 14 August 2017

A handwritten signature in black ink, reading "Mikkel Ley". The signature is written in a cursive, slightly slanted style.

Mikkel Wennemoes Hvitfeld Ley
Department of Physics
Technical University of Denmark

Table of Contents

Abstract	iii
Resumé	v
Preface	vii
List of figures	xi
List of figures	xiv
List of tables	xiv
List of symbols	xvii
Material parameter list	xxi
1 Introduction	1
1.1 Acoustofluidics	1
1.2 Phenomena in acoustofluidics	2
1.3 The motivation for this thesis work	3
1.4 Outline of this thesis	4
1.5 Publications throughout the Ph.D.	5
2 Theory	7
2.1 Basic Governing Equations	7
2.1.1 Fluid Governing Equations	7
2.1.2 Solid Governing Equations	8
2.1.3 Governing Equations for suspended microparticles	8
2.2 First-order adiabatic acoustics	9
2.2.1 Solid	9
2.2.2 Fluid	9
2.3 Second-order acoustics	12
2.3.1 Governing equations	12
2.3.2 Second order acoustic effects	12
2.4 Concluding remarks	14

3	Numerical methods	15
3.1	The Finite Element Method	15
3.1.1	Boundary conditions in the weak formulation	17
3.2	Mesh convergence	18
3.3	Concluding remarks	19
4	Effective modeling of hydrodynamic interactions	21
4.1	Motivation and approaches for calculating dense suspension dynamics . . .	21
4.2	Model system	23
4.2.1	2D Parallel plate system	24
4.2.2	Forces and effective particle transport	24
4.2.3	Effective viscosity and flow of the suspension	24
4.2.4	Boundary conditions	25
4.2.5	Dimensionless, effective transport coefficients	25
4.2.6	Dimensionless parameters	26
4.3	Numerical implementation	27
4.3.1	Numerical validation and mesh convergence test	27
4.4	Model results	28
4.4.1	Results for magnetophoresis (MAP)	28
4.4.2	Results for acoustophoresis (ACP)	32
4.5	Discussion	35
4.6	Concluding remarks	37
5	Effective modeling of acoustofluidic capillary devices	39
5.1	Introduction	39
5.2	Effective modeling	41
5.2.1	Governing equations	42
5.2.2	Boundary conditions	42
5.2.3	The outlet and perfectly matched layers	44
5.2.4	Mesh	44
5.2.5	Model validation	46
5.3	Results	48
5.3.1	Analysis of capillary C1	49
5.3.2	Analysis of capillary C2	55
5.3.3	Analysis of capillary C3	56
5.3.4	Analysis of capillary C4	57
5.3.5	Analysis of capillary C5	58
5.4	Discussion	61
5.5	Concluding remarks	63
6	Effective modeling of streaming in acoustofluidic capillary devices	65
6.1	Effective modeling of acoustic streaming	66
6.1.1	First-order effective equations	67
6.1.2	Second-order effective equations	67

6.2	Preliminary 2D effective streaming results	69
6.2.1	2D validation study of the effective model	69
6.2.2	First-order fields	71
6.2.3	Second-order fields	71
6.2.4	The role of a moving wall in second-order acoustics	72
6.3	Preliminary 3D effective streaming results	73
6.3.1	3D effective streaming in the C1 capillary	74
6.4	Discussion	78
6.4.1	Comparison with the 2D-validation model	80
6.4.2	The rescaled pressure \tilde{p}_2	80
6.4.3	The influence of the bulk driving terms for the acoustic streaming . .	81
6.4.4	Comparison with experiments and other effective models in the literature	81
7	Concluding remarks and outlook	83
A	Paper published in Lab on a Chip	85
B	Paper accepted for publication in Physical Review Applied	97
	Bibliography	119

List of Figures

1.1	Sketch of various phenomena involved in operating an acoustofluidic device	2
1.2	Concept sketch of acoustic radiation force and acoustic streaming in acoustofluidics	3
3.1	Discretezation of the computation domain Ω in COMSOL	16
4.1	Sketch of the model system.	23
4.2	Plot of the fitted dimensionless effective transport χ -coefficients	26
4.3	Plot of the particle capture fraction β	28
4.4	Specific realizations of the generic system shown in Fig. 4.1	29
4.5	Heat color plot of the normalized concentration in MAP case	30
4.6	Plot quantifying the hydrodynamic interactions effects in the map case . . .	31
4.7	Plot of the acoustic radiation force used in the ACP case	33
4.8	Heat color plot of the normalised concentration in the MAP case	33
4.9	Plot quantifying the hydrodynamic interactions effects in the acp case . . .	35
4.10	Comparison between numerics and experiment for acp model	36
5.1	A sketch of the generic capillary system for acoustic trapping considered . .	40
5.2	Sketches of the capillary cross sections C1-C5 investigated	41
5.3	The computational domain used in the numerical model of Fig. 5.1	43
5.4	A coarse version of the mesh at the surface of the computational domain . .	45
5.5	Figure quantifying the validity regime of the PML	47
5.6	Semilog plot of the mesh-convergence parameter C	48
5.7	Frequency response of the C1 capillary: numerical (a), and experimental (b)	49
5.8	The acoustic resonance field of the C1 capillary	50
5.9	Capillary C1, color plot of the pressure field p_1 in vertical x - z planes	51
5.10	Comparison between lateral trapping force: (a),(b) numerical, and (c) experimental	53
5.11	Simulated frequency response of capillary C4	57
5.12	Capillary C5, plot of the resonant fluid pressure field p_1	59
5.13	Capillary C5, plot of the resonant solid displacement field \mathbf{u}_1	59
5.14	Capillary C5, plot of the resonant pressure field p_1 in vertical x - z planes . .	60
5.15	Capillary C5, plot of the resonant lateral radiation force $\mathbf{F}_{\parallel}^{\text{rad}}$	60

6.1	Sketch of a 2D mesh grid, for a full vs. an effective streaming model	66
6.2	Color plot of the first-order fields for the C5 capillary geometry, 2D model .	71
6.3	Second-order streaming field for the C5 capillary geometry, 2D model	72
6.4	Second-order streaming fields for different solid-fluid boundary conditions .	73
6.5	1st and 2nd order fields for an effective 3D model of the C5 capillary	75
6.6	Color plot of the effective streaming in the C1 capillary	76
6.7	Picture of streaming experiment for the C1 capillary geometry	77
6.8	Repeat of Fig. 6.6(b) investigating the different streaming driving terms . .	79

List of Tables

1	Material parameters at 25 C° and 4 MHz.	xxi
4.1	Number of mesh elements and degrees of freedom in the COMSOL model .	27
5.1	The capillary geometries C1-C5 modeled in this study	40
5.2	Boundary conditions used in the coupled glass capillary-water model	43
5.3	List of the mesh parameters used in the model	46
5.4	Experimental data of drop voltage measurements for the C1 capillary	55
5.5	Simulation results for the quadratic capillary C3	56
6.1	Changes to the boundary conditions for p_1 and \mathbf{u}_1 compared to Table 5.2 .	67
6.2	Boundary conditions for the effective streaming model	69
6.3	Boundary conditions used in the full 2D validation-model	70

List of symbols

Physics symbols

Symbol	Description	Unit/value
a	Radius of a microparticle	m
c	Concentration of microparticles	m^{-3}
c_0	Reference or initial concentration	m^{-3}
c_s	Isentropic speed of sound in fluid	m s^{-1}
c_{lo}	Longitudinal speed of sound in linear elastic solid	m s^{-1}
c_{tr}	Transverse speed of sound in linear elastic solid	m s^{-1}
C	Mesh convergence parameter	1
d_0	Characteristic actuation displacement amplitude	0.1 nm
\mathbf{d}	Wire-dipole separation vector	m
D	Diffusivity of microparticles	m^2/s
DOF	Degrees of freedom in the discretized weak form	1
δ	Viscous boundary layer thickness	m
E	Young's modulus	Pa
E_{ac}	Acoustic energy density	Pa
η	Dynamic viscosity of fluid	Pa s
η_{B}	Bulk viscosity of fluid	Pa s
f	Frequency	Hz
f_0, f_1	Mono- and dipole scattering coefficients	1
\mathbf{f}	Body force density	N/m^3
\mathbf{F}	Migration force on microparticle	N
γ	Viscous boundary layer correction factor for f_1 , see Eq. (2.37c)	1
Γ	Acoustic damping factor	1
Γ_{surf}	Flux of microparticles per length	$\text{m}^{-1} \text{s}^{-1}$
$\mathbf{\Gamma}$	General flux in the discretized weak formulation	varies
H	Height of microchannel/parallel plate system	m
\mathbf{H}	Magnetic field	A m^{-1}
I	Electrical current	A
\mathbf{J}	Microparticle flux density	$\text{m}^{-2} \text{s}^{-1}$

Symbol	Description	Unit/value
k_B	Boltzmann constant	1.38×10^{-23} J/K
k	Wavenumber	m^{-1}
κ_0	Isentropic compressibility per unit volume of fluid	Pa^{-1}
L	System length	m
μ	Particle mobility	s kg^{-1}
ν	Poissons ratio	1
p	Pressure	Pa
ϕ	Microparticle volume fraction	m^{-3}
Φ	Acoustic contrast factor	1
Pe	Péclet number, $\tau_{\text{diff}}/\tau_{\text{adv}}$	1
Q	Quality factor	1
ρ	Mass density	kg/m^3
R	Radius of curvature of corner/channel	m
St	Transient Strouhal number, $\tau_{\text{adv}}/\tau_{\text{mig}}$	1
s	Logarithmic particle concentration, $\log(c/c_0)$	1
\mathbf{s}	Strain tensor	1
$\boldsymbol{\sigma}$	Stress tensor	Pa
T	Absolute temperature	K
τ	Characteristic time scale, diffusive (diff), advective (adv), migrative (mig)	s
\mathbf{u}	Solid displacement field	m
\mathbf{v}	Velocity vector	m/s
W	System width	m
χ	Dimensionless transport coefficient, see Section 4.2.5	1
ω	Angular frequency	rad s^{-1}

Mathematical operators and symbols

Symbol	Description	Unit/value
$\langle \square \rangle$	Time average of \square	varies
$ \square $	Absolute value of \square	varies
\square^*	Complex conjugate of \square	varies
\square^T	Matrix transpose of \square	varies
$\hat{\square}$	Test function of \square	varies
\square_1	First order of \square	varies
\square_2	Second order of \square	varies
$\mathbf{a} \cdot \mathbf{b}$	Scalar product between \mathbf{a} and \mathbf{b}	varies
$\mathbf{a} \times \mathbf{b}$	Cross product between \mathbf{a} and \mathbf{b}	varies
$\mathbf{a} : \mathbf{b}$	Full contraction between \mathbf{a} and \mathbf{b}	varies
\mathbf{n}	Normal unit vector	1
e	Eulers number	2.71828...
$\mathbf{e}_x, \mathbf{e}_y, \mathbf{e}_z$	Unit vectors in Cartesian coordinates	1
∂_i	Partial derivative w. r. t. i 'th coordinate	m^{-1}
$\partial\Omega$	Boundary of calculation domain	varies
i	Imaginary unit	1
\mathbf{I}	Unit tensor	1
$\text{Im}[\square]$	Imaginary part of \square	varies
\log	Logarithm with base e	1
∇	Nabla operator	m^{-1}
∇^2	Laplace operator	m^{-2}
\mathbf{r}	Position vector	m
$\text{Re}[\square]$	Real part of \square	varies
\mathbf{t}	Tangential unit vector	m
Ω	Calculation domain	varies

Material parameter list

Table 1: Material parameters at 25 C° and 4 MHz.

<i>Water</i> [1]:			
Mass density	ρ_0	997.05	kg m ⁻³
Compressibility	κ_0	452	TPa ⁻¹
Speed of sound	c_0	1496.7	m s ⁻¹
Dynamic viscosity	η	0.890	mPa s
Bulk viscosity [2]	η_B	2.485	mPa s
Effective damping coefficient [3]	Γ_{fl}	0.004	
Viscous boundary layer	δ	0.27	μm
<i>Pyrex glass</i> [4]:			
Mass density	ρ_{sl}	2230	kg m ⁻³
Young's modulus	E	62.75	GPa
Poisson's ratio	ν	0.2	
Speed of sound, longitudinal	c_{lo}	5592	m s ⁻¹
Speed of sound, transverse	c_{tr}	3424	m s ⁻¹
Effective damping coefficient [3]	Γ_{sl}	0.0004	
<i>Polystyrene</i> (ps) for 12 μm-diameter ps particles in water:			
Mass density [5]	ρ_{ps}	1050	kg m ⁻³
Compressibility [6]	κ_{ps}	249	TPa ⁻¹
Poisson's ratio [7]	ν_{ps}	0.35	
Speed of sound at 20 °C [8]	c_{ps}	2350	m s ⁻¹
Monopole coefficient, Eq. (2.37b)	f_0	0.48	
Dipole coefficient, Eq. (2.37c)	f_1	0.052-0.003i	

Chapter 1

Introduction

In modern biotechnology an ongoing challenge is the handling and manipulation of cells, bacteria, vira, and other bio-particles [9, 10, 11, 12, 13, 14, 15]. As a solution to this, microfluidics has since the 1990s proven an active research field and growing industry, as it allows for precise control of small fluid volumes, with a broad resolution range from litres per hour processing all the way to single cell measurements and manipulation. Microfluidic technology have thus found a wide range of uses within clinical diagnostics, bioscience, forensics science, and food science, with examples ranging from simple handheld blood glucose monitoring devices for diabetics, pregnancy tests, over to more sophisticated examples such as new techniques for rapid sepsis diagnostics [16], single cell manipulation [17], and increasingly faster and cheaper DNA sequencing [18]. These technologies rely on a number of physical phenomena for handling and manipulating the bio-microparticles, some of them being hydrophoresis, electrophoresis, magnetophoresis, electrophoresis, optophoresis, and acoustophoresis (see the review by [19]). However, one of the key parameters for successful commercialization of these technologies is throughput, and here only the hydrodynamic and acoustic systems are competitive [19]. Hydrodynamic systems offer simple device designs and can support high flow rates, as they rely solely on passive transport from inertial migration and drag induced by secondary flows [20]. However, they do not have the capabilities of active transport. In contrast, acoustofluidics does support active migration, basically due to the acoustic contrast between the suspending medium and the particles [21], and it is therefore an inherently label-free technique. Moreover, it exhibits high cell-viability, even over several days [22]. These aspects and other appealing traits, have increased the interest in acoustofluidic systems in recent years [23, 24].

1.1 Acoustofluidics

One of the pioneers of acoustofluidics was Coakley, who in 1989 published a journal paper [25] that investigated various types of manipulation of erythrocytes using ultrasonic standing waves fields. Since then, microscale acoustofluidic devices have been used increasingly in biology, environmental and forensic sciences, and clinical diagnostics [23, 24]. Examples include cell synchronization [26], enrichment of prostate cancer cells in blood [27], manip-

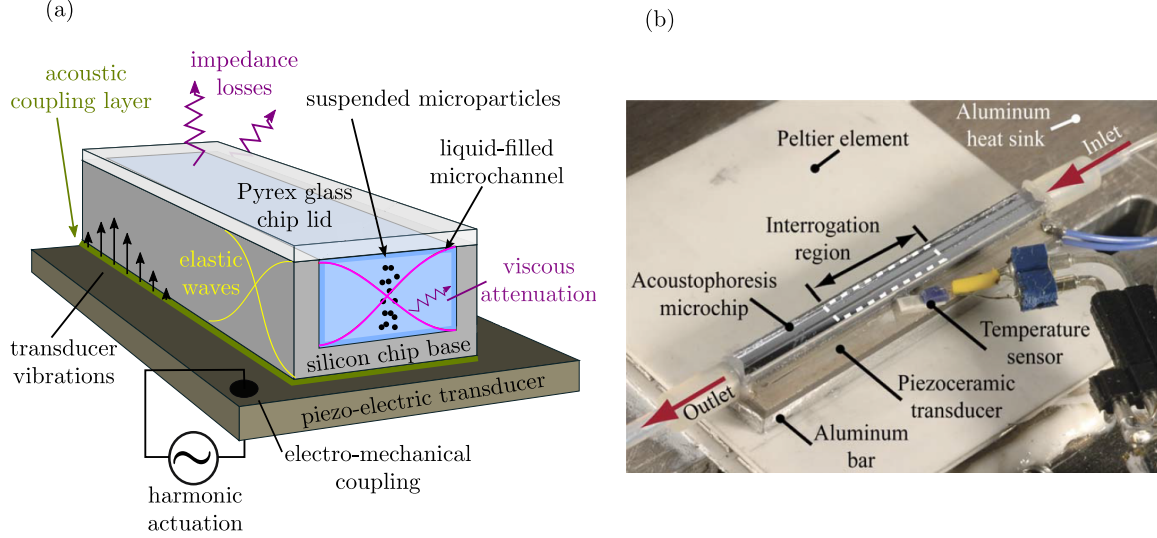


Figure 1.1: (a) Sketch of a generic acoustofluidic device of the bulk acoustic wave type, including the numerous and complex physical phenomena involved. The sketch is adapted from Barnkob [37]. (b) Photograph of an acoustofluidic device, from [38]

ulation of *C. elegans* [28], and single-cell patterning [17]. Acoustics can also be used for non-contact microfluidic trapping and particle enrichment [29, 30, 31] as well as acoustic tweezing [32, 33, 34, 35, 36].

A typical acoustofluidic device is shown in Fig. 1.1, where an acoustofluidic channel is actuated by a piezoelectric transducer that operates at MHz frequency, with an applied voltage of typically 1 to 10 V. At resonance the pressure waves (magenta) in the fluid increases drastically in magnitude, resulting in acoustic energies high enough to manipulate microparticles suspended in the fluid.

1.2 Phenomena in acoustofluidics

In acoustofluidics there are two main phenomena that transport and manipulate microparticles by the use of sound waves, namely acoustophoresis and acoustic streaming.

Acoustophoresis

When a sound wave travelling in a fluid medium hits a particle with a mass density or compressibility different from that of the fluid, the sound wave scatters on the particle, see Fig. 1.2(a).

Because the sound wave carries energy and momentum, the scattering process transfers momentum from the sound wave to the particle, and thus exerts a force on the particle. We call this force the acoustic radiation force \mathbf{F}^{rad} , and it plays a key role in acoustofluidic device technology, where it is used to sort, gather, and trap particles. Because this force is inherently label free, utilising only the difference in elastic properties between the particle

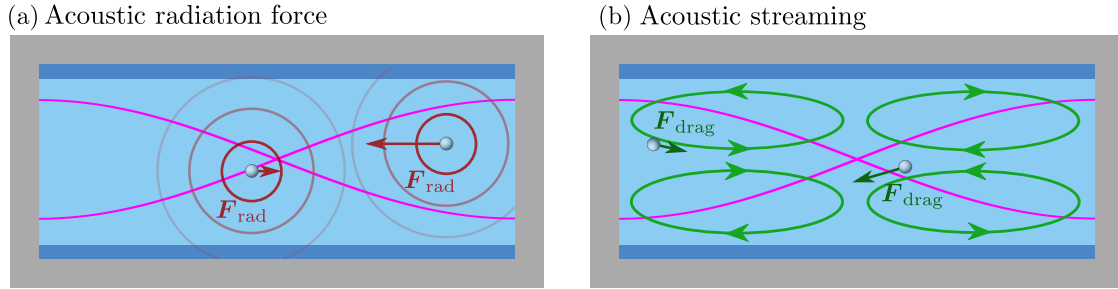


Figure 1.2: Conceptual illustration of the two main transport phenomena in acoustofluidics: (a) the acoustic radiation force, and (b) the acoustic streaming (b). The sketch shows a rectangular microchannel similar to the one seen in Fig. 1.1, with silicon walls (grey), filled with liquid (blue), and an acoustic standing half-wave in pressure is excited in the channel (magenta). (a) The standing wave scatters on the particles (grey), and the scattering process (red, wavelength not to scale) transfers momentum to the particle, thereby exerting a force on it, *i.e.* the acoustic radiation force \mathbf{F}_{rad} (dark red). (b) Close to the wall (dark blue), viscous effects generate large stresses in the liquid which causes a steady motion of the liquid, called acoustic streaming (green ellipses), which in turn exerts a drag force on the particles \mathbf{F}_{drag} (dark green).

and the fluid, it is easy to apply, and it has been shown that the ultrasonic fields does not impact biological cell viability, even over the course of several days [22], making it is an increasingly popular tool in microfluidic technology for next generation cell handling.

Acoustic streaming

Viscous effects and attenuation of the acoustic field in the fluid can cause time-average non-zero in forces on the liquid that drive a steady motion of the fluid called acoustic streaming. Acoustic streaming is typically divided into bulk-driven acoustic streaming (Eckart streaming), and boundary-driven acoustic streaming (Rayleigh streaming), where the first is due bulk absorption of the acoustic energy in the liquid, and the second is occurs due to shear effects near solid-fluid boundaries. In Fig. 1.2(b) we illustrate an example of Rayleigh streaming, where the no-slip condition forces the acoustic velocity to zero on a short length scale (dark blue layer) creating large stresses in the liquid which drive the steady streaming motion, dragging the particles with it by the Stokes drag force \mathbf{F}_{drag} .

1.3 The motivation for this thesis work

When operating an acoustofluidic device many effects are at play at the same time (Fig. 1.1(a)), and can furthermore be realised in many different designs and materials such as silicon [38, 39], glass [30], and PDMS [40]. Because of this complexity and variety it is an ongoing challenge to predict the performance of a given device, especially when ideal cases, such as axial symmetries, perfect geometries, dilute particle suspensions, and non-impacting device surroundings, no longer hold. In these cases it can sometimes appear fruitless merely guessing on a new device design, or using trial and error when trying to improve an experiment. It is for these cases we are interested in developing theoretical insight that can offer

simple design rules, and provide simple physical explanations for unexpected experimental results. We have therefore in this thesis work aimed to develop simple effective models for complex situations that captures the essential dynamics of the system, as opposed to making detailed calculations of idealised cases.

1.4 Outline of this thesis

In this thesis work we develop three effective models for experimentally relevant, yet complex acoustofluidic systems. The effective models developed in this thesis concerns: a) hydrodynamic particle-particle interactions in dense microparticle suspensions, see Chapter 4, b) the acoustic field in mm-size liquid-filled glass capillaries used for acoustic trapping, see Chapter 5, and c) acoustic streaming patterns in the glass-capillary devices considered in model b), see Chapter 6.

Chapter 2 - Theory

We outline the fundamental governing equations for: 1) A Newtonian fluid, 2) a homogeneous, isotropic, and linearly elastic solid, and 3) the concentration of particles undergoing diffusion, advection, and active migration. The solid and fluid equations are developed in the frame of adiabatic acoustics by the use of perturbation theory, and a few relevant second-order effects are discussed.

Chapter 3 - Numerical methods

The principle of the *weak formulation* for solving partial differential equations by the finite element method is introduced, and we derive the weak formulation in the case of a divergence equation and discuss the implementation of the most common boundary conditions. Lastly we introduce the concept of mesh-convergence tests as a numerical model validation tool used widely throughout this thesis work.

Chapter 4 - Effective modeling of hydrodynamic interactions

We derive an effective model for the hydrodynamic particle-particle interactions in a dense suspension of microparticles in a microfluidic channel undergoing active migration. We study two types of active migration: 1) magnetophoresis, and 2) acoustophoresis, and investigate the particle transport as a function of increasing particle concentration as it enters the high-concentration regime. From these studies we quantify the critical particle concentrations where the simple dilute-limit transport equations no longer hold, and hydrodynamic interactions have to be accounted for.

Chapter 5 - Effective modeling of acoustofluidic capillary devices

We derive an effective model for liquid-filled glass capillaries which are actuated by piezoelectric transducers, and used for acoustic trapping, separation, tweezing, and sorting. In particular we model the capillary actuation, and the capillary ends with connective tubing,

treating the latter as ideal absorbers with no significant acoustic reflections. We examine various capillary geometries reported used in the literature and study acoustic resonance structures and characteristics.

Chapter 6 - Effective modeling of streaming in acoustofluidic capillary devices

Building on the results of Chapter 5, we present preliminary results for an effective 3D model for the acoustic streaming in glass capillary devices described in chapter 5. The results were derived in the final weeks of the Ph.D.-project, and should be seen as preliminary. However, because good both qualitative and quantitative agreement is observed with experiments as well as previously published theoretical work, we have confidence in these preliminary findings.

Chapter 7 - Concluding remarks and outlook

We end the thesis with a few concluding remarks, and outline ideas for further work and future ideas for investigation.

1.5 Publications throughout the Ph.D.

This Ph.D.-thesis is largely based on two peer-reviewed journal papers, four peer-reviewed international conference contributions and four other conference contributions.

Peer-reviewed journal papers

- M. W. H. Ley and H. Bruus, *Continuum modeling of hydrodynamic particle-particle interactions in microfluidic high-concentration suspensions*, Lab Chip, **16** (2016), 1178-1188. Enclosed in Appendix A.
- M. W. H. Ley and H. Bruus, *Three-Dimensional Numerical Modeling of Acoustic Trapping in Glass Capillaries*, Phys. Rev. Applied, **8** (2017), pages. Proof version enclosed in Appendix B.

Peer-reviewed conference contributions

- M. W. H. Ley and H. Bruus, *Hydrodynamic interactions in microfluidic acoustophoresis*, Acoustofluidics, conference on microscale acoustofluidics, 11-12 September 2014, Prato, Italy, **oral presentation**.
- M. W. H. Ley and H. Bruus, *Design considerations for acoustic modes in glass capillaries used in acoustic trapping devices*, Acoustofluidics, conference on microscale acoustofluidics, 22-23 September 2016, Lyngby, Denmark, **oral presentation**.
- M. W. H. Ley, C. Johannesson, M. Evander, T. Laurell and H. Bruus, *Modeling and experiments of acoustic trapping forces in a small glass capillary*, μ TAS, conference

on microfluidics and lab-on-a-chip technology, 9-13 October 2016, Dublin, Ireland, **poster presentation**.

- J. S. Bach, M. W. H. Ley, H. Bruus, *Effective boundary-layer modelling of acoustics in 3D microchannels*, Flow 17, conference on general microfluidics, 3-5 July 2017, Paris, France, **poster presentation**.

Other conference contributions

- M. W. H. Ley and H. Bruus, *Hydrodynamic interactions in microfluidics*, DANSIS seminar, seminar on applied fluid dynamics, 20 May 2015, Lyngby, Denmark, **oral Presentation**.
- M. W. H. Ley and H. Bruus, *Hydrodynamic interaction dynamics in microfluidic acoustophoresis systems*, FLUID DTU summerschool, summer school on fluid dynamics, 9-15 August 2015, Humlebæk, Denmark, **oral Presentation**.
- M. W. H. Ley and H. Bruus, *Hydrodynamic interactions in flowthrough microfluidic acoustophoresis*, SWECACS seminar, research seminar within the SWECACS acoustofluidics research network, 2 December 2015, Lund, Sweden, **oral Presentation**.
- M. W. H. Ley and H. Bruus, *3D simulations of the acoustic glass-capillary trap*, SWECACS seminar, research seminar within the SWECACS acoustofluidics research network, 29 November 2016, Lund, Sweden, **oral Presentation**.

Chapter 2

Theory

In Chapter 1 we saw that the typical acoustofluidic setup comprises of a sub mm-sized channel infused with liquid, that suspends a number of microparticles, all subjected to ultrasound. To give a theoretical description of this, we start with the governing equations for newtonian fluids and linear elastic solids in the continuum limit, and develop these in the frame of acoustics by employing a perturbation scheme. Furthermore, to model the particle dynamics, we consider for the most part the particles as a continuous concentration field, including advection, diffusion and migration, following a Nernst–Planck like approach. For a more in-depth treatment of the theoretical topics in this thesis, we refer the reader to the textbooks by Landau and Lifshitz [41, 42], Happel and Brenner [43], Leal [44], and Bruus [45].

2.1 Basic Governing Equations

In this section we outline the basic governing equations for the fluid, the solid, and the particle concentration fields.

2.1.1 Fluid Governing Equations

To form the governing equations for the fluid, we demand continuity of the fluid mass density and the fluid momentum density. For the fluid mass density we obtain

$$\partial_t \rho = -\nabla \cdot (\rho \mathbf{v}) , \quad (2.1)$$

where ρ is the fluid mass density, and \mathbf{v} is the fluid velocity field.

For the fluid momentum density

$$\partial_t (\rho \mathbf{v}) = \nabla \cdot (\boldsymbol{\sigma} - \rho \mathbf{v} \mathbf{v}) + \mathbf{f} , \quad (2.2)$$

where $\boldsymbol{\sigma}$ is the stress tensor for the fluid and \mathbf{f} is bulk forces acting on the fluid.

For a newtonian fluid the stress tensor is

$$\boldsymbol{\sigma} = \eta [\nabla \mathbf{v} + (\nabla \mathbf{v})^T] - \mathbf{I} \left[p + \left(\frac{2}{3} \eta - \eta_B \right) \nabla \cdot \mathbf{v} \right] , \quad (2.3)$$

where η is the shear viscosity, T denotes a matrix transpose, \mathbf{I} is the unit tensor, p is the fluid pressure, and η_B is the bulk viscosity.

2.1.2 Solid Governing Equations

For the governing equation for the displacement field \mathbf{u} of a linear elastic solid, we invoke Newtons second law per unit volume

$$\rho_{\text{sl}} \partial_t^2 \mathbf{u} = \nabla \cdot \boldsymbol{\sigma}_{\text{sl}} + \mathbf{f}, \quad (2.4)$$

where the roman subscript 'sl' denotes properties of the solid, and $\boldsymbol{\sigma}_{\text{sl}}$ and \mathbf{f} again denotes the stress and the external forces, respectively, acting on the material.

For a linear elastic material, the solid stress tensor for small strains becomes

$$\boldsymbol{\sigma}_{\text{sl}} = \frac{E}{2(1+\nu)} [\nabla \mathbf{u} + (\nabla \mathbf{u})^T] + \frac{E}{1+\nu} \frac{\nu}{(1-2\nu)} \mathbf{I}(\nabla \cdot \mathbf{u}), \quad (2.5)$$

where E and ν are Youngs modulus and Poissons ratio of the material, respectively.

Lastly, it is convenient to introduce the symmetric strain tensor for the solid

$$\mathbf{s} = \frac{1}{2} [\nabla \mathbf{u} + (\nabla \mathbf{u})^T]. \quad (2.6)$$

2.1.3 Governing Equations for suspended microparticles

For the particles, we describe the local number of particles dN in a small volume dV as the particle volume concentration $c = \frac{dN}{dV}$. The particle concentration field is, like the fluid, governed by a continuity equation

$$\partial_t c = -\nabla \cdot \mathbf{J}, \quad (2.7)$$

where \mathbf{J} is the total particle current density, which can be divided into diffusion (diff), advection (adv), and migration (mig) current densities

$$\mathbf{J} = \mathbf{J}_{\text{diff}} + \mathbf{J}_{\text{adv}} + \mathbf{J}_{\text{mig}} \quad (2.8a)$$

$$= -D \nabla c + c \mathbf{v} + c \mu \mathbf{F}_{\text{mig}}. \quad (2.8b)$$

Here, D is the diffusion coefficient, and μ is particle mobility, which in the limit of low particle concentrations D and μ are given by the Stokes-Einstein relation $D = k_B T / (6\eta\pi a)$, and the inverse Stokes drag $\mu = 1 / (6\pi\eta a)$, respectively, where k_B is Boltzmanns constant, and T is the absolute temperature.

Because we want to (numerically) ensure that $c > 0$ everywhere at all times, we write the concentration in logarithmic form

$$s = \log \left(\frac{c(\mathbf{r})}{c_0} \right), \quad (2.9)$$

where c_0 is a characteristic concentration. Note that s is allowed to take on any real value and will always produce a positive value for the concentration.

2.2 First-order adiabatic acoustics

To develop the governing equations in the frame of acoustics, we employ perturbation theory for both the fluid and the solid, assuming the system to be at rest initially

$$\mathbf{v} = \mathbf{0} + \mathbf{v}_1 + \mathbf{v}_2, \quad (2.10a)$$

$$p = p_0 + p_1 + p_2, \quad (2.10b)$$

$$\rho = \rho_0 + \rho_1 + \rho_2, \quad (2.10c)$$

$$\mathbf{u} = \mathbf{0} + \mathbf{u}_1 + \mathbf{0}. \quad (2.10d)$$

Furthermore, because the external actuation is time-harmonic, all first-order field will have the harmonic time dependence $g(\mathbf{r}, t) = g(\mathbf{r})e^{-i\omega t}$, which implies that all first-order time derivatives can be written as $\partial_t \rightarrow -i\omega$.

2.2.1 Solid

For the solid we have no external bulk forces $\mathbf{f} = \mathbf{0}$, and we insert the harmonic time dependence. Thus, the solid-elastic equations (2.4) and (2.5) are only reduced slightly for first-order acoustics

$$-\rho_{\text{sl}}\omega^2\mathbf{u}_1 = \nabla \cdot \boldsymbol{\sigma}_{\text{sl}}, \quad (2.11a)$$

$$\boldsymbol{\sigma}_{\text{sl}} = \frac{E}{2(1+\nu)} [\nabla\mathbf{u}_1 + (\nabla\mathbf{u}_1)^T] + \frac{E}{1+\nu} \frac{\nu}{(1-2\nu)} \mathbf{I}(\nabla \cdot \mathbf{u}_1). \quad (2.11b)$$

Because we are working with wave propagation and acoustics, it is convenient to introduce the longitudinal (lo), and transverse (tr) speed of sound in the solid that are functions of Young's modulus, Poisson's ratio, and the solid mass density

$$c_{\text{tr}}^2 = \frac{1}{2(1+\nu)} \frac{E}{\rho_{\text{sl}}}, \quad c_{\text{lo}}^2 = 2c_{\text{tr}}^2 \frac{1-\nu}{1-2\nu}. \quad (2.12)$$

2.2.2 Fluid

For the fluid, we have two governing Eqs. (2.1) and (2.2), one scalar and one vectorial, and we have two independent scalar variables (mass density ρ_1 and pressure p_1), and one vectorial (velocity \mathbf{v}_1). To solve this we develop the equation of state, in order to relate the first-order pressure p_1 and the mass density ρ_1 . Assuming that the wave propagation in the fluid happens with negligible viscous losses (which we will justify later), we can approximate the wave propagation process to be adiabatic. Choosing pressure and entropy s , as our two thermodynamic variables, we express the isentropic compressibility of the fluid in terms of the mass density ρ

$$\kappa_0 = -\frac{1}{V} \left(\frac{\partial V}{\partial p} \right)_s = -\frac{1}{V} \left(\frac{\partial \left(\frac{M}{\rho} \right)}{\partial p} \right)_s = \frac{M}{V} \frac{1}{\rho^2} \left(\frac{\partial \rho}{\partial p} \right)_s = \frac{1}{\rho} \left(\frac{\partial \rho}{\partial p} \right)_s, \quad (2.13)$$

where M and V is the mass and the volume, respectively, of a given fluid particle. Again using that the sound propagation is adiabatic, we can Taylor expand the mass density to 1st order, and insert the isentropic compressibility

$$\rho(p) \cong \rho_0 + p_1 \left(\frac{\partial \rho}{\partial p} \right)_s = \rho_0 + p_1 \rho_0 \kappa_0 = \rho_0 + p_1 \frac{1}{c_0^2}, \quad (2.14)$$

where in the last term we have introduced the isentropic speed of sound in the fluid as

$$c_0 = \sqrt{\frac{1}{\rho_0 \kappa_0}}. \quad (2.15)$$

Using this relation between ρ_1 and p_1 , we obtain the first-order mass continuity equation (2.1)

$$-i\omega \kappa_0 p_1 = -\nabla \cdot \mathbf{v}_1, \quad (2.16)$$

and neglecting external bulk forces on the fluid, we get for the first-order momentum density equation (2.2)

$$-i\omega \rho_0 \mathbf{v}_1 = \nabla \cdot \boldsymbol{\sigma}_1 = -\nabla p_1 + \eta \nabla^2 \mathbf{v}_1 + \left(\frac{1}{3} \eta + \eta_B \right) \nabla (\nabla \cdot \mathbf{v}_1), \quad (2.17)$$

and the first-order fluid stress tensor is simply

$$\boldsymbol{\sigma}_1 = \eta [\nabla \mathbf{v}_1 + (\nabla \mathbf{v}_1)^T] - \mathbf{I} \left[p_1 + \left(\frac{2}{3} \eta - \eta_B \right) \nabla \cdot \mathbf{v}_1 \right]. \quad (2.18)$$

Decomposing the first-order field in shear and compressional waves

Next, to reach the final wave equations for the first-order fields, we decompose the first-order field into compressional and shear waves. We use the vector identity

$$\nabla^2 \mathbf{A} = \nabla (\nabla \cdot \mathbf{A}) - \nabla \times \nabla \times \mathbf{A}. \quad (2.19)$$

Using Eq. (2.19), we can split the right hand side off Eq. (2.17) into a gradient part and a curl part

$$-i\omega \rho_0 \mathbf{v}_1 = \nabla \left[-p_1 + \left(\frac{4}{3} \eta + \eta_B \right) (\nabla \cdot \mathbf{v}_1) \right] - \eta \nabla \times \nabla \times \mathbf{v}_1. \quad (2.20)$$

From here, it is natural to use a Helmholtz decomposition to split the first-order velocity into the compressional part (c) and the shear part (s),

$$\mathbf{v}_1 = \mathbf{v}_1^c + \mathbf{v}_1^s, \quad \nabla \times \mathbf{v}_1^c = \mathbf{0}, \quad \nabla \cdot \mathbf{v}_1^s = 0 \quad (2.21)$$

which implies that that the two continuity Eqs. (2.16) and (2.20) take the form

$$-i\omega \kappa_0 p_1 = -\nabla \cdot \mathbf{v}_1^c, \quad (2.22a)$$

$$-i\omega \rho_0 (\mathbf{v}_1^c + \mathbf{v}_1^s) = \nabla \left[-p_1 + \left(\frac{4}{3} \eta + \eta_B \right) (\nabla \cdot \mathbf{v}_1^c) \right] - \eta \nabla \times \nabla \times \mathbf{v}_1^s. \quad (2.22b)$$

We note that the first-order pressure only couples to the compressional velocity \mathbf{v}_1^c , and by inserting the divergence of \mathbf{v}_1^c from Eq. (2.22a), we can express the compressional velocity as the gradient of the pressure

$$\mathbf{v}_1^c = \frac{-i}{\omega\rho_0}(1 - i\Gamma)\nabla p_1. \quad (2.23)$$

Here,

$$\Gamma = \omega\kappa_0 \left(\frac{4}{3}\eta + \eta_B \right), \quad (2.24)$$

and is a dimensionless parameter characterising the bulk viscous damping in the fluid. For water at ambient temperature and a frequency of $f = 4$ MHz, $\Gamma = 4.2 \times 10^{-5} \ll 1$, meaning that viscous damping for sound wave propagation at MHz frequencies is very small. From Eq. (2.22) we can generate the three governing Helmholtz equations: one for p_1 , one for \mathbf{v}_1^c , and one for \mathbf{v}_1^s . For p_1 we take the divergence of Eq. (2.22b), and substitute $\nabla \cdot \mathbf{v}_1^c$ for p_1 from Eq. (2.22a), and for the two velocities, we separate Eq. (2.22b) in compressive and shear terms

$$\nabla^2 p_1 = -k_c^2 p_1, \quad (2.25a)$$

$$\nabla^2 \mathbf{v}_1^c = -k_c^2 \mathbf{v}_1^c, \quad (2.25b)$$

$$\nabla^2 \mathbf{v}_1^s = -k_s^2 \mathbf{v}_1^s, \quad (2.25c)$$

where

$$k_c = \frac{\omega}{c_0} \left(1 + \frac{1}{2}i\Gamma \right), \quad (2.26)$$

and

$$k_s = \frac{1+i}{\delta}, \quad (2.27)$$

where in the shear wave number k_s , we naturally get the length scale of the viscous boundary layer

$$\delta = \sqrt{\frac{2\eta}{\rho_0\omega}}. \quad (2.28)$$

For water at room temperature and an actuation frequency of $f = 4$ MHz, the viscous boundary layer is $\delta = 0.27 \mu\text{m}$. This length scale represents the distance from fluid-solid boundaries where the shear viscosity plays a role. The nature of the shear waves can be understood by noting that the real and imaginary parts of k_s are equal in size, meaning that the propagating and the decaying part of the shear wave are equally important, and will produce highly damped waves on the length scale δ , with largest magnitudes at the solid-fluid boundaries, and can largely be neglected at distances 5δ or more from any wall.

For the compressional wave, we see that Γ enters directly in the compressional wave number k_c as a small imaginary part, and can thereby readily be interpreted as a small viscous damping factor of the compressional mode, and can in some cases be neglected. This implies that the compressional part of the velocity represents a propagating wave

with very little damping and a wavelength $\lambda = \frac{2\pi c_0}{\omega}$. For device dimensions $L \gg \delta$, and at distances far away from solid-fluid boundaries, the acoustic field is well modelled by considering only the compressional waves, which are found by solving Eq. (2.25a) for p_1 , and using Eq. (2.23) to relate p_1 and \mathbf{v}_1^c .

Throughout the thesis we vary the computational complexity when calculating the acoustic field, \mathbf{v}_1 and p_1 , all depending on the aim of the specific model. Mostly we focus on the compressional part of the acoustic field (chapters 4 and 5), but for some calculations (in chapter 6), we include the effects of the shear field \mathbf{v}_1^s through an effective model in order to calculate the acoustic streaming.

2.3 Second-order acoustics

When developing the governing equations to second order, products of first-order fields can give rise non-zero time-averaged effects. This stands in contrast to all the first-order fields that inherit the harmonic time dependence $e^{-i\omega t}$ from the external actuation, and therefore time-average to zero when integrated over period $T = \frac{2\pi}{\omega}$. We define the time-average of a time-dependent field $g(t)$ as

$$\langle g \rangle = \frac{\omega}{2\pi} \int_0^{\frac{2\pi}{\omega}} g(t) dt. \quad (2.29)$$

2.3.1 Governing equations

The time averaged mass continuity equation (2.1), and momentum continuity equation (2.2) to 2nd order respectively become

$$0 = \rho_0 \nabla \cdot \langle \mathbf{v}_2 \rangle + \nabla \cdot \langle \rho_1 \mathbf{v}_1 \rangle, \quad (2.30)$$

$$\mathbf{0} = \nabla \cdot (\langle \boldsymbol{\sigma}_2 \rangle - \langle \rho_0 \mathbf{v}_1 \mathbf{v}_1 \rangle), \quad (2.31)$$

where we have used that the time-average of any time derivative $\partial_t g(t)$, where $g(t)$ is some time-periodic function, is zero $\langle \partial_t g(t) \rangle = 0$. Furthermore, the second-order fluid stress tensor becomes

$$\boldsymbol{\sigma}_2 = \eta [\nabla \mathbf{v}_2 + (\nabla \mathbf{v}_2)^T] - \mathbf{I} \left[p_2 + \left(\frac{2}{3} \eta - \eta_B \right) (\nabla \cdot \mathbf{v}_2) \right]. \quad (2.32)$$

To calculate the time average between products of first-order fields, we use the theorem

$$\langle A(t)B(t) \rangle = \frac{1}{2} \text{Re} [A^*(0)B(0)], \quad (2.33)$$

where $A(t)$ and $B(t)$ must be time-harmonic, and the asterisk denotes complex conjugation.

2.3.2 Second order acoustic effects

In the following we briefly discuss some of the central second-order concepts and phenomena occurring in microscale acoustofluidics.

Acoustic Streaming

When solving the governing Eqs. (2.30) and (2.31) for \mathbf{v}_2 and p_2 , we are solving for the so-called acoustic streaming fields, which are slow steady fluid motion happening on millisecond to second timescales compared to the fast first-order fields that oscillate on the timescale $\frac{1}{f}$, which is μs -timescales at MHz frequencies. The acoustic streaming plays an important role in microscale acoustofluidics as the steady streaming field moves the particles around as the particles are subjected to the Stokes drag force from the steady streaming velocity \mathbf{v}_2 .

The acoustic energy density

The acoustic fields, *i.e.* the first-order fields, p_1 , \mathbf{v}_1 in the fluid and \mathbf{u}_1 in the solid, physically represent small oscillatory motions and compressions and is therefore associated with a certain amount of acoustic energy. To quantify this, we introduce the acoustic energy density E_{ac} , which is the time average of the summed kinetic and potential energy of the oscillatory movement. This concept is practical for characterising a given acoustic field as it quantifies the overall field intensity by a single scalar energy measure. The acoustic energy density for typical acoustofluidic resonators are typically in the range 1-100 Pa [38], and take on the highest value when the system is actuated at its resonance frequency f_{res} .

The instantaneous acoustic energy density $E_{\text{ac}}(t)$ is the sum of the kinetic energy density $\frac{1}{2}\rho v^2$, and the potential energy density E_{pot} . Owing to the harmonic time-dependence of the first-order fields we can calculate time-average energy density using the theorem in Eq. (2.33)

Fluid

For the fluid, the local acoustic energy density is a function of the first-order fluid velocity $\mathbf{v}_1(\mathbf{r}, t)$ and the first-order pressure $p_1(\mathbf{r}, t)$

$$\begin{aligned} E_{\text{ac}}^{\text{fl}}(\mathbf{r}) &= \frac{1}{2}\rho_0 \langle (v_1(\mathbf{r}, t))^2 \rangle + \frac{1}{2}\kappa_0 \langle (p_1(\mathbf{r}, t))^2 \rangle \\ &= \frac{1}{4}\rho_0 |\mathbf{v}_1(\mathbf{r}, 0)|^2 + \frac{1}{4}\kappa_0 |p_1(\mathbf{r}, 0)|^2 . \end{aligned} \quad (2.34)$$

Note that we have neglected terms higher than second order.

Solid

For the solid, the kinetic energy is a function of the solid velocity $\mathbf{v}_1^{\text{sl}} = -i\omega\mathbf{u}_1$, and the potential energy is found by taking the full contraction between the stress tensor Eq. (2.5) and the solid strain tensor Eq. (2.6)

$$E_{\text{ac}}^{\text{sl}}(\mathbf{r}) = \frac{1}{2}\rho_{\text{sl}} \langle (-i\omega u_1(\mathbf{r}, 0))^2 \rangle + \frac{1}{2} \langle \boldsymbol{\sigma}_1^{\text{sl}} : \mathbf{s}_1 \rangle \quad (2.35)$$

$$= \frac{1}{4}\rho_{\text{sl}}\omega^2 |u_1(\mathbf{r}, 0)|^2 + \frac{1}{4} \langle \boldsymbol{\sigma}_1^{\text{sl}} : [\nabla \mathbf{u}_1 + (\nabla \mathbf{u}_1)^{\text{T}}] \rangle , \quad (2.36)$$

again we neglect the higher order terms.

The acoustic radiation force

When a sound wave propagating in a fluid hits a suspended particle with material properties different from that of the fluid, the incoming sound wave scatters on the particle [46]. Because the sound wave carries energy and momentum, the scattering of the wave implies a transfer of momentum from fluid to the particle, and thus a force can be exerted on particle by the sound wave. We call this the acoustic radiation force, and its uses will play a central role in this thesis work. For a more elaborate treatment and derivation of the acoustic radiation force, we refer the reader to the works by either Settles and Bruus [46] or Karlsen and Bruus [21].

The acoustic radiation force \mathbf{F}^{rad} acting on a fluid-suspended elastic particle with radius a_{pa} , mass density ρ_{pa} , and compressibility κ_{pa} , is, for a general acoustic wave, given by [46]

$$\mathbf{F}^{\text{rad}} = -\frac{4}{3}\pi a_{\text{pa}}^3 \left[\kappa_0 \langle (f_0 p_1) \nabla p_1 \rangle - \frac{3}{2} \rho_0 \langle (f_1 \mathbf{v}_1) \cdot \nabla \mathbf{v}_1 \rangle \right], \quad (2.37a)$$

where the monopole and dipole scattering coefficients f_0 and f_1 , respectively, are

$$f_0 = 1 - \frac{\kappa_{\text{pa}}}{\kappa_0}, \quad (2.37b)$$

$$f_1 = \frac{2(1-\gamma)(\frac{\rho_{\text{pa}}}{\rho_0} - 1)}{2\frac{\rho_{\text{pa}}}{\rho_0} + 1 - 3\gamma}, \quad \gamma = -\frac{3}{2} \left[1 + i(1 + \tilde{\delta}) \right] \tilde{\delta}, \quad (2.37c)$$

with $\tilde{\delta} = \frac{1}{a_{\text{pa}}} \sqrt{\frac{2\eta}{\omega \rho_0}}$ being normalised boundary-layer thickness.

2.4 Concluding remarks

In this chapter we presented the governing equations for solid and fluid mechanics in the frame of acoustics to 1st and 2nd order, as well as for particle suspensions described with a Nernst–Planck like approach. Because these governing equations are coupled and non-linear, they are often difficult to solve analytically, and we therefore introduce the finite element method in the next chapter, which is a general numerical scheme for solving partial differential equations.

Chapter 3

Numerical methods

As we have seen in Chapter 2, the acoustic field equations consists of coupled equations in different domains with involved geometries and different types of materials. This results in coupled partial differential equations (PDE) which are exceedingly difficult to solve by analytical means, and we therefore rely on numerical simulations as a central tool for most problems in this thesis work. As the primary numerical tool we use the so-called *finite element method* (FEM), which is used in many branches of engineering and science. The strength of FEM is the ability to provide approximate solutions to complex differential equations that are otherwise hard to solve. These solutions are called *weak solutions*. Our models are implemented in the FEM framework using the commercially available software COMSOL MULTIPHYSICS v. 5.2a [47]. Furthermore, we introduce the concept of mesh convergence to probe the numerical reliability of the results

3.1 The Finite Element Method

The basic idea in the *finite element method* is to discretize the problem in a finite set of localized basis functions. The principle of using basis functions to span a solution, is well known from e.g. Fourier analysis and spherical harmonic functions. In FEM, the computation domain is not restricted to highly symmetrical geometries, as compared to other methods, but instead allows for solving equations with several inter-dependent variables in complex geometries. The theory in this section is developed partly on [48, 49, 50], but explained here in more detail.

As a starting point we consider the case of a general differential equation for the function $g(\mathbf{r})$

$$\mathcal{L} \{g(\mathbf{r})\} = F(\mathbf{r}), \quad (3.1)$$

where \mathcal{L} is a linear differential operator and $F(\mathbf{r})$ is some source term. Next, we define the defect

$$d(\mathbf{r}) \equiv \mathcal{L} \{g(\mathbf{r})\} - F(\mathbf{r}). \quad (3.2)$$

By definition, the defect is zero for an exact solution of Eq. (3.1), called a *strong solution*. Next, the computation domain Ω is discretized in a finite number of grid points,

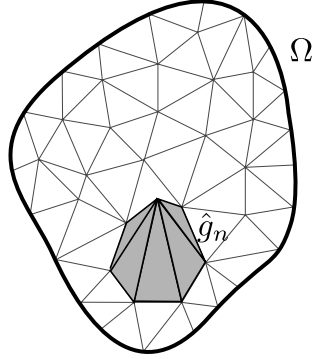


Figure 3.1: Discretization of the computation domain Ω in triangular elements. The n th basis function \hat{g}_n is 1 at the n th node, and 0 everywhere else. The figure is adapted from [49]

see Fig. 3.1, and a basis function is defined for each node in the grid. This is illustrated in Fig. 3.1 where we see a linear basis function for the n th node \hat{g}_n . The basis functions fulfil the criteria of being 1 at their own node, and 0 everywhere else, and the sum of basis functions must be continuous and piecewise differentiable. In Fig. 3.1 the shown basis function \hat{g}_n is linear, however higher order polynomials are most often also used, depending on the wanted precision versus computation power available, and the highest order derivative involved of the PDE. It is assumed that $g(\mathbf{r})$ can be approximately expanded in terms of the spatially discretized basis functions

$$g(\mathbf{r}) = \sum_n a_n \hat{g}_n, \quad (3.3)$$

where a_n are the expansion coefficients for $g(\mathbf{r})$. Mathematically, a_n is nothing but the value of $g(\mathbf{r})$ at the n th grid node. To find the weak solution for $g(\mathbf{r})$, we demand that all basis functions are orthogonal to the defect

$$\langle \hat{g}_m, d(\mathbf{r}) \rangle = 0 \quad \text{for all } m. \quad (3.4)$$

Here we have defined the inner product between two real functions as $\langle X(\mathbf{r}), Y(\mathbf{r}) \rangle \equiv \int_{\Omega} dV X(\mathbf{r})Y(\mathbf{r})$. By inserting the definition of the defect $d(\mathbf{r})$ in Eq. (3.4), we get

$$\sum_n a_n \langle \hat{g}_m, \mathcal{L}\hat{g}_n \rangle = \langle \hat{g}_m, F \rangle \quad \text{for all } m. \quad (3.5)$$

Noting that we have two summation indices (n, m) in Eq. (3.5), and because the inner product is linear, we can formulate the problem as a matrix equation

$$\mathbf{K} \mathbf{a} = \mathbf{F}, \quad (3.6)$$

where $\mathbf{K} = \{K_{mn}\}$ is called the stiffness matrix [49], and $\mathbf{a} = \{a_n\}$ contains the coefficients that are varied to satisfy Eq. (3.6). Solving this matrix equation by inverting \mathbf{K} , is called finding a *weak solution* to Eq. (3.1), and is exactly what COMSOL does, and the construction of basis functions, the stiffness matrix, and the subsequent inversion of the

matrix equation in Eq. (3.6) is all handled automatically in COMSOL.

The discrepancy between *weak* and *strong* solutions lies in the fact that we only use a finite set of basis functions. As the set is finite, the function space of the differential equation (3.1), is only approximately spanned. This means that the demand of the defect being orthogonal to all the basis functions \hat{g}_m implies that it is only approximately zero $d(\mathbf{r}) \approx 0$. This stands in contrast to strong solutions, where the defect is exactly zero $d(\mathbf{r}) = 0$.

3.1.1 Boundary conditions in the weak formulation

In physics, governing equations are often invoked from conservation laws, and we therefore derive the case of implementing a general continuity equation in the weak formulation. Our continuity equation takes the general form

$$\nabla \cdot \mathbf{\Gamma} = F, \quad (3.7)$$

where the defect is then simply $d(\mathbf{r}) = \nabla \cdot \mathbf{\Gamma} - F$. Again, we take the inner product between the basis function \hat{g}_m and the defect of Eq. (3.7)

$$\langle \hat{g}_m, \nabla \cdot \mathbf{\Gamma} - F \rangle = \int_{\Omega} dV (\hat{g}_m \nabla \cdot \mathbf{\Gamma} - \hat{g}_m F) = 0 \quad \text{for all } m. \quad (3.8)$$

Integrating the divergence term in Eq. (3.8) by parts, and using the Gauss theorem for integrals, we convert part of the integral to an integral over the boundary

$$\oint_{\partial\Omega} dA \mathbf{n} \cdot \mathbf{\Gamma} + \int_{\Omega} dV (-[\nabla \hat{g}_m] \cdot \mathbf{\Gamma} - \hat{g}_m F) = 0 \quad \text{for all } m. \quad (3.9)$$

Neumann boundary conditions

In the case of Neumann boundary conditions where the flux perpendicular to the domain boundary $\mathbf{n} \cdot \mathbf{\Gamma}$ is a known function $f(\mathbf{r})$

$$f(\mathbf{r}) = \mathbf{n} \cdot \mathbf{\Gamma} \quad \text{for } \mathbf{r} \in \partial\Omega \quad (\text{Neumann}), \quad (3.10)$$

$f(\mathbf{r})$ can be inserted directly into the boundary integral in Eq. (3.9).

Dirichlet boundary conditions

In the case of Dirichlet boundary condition, it is instead the value of $g(\mathbf{r})$ that is a known function $h(\mathbf{r})$ on the boundary

$$h(\mathbf{r}) = g(\mathbf{r}) \quad \text{for } \mathbf{r} \in \partial\Omega \quad (\text{Dirichlet}). \quad (3.11)$$

To implement the Dirichlet condition, we simply treat the flux as an unknown function $\mathbf{n} \cdot \mathbf{\Gamma} = \lambda(\mathbf{r})$, which we call the Lagrange multiplier, that must take on values at the

boundary to ensure Eq. (3.11) is satisfied. We expand the unknown flux in terms of new of a new set of basis functions

$$\lambda(\mathbf{r}) = \sum_n b_n \hat{\lambda}_n(\mathbf{r}). \quad (3.12)$$

Next, to satisfy the Dirichlet condition we introduce the constraint $R(g(\mathbf{r}))$ analogous to the defect $d(\mathbf{r})$. In the case of the Dirichlet boundary condition the constraint simply becomes $R(g(\mathbf{r})) = g(\mathbf{r}) - h(\mathbf{r}) = 0$. In exactly the same as when solving for the defect to be zero, the constraint $R(g(\mathbf{r})) = 0$ is now satisfied by demanding that all basis function $\hat{\lambda}_m$ are orthogonal to the constraint

$$\langle \hat{\lambda}_m, R(g(\mathbf{r})) \rangle = \langle \hat{\lambda}_m, g(\mathbf{r}) - h(\mathbf{r}) \rangle = 0 \quad \text{for all } m. \quad (3.13)$$

We add the inner product in Eq. (3.13) to the boundary integral in Eq. (3.9), and replace $\lambda(\mathbf{r})$ for the flux

$$\oint_{\partial\Omega} dA [\lambda(\mathbf{r}) + \hat{\lambda}_m(g(\mathbf{r}) - h(\mathbf{r}))] + \int_{\Omega} dV (-[\nabla \hat{g}_m] \cdot \mathbf{\Gamma} - \hat{g}_m F) = 0 \quad \text{for all } m. \quad (3.14)$$

This implementation ensures that the flux $\lambda(\mathbf{r})$ varies (by varying the b_n coefficients in Eq. (3.12)) until the Dirichlet boundary condition is satisfied.

3.2 Mesh convergence

To ascertain whether the chosen mesh is fine enough to resolve all spatial details of the physics sufficiently, we rely partly of visual inspection of the fields, and partly on a quantitative mesh convergence analysis. The core idea of this analysis is to check whether the numerical solution have converged. If a sufficiently fine mesh is used, the numerical results are independent of the mesh sizes used. Oppositely, if the mesh size is too coarse, spatial details on length scales smaller than the mesh sizes cannot be resolved.

To check the mesh convergence of a given field $g(\mathbf{r})$, we introduce the relative convergence parameter of the field $C(g)$ [6], where we use the solution with the finest mesh $g^{\text{end}}(\mathbf{r})$ as a reference

$$C(g) = \sqrt{\frac{\int_{\Omega} dV |g - g^{\text{end}}|^2}{\int_{\Omega} dV |g^{\text{end}}|^2}}. \quad (3.15)$$

Next, $C(g)$ can be investigated as a function of mesh size, and should behave exponentially decreasing in the converging regime. Depending on the complexity of the problem and the computational power available, values as low as 10^{-6} can be obtained. However, as we have in this work studied large and involved 3D models, we will tolerate convergence values of $C < 10^{-2}$.

3.3 Concluding remarks

In chapter 2 and 3 we introduced the basic theory and presented the weak formulation as a numerical scheme for solving the governing partial differential equations. We now turn our focus to developing an effective model for the effect of hydrodynamic particle-particle interactions in dense microparticle suspensions in microfluidic channels, using the basic theory and numerical methods presented so far.

Chapter 4

Effective modeling of hydrodynamic interactions

In this chapter we derive an effective model for hydrodynamic particle-particle interactions of a dense suspension of particles undergoing active migration in a microchannel.

The results presented in this chapter is to a large extent, with co-author permission, taken from, and based on our published journal paper *Continuum modeling of hydrodynamic particle-particle interactions in microfluidic high-concentration suspensions*, M. W. H. Ley and H. Bruus, *Lab Chip*, **16** (2016), 1178-1188. Enclosed in Appendix [A](#).

4.1 Motivation and approaches for calculating dense suspension dynamics

Our motivation for this work is found in the fact that microfluidic samples often contain bio-particles in concentrations so high that the particle-particle interactions change the flow behaviour compared to dilute suspensions, and a common problem encountered is therefore to predict the particle transport at high concentrations and design experiments accordingly.

The direct, and brute force approach to calculating the dynamics of dense suspensions is direct numerical simulation (DNS), where all the particles and the fluid are considered individually, but all solved simultaneously. One important example where DNS is readily applied is for high-concentration suspensions is full blood in blood vessels with diameters in the cm to sub-millimeter range or in artificial microfluidic channels. State-of-the-art calculations of the detailed hydrodynamics of blood involve DNS.[\[51, 52, 53, 54\]](#) DNS models can simultaneously resolve the deformation dynamics of the elastic cell membranes of up to several thousand red blood cells (RBCs) as well as the intra-cell hydrodynamics of the fluid plasma, all in full 3D [\[52\]](#). However, such calculations require a steep price in computational efforts, as large computer clusters running thousands of CPUs in parallel may be involved,[\[52\]](#) and the computations may take days.[\[51\]](#). In our scope, a direct approach is therefore too computational heavy for our wanted level of detail.

Effective medium theory - a continuum approach

Instead we turn towards a continuum description of both liquid and particles, and view the suspension as an effective medium, where computational cost may be reduced significantly by continuum modeling. Lei *et al.* [55] investigated the limit of small ratios a/H of the particle radius a and the container size H . They found that, to a good approximation, continuum descriptions are valid for $a/H \lesssim 0.02$. This is used in the computationally less demanding approach called mixture theory, or theory of interacting continua, where blood flow is modeled as two superimposed continua, representing the plasma and RBCs.[56, 57] In a recent study, Kim *et al.* [57] used the method to simulate blood flow in a microchannel, and the results compared favorably to experiments. However, it is debated how to correctly calculate the coupling between the two phases, as well as formulate the stress tensor for the solid phase RBCs. This is called the 'closure problem' of mixture theory.[58]

Using DNS to derive effective transport coefficients

In a very different field, namely the hydrodynamics of macroscopic suspensions of hard particles, such as in gravity-driven sedimentation, important in the oil and gas industry, effective medium theories had been an intense topic of study for many years, long before microfluidics. These systems have been described by effective-medium theories by the introduction of the effective viscosity of the suspension and of the effective single-particle mobility (increase of drag force). The textbook by Happel and Brenner [43] summarizes work from 1920 to 1960, in particular unit-cell modeling and infinite-array modeling, both approaches imposing a regular distribution of particles. Later, Batchelor [59] improved the effective-medium models by applying statistical mechanics for irregularly placed particles. In 1982, Mazur and Beenakker [60] developed the induced-force method for explicit calculation of the hydrodynamic interactions between many rigid spheres. A few years later, this method was extended by Ladd [61, 62] to allow for a higher number of particles to be considered in an efficient manner. In 1990, Ladd [63] used the induced-force method in high-concentration suspensions to calculate three central hydrodynamic transport coefficients: the effective suspension viscosity η , the particle diffusivity D , and the particle mobility μ , and the obtained results compare well with both experiments and with preceding theoretical work. By calculating these coefficients once and for all using detailed DNS, Ladd [63] provides a short-cut for including the complex hydrodynamic particle-particle interactions in a dense suspension using an effective continuum description.

Applying the effective medium theory to a microfluidics system

While studies of high-density suspensions with active transport are very important in lab-on-a-chip systems, such as in electro-, magneto-, and acoustophoresis,[9, 11, 12, 19] they have not been treated by the microfluidic DNS-models mentioned above. On the other hand, while the effective-medium theories do treat active transport, they have rarely been used to analyze microfluidic systems.

We derive a continuum model of high-density suspensions in microchannels exposed to an external force causing particle migration. Based on the results of Lei *et al.* [55] mentioned

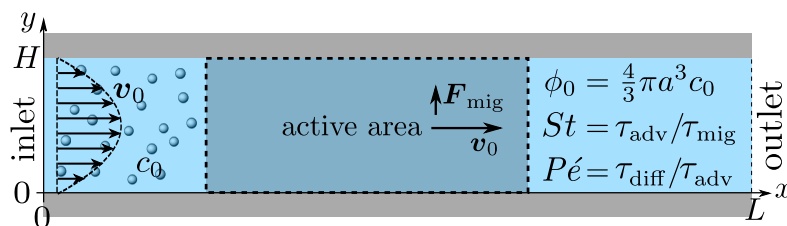


Figure 4.1: Sketch of the model system. Spherical microparticles of diameter $2a$ are suspended in a Newtonian fluid with a homogeneous number concentration c_0 , or volume fraction $\phi_0 = \frac{4}{3}\pi a^3 c_0$. The suspension enters from the inlet with velocity \mathbf{v}_0 and flows towards the localized active area, where the particles experience a transverse migration force \mathbf{F}_{mig} , which redistributes the particles before they leave the channel at the outlet. The resulting particle transport is determined by the relative strength between particle diffusion, advection and migration, which is characterized by three dimensionless numbers: the particle concentration ϕ_0 , the transient Strouhal number St , and the Péclet number Pe .

above, we are justified to use the computationally less demanding continuum description in not too small microfluidic channels, $a/H \lesssim 0.02$. Moreover, with the hydrodynamic transport coefficients obtained by Ladd,[63] we can fairly easy write down the governing equations for high-density suspensions following the Nernst–Planck-like approach presented by Mikkelsen and Bruus,[64] but here extended to include the hydrodynamic particle-particle interactions.

We establish a continuum effective-medium theory, in which the hydrodynamic interactions between particles in a high-density suspension flowing through a microchannel are modeled by including the concentration dependency of the effective suspension viscosity, the particle diffusivity and mobility, and the transfer of momentum from the particles to the suspension. We then illustrate the use of the theory by two examples: The first is strongly inspired by the magnetophoretic device studied by Mikkelsen and Bruus.[64] The second is taken from the emerging field of acoustofluidics [23, 24] and involves an acoustophoretic device, for which the dilute limit is well described,[38, 65, 66] but where the behavior in the high-concentration limit is still poorly characterized.

4.2 Model system

We consider a microchannel at ambient temperature, such as the one sketched in Fig. 4.1. In a steady-state pressure-driven flow of average inlet velocity \mathbf{v}_0 , an aqueous suspension of microparticles, with the homogeneous concentration, *i.e.* number of particles per volume c_0 (and not be confused here with the speed of sound in a fluid) at the inlet, is flowing through the microchannel. Only a section of length L is shown. The effects of side-walls, present in actual systems, are negligible for channels with a large width-to-height ratio. Localized in the channel is an active area, where the microparticles are subjected to a transverse single-particle migration force \mathbf{F}_{mig} . This force changes the particle distribution, resulting in an inhomogeneous distribution downstream towards the outlet. In this process, the particles are transported by advection, active migration, and diffusion, all of which are affected by hydrodynamic particle-particle interactions at high concentrations.

4.2.1 2D Parallel plate system

As a simple generic model system, we consider a section of length L of a microchannel with constant rectangular cross-section of height H and width W . In specific calculations we take $L = 7H$ and study for simplicity the flat-channel limit $W = 10H$, for which the system, in a large part of the center, is reasonably well approximated by a parallel-plate channel. We take the microparticles to be rigid spheres with diameter $2a$. Their local concentration (number per volume) is described by the continuous field $c(\mathbf{r})$, but often it is practical to work with the dimensionless concentration (particle volume fraction),

$$\phi(\mathbf{r}) = \frac{4}{3}\pi a^3 c(\mathbf{r}). \quad (4.1)$$

We are particularly interested in high inlet concentrations ϕ_0 between 0.001 and 0.1, and for this range with the typical values $2a = 2\text{ }\mu\text{m}$ and $H = 50\text{ }\mu\text{m}$, the number of particles in the volume $L \times W \times H$ is between 10^4 and 10^6 , which in practice renders direct numerical simulation of the suspension infeasible. We therefore employ continuum modeling in terms of the three continuous fields: the particle concentration $c(\mathbf{r})$, and the pressure $p(\mathbf{r})$ and the velocity $\mathbf{v}(\mathbf{r})$ of the suspension.

4.2.2 Forces and effective particle transport

Our continuum model for the particle current density \mathbf{J} includes diffusion (diff), advection (adv), and migration (mig), [67] for which we include hydrodynamic particle-particle interactions through $c(\mathbf{r})$,

$$\mathbf{J} = \mathbf{J}_{\text{diff}} + \mathbf{J}_{\text{adv}} + \mathbf{J}_{\text{mig}} \quad (4.2a)$$

$$= -D(c)\nabla c + c\mathbf{v} + c\mu(c)\mathbf{F}_{\text{mig}} \quad (4.2b)$$

$$= -\chi_D(\phi)D_0\nabla c + c\mathbf{v} + c\chi_\mu(\phi)\mu_0\mathbf{F}_{\text{mig}}. \quad (4.2c)$$

Here,

$$D(c) = \chi_D(\phi)D_0 \quad \text{and} \quad \mu(c) = \chi_\mu(\phi)\mu_0 \quad (4.2d)$$

is the effective single-particle diffusivity and mobility, respectively, $\chi_D(\phi)$ and $\chi_\mu(\phi)$ are concentration-dependent correction factors described in more detail in Section 4.2.5, while $\mu_0 = (6\pi\eta_0 a)^{-1}$ and $D_0 = k_B T \mu_0$ is the dilute-limit mobility and diffusivity, respectively, where k_B is the Boltzmann constant, T is the temperature, and η_0 is the dilute-limit viscosity of the suspension. We do not in this model consider any effects of van der Waals interactions or steric interactions. [67] Due to conservation of particles, the particle current density obeys a steady-state continuity equation,

$$0 = \nabla \cdot \mathbf{J}. \quad (4.3)$$

4.2.3 Effective viscosity and flow of the suspension

The flow of the suspension is governed by the continuity equations for momentum and mass. Treating the suspension as an effective continuum medium with the particle concentration

$\phi(\mathbf{r})$, its density and viscosity are

$$\rho(\phi) = \chi_\rho(\phi) \rho_0 \quad \text{and} \quad \eta(\phi) = \chi_\eta(\phi)^{-1} \eta_0, \quad (4.4)$$

with the dimensionless correction factors $\chi_\rho(\phi)$ and $\chi_\eta(\phi)^{-1}$ in front of the density ρ_0 and viscosity η_0 of pure water, respectively. A given particle experiences a drag force, when it is moved relative to the suspension by the migration force \mathbf{F}_{mig} , and in turn, an equal but opposite reaction force is exerted on the suspension. In the continuum limit this is described by the force density $c\mathbf{F}_{\text{mig}}$. In steady state, the momentum continuity equation for an incompressible suspension with the stress tensor $\boldsymbol{\sigma}$ therefore becomes

$$\mathbf{0} = \nabla \cdot [\boldsymbol{\sigma}(\phi) - \rho(\phi)\mathbf{v}\mathbf{v}] + c\mathbf{F}_{\text{mig}}, \quad (4.5a)$$

$$\boldsymbol{\sigma}(\phi) = -\mathbf{I}p + \chi_\eta(\phi)^{-1} \eta_0 [\nabla \mathbf{v} + (\nabla \mathbf{v})^T]. \quad (4.5b)$$

Likewise, the steady-state mass continuity equation for an incompressible suspension is written as

$$0 = \nabla \cdot [\chi_\rho(\phi) \rho_0 \mathbf{v}]. \quad (4.6)$$

4.2.4 Boundary conditions

We assume a concentration $c = c_0$ and a parabolic flow profile $\mathbf{v} = 6v_0 \frac{y}{H} (1 - \frac{y}{H}) \mathbf{e}_x$ at the inlet, and vanishing axial gradients $\partial_x c = 0$ and $\partial_x \mathbf{v} = \mathbf{0}$ at the outlet. At the walls, we assume a no-slip condition $\mathbf{v} = \mathbf{0}$, while the condition for c depends on the specific physical system. Lastly, we fix the pressure level to be zero at the lower corner of the outlet $p(L, 0) = 0$.

4.2.5 Dimensionless, effective transport coefficients

The dependency of the effective diffusion, mobility, viscosity and density on the particle concentration ϕ is described by the correction factors $\chi_D(\phi)$, $\chi_\mu(\phi)$, $\chi_\eta(\phi)$, and $\chi_\rho(\phi)$, respectively, which can be interpreted as dimensionless effective transport coefficients. The suspension density is a weighted average of the water density ρ_0 and the particle density ρ_p , $\chi_\rho(\phi) = (1 - \phi) + \frac{\rho_p}{\rho_0} \phi$. For bio-fluids, particles are often neutrally buoyant, so $\rho_p \approx \rho_0$ and $\chi_\rho \approx 1$. In a comprehensive numerical study of finite-sized, hard spheres suspended in a Newtonian fluid at low Reynolds numbers (the Stokes limit), the remaining transport coefficients χ_D , χ_μ , and χ_η were calculated by Ladd [63] at 14 specific values of ϕ between 0.001 and 0.45. For each of the coefficients χ , we have fitted a fourth-order polynomial to the discrete set of values χ^{-1} , while imposing the condition $\chi(0)^{-1} = 1$ to ensure agreement with the dilute-limit value,

$$\chi_\eta(\phi)^{-1} = 1 + 2.476(7) \phi + 7.53(2) \phi^2 - 16.34(5) \phi^3 + 83.7(3) \phi^4 + \mathcal{O}(\phi^5), \quad (4.7a)$$

$$\chi_D(\phi)^{-1} = 1 + 1.714(3) \phi + 6.906(13) \phi^2 - 17.05(3) \phi^3 + 61.2(1) \phi^4 + \mathcal{O}(\phi^5), \quad (4.7b)$$

$$\chi_\mu(\phi)^{-1} = 1 + 5.55(3) \phi + 43.4(3) \phi^2 - 149.6(9) \phi^3 + 562(3) \phi^4 + \mathcal{O}(\phi^5), \quad (4.7c)$$

where the uncertainty of the last digit is given in the parentheses. To quantify the quality of the fits χ_{fit} compared to the simulated data points χ_{data} , we calculated the relative

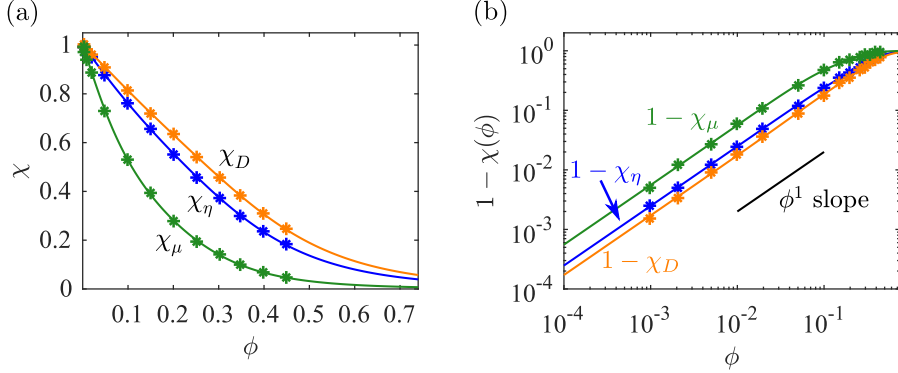


Figure 4.2: Plot of the fitted dimensionless effective transport coefficients χ_η , χ_D and χ_μ as a function of concentration ϕ . The full lines represent the fits from Eq. (4.7), while the circles are the original 14 simulation data points by [63], (a) Linear axes plot. (b) Double logarithmic plot of $1 - \chi$, where we see that the hydrodynamic interactions $1 - \chi$ fall off as ϕ^1 .

difference $\Delta\chi = \frac{\chi_{\text{data}} - \chi_{\text{fit}}}{\chi_{\text{data}}}$. We found the standard deviation of $\Delta\chi$ to be 0.003, 0.0019 and 0.0058 for χ_η , χ_D and χ_μ , respectively. Thus, the fourth-order polynomials describe the data points well. The resulting fits from Eq. (4.7) and the original data points [63] are plotted in Fig. 4.2. Note that the mobility χ_μ is the most rapidly decreasing function of concentration ϕ .

We note that the dilute-limit relation $\mu_0 = \frac{1}{6\pi a} \eta_0^{-1}$ and the definitions $\mu = \chi_\mu \mu_0$ and $\eta^{-1} = \chi_\eta \eta_0^{-1}$ do not imply equality of χ_μ and χ_η . In fact, $\chi_\mu < \chi_\eta$, which highlights the complex nature of the interaction problem at high densities.

4.2.6 Dimensionless parameters

The dynamics of the system can be characterized by three dimensionless numbers. One is the particle concentration ϕ_0 , which is a measure of the magnitude of the hydrodynamic interactions. The other two are related to the relative magnitude of the diffusion, advection and migration current densities in Eq. (4.2), each characterized by the respective time scales $\tau_{\text{diff}} = \frac{H^2}{8D_0}$, $\tau_{\text{adv}} = \frac{H}{2v_0}$, and $\tau_{\text{mig}} = \frac{H}{2\mu_0 F_{\text{mig}}}$. A small time scale means that the corresponding process is fast and thus dominating. The importance of advection relative to diffusion and of migration relative to advection is characterized by the Péclet number and the transient Strouhal number, respectively,

$$Pe = \frac{\tau_{\text{diff}}}{\tau_{\text{adv}}} = \frac{v_0 H}{4D_0}, \quad (4.8a)$$

$$St = \frac{\tau_{\text{adv}}}{\tau_{\text{mig}}} = \frac{\mu_0 F_{\text{mig}}}{v_0}, \quad (4.8b)$$

$$\phi_0 = \frac{4}{3} \pi a^3 c_0. \quad (4.8c)$$

4.3 Numerical implementation

We implement the governing equations (4.2)-(4.6) numerically in COMSOL as described in Chapter 3. To avoid spurious, numerically induced, negative values of $c(\mathbf{r})$ near vanishing particle concentration, we replace c by the logarithmic variable $s = \log(c/c_0)$. This variable can assume all real numbers, and it ensures that $c = c_0 \exp(s)$ is always positive. We implement the weak form using Lagrangian test functions of first order for p and second order for s , v_x , and v_y .

A particular numerical problem needs to be taken care of in dealing with the advection in our system. The typical average flow speed is $v_0 = 200 \text{ } \mu\text{m/s}$ in our channels of height $H = 50 \text{ } \mu\text{m}$, corresponding to a Péclet number $Pe = 1.7 \times 10^4$. To resolve this flow numerically, a prohibitively fine spatial mesh is needed. However, this problem can be circumvented by artificially increasing the particle diffusivity to $\chi_D = 50$ instead of using Eq. (4.7b). This decreases the Péclet number to $Pe = 2.3 \times 10^2$, but since $Pe \gg 1$ for both the actual and the artificial diffusivity, advection still dominates in both cases, and as discussed in the next section, the simulation results for the artificial diffusivity are accurate, but a coarser mesh suffices. In this highly advective regime $Pe \gg 1$, the detailed transport in the active area depends on the remaining parameters: the transient Strouhal number St and the inlet concentration ϕ_0 .

4.3.1 Numerical validation and mesh convergence test

The numerical implementation has been carefully checked and validated. To avoid spurious numerical errors, we have performed a mesh convergence analysis using the convergence parameter C , given in Eq. (3.15). For all fields involved in this study, C falls in the range between 10^{-5} and 10^{-3} , and it has the desired exponential decrease as function of h_{mesh}^{-1} , where h_{mesh} is the mesh element size. The number of mesh points and degrees of freedom used in our final simulations are listed in Table 4.1.

We have compared our results with previous work in the literature. Setting $\chi_\mu = \chi_\eta = 1$, our MAP model in Section 4.4.1 is identical to the one by Mikkelsen and Bruus.[64] For this setting, we have calculated the capture fraction β_{map} as a function of the rescaled quantity $(Id)^2/v_0$ (which also appears in Eq. (4.10) for St_{map}), and found exact agreement, including the remarkable data collapse, with the results presented in Fig. 3 of Mikkelsen and Bruus.[64]

The numerical stability of the finite-element simulation is controlled by the mesh Péclet number $Pe_{\text{mesh}} = h_{\text{mesh}}v_0/(\chi_D D_0)$ that involves the mesh size h_{mesh} instead of a physical length scale. We found that convergence was ensured for $Pe_{\text{mesh}} \lesssim 10$, which implies the

Table 4.1: The number of mesh elements N_{mesh} , the degrees of freedom DOF, and the mesh Péclet number Pe_{mesh} used in the numerical simulations of the MAP and ACP models.

model	N_{mesh}	DOFs	Pe_{mesh}
MAP	70,000 - 225,000	200,000 - 2,000,000	5 - 10
ACP	50,000 - 200,000	400,000 - 2,000,000	5 - 10

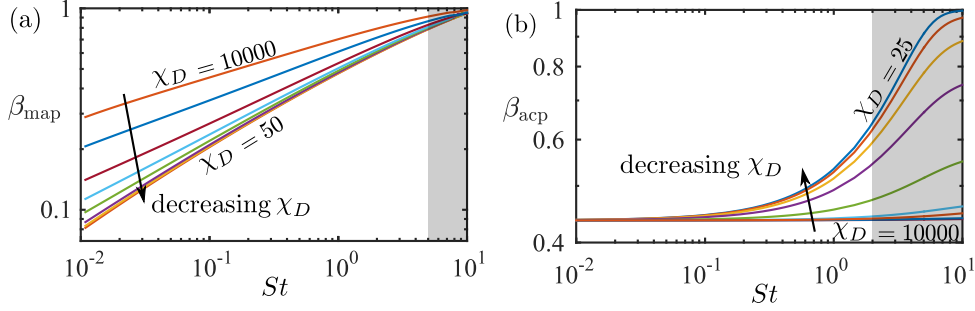


Figure 4.3: Log-log plot of (a) the capture fraction β_{map} and (b) the focusing fraction β_{acp} , both as a function of the transient Strouhal number St in the dilute limit ($\chi_\mu = \chi_\eta = 1$ and $c\mathbf{F}_{\text{mig}} = \mathbf{0}$) for $\chi_D = 25, 50, 100, 200, 500, 1000, 2000, 5000$, and 10000 . Only simulations with St -values outside the gray areas have been included in the analysis of Figs. 4.5 - 4.9.

condition $h_{\text{mesh}} \lesssim 10\chi_D D_0/v_0$ for the mesh size. The higher an advection velocity v_0 , the finer a mesh is needed. In order to obtain computation times of the order of minutes per variables (Pe, St, ϕ_0) on our standard PC, while still keeping $Pe_{\text{mesh}} \lesssim 10$, we artificially increased χ_D . In Fig. 4.3 we have plotted the capture fraction β_{map} and the focusing fraction β_{acp} as functions of the transient Strouhal number St for χ_D ranging from 25 to 10,000 in the dilute limit with $\chi_\mu = \chi_\eta = 1$ and $c\mathbf{F}_{\text{mig}} = \mathbf{0}$. It is clear from Fig. 4.3 that the $\beta(St)$ -curves converge for sufficiently small values of χ_D . For $\chi_D \leq 50$, we determine that acceptable convergence is obtained in both models, and we thus fix $\chi_D = 50$ for all calculations in this chapter. This choice of $\chi_D = 50$ allows for acceptable computation times (~ 10 min per variable set). In other words, once the Péclet number is sufficiently high, the convergence is ensured by the dominance of advection over diffusion.

4.4 Model results

To exemplify our continuum effective-medium model, we present two examples using the same channel geometry, but different particle migration mechanisms, namely magnetophoresis (MAP) and acoustophoresis (ACP). The magnetophoresis model is the one introduced by Mikkelsen and Bruus,[64] but here extended to include the concentration dependence of the effective transport coefficients χ introduced in Section 4.2.5. This model primarily serves as a model validation. The acoustophoresis model is inspired by the many experimental works reported in Lab on a Chip.[23, 39, 22, 68, 69]

4.4.1 Results for magnetophoresis (MAP)

As in Mikkelsen and Bruus [64], we consider the parallel-plate system sketched in Fig. 4.4(a) of height $H = 50 \mu\text{m}$, length $L = 350 \mu\text{m}$, and the boundary conditions of Section 4.2.4. The particles are paramagnetic with magnetic susceptibility $\chi_{\text{mag}} = 1$ and diameter $2a = 2 \mu\text{m}$. A pair of long parallel thin wires is placed perpendicular to the xy -plane with their midpoint at $\mathbf{r}_0 = (x_0, y_0) = (250, 55) \mu\text{m}$, separated by $\mathbf{d} = d\mathbf{e}_x$, and carrying electric

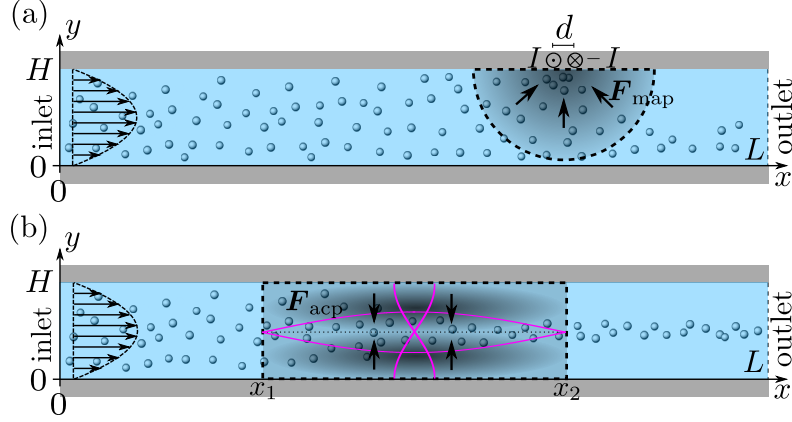


Figure 4.4: Specific realizations of the generic system shown in Fig. 4.1 with height $H = 50 \mu\text{m}$ and length $L = 350 \mu\text{m}$. The microparticles are rigid spheres of diameter $2a = 2 \mu\text{m}$ and a paramagnetic susceptibility $\chi_{\text{mag}} = 1$. A Poiseuille flow with mean velocity v_0 is imposed at the inlet. (a) Magnetophoresis: a pair of thin long wires carrying electrical currents $\pm I$ is placed at the top of the channel $100 \mu\text{m}$ upstream from the outlet. The resulting magnetic force \mathbf{F}_{map} (gray scale) attracts the particles towards the wires. (b) Acoustophoresis: a standing pressure half-wave (magenta) is imposed between x_1 and x_2 . The resulting acoustic force \mathbf{F}_{acp} (gray scale) causes the particles to migrate towards the pressure node at $y = H/2$.

currents $\pm I$. The currents lead to a magnetic field, which induces a paramagnetic force \mathbf{F}_{map} on each particle resulting in magnetophoresis. For a particle at position \mathbf{r} , the force is given by [64]

$$\mathbf{F}_{\text{map}} = -\frac{2}{\pi} \frac{\chi_{\text{mag}}}{\chi_{\text{mag}} + 3} \mu_0^{\text{em}} a^3 (Id)^2 \frac{\mathbf{r} - \mathbf{r}_0}{|\mathbf{r} - \mathbf{r}_0|^6}, \quad (4.9)$$

where μ_0^{em} is the vacuum permeability. Note how the rapid fifth-power decrease as a function of the wire distance $|\mathbf{r} - \mathbf{r}_0|$, signals that \mathbf{F}_{map} is a short-ranged local force. Dipole-dipole interactions are neglected. Using the expression for \mathbf{F}_{map} , we can determine the migration time τ_{mig} for a particle to migrate vertically from the channel center $(x, y) = (x_0, \frac{1}{2}H)$, directly below the wires, to the wall $(x, y) = (x_0, H)$. From this we infer the magnetic transient Strouhal number St_{map} ,

$$St_{\text{map}} = \frac{\tau_{\text{adv}}}{\tau_{\text{map}}} = \frac{16}{3\pi^2} \frac{\mu_0^{\text{em}} (Id)^2 a^2}{v_0 \eta_0 H^5}. \quad (4.10)$$

Wall boundary conditions for the particles

Following the simplifying model of Mikkelsen and Bruus,[64] we assume that once a particle reaches the wall near the wires, it sticks and is thus removed from the suspension. For the upper wall at $y = H$, we therefore set the total particle flux in the y -direction equal to the active migration $J_y = c\mu F_{\text{map},y}$, while at the passive bottom wall at $y = 0$, we choose the standard no-flux condition $J_y = 0$. For short times, this is a good model, but eventually in a real system, the build-up of particles at the wall is likely to occur, which leads to a dynamically change of the channel geometry.

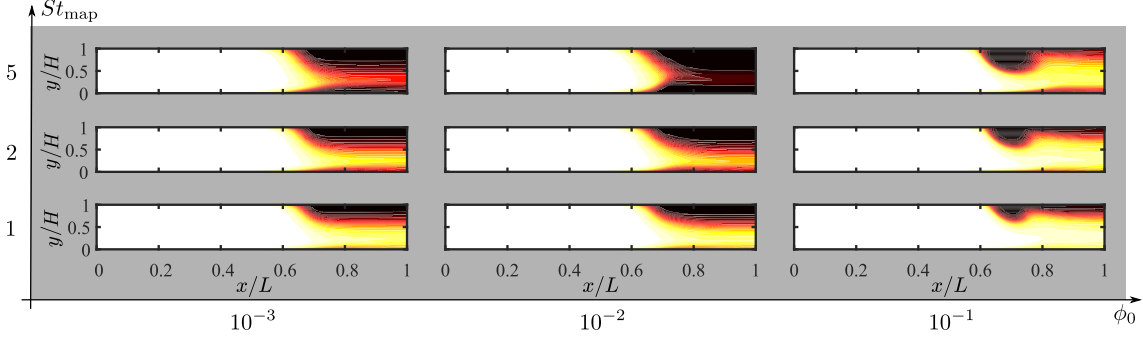


Figure 4.5: Heat color plot of the normalized concentration field $\frac{\phi(\mathbf{r})}{\phi_0}$ from 1 (white, inlet concentration) to 0 (black, no particles) in the magnetophoretic system Fig. 4.4(a), for the nine combinations of $\phi_0 = 0.001, 0.01, 0.1$ with $St_{\text{map}} = 1, 2, 5$.

Particle capture as a function of ϕ_0 and St_{map}

In Fig. 4.5 we have plotted the normalized steady-state particle concentration $\frac{\phi(\mathbf{r})}{\phi_0}$ of the system shown in Fig. 4.4(a) for the nine combinations of $\phi_0 = 0.001, 0.01, 0.1$ with $St_{\text{map}} = 1, 2, 5$. Firstly, it is evident from the figure that for a given fixed ϕ_0 and increasing St_{map} , an increasing number of particles are captured by the wire-pair, thus decreasing $\phi(\mathbf{r})$ in a region of increasing size down-stream from the wires. Note also how the slow-moving particles near the bottom wall are pulled upwards by the action of the wires, leaving a decreased particle density there. Secondly, for a fixed St_{map} , the particle capture is non-monotonic as a function of ϕ_0 : it increases going from $\phi_0 = 0$ via 0.001 to 0.01, but then decreases going from 0.01 to 0.1. Thirdly, for the highest concentration $\phi_0 = 0.1$, the morphology of the depleted region has changed markedly: a small region depleted of particles forms around the wires at the top wall together with narrow downstream depletion regions along both the top and bottom wall. All three regions increase somewhat in size for increasing St_{map} .

The normalized capture rate β_{map}

We analyze the particle capture quantitatively in terms of the normalized capture rate β_{map} defined as the ratio between the flux Γ_{topwall} of particles captured on the top wall by the wires, and the flux Γ_{inlet} of particles entering through the inlet,[64]

$$\beta_{\text{map}} = \frac{\Gamma_{\text{topwall}}}{\Gamma_{\text{inlet}}}, \quad (4.11a)$$

$$\Gamma_{\text{surf}} = \left| \int_{\text{surf}} d\ell \, \mathbf{n} \cdot \mathbf{J} \right|, \quad (4.11b)$$

where \mathbf{n} is the surface normal of a given surface. In Fig. 4.6(a), we have plotted β_{map} as a function of ϕ_0 for different St_{map} values. All of the curves in this plot show the same qualitative behavior: the capture fraction increases with inlet concentration until a certain point, beyond which it declines.

This general behavior is illustrated by the three specific cases $\phi_0 = 0.02, 0.045, \text{ and } 0.1$ denoted by the purple bullets A, B and C on the purple " $St_{\text{map}} = 1$ "-curve. For these three cases, we have in Fig. 4.6(b1,c1,d1) plotted the magnetically-induced change $\Delta \mathbf{v} = \mathbf{v} - \mathbf{v}_0$

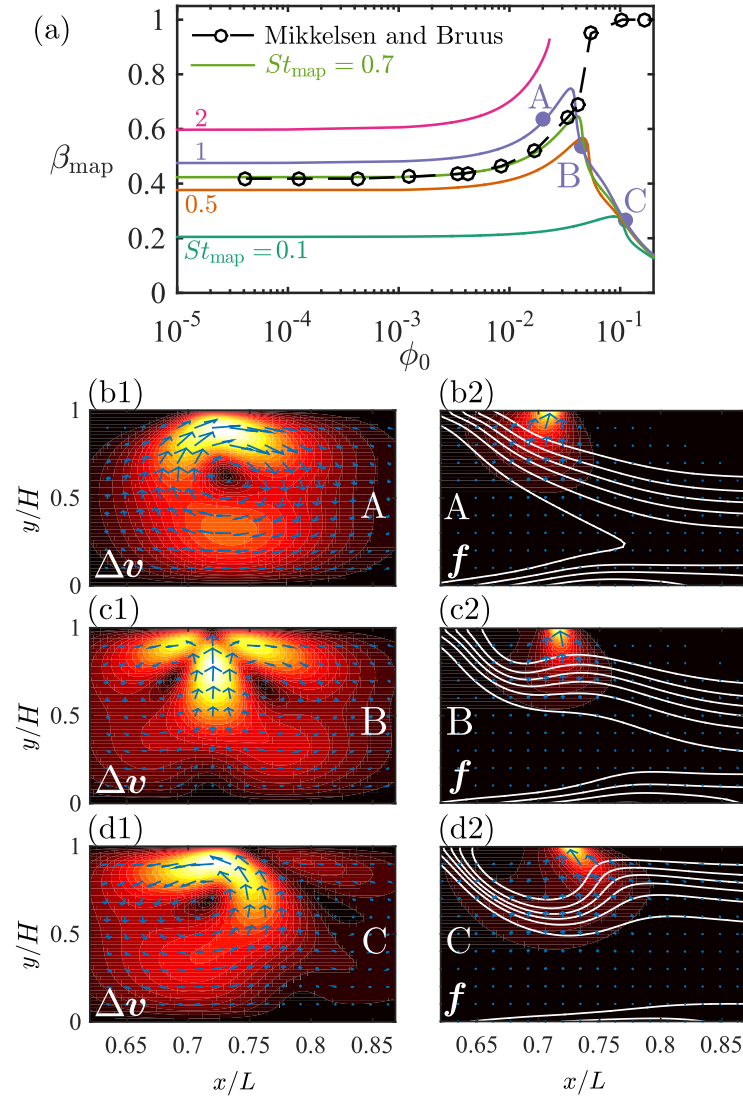


Figure 4.6: (a) Lin-log plot of the capture fraction β_{map} as a function of the inlet concentration ϕ_0 for different transient Strouhal numbers St_{map} (full lines). The original results of Mikkelsen and Bruus [64] are plotted as circles connected by a dashed line. The purple bullets on the curve for $St_{\text{map}} = 1$ mark the three situations A, B, and C plotted in (b)-(d) below. (b1), (c1) and (d1) Color plot from 0 (black) to $\{1.0, 1.6, 2.0\}v_0$ (white) and vector plot of the particle-induced velocity $\Delta \mathbf{v} = \mathbf{v} - \mathbf{v}_0$ near the wire-pair for situation A, B and C, respectively. (b2), (c2) and (d2) Color plot from 0 (black) to $2 \times 10^5 \text{ N/m}^3$ (white) and vector plot of the external force on the suspension $\mathbf{f} = c\mathbf{F}_{\text{map}}$. The white lines are contour lines of the concentration field $\phi(\mathbf{r})$.

in the suspension velocity, and in Fig. 4.6(b2,c2,d2) the magnetic force density $\mathbf{f} = c\mathbf{F}_{\text{map}}$ overlaid by contour lines of c (white). For A in Fig. 4.6(b1) and (b2) with $\phi_0 = 0.02$, more particles are captured compared to the dilute case, because $c\mathbf{F}_{\text{map}}$ induces a clockwise flow-roll that advects the upstream particles closer to the wires. For B in Fig. 4.6(c1) and (c2) with $\phi_0 = 0.045$, $c\mathbf{F}_{\text{map}}$ induces two flow rolls, of which the upstream one rotates counter

clockwise and advects particles away from the wires, thus lowering the capture compared to A. For C in Fig. 4.6(d1) and (d2) with $\phi_0 = 0.1$, $c\mathbf{F}_{\text{map}}$ induces a single strong counter-clockwise flow roll that more efficiently advects the upstream particles away from the wires, and β_{map} decreases further.

While the initial increase in β_{map} for ϕ_0 increasing from 0 to 0.03 is in agreement with Mikkelsen and Bruus,[64] black crosses in Fig. 4.6(a), the following decrease in β_{map} for ϕ_0 increasing beyond 0.03 was not observed by them. The deviation is not due to our inclusion of the effective transport coefficients χ_η and χ_μ , since repeating the simulations [64] with $\chi_\eta = \chi_\mu = 1$ resulted in a curve indistinguishable from the green curve $St_{\text{map}} = 0.7$ in Fig. 4.6(a). We speculate that this deviation is due to our improved mesh resolution.

4.4.2 Results for acoustophoresis (ACP)

For the acoustic migration force, we consider a situation where the acoustic field is localized to a small region in the channel. When a bulk acoustic wave is excited in a device, the acoustic field is present everywhere in the device. Despite of this, the presence of 'hot spots' has been observed experimentally [38], where the acoustic field appear to be localized to certain places. To make a simple model for the acoustic force, we consider the inviscid case of an acoustic field without damping ($\Gamma = 0$), which means that we neglect any effect of the shear field \mathbf{v}_1^s . These considerations reduces the problem of finding the acoustic field to the Helmholtz Eq. (2.25a) for the acoustic pressure p_1 in a simple geometry. At resonance and in a rectangular geometry with the confinements $x_1 \leq x \leq x_2$ and $0 \leq y \leq H$, the solution to p_1 , becomes a simple product of sines and cosines

$$p_1 = p_a \sin\left(\pi \frac{x - x_1}{x_2 - x_1}\right) \sin\left(\pi \frac{y}{H}\right) e^{-i\omega t}, \quad x_1 \leq x \leq x_2, \quad (4.12)$$

where p_a is the acoustic field amplitude, typically of the order 0.1 MPa [39, 38]. The fluid velocity \mathbf{v}_1^c is found directly by inserting p_1 in Eq. (2.22b). In the case of a standing wave field, the acoustic radiation force reduce to a potential force [46]

$$\mathbf{F}^{\text{rad}} = -\nabla U_{\text{rad}}, \quad (4.13a)$$

$$U_{\text{rad}} = \frac{4\pi}{3}a^3 \left[\text{Re}[f_0] \frac{1}{2}\kappa_0|p_1|^2 - \text{Re}[f_1] \frac{3}{4}\rho_0|v_1^c|^2 \right]. \quad (4.13b)$$

When the expressions for p_1 and \mathbf{v}_1^c are inserted in Eq. (4.13), the acoustic radiation force becomes

$$F_{\text{rad},x} = \frac{4}{3}\pi a^3 E_{\text{ac}} k_x \sin(2\tilde{x}) \left[-\left(f_0 + \frac{3k_x^2}{2k^2}f_1\right) \cos^2(\tilde{y}) + \frac{3k_y^2}{2k^2}f_1 \sin^2(\tilde{y}) \right], \quad (4.14a)$$

$$F_{\text{rad},y} = \frac{4}{3}\pi a^3 E_{\text{ac}} k_y \sin(2\tilde{y}) \left[+\left(f_0 + \frac{3k_y^2}{2k^2}f_1\right) \sin^2(\tilde{x}) + \frac{3k_x^2}{2k^2}f_1 \cos^2(\tilde{y}) \right], \quad (4.14b)$$

where $\tilde{x} = k_x(x - \frac{2}{7}L)$ and $\tilde{y} = k_y y$ are dimensionless coordinates, and k_x , k_y , and $k^2 = k_x^2 + k_y^2 = \frac{\omega^2}{c_0^2}$ are the wave numbers. For water-suspended polystyrene spheres with radius

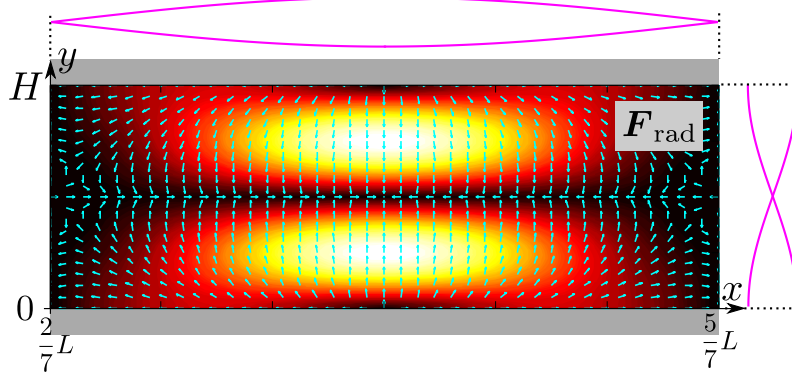


Figure 4.7: The magnitude (heat color plot from zero [black] to maximum [white]) and the direction (vector plot) of the acoustophoretic force \mathbf{F}^{rad} given in Eq. (4.14). The Magenta lines denote the standing pressure half-wave p_1

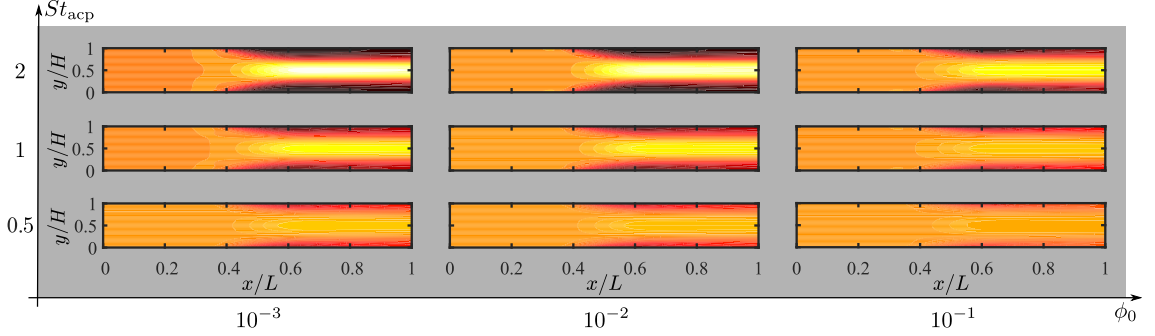


Figure 4.8: Heat color plot of the normalized concentration field $\frac{\phi(\mathbf{r})}{\phi_0}$ from 1.73 (white, maximum value) to 0 (black, no particles) in the acoustophoretic system Fig. 4.4(b), for the nine combinations of $\phi_0 = 0.001, 0.01, 0.1$ with $St_{\text{acp}} = 0.5, 1, 2$.

$a \geq 1 \mu\text{m}$, we have $f_0 = 0.444$ and $f_1 = 0.034$ [6]. The acoustic energy density is set to $E_{\text{ac}} = 10^2 \text{ Pa}$. In Fig. 4.7 we plot the resulting acoustic radiation force from Eq. (4.14), and we note that the acoustic radiation force will tend to focus the particles at the pressure node at $y = \frac{1}{2}H$

Given \mathbf{F}^{rad} , we then calculate the transient Strouhal number from the acoustic migration time τ_{mig} in the dilute limit ($\chi_\mu = 1$) for a single particle migrating from $(x, y) = (\frac{1}{2}L, \frac{1}{8}H)$ to $(x, y) = (\frac{1}{2}L, \frac{3}{8}H)$, [38] and from the advection time given by $\tau_{\text{adv}} = \frac{H}{4v_0}$,

$$St_{\text{acp}} = \frac{\tau_{\text{adv}}}{\tau_{\text{mig}}} = \frac{4\pi^2}{\ln(\cot \frac{\pi}{8})} \frac{a^2 E_{\text{ac}} \Phi}{\eta_0 H v_0}. \quad (4.15)$$

Here, $E_{\text{ac}} = p_a^2 / (4\rho_0 c_{\text{liq}}^2)$ is the acoustic energy density (typically 1-100 Pa), c_{liq} is the speed of sound in the carrier liquid, and $\Phi = \frac{1}{3}f_0 + \frac{1}{2}f_1$ is the so-called acoustic contrast factor. [6]

Wall Boundary condition for the particles

As the particles in this model enter from the inlet, focus towards the channel center $y = \frac{1}{2}H$, and leave through the outlet, we choose the simple no-flux boundary condition, $\mathbf{n} \cdot$

$\mathbf{J}|_{y=0,H} = 0$, for the bottom and top walls.

Particle capture as a function of ϕ_0 and St_{acp}

In Fig. 4.8 is plotted the normalized steady-state particle concentration $\frac{\phi(\mathbf{r})}{\phi_0}$ of the system shown in Fig. 4.4(b) for the nine combinations of $\phi_0 = 0.001, 0.01, 0.1$ to $St_{\text{acp}} = 0.5, 1, 2$. Clearly, for a given fixed ϕ_0 and increasing St_{acp} , an increasing number of particles are focused in the center region. This is expected since St_{acp} is proportional to the acoustic energy density E_{ac} . For $\phi_0 = 0.001$, the center-region concentration (white) is 1.73 times the inlet concentration (orange). Secondly, for a fixed St_{acp} , the particle focusing is monotonically decreasing as a function of ϕ_0 as seen from the decrease in both the width of the particle-free black regions and the magnitude of the downstream center-region concentration. See in particular the change from $\phi_0 = 0.01$ to 0.1.

To quantify the acoustic focusing for a given inlet concentration, we introduce in analogy with Eq. (4.11) the normalized flux β_{acp} of focused particles leaving through the middle 30% of the outlet,

$$\beta_{\text{acp}} = \frac{\Gamma_{\text{center}}}{\Gamma_{\text{inlet}}}, \quad (4.16a)$$

$$\Gamma_{\text{center}} = \left| \int_{0.35W}^{0.65W} dy J_x(L, y) \right|, \quad (4.16b)$$

In the lin-log plot Fig. 4.9(a) of β_{acp} versus ϕ_0 for the four Strouhal numbers $St_{\text{acp}} = 0.1, 0.5, 1$, and 2, the above-mentioned monotonic decrease in acoustophoretic focusing is clear. Especially for ϕ_0 exceeding 0.01 a dramatic reduction in focusability sets in.

To determine the dominant hydrodynamic interaction mechanism behind this reduction, we introduce the normalized particle focusing fraction $\Delta\beta_{\text{acp}}(\phi_0, St_{\text{acp}})$ by the definition,

$$\Delta\beta_{\text{acp}}(\phi_0, St_{\text{acp}}) = \frac{\beta_{\text{acp}}(\phi_0, St_{\text{acp}}) - \beta_{\text{acp}}(\phi_0, 0)}{\beta_{\text{acp}}(0, St_{\text{acp}}) - \beta_{\text{acp}}(0, 0)}. \quad (4.17)$$

Here, the difference in normalized center out-flux β_{acp} at an inlet concentration ϕ_0 between "acoustics on" ($St_{\text{acp}} > 0$) and "acoustics off" ($St_{\text{acp}} = 0$), is calculated relative to the same difference computed in the dilute limit $c\mathbf{F}_{\text{mig}} = \mathbf{0}$ and $\chi_\mu = \chi_\eta = 1$, which is written as $\phi_0 = 0$. We notice that $\Delta\beta_{\text{acp}}(\phi_0, St_{\text{acp}})$ is unity if there is no hydrodynamics interaction effects, and zero if there is no acoustophoretic focusing. In Fig. 4.9(b), using the full model ($\chi_\mu = \chi_\mu(\phi)$ and $\chi_\eta = \chi_\eta(\phi)$ denoted "All effects"), $\Delta\beta_{\text{acp}}$ is plotted versus ϕ_0 (black lines) for the same four St_{acp} values as in Fig. 4.9(a). We note that for the full model (black lines), $\Delta\beta_{\text{acp}}$ is almost independent of the strength St_{acp} of the acoustophoretic force, which makes it ideal for studying the interaction effects through its ϕ_0 dependency.

To elucidate the origin of the observed reduction in focusability, we also plot the following special cases: "No effects" with $\chi_\mu = \chi_\eta = 1$ and $\mathbf{F}_{\text{mig}} = \mathbf{0}$ (red lines), "only $c\mathbf{F}_{\text{mig}}$ " with $\chi_\mu = \chi_\eta = 1$ (blue lines), "only χ_η " with $\chi_\mu = 1$ and $\chi_\eta = \chi_\eta(\phi)$ (purple lines), and "only χ_μ " with $\chi_\mu = \chi_\mu(\phi)$ and $\chi_\eta = 1$ (green lines). These curves reveal that most of the interaction effect is due to the effective mobility: the green curves "only χ_μ " are nearly identical to the black curves "All effects", and both groups of curves show no or little dependence on St_{acp} . The effective suspension viscosity $\chi_\eta(\phi)$ and the particle-induced bulk force $c\mathbf{F}^{\text{rad}}$ on the suspension only have a minor influence on $\Delta\beta_{\text{acp}}$.

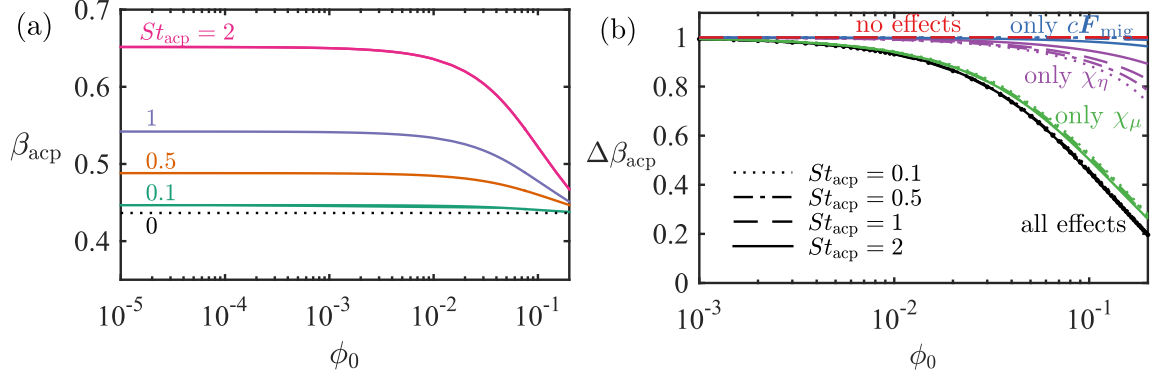


Figure 4.9: (a) Lin-log plot of the acoustic particle focusing fraction β_{acp} (given by Eq. (4.16a)) versus the inlet concentration ϕ_0 for four different St_{acp} values. (b) Lin-log plot of the rescaled particle focusing fraction $\Delta\beta_{acp}$, given by Eq. (4.17), as a function of ϕ_0 . The line styles denote different St_{acp} values, and the colors denote the inclusion of one or all hydrodynamic interaction effects, described in Section 4.2, purple: only effective suspension viscosity $\chi_\eta(\phi)$, blue: only momentum transfer from the particles to the suspension cF_{mig} , and red: no interaction effects included.

Finally, in Fig. 4.10 we show the first step towards an experimental validation of our continuum model of hydrodynamic interaction effects. In the figure are seen two micrographs of acoustophoretic focusing of 5.1- μm -diameter polystyrene particles in water in the silicon-glass microchannel setup described in Augustsson *et al.*[38]. The micrographs are recorded at Lund University by Kevin Cushing and Thomas Laurell under stop-flow conditions $v_0 = 0$ after 0.43 s of acoustophoresis with the acoustic energy $E_{ac} = 10^2$ Pa. The field of view is near the right edge x_2 of the active region sketched in Fig. 4.4(b). The good focusing obtained at the low density $\phi_0 = 0.001$ is well reproduced by our model, see Fig. 4.10(a) and (c). Likewise, the much reduced focusing obtained at the high density $\phi_0 = 0.1$ is also well reproduced by our model, see Fig. 4.10(b) and (d). Moreover, which is not shown in the figure, the observed transient behavior of the two cases is also reproduced by simulations: For the low concentration $\phi_0 = 0.001$, the particles are migrating towards to pressure node directly in straight lines, while for the high concentration $\phi_0 = 0.1$, pronounced flow rolls are induced, similar to those shown in Fig. 4.6.

4.5 Discussion

The results of the continuum effective model simulations of the MAP and the ACP models show that the dominating transport mechanisms differ. For the ACP model, the behavior of a suspension in the high-density regime $\phi_0 \gtrsim 0.01$ is dominated by the strong decrease in the effective single-particle mobility χ_μ shown in Fig. 4.2. Here, the particle-particle interactions are so strong that the suspension moves as a whole with suppressed relative single-particle motion. The response is a steady degradation of the focusing fraction β_{acp} shown in Fig. 4.9, as it becomes increasingly difficult for a given particle to migrate towards the center line, where the concentration increases and the mobility consequently decreases. In contrast, for the MAP model, the capture fraction β_{map} increases as ϕ_0 increases from

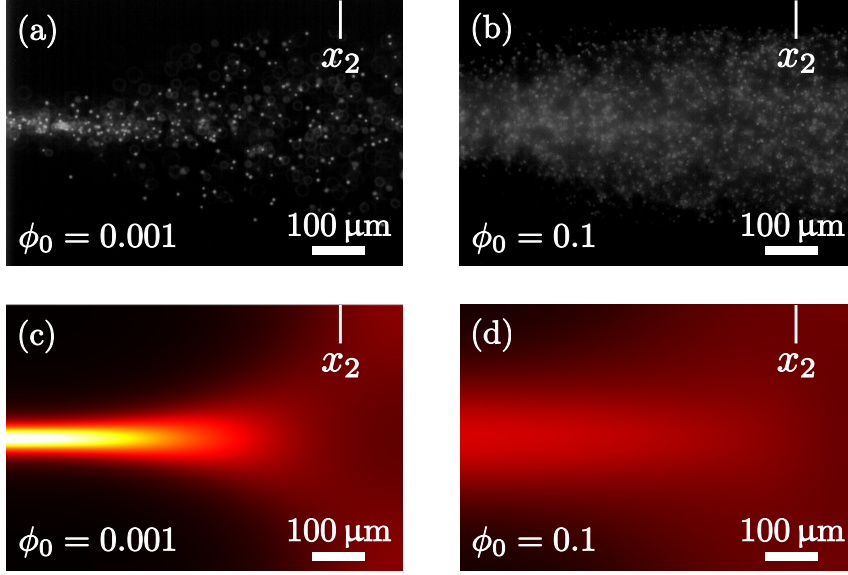


Figure 4.10: Topview near the right edge x_2 of the acoustic active region of the particle concentration in a 370-μm-wide microchannel after 0.43 s of acoustophoresis with the acoustic energy $E_{ac} = 10^2$ Pa on 5.1-μm-diameter polystyrene particles under stop-flow conditions $v_0 = 0$. (a) Experiment with $\phi_0 = 0.001$. (b) Experiment with $\phi_0 = 0.1$. (c) Continuum modeling with $\phi_0 = 0.001$. (d) Continuum modeling with $\phi_0 = 0.1$. The experimental micrographs courtesy of Kevin Cushing and Thomas Laurell, Lund University.

0 to 0.03, confirming the results of Mikkelsen and Bruus.[64] The reason for the increased capture is that the particle concentration in the near-wire region is low due to the removal of particles, leaving the single-particle mobility unreduced there, while in the region a little farther away, particles attracted by the wires pull along other particles in a positive feedback due to the high-density "stiffening" of the suspension there. Thus, for the MAP system, the dominating interaction effect is through the particle-induced body force $c\mathbf{F}_{mig}$ in Eq. (4.5a).

For ϕ_0 increasing beyond 0.03, the observed non-monotonic behavior of β_{map} and continued monotonic behavior of β_{acp} as a function of increasing ϕ_0 , depends on whether or not the specific forces and model geometry lead to the formation of flow rolls, such as shown for the MAP model in Fig. 4.6. The flow-roll-induced decrease observed in the capture efficiency β_{map} for $\phi_0 \gtrsim 0.03$, see Fig. 4.9(a), was not observed by Mikkelsen and Bruus [64] presumably because of their relatively coarse mesh. For the ACP model, no strong influence from induced flow rolls was observed, and the resulting decrease in focus efficiency was monotonic as a function of ϕ_0 . This difference in response is caused by differences in spatial symmetry and in the structure of the two migration forces. The MAP model is asymmetric around the horizontal center line, while the ACP model is symmetric, which accentuates the appearance of flow rolls in the former case. Moreover, the rotation of the body force density $c\mathbf{F}_{mig}$ can be calculated as $\nabla \times [c\mathbf{F}_{mig}] = c\nabla \times \mathbf{F}_{mig} - \mathbf{F}_{mig} \times \nabla c$. In the MAP model, both of these rotations are non-zero, while in the ACP model, the first term is zero as \mathbf{F}^{rad} is a gradient force, and this feature leads to significant flow rolls in the MAP model and weak ones in the ACP model.

In the above discussion of the results of our model, we have attempted to describe general aspects of hydrodynamic interaction effects, which may be used in future device design considerations. Given the sensitivity on the specific geometry and on the form of external forces, it is clear that detailed design rules are difficult to establish. However, the simplicity of the model allows for relatively easy implementation in numerical simulations of specific device setups.

4.6 Concluding remarks

This concludes our treatment of hydrodynamic particle-particle interaction in microfluidic channels, and we will in next chapter change our focus and present an effective model for mm-sized glass capillaries device used for acoustic trapping.

Chapter 5

Effective modeling of acoustofluidic capillary devices

In this chapter, we develop an effective theoretical model for a class of mm-sized glass capillaries system used widely in different acoustofluidic systems.

The results presented in this chapter is to a large extent, with co-author permission, taken from and based on our journal paper, in print, *Three-Dimensional Numerical Modeling of Acoustic Trapping in Glass Capillaries* M. W. H. Ley and H. Bruus, Phys. Rev. Applied, **8** (2017), pages. Proof version enclosed in Appendix [B](#).

5.1 Introduction

The aim of this work is developing an effective model for a class of mm-sized glass capillaries system used in many experimental studies [70, 71, 72, 30, 31] and clinical applications, such as isolation of cell-secreted membrane vesicles [73] and capture and enrichment of bacteria from blood samples for rapid sepsis diagnostics [16]. A sketch of the generic capillary system is shown in Fig. 5.1, while typical material parameters are listed in Table 1.

The capillary is typically actuated locally by a piezoelectric transducer, which is coupled to the capillary either by epoxy glue or by a small drop of glycerol, the latter allowing for removal and reuse of both the capillary and the transducer. The device is driven at a resonance frequency to obtain the largest possible acoustic field in the fluid. In the optimal case, the main component of the resonance field is a vertically standing bulk acoustic wave (SBAW) along the z direction, which unavoidably is mixed with a traveling bulk acoustic wave (TBAW) in the axial x direction along the capillary away from the transducer region.

The resulting acoustic radiation forces trap particles above or near the transducer in all spatial directions and are often strong enough to retain a single microparticle against the drag from a fluid flow.

In contemporary acoustofluidics it is a challenge to model and optimize the design of a given device. Examples of recent advances in modeling include Lei *et al.* [72], who modeled the three-dimensional (3D) fluid domain without taking the solid domain into account;

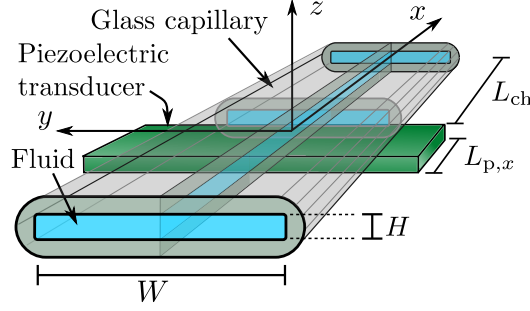


Figure 5.1: A sketch of a generic capillary system for acoustic trapping. A mm-sized glass capillary (gray) filled with water (blue), is attached to a piezoelectric transducer (green) operated in the MHz range. At certain frequencies a resonant acoustic field builds up, in which case the acoustic radiation forces are strong enough to trap suspended microparticles in all spatial directions, and even retain them against drag from an axial fluid flow through the capillary.

Table 5.1: Capillary geometries modeled in this study: C1 from Hammarström *et al.* [30], C2 from Lei *et al.* [72], C3 from Mishra *et al.* [71], C4 from Gralinski *et al.* [74], and C5 a capillary design proposed in this chapter. Besides the symbols defined in Fig. 5.3, R_{cu} is the radius of curvature of the fluid channel corners, f_{res}^{exp} and f_{res} is the experimental and numerical resonance frequency, respectively, and Q is the numerically calculated quality factor.

Device	L [mm]	W [mm]	H [mm]	H_{gl} [mm]	R_{cu} [μm]	$L_{p,x}$ [mm]	$L_{p,y}$ [mm]	f_{res}^{exp} [MHz]	f_{res} [MHz]	Q	d_0 [nm]
C1	2.0	2.0	0.20	0.14	25	1.16	2.0	3.970	3.906	53	0.10
C2	2.0	6.0	0.30	0.30	25	1.0	1.0	2.585	2.495	78	0.10
C3	8.5	0.1	0.10	0.05	19	15	1.0	7.900	6.406	222	0.10
C4	10.0	0.85	0.85	0.225	425	4.0	1.0	1.055	0.981	109	0.10
C5	2.0	0.5	0.20	0.14	25	1.16	0.50		4.201	53	0.10

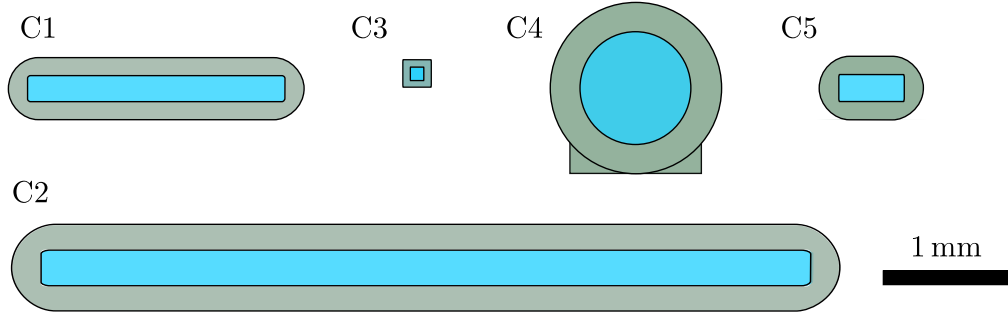


Figure 5.2: Sketches (to scale with respect to the 1 mm black scalebar) of the glass capillary cross sections C1-C5 investigated in this study.

Muller and Bruus [1, 75], who made detailed models in 2D of the thermoviscous and transient effects in the fluid domain; Gralinski *et al.* [74], who modeled circular capillaries in 3D with fluid and glass domains without taking absorption and outgoing waves into account; Hahn and Dual [3], who calculated the acoustic field in a 3D model for a glass-silicon device (not a capillary system) and characterized the various loss mechanisms; and Garofalo *et al.*, who studied a coupled transducer-silicon-glass-water system in 2D [76].

Though many elements of a complete theoretical description of the capillary devices have been included in part in previous published work, no model have been presented, to the authors knowledge, including all of the above-mentioned elements in a single model in 3D.

We model the acoustic pressure field in the liquid coupled to the displacement field of the glass wall, taking into account mixed standing and traveling waves as well as absorption. We model the outlets, which in practise are connected to long tubes, either as being free reflecting surfaces or perfect absorbers of outgoing acoustic waves. Our model explains the dynamical mechanism that leads to the formation of localized acoustic resonance modes in the straight capillaries that are without geometrical cavities in the axial x direction. We furthermore compare prior experimental results from the four devices listed in Table 5.1 with predictions of our model, in particular the frequency response, the levitating resonance modes, and the acoustic trapping forces.

5.2 Effective modeling

As mentioned above, the full capillary device consist of many different sub-elements that together make up the device. In order to make a numerical model that realistically can run on a desktop computer, we have chosen to model a) the piezoelectric transducer, and b) the glass capillary ends and the connective tubing by the use of effective models. a) While piezoelectric transducers are widely commercially available, material parameters are numerous and can be frequency dependent, making a coupled numerical model prone to error and hard to troubleshoot, without first making an isolated model for piezoelectric resonance mode and compare with experiments. b) Simulating the full capillary length

over several centimeters of length entailing up hundreds of acoustic wavelengths is not feasible for a full 3D finite element model.

We model a) by assuming an effective mechanical actuation on the bottom of the capillary, thus avoiding simulating the transducer all-together, and b) is modelled using the technique of perfectly matched layers (PML), which is a domain acting as an ideal absorber of all outgoing waves. The details of both a) and b) will be described in the following. Lastly, because the channel dimensions $L, W, H \gg \delta$, we choose to model fluid with pressure acoustics, neglecting the viscous boundary layers, though we introduce effective damping through the wave number [3] in both the solid and the fluid .

5.2.1 Governing equations

The fluid is modelled as pressure acoustics with the Helmholtz equation, derived in Eq. (2.25a)

$$\nabla^2 p_1 + k_c^2 p_1 = 0, \quad k_c = \frac{\omega}{c_0}(1 + i\Gamma_{\text{fl}}), \quad (5.1)$$

and the solid is modelled by the solid-elastic equations, given by Eqs. (2.11a) and (2.11b)

$$\nabla \cdot \boldsymbol{\sigma}_{\text{sl}} = -\rho_{\text{sl}}\omega^2(1 + i\Gamma_{\text{sl}})^2 \mathbf{u}_1, \quad (5.2a)$$

$$\frac{1}{\rho_{\text{sl}}}\boldsymbol{\sigma}_{\text{sl}} = c_{\text{tr}}^2 \left[\nabla \mathbf{u}_1 + (\nabla \mathbf{u}_1)^T \right] + (c_{\text{lo}}^2 - 2c_{\text{tr}}^2)(\nabla \cdot \mathbf{u}_1)\mathbf{I}, \quad (5.2b)$$

here, the solid stress tensor is given in terms of the longitudinal and transverse speed of sound in the solid, see Eq. (2.12). Following the thorough analysis by Hahn and Dual [3], we introduce effective absorption in both our fluid (fl) and solid (sl) equations, by modifying the compressional wave number k_c , setting $\Gamma = \Gamma_{\text{fl}}$ for the fluid, and time derivative as $\partial_t \rightarrow -i\omega(1 + i\Gamma_{\text{sl}})$ for the solid. $\Gamma \ll 1$ is thus an effective absorption parameter, representing all damping in the system, with values for the respective materials listed in Table 1.

5.2.2 Boundary conditions

The applied boundary conditions are summarized in Table 5.2 and Fig. 5.3. Due to mirror symmetry about the y - z and x - z planes, we only model a quarter of the system, and symmetry conditions are applied on the two symmetry planes. The stress is zero on all outer boundaries facing the air, and the stress and the velocity fields are continuous across all internal boundaries.

The model of the piezoelectric actuation on the interface $\partial\Omega_{\text{pz}}$ is not straightforward, as neither the excited modes of the piezoelectric transducer nor the coupling layer by which the transducer is attached to the glass capillary have been characterized experimentally in the published studies. We therefore choose to explore the effects of two idealized generic actuation conditions that mimic a simple uniform contraction-expansion mode that pushes and pulls on the glass capillary surface through a coupling layer consisting of either a rigid epoxy glue or a fluid glycerol film. From previous work [6], we know that a wall displacement amplitude $d_0 = 0.1 \text{ nm}$ leads to realistic values for experimentally measured

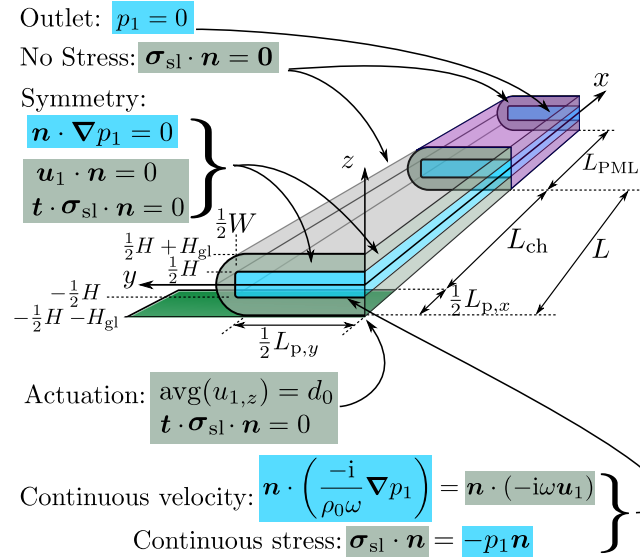


Figure 5.3: The computational domain used in the numerical model of Fig. 5.1 reduced to the quadrant $x > 0$ and $y > 0$ due to symmetry. Shown are the solid wall (gray), the water channel (blue), the actuation plane (green), the perfectly matched layer (PML, purple), and arrows allocating the boundary conditions to their respective boundaries.

pressures [39, 38, 66], so we use this value throughout this chapter. To mimic the rigid epoxy glue, we assume a simple uniform displacement amplitude $u_{1,z} = d_0$ in the z direction without transverse motion, Eq. (5.3a), while to mimic the fluid glycerol layer with a typical thickness of 10 - 100 μm that easily can accommodate nm-sized fluctuations as well as transverse displacement, we assume that only the area-average $\langle u_{1,z} \rangle_{\text{pz}}$ of the normal displacement $u_{1,z}$ is d_0 while the shear stress is zero, Eq. (5.3b),

$$u_{1,z} = d_0, \quad u_{1,x} = u_{1,y} = 0, \quad \text{rigid displacement,} \quad (5.3a)$$

$$\langle u_{1,z} \rangle_{\text{pz}} = d_0, \quad \sigma_{1,xz} = \sigma_{1,yz} = 0, \quad \text{average displacement.} \quad (5.3b)$$

Finally, the area-averaged actuation condition Eq. (5.3b) is imposed on the displace-

Table 5.2: Boundary conditions imposed on the solid and fluid domains in the model shown in Fig. 5.3.

Name	Domain \leftarrow boundary	Boundary condition
No stress	Solid domain \leftarrow air	$\boldsymbol{\sigma}_{\text{sl}} \cdot \mathbf{n} = \mathbf{0}$
Continuous stress	Solid domain \leftarrow fluid	$\boldsymbol{\sigma}_{\text{sl}} \cdot \mathbf{n} = -p_1 \mathbf{n}$
Mech. actuation	Solid domain \leftarrow transducer	Eq. (5.3a) or Eq. (5.3b)
Symmetry	Solid domain \leftarrow symmetry	$\mathbf{u}_1 \cdot \mathbf{n} = 0, \quad \mathbf{t} \cdot \boldsymbol{\sigma}_{\text{sl}} \cdot \mathbf{n} = 0$
Continuous velocity	Fluid domain \leftarrow solid	$\mathbf{v}_1^c \cdot \mathbf{n} = -i\omega \mathbf{u}_1 \cdot \mathbf{n}$
No stress	Fluid domain \leftarrow air	$p_1 = 0$
Symmetry	Fluid domain \leftarrow symmetry	$\mathbf{n} \cdot \nabla p_1 = 0$

ment field $u_{1,z}$ on the actuation interface using an envelope function $F(x)$,

$$\int_0^{\frac{1}{2}L_{p,x}} \frac{2dx}{L_{p,x}} \int_0^{\frac{1}{2}L_{p,y}} \frac{2dy}{L_{p,y}} (u_{1,z} - d_0) F(x) = 0, \quad (5.4a)$$

$$\text{with } F(x) = -\tanh\left(\frac{x - \frac{1}{2}L_p}{\Delta L_p}\right), \quad (5.4b)$$

where the transition length is set to $\Delta L_p = 100 \text{ } \mu\text{m}$.

5.2.3 The outlet and perfectly matched layers

In most setups, the capillary is connected to the microfluidic circuit through tubings at the ends. If a large section of the capillary is inserted into a connecting elastic tube [72], this might cause significant absorption. Furthermore, the water domain continues uninterrupted from the capillary into the connecting tube, so an extreme case is that none of the acoustic waves going out from the actuation region are reflected at the ends of the capillary. This situation we model using a perfectly matched layer (PML), which is a domain acting as an artificial perfect absorber of all outgoing TBAWs along the x axis. In our model the region $x < L$ is normal, while the PML of length L_{PML} is at $L < x < L + L_{\text{PML}}$, see Fig. 5.3. Following Collino and Monk [77], ideal absorption along the x direction for $x > L$ can be obtained by a complex-valued coordinate stretching of x in the PML domain. This stretching is based on a real-valued function $s(x)$, which is zero in the normal region $x < L$ and is smoothly increasing from zero in the PML as

$$s(x) = k_{\text{PML}} \left(\frac{x - L}{L_{\text{PML}}}\right)^2, \text{ for } L \leq x \leq L + L_{\text{PML}}, \quad (5.5a)$$

where $k_{\text{PML}} > 0$ is the absorption strength. The coordinate stretching is implemented in the model by changing all occurrences of ∂_x and the integral measure dx as

$$\partial_x \rightarrow \partial_{\tilde{x}} = \frac{1}{1 + is(x)} \partial_x, \quad (5.5b)$$

$$dx \rightarrow d\tilde{x} = [1 + is(x)] dx, \quad (5.5c)$$

where the latter appears in the weak-form implementation of the governing equations and boundary conditions, see Chapter 3. The values of L_{PML} and k_{PML} are also discussed in Section 5.2.5. The coordinate stretching in the PML introduces a positive imaginary part in the wave numbers in the x direction, and thus dampens the outgoing waves exponentially along the x axis.

The opposite limit of zero absorption is handled by dropping the PML and imposing the no-stress condition at $x = L$.

5.2.4 Mesh

The mesh is generated by first defining a mesh in the y - z plane, see Fig. 5.4(a), and then extruding it equidistantly along the x axis using the 'Swept Mesh' function in COMSOL

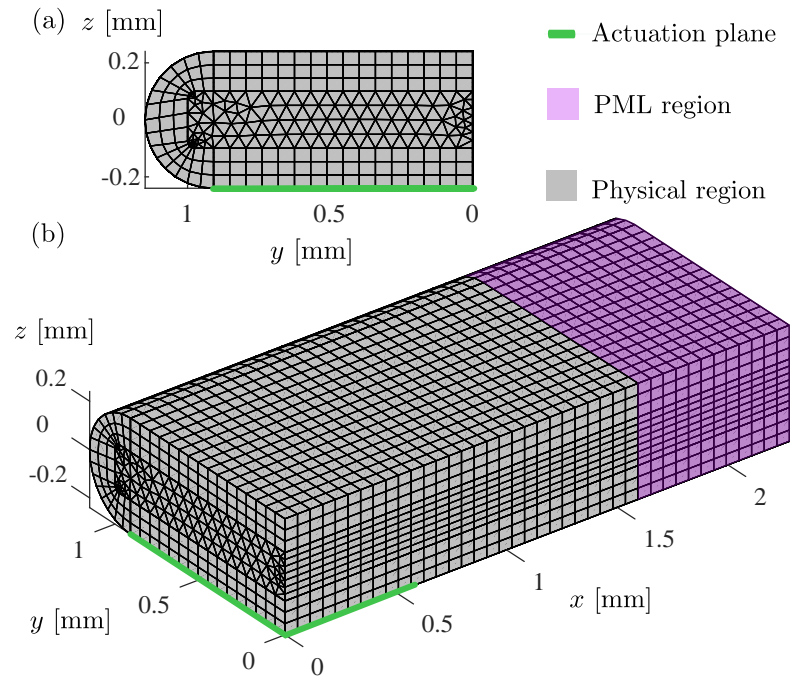


Figure 5.4: A coarse version of the mesh at the surface of the computational domain of Fig. 5.3 for a mesh size of $d_{\text{mesh}} = 57.2 \mu\text{m}$, which is twice the value used in most calculations, see Table 5.3. (a) The 2D mesh in the y - z plane consisting of a structured mesh in the solid, a free triangular mesh in the fluid, and a refined mesh at the corners of the fluid domain as well as at the vertical symmetry line $y = 0$. (b) The full 3D mesh generated by extruding the 2D mesh shown in (a) along the x direction with equidistant spacing.

Table 5.3: List of the mesh parameters used in the model. The maximum mesh element size is set to $d_{\text{mesh}} = H/7$ with three exceptions: (1) For the reference field g_{ref} of C1 in Eq. (3.15) and Fig. 5.6, where $d_{\text{mesh}}^{\text{ref}} = 0.9d_{\text{mesh}}$, (2) for Fig. 5.7, where $d_{\text{mesh}} = 40.0 \mu\text{m}$, and (3) For C4 where $d_{\text{mesh}} = H/20$.

Location	Linear size	No. of elements	Mesh size
<i>y-z plane</i>			
Bulk fluid	H	7	d_{mesh}
Bulk solid	H_{gl}	6	d_{mesh}
Corner solid-fluid	$\frac{1}{2}\pi R_{\text{cu}}$	10	$0.168 d_{\text{mesh}}$
fluid symmetry edge	H	15	$0.5d_{\text{mesh}}$
<i>x direction (extruded)</i>			
Bulk fluid	$L + L_{\text{PML}}$	80	d_{mesh}
Bulk solid	$L + L_{\text{PML}}$	80	d_{mesh}

Multiphysics, see Fig. 5.4(b). The size of the mesh elements is controlled by the maximum mesh size d_{mesh} , except elements on the z axis (the intersection of the two symmetry planes) and on the corner edges of the fluid channel (where the curvature is large), both of which are assigned a smaller maximum mesh size. All mesh sizes used in the model are listed in Table 5.3. Unless stated otherwise, we have set $d_{\text{mesh}} = H/7$.

5.2.5 Model validation

PML validation

We test the PML for capillary C1 as follows, see Fig. 5.5. The length L_{PML} of the PML is comparable to the longest wavelength of the system [78], here the longitudinal wave length $\lambda_{\text{lo}} = 2\pi c_{\text{lo}}/\omega = 1.4 \text{ mm}$ in Pyrex at 4 MHz. By running parametric sweeps in $L_{\text{PML}} \approx \lambda_{\text{lo}}$ and $k_{\text{PML}} > 0$, we find that for L_{PML} as short as $0.25\lambda_{\text{lo}}$, the results are independent of the PML strength in the range $10 < k_{\text{PML}} < 10^4$, (see Fig. 5.5(c)) showing that for this broad parameter range, the outgoing waves are absorbed before reaching the PML back edge at $x = L + L_{\text{PML}}$. At too low k_{PML} values (< 5), backscattering arises from the back-edge at $x = L + L_{\text{PML}}$, and for too high k_{PML} values ($> 10^4$) the effective material properties changes too abruptly at the PML-interface, causing backscattering at $x = L$.

To further show the independence of the results on the PML, we set $L_{\text{PML}} = 0.25\lambda_{\text{lo}}$ and $k_{\text{PML}} = 10^3$, and vary the length L_{ch} of the capillary between the piezoelectric transducer and the PML front edge. In Fig. 5.5, p_1 and u_z are plotted versus x for four fixed (y, z) coordinates, and it is seen that for $L_{\text{ch}} \gtrsim \lambda_{\text{lo}}$, the resulting fields coincide everywhere outside the PML domain. For smaller values $L_{\text{ch}} \lesssim \lambda_{\text{lo}}$ we do observe deviations in the response, indicating that the outgoing waves are not fully established before they enter the PML and are absorbed. Consequently, in the following, we choose the fixed parameter values $L_{\text{ch}} = 1 \text{ mm}$, $L_{\text{PML}} = 0.25\lambda_{\text{lo}} = 0.35 \text{ mm}$, and $k_{\text{PML}} = 10^3$.

Mesh size validation

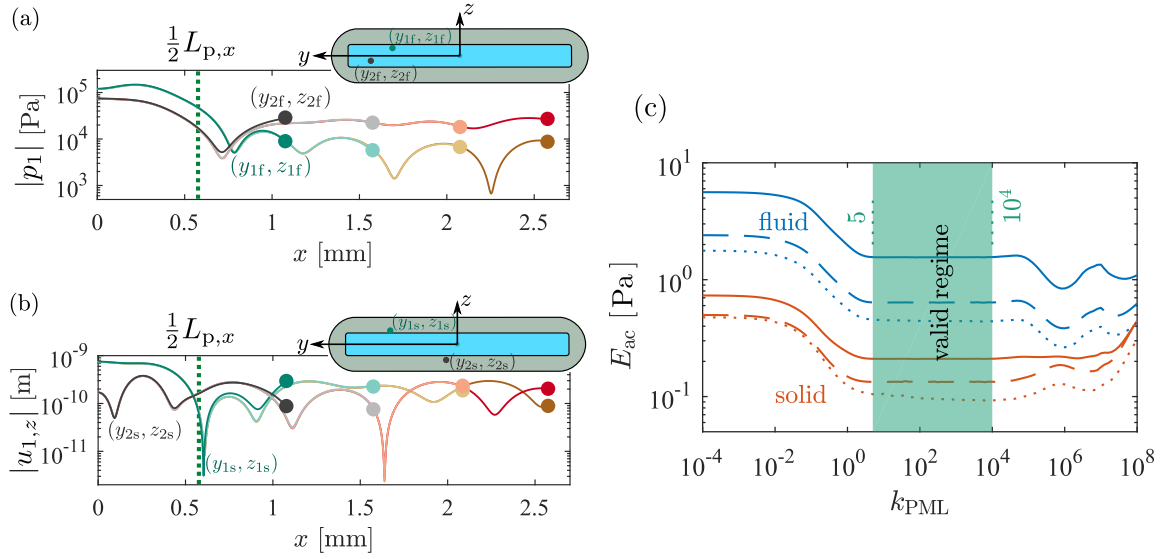


Figure 5.5: The acoustic field in capillary C1 as a function of the front-edge position $L = \frac{1}{2}L_{p,x} + L_{ch}$ of the PML domain with fixed $L_{PML} = 0.25\lambda_L$ and $k_{PML} = 10^3$. (a) The pressure amplitude $|p|$ versus x (colored lines) terminating at L (colored points) for the two (y, z) positions $(y_{1f}, z_{1f}) = (0.3W, 0.35H)$ and $(y_{2f}, z_{2f}) = (0.4W, -0.25H)$ (green and black points in the inset). The line colors correspond to $L_{ch} = 0.5, 1.0, 1.5, 2.0$ mm from green (black) to brown (red). The vertical green dotted line at $x = \frac{1}{2}L_{p,x}$ marks the edge of actuation region. (b) Similar plot for the vertical displacement amplitude $|u_z|$, but here for the two (y, z) positions $(y_{1s}, z_{1s}) = (0.3W, 0.6H)$, and $(y_{2s}, z_{2s}) = (0.05W, -0.7H)$. (c) The acoustic in the fluid as a function of k_{PML} , for both fluid (blue) and solid (orange). The line-styles denote integration over different device regions: Actuation region $x < \frac{1}{2}L_p$ (full lines), device region $x < L$ (dashed lines), and computation region $x < L + L_{PML}$ (dotted lines). We choose the valid region as the range in k_{PML} for which the energy density does not vary in the device region, *i.e.* flat curves of the dashed lines.

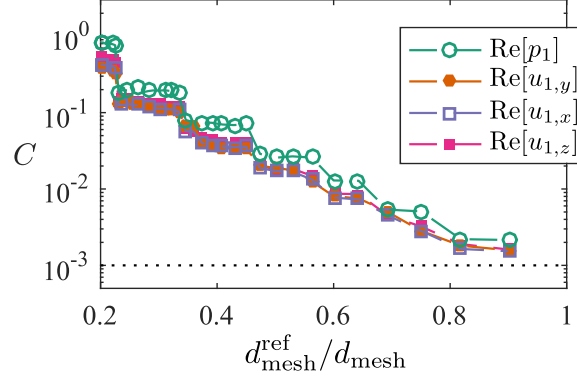


Figure 5.6: Semilog plot of the convergence parameter C defined in Eq. (3.15) versus $d_{\text{mesh}}^{\text{ref}}/d_{\text{mesh}}$, the inverse of the maximum mesh size. The mesh parameter values are listed in Table 5.3.

For a given field variable g , we perform a mesh convergence test based on the convergence parameter $C(g)$, which is defined in Eq. (3.15). Here, the integration volume over which $C(g)$ is calculated is the domain in which g is defined, but excluding the PML domain, *i.e.* $0 < x < L$. The field g is calculated with the above-mentioned characteristic mesh size d_{mesh} , and g_{ref} is the reference field calculated with the finer mesh $d_{\text{mesh}}^{\text{ref}} = 0.9d_{\text{mesh}}$. We cannot use a smaller value of $d_{\text{mesh}}^{\text{ref}}$, because this value combined with the length $L = 2.5$ mm results in a memory consumption of 85 GB RAM out of the 128 GB available on our workstation, see Section 5.3. With these values, our simulation involve 2×10^6 degrees of freedom and a computation time around 15 minutes per parameter set. In Fig. 5.6, semilog plots of C versus $d_{\text{mesh}}^{\text{ref}}/d_{\text{mesh}}$ for all four fields are shown. The plots exhibit an exponential decrease of C , which indicates good numerical mesh convergence. For the chosen mesh sizes we obtain $C \approx 0.002$, which is an acceptable level for the present study.

5.3 Results

We characterize numerically the four different glass capillaries C1, C2, C3, and C4 listed in Table 5.1, for which we find experimental results in the literature: C1 from Hammarström *et al.* [30] (and also employed in Refs.[29] and [31]), C2 from Lei *et al.* [72], C3 from Mishra *et al.* [71], and C4 from Gralinski *et al.* [74]. We also characterize a low-aspect ratio version of C1 denoted C5. Sketches showing the cross sections of the C1-C5 capillaries are shown in Fig. 5.2

We simulate the acoustic fields for these five capillary systems, each with the two different actuation boundary conditions Eqs. (5.3b) and (5.3a), and each both with and without the absorbing PML region. Supplementary to these studies, we simulate geometrical variations to study the effects of the capillaries manufacturing tolerances and the length-dependent reflections from the capillary end. This amounts to more than 20 dif-

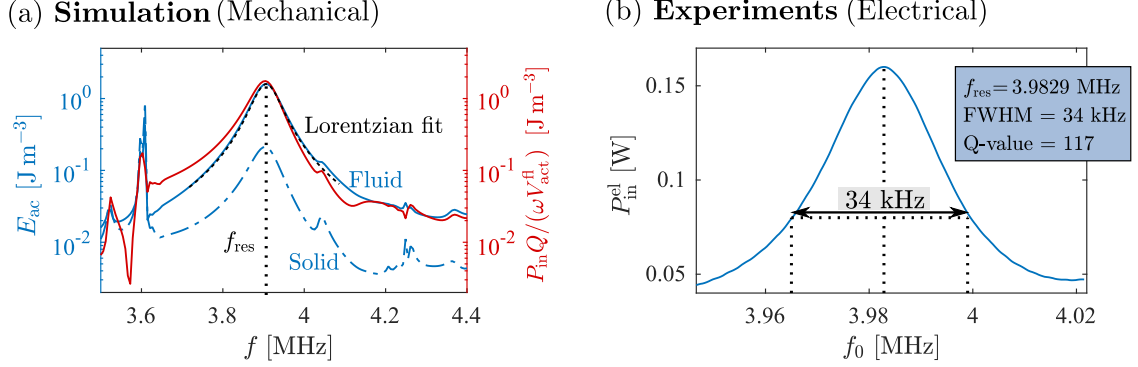


Figure 5.7: (a) **Simulations:** Semilog plot of simulation results for capillary C1 of the acoustic energy density E_{ac} (left axis) in the fluid (blue full line) and in the solid (blue dashed line) above the transducer, and the normalized power input $QP_{in}/(\omega V_{act}^{fl})$ (red line, right axis) from the transducer as a function of frequency f . E_{ac} is fitted well by a Lorentzian peak (black dashed line) having a resonance frequency $f_{res} = 3.906$ MHz, a full-width-half-maximum line width of FWHM = 0.07369 MHz, a quality factor of $Q = 53.0$, and a maximum of $E_{ac} = 1.60 Pa^3$. (b) **Experiments:** Frequency response (181 data points) of the electrical power delivered to the piezoelectric transducer P_{in}^{el} . From this curve a precise measurement of the resonance frequency is extracted, along with a rough estimate of the Q-value. The experiment was performed by Mikael Evander at Lund University, Sweden.

ferent capillary configurations, each swept in frequency using 50 values or more, resulting in over 1000 simulations, all of which show good numerical convergence without spurious effects. We remark that a simulation of a given frequency and geometry takes between 2 and 15 minutes on our workstation, a Dell Inc Precision T3610 Intel Xeon CPU E5-1650 v2 at 3.50 GHz with 128 GB RAM and 6 CPU cores.

To gain an overall understanding of these systems, we focus in the following subsections on different acoustofluidic aspects for each capillary.

5.3.1 Analysis of capillary C1

For capillary C1 [30], we mimic the experimental use of glycerol to attach the transducer by applying the area-average condition Eq. (5.3b) for the actuation. Moreover, to avoid the complications arising from reflections at the end of the capillary, we first assume perfect absorption of outgoing waves and thus use the PML.

First, we study the frequency response. In Fig. 5.7 we show a semilog plot of the volume-averaged acoustic energy density in the fluid volume above the transducer ($0 < x < \frac{1}{2}L_{p,x}$), E_{ac}^{fl} for the fluid volume V_{act}^{fl} , and E_{ac}^{sl} for the solid volume V_{act}^{sl} , as a function of actuation frequency f . A levitating resonance, strongly dominated by the energy density in the fluid, is identified at $f_{res} = 3.906$ MHz, only 2% lower than the experimental value $f_{res}^{exp} = 3.970$ MHz and 4% from the simple half-wave value $c_H/(2H) = 3.74$ MHz. The resonance peak is fitted well by a Lorentzian line shape centered around $f_{res} = 3.906$ MHz with a quality factor $Q = 53.0$.

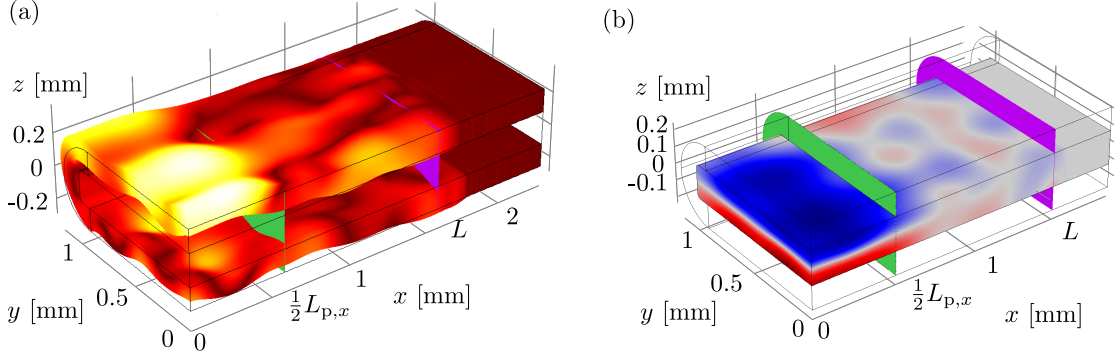


Figure 5.8: (a) The displacement field \mathbf{u}_1 in the solid (not drawn to scale) overlaid with a color plot of its magnitude u_1 from 0 nm (dark red) to 1.2 nm (white) for capillary C1 at the levitating resonance $f_{\text{res}} = 3.906$ MHz as in (b). (b) Color plot of the pressure field p_1 in the fluid from -0.18 MPa (blue) to 0.18 MPa (red) of capillary C1 at the levitating half-wave resonance $f_{\text{res}} = 3.906$ MHz. The green and purple planes represent the end of the actuation region and the beginning of the PML domain, respectively.

As a check, we compare the input power to the Q factor, which is defined as

$$Q = 2\pi \frac{\text{Total energy stored}}{\text{Energy lost per cycle}} = \omega \frac{\int_{\Omega} dV E_{\text{ac}}^{\text{tot}}}{P_{\text{out}}}, \quad (5.6)$$

where P_{out} is the power dissipation rate out of the system, and $E_{\text{ac}}^{\text{tot}} = E_{\text{ac}}^{\text{fl}} + E_{\text{ac}}^{\text{sl}}$ is the total stored acoustic energy density. In steady state, the time averages of the input and output power must be equal $P_{\text{out}} = P_{\text{in}}$, and we find the time-averaged power delivered by the transducer as

$$P_{\text{in}} = \int_{A_{\text{act}}} \langle (-i\omega \mathbf{u}_1) \cdot \boldsymbol{\sigma}_{\text{sl}} \cdot \mathbf{n} \rangle da. \quad (5.7)$$

Combining Eqs. (5.6) and (5.7), we get the approximate relation $E_{\text{ac}}^{\text{tot}} = Q P_{\text{in}} / (\omega V_{\text{act}}^{\text{fl}})$, which we plot on the right vertical axis (red) in Fig. 5.7(a), and note that it compares well with the directly calculated acoustic energy densities.

Besides the main levitating resonance peak, minor resonances without specific structure are also present, reflecting the many complex modes in the coupled fluid-solid system. None of these have particular good trapping properties, and they would probably not be observed in acoustophoretic experiments.

Next, we study the acoustic field. Upon inspection of the pressure and displacement fields at the resonance f_{res} , we find them to be mainly a standing wave above the actuation plane combined with an outgoing traveling wave away from the transducer region for $x > \frac{1}{2} L_{\text{p},x}$, see Fig. 5.8. The amplitude of the acoustic fields p_1 and \mathbf{u}_1 are largest above the transducer. The fluid pressure p_1 is a nearly-perfect vertical half-wave with a horizontal nodal plane near the channel center, which enables microparticle levitation given its maximum of 0.19 MPa for an actuation amplitude $d_0 = 0.1$ nm. Because of this feature, we call this type of resonance the levitating half-wave resonance in the following. At the edge of the transducer, the pressure amplitude drops an order of magnitude, which according to Eq. (2.37a) gives rise to the lateral forces that constitute the acoustic trap.

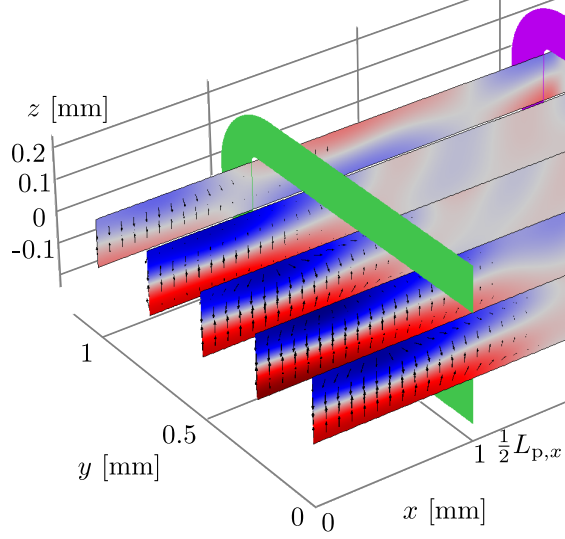


Figure 5.9: Capillary C1, color plot of the pressure field p_1 from -0.18 MPa (blue) to 0.18 MPa (red) in vertical planes placed equidistantly in steps of $\frac{1}{8}W$ starting at $y = 0$, showing the nearly horizontal nodal plane (gray) wobbling around $z = -0.05H$ at resonance $f_{\text{res}} = 3.906$ MHz. The acoustic radiation force \mathbf{F}^{rad} on $12\text{-}\mu\text{m}$ -diameter polystyrene test particles (black arrows with logarithmic lengths for visual clarity) has a maximum magnitude of 22 pN.

For the displacement field in the solid, we find its maximum value to be 1.2 nm, which is an order of magnitude larger than the average actuation amplitude $d_0 = 0.1$ nm. Besides the outgoing displacement waves leaving the capillary in the axial x direction, we also note the presence of circumferential displacement waves with short wave lengths around $\frac{1}{4}W$. The glycerol-like, area-averaged actuation Eq. (5.3b) allows for fluctuations, because it only fixes the mean vertical displacement $u_{1,z}$. At resonance f_{res} we find $u_{1,z} = (1.0 \pm 2.8)d_0$ on the actuation plane. We note that the standard deviation $2.8d_0 = 0.28$ nm is very small compared to a typical coupling-layer thickness of around 0.1 mm.

Despite the absence of a geometrical cavity along the capillary, we nevertheless find that a localized SBAW can exist in the region above the transducer. This SBAW is supported by a dynamically defined cavity that arises at resonance, because the displacement of the confining glass walls becomes an order of magnitude larger in the actuation region than elsewhere. Due to its dynamic nature, the cavity is leaky: the waves in the axial direction away from the actuator region are not evanescent, but they appear as TBAWs. The presence of the TBAWs reduces the Q value of the resonance state from previously reported values of $200 - 500$ [39] to ~ 50 , a value that however is large enough to ensure a well-defined resonance. While combinations of standing and traveling waves have been studied for surface acoustic wave (SAW) systems [40, 79, 80, 81], it is remarkable that they appear here in a study of bulk acoustic wave (BAW) systems.

To characterize the trapping capabilities of the device, we study the radiation force \mathbf{F}^{rad} Eq. (2.37a) acting on a $12\text{-}\mu\text{m}$ -diameter polystyrene (ps) test particle suspended in the fluid above the transducer. The z component F_z^{rad} of \mathbf{F}^{rad} , derived from the nearly

perfect standing half-wave in the vertical direction, levitates the test particle and holds it close to the pressure nodal plane. In the actuation region, this plane is nearly horizontal with a vertical position between $-0.1H$ and 0 . Away from the actuation region, it gradually changes its vertical position and fades away, see Fig. 5.9. The maximum levitating force on the test particle is $F_z^{\text{rad}} = 22 \text{ pN}$, which is nearly 50 times larger than the buoyancy-corrected gravitational force $F^{\text{grv}} = 0.44 \text{ pN}$.

The lateral trapping force $\mathbf{F}_{\parallel}^{\text{rad}}$ is given by the x and y components F_x^{rad} and F_y^{rad} of Eq. (2.37a), and it acts as a retention force when a fluid flow is imposed. In Fig. 5.10(a) for the C1 capillary at resonance f_{res} , $\mathbf{F}_{\parallel}^{\text{rad}}$ is plotted in the plane $z = -0.05H$ (vector plot) together with its magnitude $F_{\parallel}^{\text{rad}}$ (color plot). We see two clear trapping points within the actuation region, which are surrounded by strong gradients in the x and y directions, thus enabling lateral particle trapping. The maximum value F_x^{rad} within the actuation region is of particular interest, because it serves as a measure for the overall trapping strength of the device. We find $F_x^{\text{rad}} = 0.44 \text{ pN}$ at the position $(x, y, z) = (0.3L_{p,x}, 0, -0.05H)$. Outside the actuation region, a number of weaker, secondary trapping points are observed as shown in Fig. 5.10(b). Their presence is emphasized by re-scaling the color range, and we note their positions appear to be random. This finding is in qualitative agreement with experimental observations under stop-flow conditions [82].

We also verify the capability of the device to trap particles by simulating the trajectories of test particles initially placed on a regular grid throughout the trapping region and ending up in the trapping points (not shown).

Finally, we comment on calibration of the acoustic energy density $E_{\text{ac}}^{\text{fl}}$ in the fluid, which controls the magnitude of the trapping force in the capillary device. Because in practise it is not possible to calculate $E_{\text{ac}}^{\text{fl}}$ in a capillary device for a known ac voltage applied to the piezoelectric transducer, it is of importance to measure it in any given experiment. The first method is the drop voltage method [72], where at first $E_{\text{ac}}^{\text{fl}}$ is set high enough to levitate a test particle. Then the ac voltage and thus $E_{\text{ac}}^{\text{fl}}$ is lowered until the particle drops out of the trap, at which point $F_z^{\text{rad}}(E_{\text{ac}}^{\text{fl}}) = \frac{4}{3}\pi a^3(\rho_{\text{pa}} - \rho_{\text{fl}})g$, and $E_{\text{ac}}^{\text{fl}}$ can be found.

The second method is to increase the flow rate, and thus the flow speed v_{flow} , through the device until it reaches critical magnitude, where the maximum lateral retention force $F_{\parallel}^{\text{rad,max}}$ cannot balance the Stokes drag force on the particle any longer. From a scaling argument, and introducing a coefficient α dependent on the device composition and geometry, we can write

$$F_{\parallel}^{\text{rad,max}} = \alpha \frac{4\pi}{3} a^3 E_{\text{ac}}^{\text{fl}} \frac{\omega}{c_{\text{fl}}}, \quad \alpha = 0.0139, \quad (5.8)$$

where the value for α is found by simulation on the C1 capillary. The flow speed at which the Stokes drag exactly balances $F_{\parallel}^{\text{rad,max}}$ is denoted $v_{\text{max}}^{\text{flow}}$, so we can write

$$F_{\parallel}^{\text{rad,max}} = 6\pi\eta_{\text{fl}}a\chi v_{\text{max}}^{\text{flow}}, \quad \chi = \chi_{\text{paral}}^{z=0} = 1.064, \quad (5.9)$$

where χ is the wall-induced drag enhancement in the center plane of a parallel-plate channel [43], and the value is for the C1 capillary and the given test particle. Approximating the fluid channel to be rectangular, the maximum flow velocity can be related to the maximum

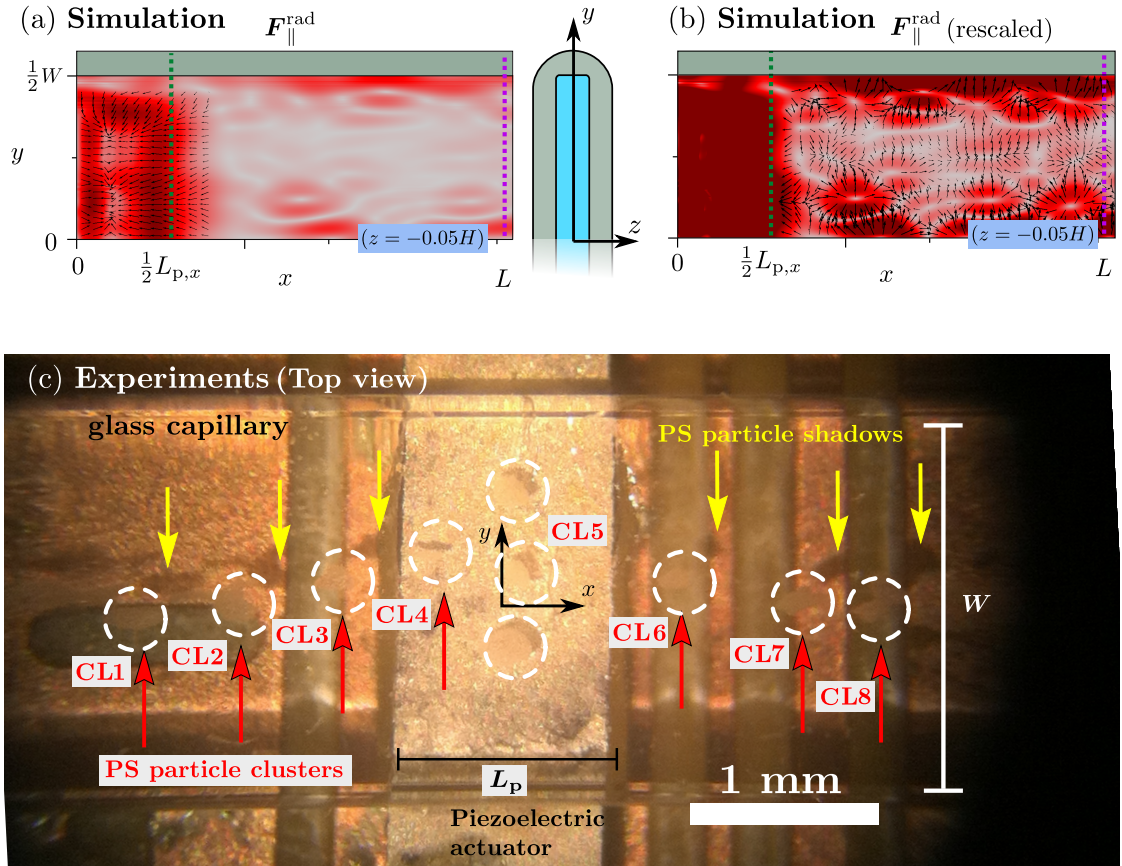


Figure 5.10: Capillary C1. (a) Simulation of the lateral acoustic radiation force $F_{\parallel}^{\text{rad}}$ (black arrows with logarithmic length) and its magnitude (color plot from 0 pN [gray] to 0.44 pN [dark red]) acting on 12- μm -diameter polystyrene beads in the x - y plane at $z = -0.05H$ at resonance $f_{\text{res}} = 3.906$ MHz. The inset is the cross-section geometry with $W = 2$ mm. (b) Same as (a) but with its maximum color (dark red) decreased to 0.10 pN to emphasize the secondary trapping points. (c) Experiment: Top-view photograph of a stop-flow experiment showing clusters of 7- μm -diameter polystyrene beads at certain nodes CL_n with $n = 1, 2, \dots, 8$ marked by red arrows and white circles. Initially the beads are evenly distributed, then they migrate into lines, and finally into separate clusters. The trapping points compare well with the predicted trapping points, shown in (a) and (b). The function generator sweeps frequencies from 3.9 to 4.3 MHz with 10 ms per frequency, and the sweeps are performed once every second. The transducer voltage was set to $V_{\text{pp}} = 10$ V.

flow rate Q_{\max}^{flow} as $v_{\max}^{\text{flow}} = \frac{\beta}{HW} Q_{\max}^{\text{flow}}$, where β is an aspect-ratio dependent constant [45], which for C1 is $\beta = 1.74$. Combining Eqs. (5.8) and (5.9) leads to

$$E_{\text{ac}}^{\text{fl}} = \frac{9\beta\chi}{2\alpha} \frac{\eta_{\text{fl}} c_{\text{fl}} Q_{\max}^{\text{flow}}}{\omega a^2 HW}. \quad (5.10)$$

With the assumed actuation amplitude $d_0 = 0.1$ nm, we find the maximum acoustic energy density to be 1.60 Pa, which yields the maximum flow speed and rate of $v_{\max}^{\text{flow}} = 3.1$ $\mu\text{m/s}$ and $Q_{\max}^{\text{flow}} = 0.043$ $\mu\text{L/min}$. We emphasize that this calibration method only works if the in-plane streaming velocity is small compared to the flow velocity.

Comparison with experiments

In the following we present a preliminary comparison with experiments carried out by Carl Johansson and Mikael Evander in the group of Professor Thomas Laurell at Department of Biomedical Engineering, at Lund University, Sweden.

Frequency response

In Fig. 5.7(b) we plot the electrical power delivered to the transducer $P_{\text{in}}^{\text{el}}$ as a function of frequency. The simulated resonance frequency (see Fig. 5.7(a)) matches well with the experimental value (within 2%), and the Q-value is estimated from the experiment by evaluating full width half maximum line, to be $Q = 117$, which is a factor two higher than our theoretical prediction ($Q = 53$). As we will see in section Section 5.3.4, this difference could easily be due to end reflections from the connecting tubing that could cause partial backscattering of the acoustic wave and thereby decrease the outgoing leakage of acoustic energy, resulting in an increase of the Q-value. To what extent the connective tubing causes acoustic backscattering is unclear at this point.

Trapping points

In Fig. 5.10 we compare the theoretically predicted trapping points, in (a) and (b), with experimental measurements (c). The experiment shows a stop-flow measurement of 7- μm -diameter polystyrene particle gathering in clusters in the C1 capillary, where a resonance mode was found by tuning the actuation frequency that showed minimal acoustic streaming. Initially, the particles are evenly distributed in the experiment. As the ultrasound is turned on, the particles gather in lines at first, and then afterwards in clusters as shown. Comparing the predicted trapping points from simulation with the experiment, it is clear that the pattern and number of trapping points is roughly the same. Moreover, in both cases, the trapping pattern appears somewhat irregular, which causes us to suspect that the system is very sensitive towards small perturbations in e.g. geometry, temperature, material parameters, etc., which is also what is observed experimentally.

Calibration of the acoustic energy density

Because the piezoelectric transducer is not included in this model modelled, we do not know the acoustic energy as a function of applied voltage without performing a calibration measurement. We have therefore performed a drop-voltage calibration (see Section 5.3.1) of the acoustic energy density in the capillary. In Table 5.4 nine drop-voltage measurements are shown, performed with 12- μm -diameter polystyrene particles. Assuming a per-

Table 5.4: Experimental data of drop voltage measurements performed for the C1 capillary for three different 12- μm -diameter polystyrene beads that were caught in the center at the trap at above the transducer (see Fig. 5.1). The actuation voltage was lowered until the acoustic forces could no longer levitate the particle and it would drop to the bottom of the capillary. At this (drop) voltage the acoustic forces exactly balances the buoyancy-corrected gravity forces on the particles. The experiments were performed by Carl Johannesson and Mikael Evander at Lund University, Sweden.

Bead Number	1	1	1	2	2	2	3	3	3	Mean	St. Dev.
Drop voltage [mV]	28	27	29	30	29	30	30	32	32	29.7	1.66

fect standing half wave in the z direction and no modulations in the x and y directions, the maximum acoustic levitating force is $F_{\text{rad},z}^{\text{max}} = 4\pi a^3 \Phi \frac{\omega}{c_0} E_{\text{ac}}^{\text{fl}}$. This is balanced by the buoyancy corrected gravitational force on the particle $F_{\text{grav}} = \frac{4}{3}\pi a^3 (\rho_p - \rho_0)g$. At the drop voltage (29.7 mV) the two forces are equal, and since the acoustic energy density scales as the square of the applied voltage $E_{\text{ac}} \propto V_{\text{pp}}^2$, the calibrated energy density becomes

$$E_{\text{ac}}^{\text{fl}} = \frac{c_0(\rho_p - \rho_0)g}{3\omega\Phi} \left(\frac{V_{\text{pp}}}{29.7 \text{ mV}} \right)^2 = 72 \text{ Pa} \left(\frac{V_{\text{pp}}}{1 \text{ V}} \right)^2, \quad (5.11)$$

which implies that at typical operating voltages between 1 to 10 V, the acoustic energy density $E_{\text{ac}}^{\text{fl}}$ will be between 72 and 7200 Pa. This is an unexpected high, and surprising result compared to other typical acoustofluidic devices in the literature, which for the same transducer voltage, ranges e.g. between 0.085 and 8.5 Pa for Lei *et al.* [72] (for a similar glass capillary device), and between 27 and 2700 Pa for Augustsson *et al.* [38] (for a silicon-glass channel). This could suggest that coupling the capillary and transducer with a thin glycerol layer gives an efficient mechanical coupling.

5.3.2 Analysis of capillary C2

In the experiment, capillary C2 is held in place by two rubber sleeves [72], which may justify a generic study using the absorbing PML region. Capillary C2 differs from capillary C1 by being more flat, having a cross-section aspect ratio of 1:20 in contrast to that of 1:10 for the latter [30]. A more significant difference is that the transducer of C2 was attached by glue and not by glycerol as for C1. We therefore study the different responses arising from using these two actuation conditions.

Using the glycerol-like area-averaged actuation condition Eq. (5.3b), a strong levitating half-wave resonance resembling the one in C1 and having a quality factor $Q = 78$, is found at $f_{\text{res}}^{\text{avg}} = 2.495 \text{ MHz}$ equal to the simple half-wave value $c_0/(2H)$. The maximum levitating force is $F_z^{\text{rad}} = 18 \text{ pN}$.

Changing to the glue-like rigid actuation condition Eq. (5.3a), the resonance frequency drops slightly to $f_{\text{res}}^{\text{rgd}} = 2.345 \text{ MHz}$, fairly close to the experimentally observed resonance at 2.585 MHz, while the quality factor decreases to $Q = 61$, the acoustic energy density increases by 9%, and the maximum levitating force is nearly doubled to become $F_z^{\text{rad}} = 33 \text{ pN}$. Qualitatively, the frequency spectrum changes from having an additional resonance peak close to the levitating resonance of $f_{\text{res}} = 2.495 \text{ MHz}$ using the glycerol-like condition,

Table 5.5: Simulation results for the quadratic capillary C3: the levitating half-wave resonance frequency f_{res} , the quality factor Q , and the acoustic energy density $E_{\text{ac}}^{\text{fl}}$. The side length $W = H$ and glass thickness H_{gl} are varied within the fabrication specifications, and we use either the average actuation condition "A"Eq. (5.3b) or the rigid condition "R"Eq. (5.3a). The experimental resonance frequency is $f_{\text{res}}^{\text{exp}} = 7.90$ MHz.

$W = H$ [μm]	H_{gl} [μm]	Actu- ation	f_{res} [MHz]	Q –	$E_{\text{ac}}^{\text{fl}}$ [Pa]
90	40	A	8.230	114	67
90	60	A	7.964	60	28
90	60	R	7.950	117	163
100	50	A	7.350	91	40
100	50	R	7.313	157	120
110	40	A	6.670	124	26
110	40	R	6.640	148	84
110	60	A	6.590	79	28

to having no extra resonances using the glue-like condition. The spatial structure of the resonance field in the fluid at f_{res} largely remains the same for the two different boundary conditions.

5.3.3 Analysis of capillary C3

For the quadratic capillary C3 [71], we use the nominal geometry parameters $W = H = 100 \mu\text{m}$ and $H_{\text{gl}} = 50 \mu\text{m}$ with PML absorption, and we predict numerically the frequency of the levitating half-wave resonance to be $f_{\text{res}} = 7.35$ MHz, only 2% from the simple half-wave value $c_0(2H) = 7.49$ MHz, and 7% lower than the experimental value, $f_{\text{res}}^{\text{exp}} = 7.90$ MHz. This discrepancy leads us to study changes in predicted acoustic response as a function of geometrical variations within the fabrication uncertainties listed by the producer (VitroCom #8510, Mountain Lakes, NJ): $\pm 10\%$ for W and H , and $\pm 20\%$ for H_{gl} . Some of the resulting numerical predictions for the resonance frequency f_{res} and Q values, using both the averaged and rigid actuation condition, are listed in Table 5.5.

For these thin-walled capillaries, the levitating half-wave resonance depends strongly on the channel height H and width W , and much less on the glass thickness H_{gl} . The 10% variation $H = W = (100 \pm 10) \mu\text{m}$ leads to a 10% variation in $f_{\text{res}} \approx (7.4 \pm 0.7)$ MHz for fixed H_{gl} , while the 20% variation in $H_{\text{gl}} = (50 \pm 10) \mu\text{m}$ leads to variations less than 2% in f_{res} for fixed H and W . Moreover, in agreement with the results for C2, $E_{\text{ac}}^{\text{fl}}$ and the Q factor for the glue-like rigid actuation condition R are increased by a factor 3 - 6 and 1.2 - 3, respectively, compared to those of the glycerol-like averaged condition A. The maximum levitating force with $H = W = 100 \mu\text{m}$ for condition R is $F_z^{\text{rad}} = 3690$ pN, while it drops to 1380 pN for condition A. The two actuation types lead to the same levitating resonance frequency within 0.5%.

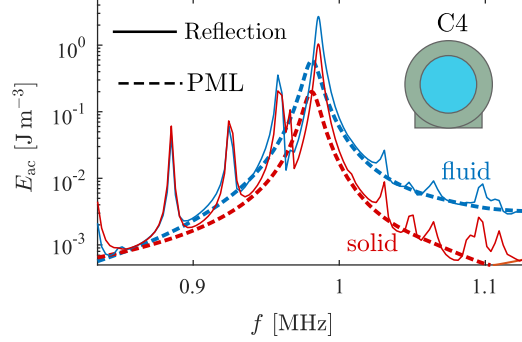


Figure 5.11: Simulated frequency response of capillary C4 (the insert shows its cross section), with total length of $L = 10$ mm and using the glue-like actuation condition Eq. (5.3b). Semi-log plot of the volume-averaged acoustic energy density E_{ac}^{fl} in the trapping region ($x < \frac{1}{2}L_p$) for the fluid (blue) and the solid (red) both with PML (thick dashed lines, $k_{\text{PML}} = 10^3$, $f_{\text{res}}^{\text{PML}} = 0.9812$ MHz) and without (solid lines, $k_{\text{PML}} = 0$, $f_{\text{res}}^0 = 0.9856$ MHz).

5.3.4 Analysis of capillary C4

In the original work on the circular capillary C4 [74], effects due to reflections at the end of the capillary were discussed. We therefore study numerically the frequency response with PML absorption (perfect absorption of all out-going waves) and without it (reflection of all out-going waves at the end-wall without absorption).

For the case with PML absorption, we find the levitating half-wave resonance to have the following characteristics: $f_{\text{res}} = 0.9753$ MHz, $Q = 109$, $E_{ac}^{\text{fl}} = 0.96$ Pa, and maximum levitating force $F_z^{\text{rad}} = 1.6$ pN using the glycerol-like condition Eq. (5.3b), and $f_{\text{res}} = 0.9818$ MHz, $Q = 79$, $E_{ac}^{\text{fl}} = 0.57$ Pa, and maximum levitating force $F_z^{\text{rad}} = 2.6$ pN using the glue-like condition Eq. (5.3a). These values for f_{res} are close to the experimental value of 0.981 MHz and the theoretical value $\gamma_{11}c_{\text{fl}}/(\pi H) = 1.03$ MHz based on the simple hard-wall cylinder geometry, where $\gamma_{11} = 1.841$ is the first zero of the derivative $J_1'(x)$ of the first Bessel function. As for the other capillaries, the choice of actuation condition leads to no qualitative, and only minor quantitative differences in the frequency spectrum.

When the PML is removed by imposing the zero-stress condition at $x = L$, the out-going waves from the transducer region are reflected by the end wall, and complex interference effects arise in the capillary. For fixed $L_{p,x}$, the channel length L is varied between 1 mm and 10 mm, and relative to the PML case, we find that the levitating resonance frequency only changes about 1%, while the Q value and E_{ac}^{fl} typically increases by 200–300% and 400–600%, respectively. This result illustrates that whether the capillary ends are reflecting or fully absorbing, does not affect the frequency of the main levitating mode significantly, while it has a crucial influence on the Q factors and acoustic energies, as well as on the existence of secondary resonance modes. In contrast, the internal attenuation, given by the Γ factors, is unimportant, since the associated attenuation lengths $L_{\text{fl}} = \frac{c_0}{\omega\Gamma_{\text{fl}}} \approx 60$ mm and $L_{\text{sl}} = \frac{c_{\text{sl}}}{\omega\Gamma_{\text{sl}}} \approx 2$ m are longer than the capillary half-length $L \approx 20$ mm.

For the longest capillary $L = 10$ mm, we plot in Fig. 5.11 E_{ac} as a function of frequency f near the levitating half-wave resonance f_{res} with and without PML absorption.

Firstly, we note that f_{res} in the two cases differs less than 0.4%. Secondly, without PML absorption, the energy is not lost by the out-going waves, and consequently, the line shape becomes higher and more narrow. Indeed, the resonance amplitude $E_{\text{ac}}^{\text{fl}}$ increases from 0.58 Pa (PML) to 2.69 Pa (no PML), while the Q factor increases from 109 (PML) to 252 (no PML). Thirdly, without PML, the reflections from the end wall give rise to a number of additional, nearly equidistant, smaller resonance peaks, reminiscent of a Fabry-Pérot-like interference condition for the acoustic wave in the x direction. Finally, without PML, the reflections lead to a more irregular spatial pattern of the levitating resonance mode in the actuation region (not shown), as compared to that of the mode with PML absorption and no reflections.

Due to the complex nature of the coupling between pressure waves in the fluid and the compressional and shear waves in the solid, we have only been able to interpret f_{res} for the levitating resonance mode and no other modes in simple terms of the three sound speeds of the system, listed in Table 1, combined with the geometrical length scales of capillary C4, listed in Table 5.1.

5.3.5 Analysis of capillary C5

We end our numerical modeling of the capillaries by a study of capillary C5, which is a geometry defined by us and not studied in the literature. The focus here is to obtain a more regular spatial pattern of the mode with spatial variations on the longest possible length scale.

The study in Section 5.3.4 of the circular capillary C4 reveals that spatial irregularities in the levitating resonance mode are reduced when the reflections from the end wall are absorbed by a PML. This tendency we also find in the study in Section 5.3.1 of the wide flat capillary C1, where, even in the presence of a PML, the levitating resonance mode has significant spatial variations, see Figs. 5.8 and 5.10(b). These spatial variations are caused by the relative high mode numbers in the solid, and therefore we design capillary C5 as a version of capillary C1 with its width reduced by a factor of 4 to $W = 0.5$ mm, thus reducing the cross-section aspect ratio $\frac{W}{H}$ from 10 to 2.5.

The separation of resonance frequencies increases in the narrow capillary C5. In the range between 3.5 and 4.4 MHz it contains only two resonance peaks (at 3.572 MHz and 4.201 MHz), whereas capillary C1 in the same interval contains three pronounced peaks and four smaller ones. The resonance at $f_{\text{res}} = 4.201$ MHz, with $Q = 53$, is a levitating mode well suited for acoustic trapping, and in Figs. 5.12 and 5.13 we plot the corresponding pressure field p_1 and displacement field \mathbf{u}_1 . The spatial structure of the resonance is more regular, especially in the solid, where the displacement in the y - z plane now resembles a simple fundamental mode with a pivoting motion about a single stationary point away from the symmetry plane (the black point on the y axis in the the inset of Fig. 5.13). Compared to that of capillary C1, the levitating mode of capillary C5 stretches far outside the actuation region, it is more regular in space, but its amplitude is reduced approximately by a factor of 1.8, and the maximum levitating force drops a factor of 3 to $F_z^{\text{rad}} = 7$ pN. The pressure nodal surface of the levitating mode is weakly wobbling around the horizontal plane located at $z = -0.03H$, see Fig. 5.14. This wobbling is less pronounced than the

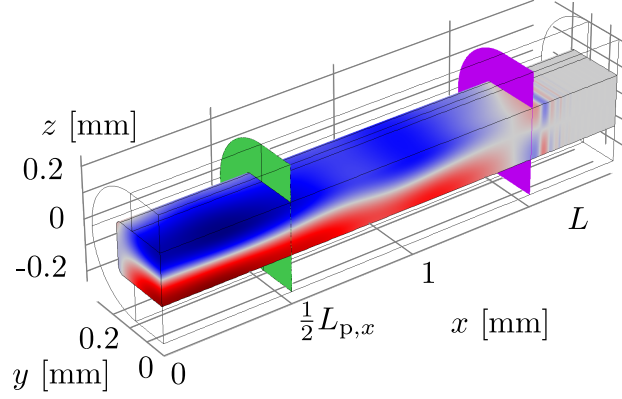


Figure 5.12: Capillary C5, color plot of the pressure field p_1 in the fluid from -0.10 MPa (blue) to 0.10 MPa (red) at the resonance frequency $f_{\text{res}} = 4.201$ MHz. The green and purple planes represent the end of the actuation region and the beginning of the PML domain, respectively.

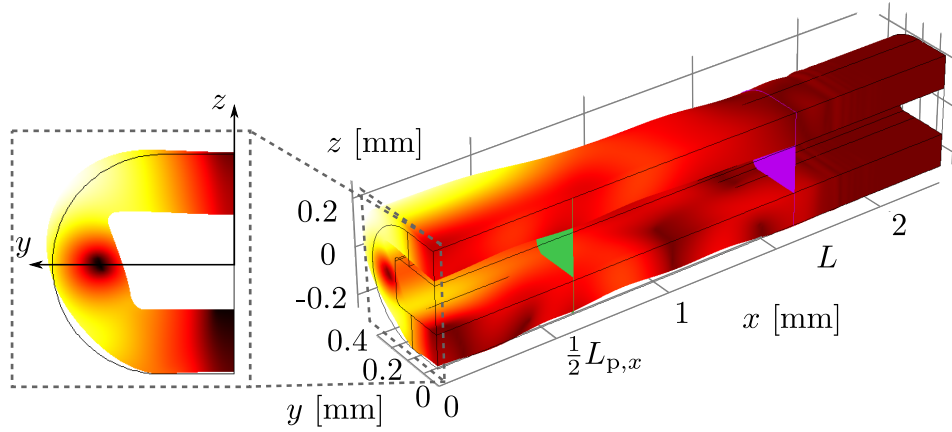


Figure 5.13: Capillary C5, the displacement field \mathbf{u}_1 in the solid (not drawn to scale) overlaid with a color plot of its magnitude u from 0 nm (dark red) to 1.2 nm (white) at resonance frequency $f_{\text{res}} = 4.201$ MHz as in Fig. 5.12

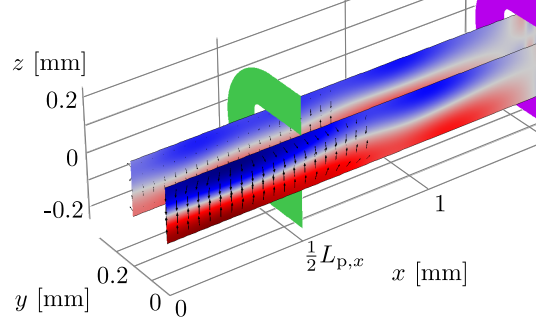


Figure 5.14: Capillary C5, color plot of the pressure field p_1 from -0.10 MPa (blue) to 0.10 MPa (red) in vertical planes placed equidistantly in steps of $\frac{3}{8}W$ starting at $y = 0$ showing the nearly horizontal nodal plane (gray) near $z = -0.03H$ at resonance $f_{\text{res}} = 4.201$ MHz. The acoustic radiation force \mathbf{F}^{rad} on $12\text{-}\mu\text{m}$ -diameter polystyrene test particles (black arrows with logarithmic lengths for visual clarity) has a maximum magnitude of 7 pN.

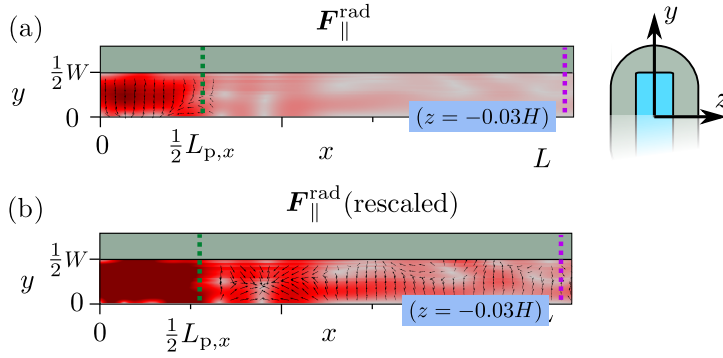


Figure 5.15: Capillary C5. (a) The lateral acoustic radiation force $\mathbf{F}_{\parallel}^{\text{rad}}$ (black arrows) and its magnitude (color plot from 0 pN [gray] to 0.13 pN [dark red]) acting on $12\text{-}\mu\text{m}$ -diameter polystyrene beads in the x - y plane at $z = -0.03H$ at resonance $f_{\text{res}} = 4.201$ MHz. The inset is the cross-section geometry with $W = 0.5$ mm. (b) Same as (a) but with its maximum color (dark red) decreased to 0.05 pN (dark red) to emphasize the secondary trapping points.

one we find in capillary C1, which moreover is displaced farther downward, namely to $z = -0.05H$.

Compared to capillary C1, the reduced pressure amplitude in capillary C5 leads to a corresponding reduction in the lateral radiation force by a factor of $1.8^2 = 3.2$, plotted for $z = -0.03H$ in Fig. 5.15, and it has a more regular spatial structure compared to that shown in Fig. 5.10. The main lateral trapping points are now confined to the intersection of the nodal plane and the x - z plane inside the actuation region, although the levitating mode extends far beyond the actuation region, see Fig. 5.14. There do exist secondary trapping points outside the actuation region, and compared to those of capillary C1 they are relatively strong, but they are fewer in number and appear in a more regular pattern. This finding is in qualitative agreement with experimental observations on the circular capillary C4 [74].

5.4 Discussion

The main outcome of our numerical modeling of glass capillary devices is that for all five capillaries C1 - C5 in our study, we find that a localized acoustic resonance mode, the so-called levitating mode, exists even though the completely straight capillaries do not contain any geometrical cavities in the axial x direction. This levitating mode is the result of a strong vertical SBAW forming in the region $x < \frac{1}{2}L_p$ of the capillary directly above the transducer. Although the bottom glass wall attached to the transducer is only displaced $d_0 = 0.1$ nm, the opposite top glass wall above the transducer is displaced an order of magnitude more, $\sim 10d_0$. This relatively large displacement results in a dynamically defined cavity that provides sufficiently confinement for the vertical SBAW, although acoustic energy is lost by a horizontal TBAW radiating away from the cavity for $x > \frac{1}{2}L_p$. The levitating modes have a relatively high Q value, 50 or higher, and they all exhibit good trapping characteristics: a nearly horizontal pressure nodal plane near the center of the channel, see Figs. 5.9 and 5.14, with sufficiently strong lateral acoustic forces, see Figs. 5.10 and 5.15.

The values of the levitating resonance frequencies f_{res} are in good agreement with the experimental values obtained for capillary C1 - C4 [30, 72, 71, 74] as listed in Table 5.1. They vary less than 1% as we change the boundary condition at the outlet from an ideally absorbing PML region to the no-stress condition of a capillary facing air, and as we change the actuation from glycerol-like area-averaged displacement to glue-like rigid displacement. However, we find that varying these idealized generic boundary conditions does result in significant changes of the acoustic energy density $E_{\text{ac}}^{\text{fl}}$, the acoustic force \mathbf{F}^{rad} on a test particle, as well as the resonance quality factor Q . In general we find two opposing trends: On the one hand the absorption of the PML region reduces both the acoustic energy and the trapping forces by a factor of 2 - 6, which is a drawback for achieving good trapping. On the other hand, the presence of the PML region has three beneficial aspects: it removes the sensitivity to reflections of acoustic waves at the outlet wall, it results in more regular spatial variations, and it makes the trapping strength independent of the position of the transducer relative to the capillary ends.

The sub-millimeter dimensions of the capillary cross section implies that the levitating resonance frequency f_{res} is sensitive to the exact geometry. We find that when changing the geometry within the tolerances listed by the manufacturer of the capillaries, the value of the levitating resonance can vary as much as 10% or up to 0.7 MHz for a 7-MHz resonance. Because the levitating resonance is close to an ideal standing half-wave resonance in the channel of height H , we have $f_{\text{res}} \propto H^{-1}$, and the most critical length parameter therefore becomes H .

Turning to the acoustic radiation force acting on a 12- μm -diameter polystyrene test particle in the device, our model correctly predicts that this force is present in the actuation region with a magnitude large enough to support one or more stable trapping points there. For the assumed actuation amplitude $d_0 = 0.1$ nm, the maximum levitating force F^{rad} is in the range from 2 pN (the circular capillary C4) to 3690 pN (the square capillary C3), which is between 5 and 8000 times the buoyancy-corrected gravitational force F^{grv} , of course depending on the transducer length $L_{p,x}$. Our model also correctly predicts

the existence of weaker, secondary trapping points in the region outside the actuation region, see Figs. 5.10(b) and 5.15(b), in agreement with published experiments [74, 82]. However, even without the PML absorption, the magnitude of the lateral acoustic force $F_{\parallel}^{\text{rad}}$ is small for most geometries, $F_{\parallel}^{\text{rad}}/F^{\text{grv}} \approx 1 - 10$, the exception being capillary C3 with $F_{\parallel}^{\text{rad}}/F^{\text{grv}} > 100$. This indicates that the performance of actual acoustic capillary traps may depend on additional forces such as streaming-induced drag forces and particle-particle interactions. For idealized systems with a rectangular cross section and translation invariance in the axial x direction, the critical particle radius a_c , below which streaming drag dominates, can be estimated by $a_c = \delta\sqrt{3\Psi/\Phi}$ [6], where δ is the boundary-layer thickness, Ψ is the streaming coefficient ($= \frac{3}{8}$ for a planar wall), and Φ is the acoustic contrast factor characterizing the strength of the acoustic radiation force. For the levitating mode in 3D, the lateral component of the radiation force is smaller by a factor α than the levitating vertical one, see Eq. (5.8), so in this case, we estimate $a_c = \delta\sqrt{3\Psi/(\alpha\Phi)}$. Numerically, we find $\alpha \approx 0.01$, see Eq. (9), and this relative weakening of the lateral radiation force indicates that the critical particle radius may be one order of magnitude larger than the $1\text{ }\mu\text{m}$ found for typical BAW devices [6, 66].

While a wide capillary is good for enhanced throughput, it suffers from the existence of high-mode, short-wavelength elastic waves propagating around the perimeter of the capillary. We find that reducing the aspect ratio removes these perimeter waves, while maintaining the good characteristics of the levitating mode. Other irregular spatial patterns in the levitating mode and the acoustic trapping force are induced by reflections of acoustic waves at the end of the capillary. We find that by implementing an ideally absorbing PML region, these reflections are removed, and a more regular spatial behavior of the trap is obtained. While the reduction in aspect ratio reduces the throughput and the introduction of absorption reduces the trapping force by a factor 2 - 6, the resulting increased regularity in spatial behavior, the increased separation of modes in frequency implying reduced mixing of unwanted modes, and the decreased sensitivity to the exact location of the transducer relative to the capillary ends, may be beneficial design considerations worth taking into account. The re-designed devices may be more robust to small perturbations in the device geometry and mechanical actuation.

Our numerical modeling of the capillary systems for acoustic trapping is in fair agreement with existing experimental data in the literature. However, to fully establish its capability as a design tool for optimizing acoustic trapping, more experimental data is needed to characterize the acoustic properties more fully. Here, stop flow experiments as in Ref. [82] would be helpful, as would more systematic reporting of the acoustic energy density present in the devices using, say, the drop-voltage method [72] or the flow-versus-retention-force briefly mentioned in Section 5.3.1. Also systematic reporting of the magnitude of the acoustic streaming would be helpful, because there might be situations in the capillary systems, where the acoustic streaming is so large that it is comparable to the flow velocities in the channel. If this were the case, then our analysis of the lateral acoustic forces must be supplemented by a discussion of the drag forces from acoustic streaming.

5.5 Concluding remarks

In this chapter we developed and tested a full-3D numerical model for a liquid-filled glass capillary actuated by ultrasound. Experimentally it is well known that acoustic streaming play a large role for these capillary devices, and we therefore explore an effective model for calculating the acoustic streaming in 3D in the next chapter.

Chapter 6

Effective modeling of streaming in acoustofluidic capillary devices

Experimentally it is observed for the capillary trapping system C1 that the acoustic streaming plays an important role for the particle dynamics because the direction of strong radiation force (z dir.) is perpendicular to the primary acoustic streaming rolls (x - y plane) [30]. This is in opposition to the device type shown in Fig. 1.1, where both the primary acoustic streaming and radiation force takes place in the same plane [66], making a two-dimensional model sufficient for a reliable description of the acoustophoretic particle dynamics. However, for the capillary-type of devices shown in Fig. 5.1, the dynamics have to be resolved in all three dimensions.

Most streaming calculations in the literature are performed in only in two dimensions [1, 40], but for some simple geometries, streaming calculations in 3D has also been demonstrated, e.g. the streaming around a sphere [83], and the torque, rotation, and streaming around a speherical particle [84]. In numerical calculations, the viscous boundary layers close to the fluid-solid interfaces have to be resolved using a very fine mesh, because it is typically in these thin boundary layers that large shear stresses are created that in turn drive the acoustic streaming.

This is particularly the case for bulk acoustic wave devices. Since the viscous boundary layer length δ , given by Eq. (2.28), is between $0.50\text{ }\mu\text{m}$ to $0.2\text{ }\mu\text{m}$ at frequencies between 1 to 10 MHz, they require a very fine mesh compared to the typical device length scale of $L \sim 1\text{ mm}$. This is illustrated in Fig. 6.1, showing the mesh of a 2D-rectangular fluid domain, where to the left is seen the mesh needed to resolve the viscous boundary layer length δ , and to the right is seen a coarse mesh sufficient to resolve the bulk dynamics of the acoustic pressure field.

Such a fine mesh is difficult to realise in 3D calculations on a normal PC for the capillary-type device shown in Fig. 5.1., but non the less necessary because no direction is translationally invariant as mentioned above. It is therefore necessary to establish an effective model that allows for 3D streaming calculations over mm length scales or larger. Examples of such effective models already exist in the literature [72, 86], however these works do not consider the solid dynamics and how that might affect the streaming, and

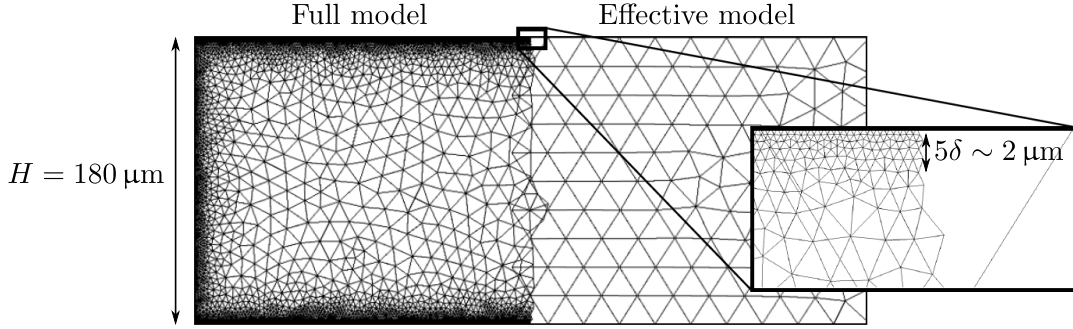


Figure 6.1: Mesh grid in two dimensions for a rectangular fluid domain, to the left showing the needed mesh to resolve the viscous boundary layers of length $\sim 5\delta$, *i.e.* a full model vs. right, showing the mesh needed for an effective model to the right, where a far coarser mesh can be used. The figure is adapted from [85].

as we will see in the following, accounting correctly for the coupled solid-fluid interactions can change the streaming field radically.

In this chapter we first perform a 2D validation study, comparing a full model, and an effective model for the streaming. To do this, we use analytical results obtained in a recent study in our group by my fellow Ph.D. student, Jacob Sørensen Bach [85, 87], that allows calculation of the effective streaming velocity resulting from the wall-oscillations of a curved surface. Using the full model in 2D, we illustrate that one should take great care in implementing the solid-fluid boundary conditions for the second-order fields when calculating the acoustic streaming near a moving wall. Lastly, we show two examples of effective streaming calculations in 3D for the C1, and C5 capillaries using the effective model.

The results presented in this chapter were finished only in the final weeks of the Ph.D.-project (late July and August 2017), and should be seen as preliminary results. However, because these results to a large extent build on the well-tested model presented in Chapter 5, together with the convincing comparison with experimental results, we have confidence in these results.

6.1 Effective modeling of acoustic streaming

In order to develop an effective model that accommodates calculation of the acoustic streaming we use an analytical theory [85, 87] for the dynamics in the viscous boundary layer, for both the acoustic fields (\mathbf{v}_1, p_1) , as well as the steady streaming fields (\mathbf{v}_2, p_2) .

The effective model allows for calculation of the acoustic streaming by considering only the compressional part of the acoustic field, treating the problem as simple pressure-acoustics, solving the Helmholtz Eq. (2.25a) for the pressure p_1 , without resolving the viscous boundary layers. Next, using the solid displacement \mathbf{u}_1 at the solid-fluid interface and the pressure p_1 as inputs, we calculate the effective streaming \mathbf{v}_2 near the wall, avoiding the fine mesh at the boundary layer shown in Fig. 6.1 (left), and can instead

suffice with the much coarser mesh (Fig. 6.1, right) for the effective model.

6.1.1 First-order effective equations

We use the same first-order governing equations as in Chapter 5, namely Eq. (5.2) for the solid, and Eq. (5.1) for the fluid. However, for the damping in the fluid we use physical bulk damping Γ given in Eq. (2.24) instead of using the effective value used in Chapter 5 and listed in Table 1.

Boundary conditions for the effective first-order model

With two exceptions, we reuse all the boundary conditions applied to the first-order effective fields p_1 , \mathbf{u}_1 as listed in Table 5.2 in Chapter 5, with the two exceptions listed in Table 6.1. The first change is that of using anti-symmetry boundary conditions, and the second is a modification to the "Continuous velocity" boundary condition at the solid-fluid interfaces, see Table 6.1. We change the continuous velocity boundary condition to account for the viscous damping at the solid-fluid boundaries, and the dynamics of the shear velocity \mathbf{v}_1^s described in Section 2.2.2 by modifying the normal derivative of p_1 (for a full treatment see the work by Bach and Bruus [85, 87])

$$\mathbf{n} \cdot \nabla p_1 = i\omega\rho_0 \left(\mathbf{n} - \frac{i}{k_s} \nabla_{\parallel} \right) \cdot (\partial_t \mathbf{u}_1) + \frac{i}{k_s} \left[(\mathbf{n} \cdot \nabla)^2 + k_c^2 \right] p_1, \quad (6.1)$$

where the parallel nabla operator is $\nabla_{\parallel} = \mathbf{t}_1(\mathbf{t}_1 \cdot \nabla) + \mathbf{t}_2(\mathbf{t}_2 \cdot \nabla)$, and \mathbf{t}_1 and \mathbf{t}_2 are the tangential vectors at the solid fluid interface.

6.1.2 Second-order effective equations

In second order, the solid is not modelled as it cannot sustain any steady motion, *i.e.* $\langle \mathbf{u}_2 \rangle = \mathbf{0}$, and for the fluid we model the steady streaming fields $\langle \mathbf{v}_2 \rangle$ and $\langle p_2 \rangle$. In the following we omit $\langle \cdot \rangle$ and simply denote the time-averaged streaming field \mathbf{v}_2 and p_2 , as we only deal with the time-averaged values for the second-order fields. To arrive at the effective governing equations to second order, we revisit the divergence of the momentum flux density tensor $\nabla \cdot (-\rho_0 \langle \mathbf{v}_1 \mathbf{v}_1 \rangle)$ in Eq. (2.31). As pointed out in a recent work by Riaud *et al.* [36], it can be an advantage to split the divergence of this term into a potential part and a bulk force acting on the fluid [36, 85]

$$-\rho_0 \nabla \cdot \langle \mathbf{v}_1 \mathbf{v}_1 \rangle = \frac{1}{4} \nabla \left(\kappa_0 |p_1|^2 - \rho_0 |\mathbf{v}_1^c|^2 \right) + \frac{\Gamma \omega}{c_0^2} \langle \mathbf{v}_1^c p_1 \rangle, \quad (6.2)$$

Table 6.1: Changes in the boundary conditions imposed on the first-order fields for the the effective model derived in this chapter as compared to the boundary conditions listed in Table 5.2.

Name	Domain \leftarrow boundary	Boundary condition
Anti-symmetry	Solid domain \leftarrow anti-symmetry	$\mathbf{t} \cdot \mathbf{u}_1 = 0$, $\mathbf{n} \cdot \boldsymbol{\sigma}_{sl} \cdot \mathbf{n} = 0$
Continuous velocity	Fluid domain \leftarrow solid	Eq. (6.1)
Anti-symmetry	Fluid domain \leftarrow anti-symmetry	$p_1 = 0$

which is valid far away from the solid-fluid boundaries where the shear mode is negligible $\mathbf{v}_1^s = \mathbf{0}$. Because the first term is a potential force, we can absorb it into a rescaled second-order pressure

$$\tilde{p}_2 = p_2 - \frac{1}{4} \left(\kappa_0 |p_1|^2 - \rho_0 |\mathbf{v}_1^c|^2 \right). \quad (6.3)$$

The numerical advantage of introducing this rescaled pressure is significant, and we will return to this in the discussion of Section 6.4. Inserting Eqs. (6.2) and (6.3) in the second-order mass and momentum continuity Eqs. (2.30) and (2.31), we obtain the effective second-order governing equations

$$\mathbf{0} = \nabla \cdot \tilde{\boldsymbol{\sigma}}_2 + \frac{\Gamma \omega}{c_0^2} \langle p_1 \mathbf{v}_1^c \rangle, \quad (6.4a)$$

$$0 = \nabla \cdot (\rho_0 \mathbf{v}_2 + \frac{1}{c_0^2} \langle p_1 \mathbf{v}_1^c \rangle), \quad (6.4b)$$

where

$$\tilde{\boldsymbol{\sigma}}_2 = \eta [\nabla \mathbf{v}_2 + (\nabla \mathbf{v}_2)^T] - \mathbf{I} \left[\tilde{p}_2 + \left(\frac{2}{3} \eta - \eta_B \right) (\nabla \cdot \mathbf{v}_2) \right]. \quad (6.5)$$

Boundary conditions

The boundary conditions for the second-order streaming fields \tilde{p}_2 and \mathbf{v}_2 are explained in the following, and summarised in Table 6.2 to give an overview.

To account for the dynamics of the shear velocity field \mathbf{v}_1^s that plays an important role near solid-fluid boundaries, we rely on analytical results to make an effective model of the acoustic streaming near the solid walls. Building on the concept of limiting velocity, first introduced by Nyborg [88], that calculated the effective streaming velocity near a curved boundary for a perpendicularly oscillating wall, we use an expanded theory by Bach and Bruus [85, 87] to include wall-oscillations in any direction, referred to here as the effective slip-velocity theory. By demanding that the wall velocities of the solid and fluid must be equal in all material points (using the Lagrangian picture), the tangential effective slip-velocity at the solid-fluid boundaries was derived in [85, 87] and is a function of the compressional velocity \mathbf{v}_1^c (Eq. (2.23)) and the solid displacement \mathbf{u}_1

$$\begin{aligned} \mathbf{v}_{2\parallel} = & \frac{-1}{\omega} \left\{ \frac{1}{2} \left\langle [(\partial_t \mathbf{u}_1 - \mathbf{v}_1^c) \cdot \nabla_{\parallel}] (\partial_t \mathbf{u}_1 - \mathbf{v}_1^c) \right\rangle \right. \\ & + \left\langle (\partial_t \mathbf{u}_1 - \mathbf{v}_1^c) [i \nabla_{\parallel} \cdot \partial_t \mathbf{u}_1 - 2i \partial_n (\mathbf{n} \cdot \mathbf{v}_1^c) + i k_s \mathbf{n} \cdot (\partial_t \mathbf{u}_1 - \mathbf{v}_1^c)] \right\rangle \\ & \left. - \left\langle [(\partial_t \mathbf{u}_1 - \mathbf{v}_1^c) \cdot \nabla_{\parallel}] (i \partial_t \mathbf{u}_1) \right\rangle + \left\langle (i \partial_t \mathbf{u}_1 \cdot \nabla_{\parallel}) \cdot \mathbf{v}_1^c \right\rangle \right\}, \end{aligned} \quad (6.6)$$

where $\partial_n = \mathbf{n} \cdot \nabla$ denotes the derivative in the normal direction, and we again use that the parallel nabla operator is $\nabla_{\parallel} = \mathbf{t}_1 (\mathbf{t}_1 \cdot \nabla) + \mathbf{t}_2 (\mathbf{t}_2 \cdot \nabla)$. For the symmetry boundaries we apply $\mathbf{n} \cdot \mathbf{v}_2 = 0$, and $\mathbf{t} \cdot \tilde{\boldsymbol{\sigma}}_2 \cdot \mathbf{n} = 0$, and at the end of PML at $x = L + L_{\text{PML}}$, we demand no-stress for \tilde{p}_2 . Furthermore, to fix pressure level, we demand that the volume-average

of \tilde{p}_2 is zero. Here it is worth noting that the second-order fields are symmetric regardless whether the first-order fields are symmetric (Table 5.2) or anti-symmetric (Table 6.1).

Lastly, to avoid spurious contributions from the PML, we apply a stepping function

$$f_{\text{str}}(x) = \begin{cases} 1 & \text{for } x \leq 0.8L \\ 0 & \text{for } x > 0.8L, \end{cases} \quad (6.7)$$

which we multiply onto the driving terms of the streaming, acting as a boolean cut-off for the bulk $\langle p_1 v_1^c \rangle$ terms in Eq. (6.4), and the effective slip velocity $\mathbf{v}_{2\parallel}$ in Eq. (6.6).

6.2 Preliminary 2D effective streaming results

In the following we present a number of preliminary results for the effective model in 2D, starting with a validation study consisting of a coupled solid-fluid y - z cross section of the C5 capillary geometry (see Table 5.1 and Fig. 5.2) where we compare the effective streaming model (presented above) with a full model where the viscous boundary layers are resolved. Furthermore we compare the effect of applying different boundary conditions for the streaming field in the full model, illustrating the breakdown of the Eulerian picture close the solid-fluid boundaries.

6.2.1 2D validation study of the effective model

In order to rely on the effective model, we validate the effective model by comparing with a full model in two dimensions, resolving the viscous boundary layers, since this is still computational feasible. We consider the y - z cross section of the C5 capillary (see Fig. 5.2), and excite a half-wave resonance mode in the y -direction at a frequency close to $f = \frac{c_0}{2W}$. Note that this resonance mode is different from the levitating half-wave resonance mode investigated in Chapter 5, where the standing pressure wave is in the z direction across the channel height.

Full model setup in 2D

For the solid, we use the same first-order governing equations as in Chapter 5 for the displacement \mathbf{u}_1 , namely Eq. (5.2), and for the fluid, we use the unmodified first-order equations, given in Eqs. (2.16)-(2.18), for the fluid velocity \mathbf{v}_1 and pressure p_1 .

Table 6.2: Boundary conditions imposed on the effective second-order streaming field \tilde{p}_2 and \mathbf{v}_2

Name	Domain \leftarrow boundary	Boundary condition
Effective slip velocity	Fluid domain \leftarrow solid	Eq. (6.6)
No stress	Fluid domain \leftarrow air	$\tilde{p}_2 = 0$
Symmetry	Fluid domain \leftarrow symmetry	$\mathbf{n} \cdot \mathbf{v}_2 = 0, \mathbf{t} \cdot \tilde{\boldsymbol{\sigma}}_2 \cdot \mathbf{n}$
Average zero pressure	Fluid domain \leftarrow domain average	$\int_{\Omega} \tilde{p}_2 dV = 0$

For the second order we model the fluid by the second-order mass and momentum conservation equations given in Eqs. (2.30) and (2.31), and the second-order stress tensor σ_2 in Eq. (2.32), and again the solid displacement is zero to second order $\langle \mathbf{u}_2 \rangle = \mathbf{0}$. Note here, that because we here resolve the full first-order velocity \mathbf{v}_1 (including viscosity), and not only the compressional part \mathbf{v}_1^c , the boundary conditions for both the first- and second-order equations change compared to the effective model. All boundary conditions for the full 2D model are listed in Table 6.3. Note in particular the solid-fluid boundary condition for the second-order velocity, where, to match the velocities correctly in the Lagrange (L) picture at the solid-fluid interface $(\mathbf{v}_2)^L = (\langle \mathbf{u}_2 \rangle)^L = \mathbf{0}$, we have to include the Stokes drift term [89, 90]

$$\mathbf{v}_2 + \langle (\mathbf{u}_1 \cdot \nabla) \mathbf{v}_1 \rangle = \mathbf{0}, \quad (6.8)$$

which accounts for the fact that the governing equations for the fluid were derived in the Euler picture.

Actuation in 2D

In order to actuate the standing half-wave resonance mode across the channel width, which is anti-symmetric, the actuation has to also be inherently anti-symmetric. Actuating the solid from the bottom at $z = -\frac{H}{2} - H_{\text{gl}}$, we reuse the concept of an average actuation displacement from Eq. (5.3b), but split the actuation line in two, and demand a positive average actuation height of $+d_0$ for $y < 0$ (left side), and a negative average actuation height of $-d_0$ for $y > 0$ (right side)

$$0 = \int_{\text{act}, y < 0} (u_{1,z} - d_0) dy, \quad 0 = \int_{\text{act}, y > 0} (u_{1,z} + d_0) dy, \quad (6.9)$$

where the 'act' subscripts of the integral implies that $z = -\frac{H}{2} - H_{\text{gl}}$.

Table 6.3: Boundary conditions for the full 2D model imposed on the solid and fluid domains, for both first- and second-order fields.

Name	Domain \leftarrow boundary	Boundary condition
<i>First order</i>		
No stress	Solid domain \leftarrow air	$\sigma_{\text{sl}} \cdot \mathbf{n} = \mathbf{0}$
Continuous stress	Solid domain \leftarrow fluid	$\sigma_{\text{sl}} \cdot \mathbf{n} = \sigma_1 \cdot \mathbf{n}$
Mech. actuation	Solid domain \leftarrow transducer	Eq. (6.9)
Continuous velocity	Fluid domain \leftarrow solid	$\mathbf{v}_1 = -i\omega \mathbf{u}_1$
No stress	Fluid domain \leftarrow air	$p_1 = 0$
<i>Second order</i>		
Lagrangian wall velocity	Fluid domain \leftarrow solid	$\mathbf{v}_2 = -\langle (\mathbf{u}_1 \cdot \nabla) \mathbf{v}_1 \rangle$
Average zero pressure	Fluid domain \leftarrow domain average	$\int_{\Omega} p_2 dA = 0$

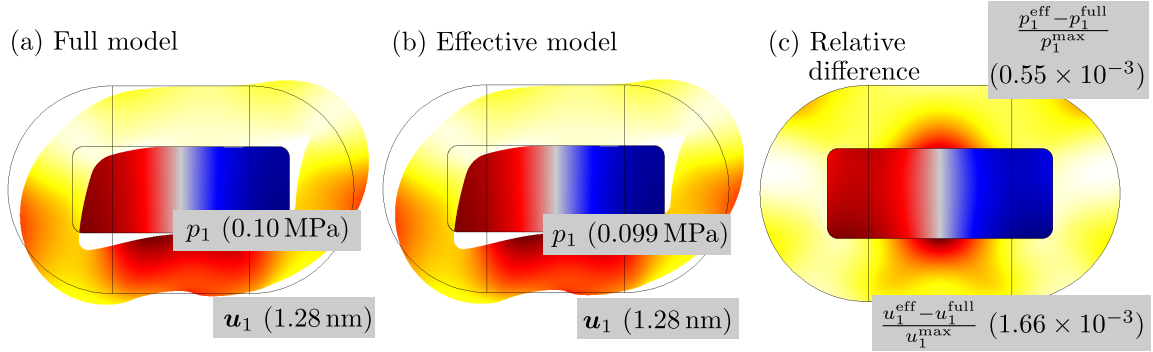


Figure 6.2: Plot of the first-order fields p_1 (red to blue) and u_1 (heat color) at resonance, with $f_{\text{res}} = 1.5450$ MHz, in a 2D y - z cross-section of the C5 capillary geometry, and with the maximum field values given in the grey inserts. The solid is actuated at resonance by the anti-symmetric average actuation condition from Eq. (6.9), and the fields in (a) and (b) are rescaled corresponding to an acoustic energy density in the fluid of $E_{\text{ac}}^{\text{fl}} = 1$ Pa. (a) Full model (resolved viscous boundary layers), see Section 6.2.1, (b) Effective model, see Section 6.1.1, and (c) local relative difference difference between the full and the effective model for the same actuation conditions.

6.2.2 First-order fields

In Fig. 6.2 we plot the first-order fields p_1 and u_1 at the half-wave resonance across the channel width for the full model (a), and the effective model (b). In the plots, we have rescaled the magnitude of the fields to correspond to an acoustic energy density in the fluid of $E_{\text{ac}}^{\text{fl}} = 1$ Pa.

For the the same actuation conditions, the full and effective models exhibit the same resonance frequency $f_{\text{res}} = 1.5450$ MHz, acoustic energy density $E_{\text{ac}}^{\text{fl}}$, and acoustic fields p_1 and u_1 , with a relative difference of 10^{-5} , 0.30%, 0.055%, and 0.17%, where in Fig. 6.2(c) we have plotted the relative difference for u_1 and p_1 between the two models, full and effective.

From this comparison it is clear that effective model reproduces the full model with respect to the first-order fields, resonance frequency, and acoustic energy to a precision of 0.3% or lower. With this successful reproducibility by the effective model of the first-order fields, we continue with a comparison of the second-order streaming fields.

6.2.3 Second-order fields

In Fig. 6.3 we plot the second-order streaming fields v_2 in the fluid domain, calculated using the first-order fields as inputs, plotted in Fig. 6.2, for (a) the full model, (b) the effective model, and (c), the relative difference between the two.

In plot (c) we exclude the viscous boundary-layer areas closest to the top and bottom walls in distances of 5δ from each wall, *i.e.* excluding areas $z > \frac{H}{2} - 5\delta$ and $z < -\frac{H}{2} + 5\delta$. We do this because the streaming calculated by the effective model does not contain the shear-contributions to streaming, but only the contributions from the compressional part, and since the shear-contributions decays exponentially away from the walls [85, 87], we can expect the effective streaming field to be valid in all regions except a few distances δ

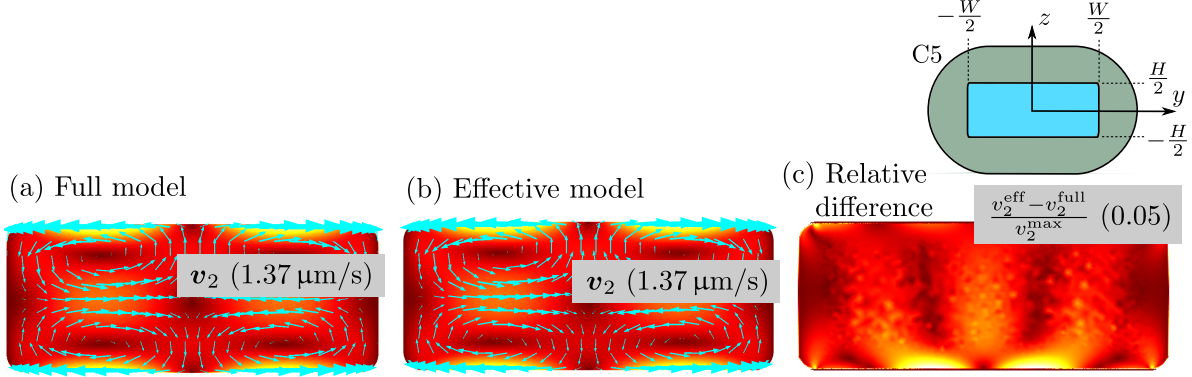


Figure 6.3: Color plot of the second-order streaming field, (corresponding first-order fields in Fig. 6.2) for a y - z cross-section of the C5 capillary shown in the inset to the upper right. The heat color and the arrows show the magnitude and direction of \mathbf{v}_2 , with the maximum values given in the grey inserts. The fields are rescaled corresponding to an acoustic energy density in the fluid of $E_{ac}^{\text{fl}} = 1 \text{ Pa}$. (a) Full model (resolved viscous boundary layers), see Section 6.2.1, (b) Effective model (see Section 6.1.2), and (c) the relative difference difference between (a) and (b), excluding the top and bottom boundary layer regions, at distances 5δ from the wall, *i.e.* excluding the regions $z > \frac{H}{2} - 5\delta$, and $z < -\frac{H}{2} + 5\delta$.

from the walls. In the valid region, we see a relative difference in most of the fluid region no larger than 1 to 2%, and with a maximum of 5% as we approach the viscous boundary layers close the bottom wall.

6.2.4 The role of a moving wall in second-order acoustics

In the acoustic streaming literature, different choices of boundary conditions can be found when setting the solid-fluid boundary condition for the streaming velocity \mathbf{v}_2 . In some works a no slip-condition is chosen [6, 40, 80], in other works a local mass conservation criterion is used [1], and in yet other works [84] (including this) the Lagrangian moving wall condition is used (Eq. (6.8)). The three mentioned boundary conditions are given by

$$\mathbf{v}_2 = -\langle \mathbf{u}_1 \cdot \nabla \mathbf{v}_1 \rangle. \quad (\text{Lagrangian moving wall}) \quad (6.10a)$$

$$\mathbf{v}_2 = \mathbf{0}, \quad (\text{No-slip}) \quad (6.10b)$$

$$\mathbf{n} \cdot \mathbf{v}_2 = -\frac{1}{\rho_0} \mathbf{n} \cdot \langle \rho_1 \mathbf{v}_1 \rangle. \quad (\text{Local mass conservation}) \quad (6.10c)$$

To examine the difference, if any, of using these boundary conditions, we have repeated the full model calculation of the acoustic streaming velocity \mathbf{v}_2 from Fig. 6.3(a) in Fig. 6.4 and implemented the three different boundary conditions from Eq. (6.10).

From Fig. 6.4 it is clear that the resulting streaming velocities are both qualitatively and quantitatively different for all three boundary conditions. Comparing the calculated streaming in Fig. 6.4 to experimental measurements of a similar device by Muller *et al.* [66], where a standing half-wave in pressure is also excited across the width of the channel, the measured streaming field is found to be a quadrupolar pattern similar to that shown in (a). Moreover, the magnitude of the experimental streaming field, normalised to an acoustic

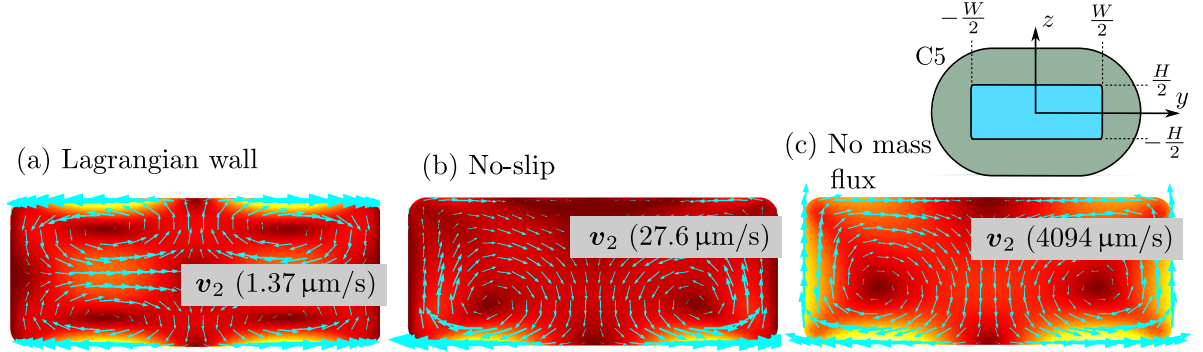


Figure 6.4: Recalculation of the full model streaming field shown in Fig. 6.3(a) for different applied boundary conditions for \mathbf{v}_2 at the solid-fluid boundaries. The heat-color and arrow plots denote the magnitude and the direction of \mathbf{v}_2 , respectively, and maximum values are given in the grey inserts. (a) Lagrangian moving wall Eq. (6.10a), (b) No-slip Eq. (6.10b), and (c) Local mass conservation Eq. (6.10c). All three streaming fields are calculated using the same first-order fields shown in Fig. 6.2(a), corresponding to an acoustic energy in the fluid of $E_{ac}^{\text{fl}} = 1 \text{ Pa}$.

energy of $E_{ac}^{\text{fl}} = 1 \text{ Pa}$, is measured to be $0.97 \mu\text{m/s}$, which compares reasonably well with the $1.37 \mu\text{m/s}$ streaming magnitude found in Fig. 6.4(a).

The streaming fields for the other two boundary conditions in Fig. 6.4(b) and (c), do not compare well with neither experiments, nor the effective model result in Fig. 6.3(b), and their magnitudes seem unreasonably large compared to experimental results for the same acoustic energy, being one and three orders of magnitude larger, for (b) and (c), respectively. From this we conclude that to obtain a correct description of the acoustic streaming velocity near a wall, one can seemingly get spurious results if not accounting for the Stokes drift caused by the difference between the Euler and Lagrange pictures in second order acoustics.

Having validated the effective model against a full model in 2D, and found the effective model able to reproduce the full model within 5% relative difference, we now turn to results for 3D models.

6.3 Preliminary 3D effective streaming results

In the following we present 3D acoustic streaming results for the C5 and C1 capillaries (see Table 5.1) calculated using the effective model. Lastly, we examine the influence of the different driving terms of the acoustic streaming in the C1 capillary by comparing the effect of the bulk driving terms $\langle p_1 \mathbf{v}_1^c \rangle$ in Eq. (6.4) vs. the boundary-driving terms $\mathbf{v}_{2\parallel}$ (Eq. (6.6)), and unexpectedly find that the bulk driving terms play an essential role in our calculations for driving the in-plane streaming, which is a surprising result for a bulk acoustic wave device. Furthermore, we report that using this implementation for calculating the effective streaming in COMSOL MULTIPHYSICS, we found good and consistent numerical stability, and convergence, of the 3D calculations for both the C1 and C5 capillary.

Effective streaming in the C5 capillary

In order to compare our 2D results from Section 6.2.2 with a similar case in 3D, we excite the same anti-symmetric resonance mode in 3D for the C5 capillary as shown in Fig. 6.2(b). We do this by using the anti-symmetry boundary conditions for u_1 and p_1 listed in Table 6.1, and we actuate the system from the bottom at $z = -\frac{1}{2}H - H_{gl}$ in the region $x < \frac{1}{2}L_p$, and free stress for $x > \frac{1}{2}L_p$ as shown in Fig. 5.3. The resonance frequency is found to be $f_{res} = 1.524\text{MHz}$, only 1.3% from the 2D model, and the fields are normalized to an acoustic energy density in the fluid above the actuation region of $E_{ac}^{fl} = 1\text{Pa}$. In Fig. 6.5 we plot the first- and second-order fields for the anti-symmetric resonance mode.

For both the first- and second-order fields, we observe good agreement between the 2D and the 3D case, see Figs. 6.2 and 6.3, but with slow axial variations in the x direction in the 3D case. These axial variations are clear for the pressure p_1 that retains the same standing half-wave structure along the x direction but slowly decreases in amplitude outside the actuation region ($x > \frac{1}{2}L_p$), and exhibits a change of phase around $x = 0.75L$ (the sixth cross sec. plane) where the high and low pressures switches side. The magnitude of the fields also compare rather well between the 2D and 3D case with relative deviations of 2% for u_1 , 14% for p_1 , and 33% for v_2 , which is decent considering that the 2D model cannot describe any motion out of the y - z plane.

The acoustic streaming in 3D retains its quadropolar structure from the 2D case (Fig. 6.3(b)), but decays in amplitude along the channel length and begin to exhibit more streaming out of the y - z plane, see the zoom-in at $x = 0.45L$ in Fig. 6.5(c). In summary, good agreement between the 2D and the 3D case is obtained.

6.3.1 3D effective streaming in the C1 capillary

Because the C1 capillary geometry has been used extensively as an acoustic trapping device in the literature [29, 30, 31, 73] a large amount of experiments have been performed using this capillary geometry, making it an interesting test-case for comparing our calculations to experiments. Furthermore, because the acoustic streaming flow is easily visualised in experiments with tracer particles, we can compare experimental data directly to our model. In Fig. 6.6 we plot the calculated acoustic streaming resulting from the levitating resonance mode of the C1 capillary shown in Fig. 5.8 since we expect this mode to be the main mode suited for acoustic trapping. In the plot we scale the streaming amplitudes corresponding to an acoustic energy density in the fluid above the actuation region of $E_{ac}^{fl} = 1\text{Pa}$.

In Fig. 6.6(b) we plot the in-plane streaming velocity $\mathbf{v}_2^{\text{in-plane}}$ (only the x and y components) that exhibits two large circular flow structures in the x - y plane, going clockwise, and referred to here as the in-plane streaming rolls, with a maximum in-plane speed of $0.47\text{ }\mu\text{m/s}$, as well as smaller Rayleigh-Schlichting flow rolls in y - z planes close solid boundary at $y = \frac{1}{2}W$, see the zoom-in Fig. 6.6(a). Furthermore we note that the streaming field is fairly confined to the actuation region ($x < \frac{1}{2}L_p$), and quickly dies out outside this region.

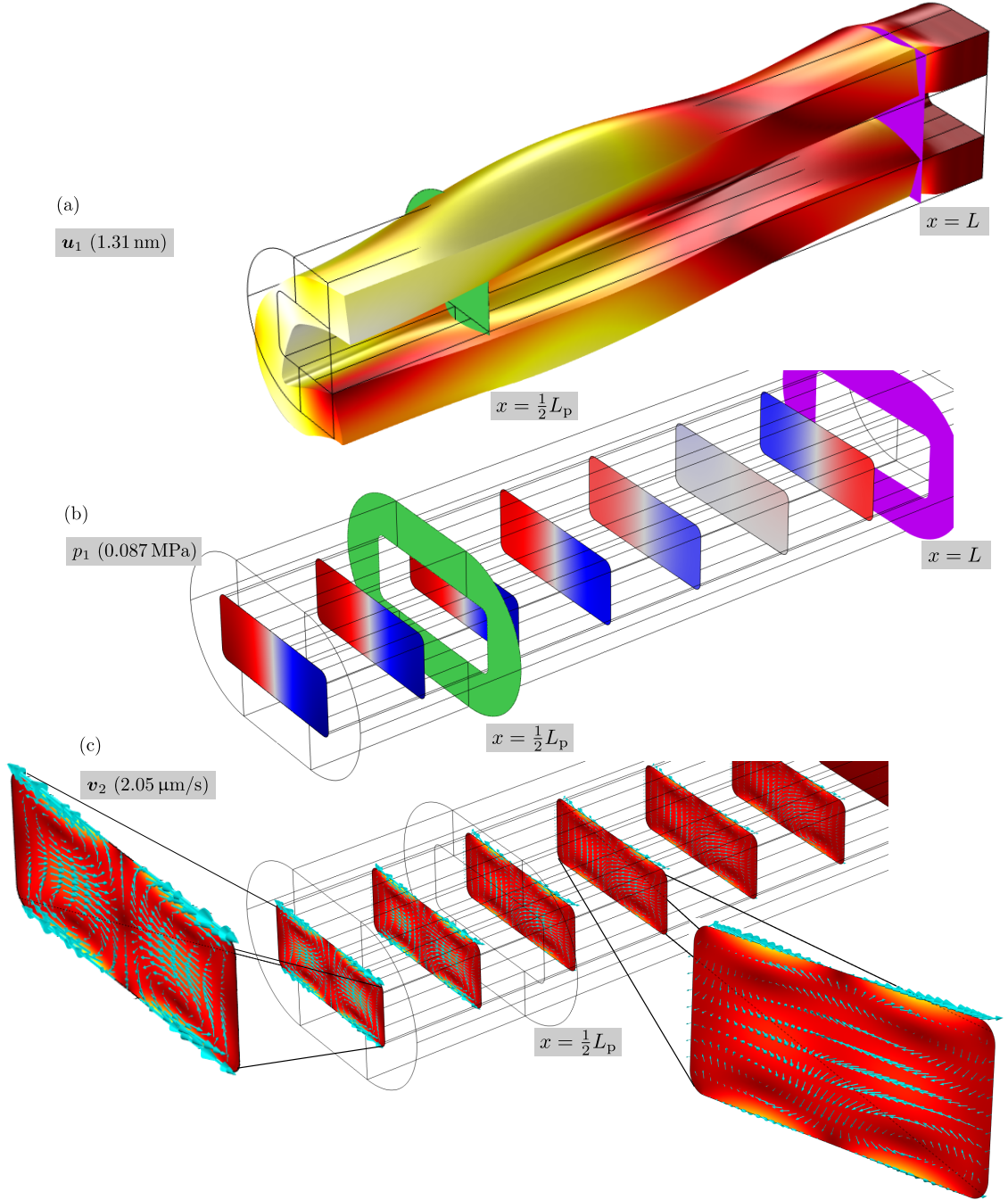


Figure 6.5: First- and second-order fields for the C5 capillary geometry (see Table 5.1) for the anti-symmetric resonance mode with a standing pressure half-wave across the channel width. The resonance frequency is $f_{\text{res}} = 1.524 \text{ MHz}$, and the fields are normalized to $E_{\text{ac}}^{\text{fl}} = 1 \text{ Pa}$ in the actuation region ($x < \frac{1}{2}L_p$). (a) The solid displacement field \mathbf{u}_1 (not drawn to scale) overlaid with a color plot of its magnitude u_1 from 0 nm (dark red) to 1.31 nm (white). (b) Color plot of the pressure p_1 , going from -0.087 MPa (blue) to 0.087 MPa (red) plotted in y - z cross sections at $x = \{0, 0.15, 0.3, \dots, 0.9\}L$, and the green and purple planes denote the end of the actuation region ($x = \frac{1}{2}L_p$), and the beginning of the PML domain ($x = L$), respectively. (c) Heat color and arrow plot of the streaming velocity \mathbf{v}_2 , going from 0 (dark red) to $2.06 \mu\text{m/s}$ (white) shown in y - z cross sections at $x = \{0, 0.15, 0.3, \dots, 0.9\}L$.

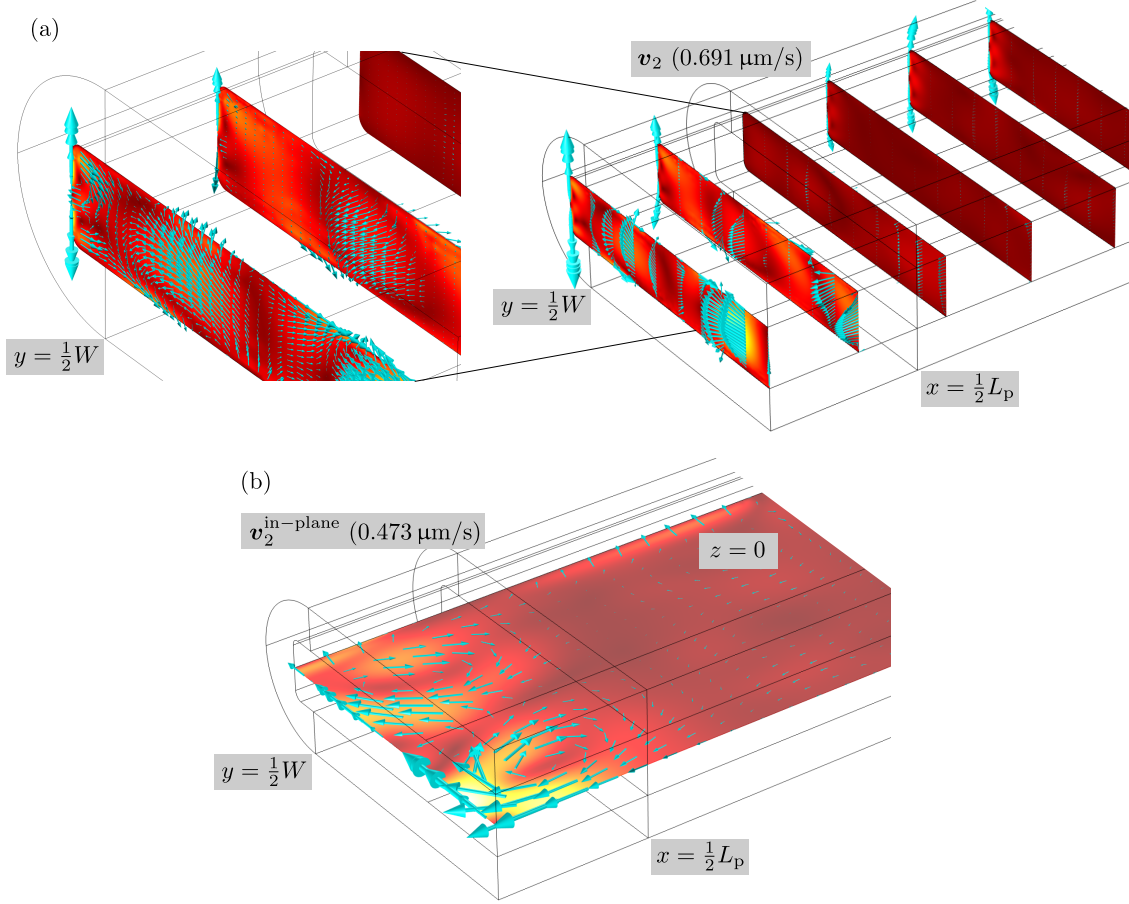


Figure 6.6: Streaming field in the C1 capillary geometry for the resonance mode shown in Fig. 5.8, here normalized to an acoustic energy density in the fluid of $E_{\text{ac}}^{\text{fl}} = 1 \text{ Pa}$ in the actuation region ($x < \frac{1}{2}L_p$). (a) Arrow and heat-color plots of v_2 denoting the magnitude and the direction, going from 0 $\mu\text{m/s}$ (dark red) to 0.691 $\mu\text{m/s}$ (white) shown in y - z cross sections at $x = \{0, 0.15, 0.3, \dots, 0.75\}L$. (b) Arrow and color plot of the in-plane streaming $v_2^{\text{in-plane}}$ (x and y components only) in the $z = 0$ plane, going from 0 $\mu\text{m/s}$ (dark red) to 0.473 $\mu\text{m/s}$ (white).

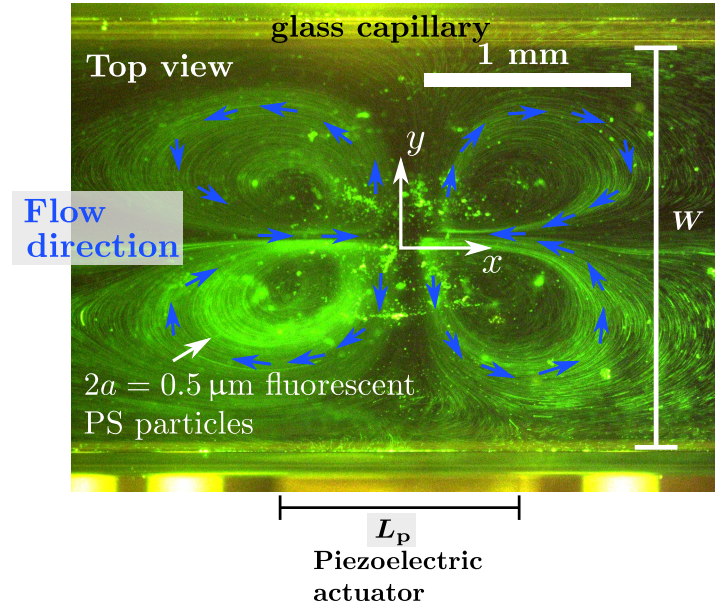


Figure 6.7: Top-view of an acoustic streaming experiment for the C1 capillary (see Fig. 5.1), where the streaming flow is visualised by 0.5-micrometer-diameter fluorescent polystyrene particles. The transducer voltage was set to 10 V (peak-to-peak), and the streaming velocity was estimated roughly to be ~ 1 mm/s by visually comparing known inlet-flow speeds to the streaming rolls. The image was taken by Carl Johannesson, Lund University, Sweden.

Comparison with experiments

In order to compare the calculated streaming in the C1 capillary with experiments, we show a photograph in Fig. 6.7 of an acoustic streaming experiment for the C1 capillary, performed by Carl Johannesson, Lund University, Sweden. The image shows a top-view of the C1 capillary where the streaming is visualised with 0.5- μ m-diameter fluorescent polystyrene particles. The transducer voltage was set to 10 V (peak-to-peak), and the in-plane streaming speed was streaming velocity was estimated roughly to be ~ 1 mm/s by visually comparing known inlet-flow speeds to the streaming rolls. Comparing the calculated streaming with the experiment in the the positive quadrant ($x, y > 0$) we observe overall good agreement. However, we note that the experiment only exhibits one large in-plane flow roll, where our calculation has two, though with same shape and direction of rotation. Lastly, we note in the calculated streaming, that the flow roll closest to the center at $(x, y) = (0, 0)$ appear to be dominant over the other, which supports the comparison with experiments. Furthermore we find that the experimental streaming field also decays rapidly outside the actuation region, on a length scale similar to that seen in the acoustic streaming calculation.

Lastly, comparing the flow speeds of the in plane flow roll, we use the drop-voltage calibration in Section 5.3.1, where it was found that an actuation voltage of 10 V corresponds an acoustic energy density in the fluid of $E_{ac}^{fl} = 7200$ Pa, which in the experiment gave an

in-plane streaming magnitude of roughly 1 mm/s. Because the acoustic streaming field is proportional to the acoustic energy density $v_2 \propto E_{ac}^{fl}$, we can rescale the calculated in plane streaming in Fig. 6.6(b) to an energy density of $E_{ac}^{fl} = 7200$ Pa, giving a calculated in-plane streaming magnitude of $v_2^{\text{in-plane}} = 3.4$ mm/s, which is within half an order of magnitude of the experimental measurement of 1 mm/s. Considering that the mechanical coupling layer between transducer and the glass capillary is made by applying a small drop of glycerol to the transducer, which evaporates over time, and is difficult to accurately reproduce experimentally, it is reasonable to assume that the acoustic energy density will vary between experiments for a the same applied transducer voltage. We therefore conclude that this result represents reasonable agreement between theory and experiment, quantitatively as well qualitatively.

Investigating the different driving terms for acoustic streaming

In the governing equations for the effective streaming model, Eqs. (6.3)-(6.6), we can split the contributions to the acoustic streaming into bulk driving terms (Bulk), being the $\langle p_1 v_1^c \rangle$ terms in Eq. (6.4), and boundary driving terms (Bdy.), represented by the effective slip velocity condition in Eq. (6.6) applied at all solid-fluid boundaries. This allows us to switching off each contribution individually by setting

$$\text{Bulk: off} \Rightarrow \text{set } \langle p_1 v_1^c \rangle = \mathbf{0} \text{ in Eq. (6.4),}$$

$$\text{Bdy: off} \Rightarrow \text{set } v_{2\parallel} = \mathbf{0} \text{ in Eq. (6.6).}$$

In Fig. 6.8 we repeat the in-plane streaming calculation from Fig. 6.6(b), but switch the two contributions either on or off in in all four combinations.

Comparing (a)-(d) in Fig. 6.8 it is clear that the bulk driving terms are, to a very large part, responsible for the in-plane streaming. This is clear from the isolated case of only including boundary-driven streaming in (b) compared to the total streaming in (d), whose magnitude is down by factor two and contributes only significantly to the streaming close the solid side wall at $y = \frac{1}{2}W$. Furthermore, when comparing (c) (only Bulk) and (d) (both Bulk and Bdy.) very little difference is observed. This is a surprising result for a bulk acoustic wave device, where boundary-driven streaming is often considered as the primary driving mechanism. Furthermore, our findings are in conflict with the work of Lei *et al.* [72] that calculated the effective streaming for the C2 capillary (see Table 5.1), which is very similar to the C1 geometry, and found the same large in-plane streaming-roll structures, in agreement with experiments, without including any bulk-driving effects. The discrepancies between the model of Lei *et al.* [72] and this work are unclear at this point.

6.4 Discussion

In this work we are, to the best of our knowledge, the first to simultaneously resolve the dynamics of the coupled solid-fluid first-order fields in 3D, and use them as detailed inputs for calculating the effective streaming field v_2 , with a theory for the boundary driven streaming that accommodates for a general wall displacement u_1 [85, 87]. However,

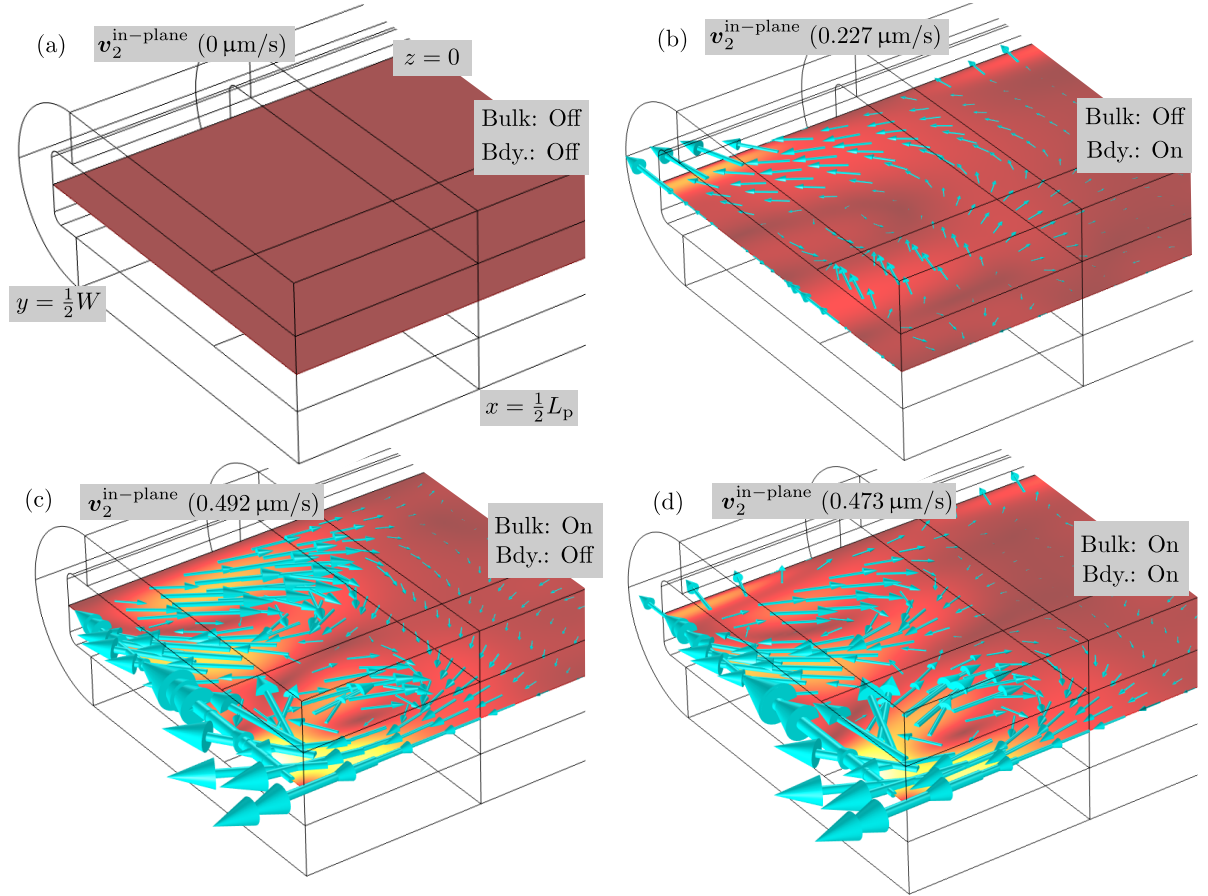


Figure 6.8: Replot of Fig. 6.6(b) where the bulk (Bulk), and boundary (Bdy.) driving terms are switched on and off in the streaming calculation. This corresponds to setting $\langle p_1 \mathbf{v}_1^c \rangle = \mathbf{0}$ in Eq. (6.4) for no bulk driving terms (Bulk: Off), and to setting $\mathbf{v}_{2\parallel} = \mathbf{0}$ in Eq. (6.6) for no boundary driving terms (Bdy.: Off). The color, and arrow length denotes the magnitude, and the direction of $\mathbf{v}_2^{\text{in-plane}}$, going from 0 $\mu\text{m/s}$ (dark red) to 0.492 $\mu\text{m/s}$ (white), and the same arrow and color scaling is used in all four plots (a)-(d).

several discrepancies exist between our model and other published effective models, as well as discrepancies with experimental measurements, all of which needs to be addressed. In the following, we therefore shortly discuss 1) the comparison with the full-2D model, 2) crucial technical points to make the model work numerically, 3) the surprising role of the bulk driving terms, and 4) comparison with experiments and other models in the literature.

6.4.1 Comparison with the 2D-validation model

From the results in Section 6.2 it is clear that our effective model for calculating the streaming reproduces the results of the full model well in the 2D case, and from the literature the full model is known to compare well with experiments [66]. However, as pointed out in Section 6.2.4, there is some ambiguity in the literature about what boundary condition to apply to the streaming velocity field at solid-fluid boundaries. Our investigation suggests that letting the fluid follow the solid wall in the Lagrange picture, by correcting for the Stokes-drift (Eq. (6.10a)), seems to be the correct approach. Though the Lagrangian wall condition does not exhibit strict *local* mass conservation, it can be shown to have *global* mass conservation [85, 87]. The reason for the apparent success of previous published theoretical work in spite of using the seemingly faulty no-slip condition (Eq. (6.10b)), or the no-mass flux condition (Eq. (6.10c)) in the uncorrected Euler picture, is found in the fact that the normal-direction planar wall actuation leads to no, or negligible, Stokes-drift. However this is not true for a more general mode of actuation, as is the case in our model where the solid actuation of the fluid domain is simulated, and not an idealised actuation function put in manually.

6.4.2 The rescaled pressure \tilde{p}_2

In Eq. (6.3) we introduced a rescaling of the second-order pressure p_2 in order to absorb the potential part of the Reynolds stress into a rescaled pressure \tilde{p}_2 . In our numerical implementation in COMSOL MULTIPHYSICS, we observe that without the pressure rescaling the model exhibits poor numerical convergence, and produces spurious and unphysical results. With the rescaled pressure \tilde{p}_2 however, we observe consistent and good numerical convergence. To understand this, we look at the scaling between the potential term and the bulk driving term in Eq. (6.2), and note that the latter of the two force terms is several orders of magnitude lower than the potential term. Comparing just the kinetic energy of the potential term $\frac{1}{4}\nabla\rho_0|v_1^c|^2$ with the bulk driving term we get

$$\frac{|\frac{\Gamma\omega}{c_0^2}\langle v_1 p_1 \rangle|}{|\nabla\rho_0(v_1^c)^2|} \approx \frac{\Gamma p_1}{\rho_0 c_0 v_1^c} \approx \frac{10^{-5} 10^5}{10^3 10^3 10^{-1}} = 10^{-4}, \quad (6.11)$$

where we approximate $\nabla \sim k_0 = \frac{\omega}{c_0}$, $p_1 \sim 0.1$ MPa, and $v_1^c \sim 0.1$ m/s. Furthermore, because v_1^c and p_1 is largely out of phase, taking the time-average will further decrease the ratio in Eq. (6.11). In the trapping region ($x < \frac{1}{2}L_p$) we find $\frac{\int_{\Omega}\langle v_1^c p_1 \rangle dV}{\int_{\Omega}|v_1^c||p_1|dV} = 0.03$ for the C1 capillary resonance mode in Fig. 5.8, lowering the scaling in Eq. (6.11) further by two orders of magnitude to 10^{-6} .

This implies that without the pressure rescaling, the numerical algorithm in COMSOL is trying to balance a huge potential force with the normal second-order pressure p_2 , and has to, on top of that, calculate the tiny side-effect resulting from the small (10^{-6}) part of stress that is not a potential force, and often fails at this. With the pressure rescaling \tilde{p}_2 however, these problems disappear completely. This rescaling and its benefits was also pointed out recently by Riaud *et al.* [36], and in this work we have also seen the importance of performing this pressure rescaling when possible.

6.4.3 The influence of the bulk driving terms for the acoustic streaming

A point regarding our work compared to already published work, relates to other suggested approaches for calculating the acoustic streaming in 3D using effective models. Lei *et al.* [91] discusses the difference between full models, where the viscous boundary layers are resolved, versus effective model approaches using the limiting velocity theory [88], very similar to our discussion in Section 6.1. One key difference between our approach and that of Lei *et al.* [91] is the inclusion of the bulk driving terms $\langle p_1 \mathbf{v}_1^c \rangle$ in Eq. (6.4), which is neglected in [91]. In the light of our investigation of including/excluding the different bulk and boundary contributions when calculating the acoustic streaming, exemplified in Fig. 6.8, our results suggest that the bulk driving terms cannot be neglected, but are in fact to a large part responsible for generating the experimentally observed in-plane acoustic streaming rolls. Exactly in what situations the bulk terms play a significant role for generating acoustic streaming is so far not quantified in this work, but one possible explanation could be that having a mix of both standing and travelling waves in the capillary simulation could create situations where the pressure p_1 and velocity \mathbf{v}_1^c get slightly in phase, thus creating significant values of the time-averaged driving term $\langle p_1 \mathbf{v}_1^c \rangle$, compared to the usual idealised 1D standing-wave case, where velocity and pressure are exactly $\frac{\pi}{2}$ out of phase and the bulk driving terms are zero.

6.4.4 Comparison with experiments and other effective models in the literature

When comparing the calculated streaming field for the C1 capillary with experiments we observe overall good agreement. The structure of the streaming field compares relatively well, and the measured magnitudes is within half an order of magnitude of the calculated velocities. Because these comparisons are only preliminary, more thorough comparisons with experiments are needed. This could e.g. be done by measuring the streaming field by particle image velocimetry or particle tracking, together with an acoustic energy density calibration performed immediately after, in the same experiment, as we have reasons to expect that the acoustic energy density varies between experiments for the same applied transducer voltage, due to the fairly irreproducible method of applying the mechanical coupling layer (small drop of glycerol) between the capillary and the transducer. One discrepancy however, that is already clear from the preliminary comparisons with experiment is that we find two separate in-plane streaming rolls, see Fig. 6.6(b), both rotating counter clockwise, where only one is observed in the experiment, see Fig. 6.7. Different reasons

explaining this discrepancy could be non-perfect glass capillary geometries, acoustic reflections from the surroundings, or that the mechanical actuation used in our calculations does not reflect the physics of the experiment fully, all of which, could potentially impact the acoustic field in the capillary.

In the literature on effective modeling of acoustic streaming Lei *et al.* have published several works on acoustic streaming in glass capillary devices [72, 86] and demonstrate good agreement between model and experiments. In their model they consider a fluid domain in 3D and excite the acoustic field by applying a normal acceleration on the bottom of the fluid domain controlled by a Gaussian function with a manually set position, and decay coefficients corresponding to decay lengths in the x - and y -direction, L_x , and L_y , for the Gaussian function $e^{-(x/L_x)^2-(y/L_y)^2}$. The authors report that their results are insensitive to the chosen Gaussian decay coefficients by having examined five sets of coefficients. However, converting the coefficients to the corresponding decay lengths, the smallest and, largest decay lengths are 0.7 mm, and 1.4 mm, respectively, which are both considerably lower than the capillary width $W = 6$ mm, which is the physically relevant length scale to compare with, and does therefore not span a range that makes it possible to claim that the streaming is insensitive to the choice of decay lengths. To claim this, one would have to examine decay lengths being smaller than, similar to, and much larger than the capillary width W . Furthermore, from an experimental point of view, it is very unlikely that the streaming would in fact be insensitive to the chosen actuation, given that it is found in several experiments [72, 30] that the in-plane streaming to a high degree is confined to the length of the transducer attached to the capillary, and can therefore not be insensitive to the chosen actuation position and decay length. This point is confirmed by our model, where we observe a clear confinement of the streaming to actuation area, very similar what is experimentally observed.

Chapter 7

Concluding remarks and outlook

As a concluding part of the thesis we briefly outline challenges and ideas for further work regarding *hydrodynamic particle-particle interaction in microfluidics* treated in Chapter 4, and *effective modelling of liquid-filled glass capillaries used for acoustic trapping* treated in Chapters 5 and 6.

Hydrodynamic particle-particle interactions in microfluidics

One important and major step forward in developing this theory would be to include other particle-particle interaction mechanisms besides the hydrodynamic interactions considered in this work. Especially the acoustic interactions (secondary scattering) between particles [92], and the magnetic dipole-dipole interactions would be relevant to include for the model in Chapter 4 in further work, as these types interactions have been shown to play a role in experiments [93], and at the particle concentrations considered in our model, the particles could potentially change the acoustic field [94], or the magnetic fields themselves, which would in turn change the dynamics of the suspension.

Another important extension of the model would be to include the effect of soft deformable particles, which is highly relevant in the context of biofluids. For instance in blood, the deformability of erythrocytes is known to play a large role for the viscoelastic properties of blood as an effective medium.

Effective modelling of liquid-filled glass capillaries used for acoustic trapping

With an effective model developed now able to calculate the acoustic radiation force and the acoustic streaming, it is possible to simulate particle trajectories and compare more detailed to experiments, such as particle image velocimetry, or particle tracking measurements. This would provide a better basis for quantifying discrepancies between theory and experiment. Next, a relevant problem to consider is the role of the effective actuation boundary condition in a more systematic study. At this point only two different types of boundary conditions were tested, and especially the impact on the acoustic streaming for different boundary conditions needs to be investigated further. In line with this, it is also of interest to understand the role of the mechanical coupling layer and the piezoelectric transducer, ultimately having a model taking only the applied electrical voltage and the driving fre-

quency as inputs. However, in order to realise such a model, isolated models for the fluid coupling layer and the piezoelectric transducers would have to be developed and validated on their own before making a coupled fluid-channel-actuator model. This could prove difficult since simulating the behaviour of piezoelectric materials involves many material parameters that can change with both frequency and fabrication history of the specific transducer, and is therefore in the least a simple task.

Lastly, we know from experiments that a seed cluster of large polystyrene particles can act as a catalyst for trapping sub-micrometer particles [30, 73], which is an otherwise very challenging and sought after technological feature in biotechnology in general. It is therefore of great interest to understand the role of this seed cluster theoretically and its physical working principle as a catalyst for catching sub-micrometer particles, in order to further improve this technology in the future.

Appendix A

Paper published in Lab on a Chip

Title: Continuum modeling of hydrodynamic particle-particle interactions in microfluidic high-concentration suspensions

Authors: Mikkell W. H. Ley and Henrik Bruus.

Reference: Published in Lab on a Chip **16**, (2016), 1178-1188 (11 pages)



Cite this: *Lab Chip*, 2016, 16, 1178

Continuum modeling of hydrodynamic particle–particle interactions in microfluidic high-concentration suspensions

Mikkel W. H. Ley and Henrik Bruus*

A continuum model is established for numerical studies of hydrodynamic particle–particle interactions in microfluidic high-concentration suspensions. A suspension of microparticles placed in a microfluidic channel and influenced by an external force, is described by a continuous particle-concentration field coupled to the continuity and Navier–Stokes equation for the solution. The hydrodynamic interactions are accounted for through the concentration dependence of the suspension viscosity, of the single-particle mobility, and of the momentum transfer from the particles to the suspension. The model is applied on a magnetophoretic and an acoustophoretic system, respectively, and based on the results, we illustrate three main points: (1) for relative particle-to-fluid volume fractions greater than 0.01, the hydrodynamic interaction effects become important through a decreased particle mobility and an increased suspension viscosity. (2) At these high particle concentrations, particle-induced flow rolls occur, which can lead to significant deviations of the advective particle transport relative to that of dilute suspensions. (3) Which interaction mechanism that dominates, depends on the specific flow geometry and the specific external force acting on the particles.

Received 2nd February 2016,
Accepted 23rd February 2016

DOI: 10.1039/c6lc00150e

www.rsc.org/loc

1 Introduction

The ability to sort and manipulate biological particles suspended in bio-fluids is a key element in contemporary lab-on-a-chip technology.^{1–7} Such suspensions often contain bio-particles in concentrations so high that the particle–particle interactions change the flow behavior significantly compared to that of dilute suspensions. The main goal of this paper is to present a continuum model of hydrodynamic interaction effects in particle transport of high-concentration suspensions moving through microchannels in the presence of external forces.

One important example of high-concentration suspensions is full blood in blood vessels with diameters in the cm to sub-millimeter range or in artificial microfluidic channels. State-of-the-art calculations of the detailed hydrodynamics of blood involve direct numerical simulations (DNS).^{8–11} DNS models can simultaneously resolve the deformation dynamics of the elastic cell membranes of up to several thousand red blood cells (RBCs) as well as the inter-cell hydrodynamics of the fluid plasma, all in full 3D.⁹ However, such calculations require a steep price in computational efforts, as large computer clusters running thousands of CPUs in parallel may be

involved,⁹ and the computations may take days.⁸ The computational cost may be reduced significantly by continuum modeling. Lei *et al.*¹² investigated the limit of small ratios a/H of the particle radius a and the container size H . They found that, to a good approximation, continuum descriptions are valid for $a/H \lesssim 0.02$. This is used in the computationally less demanding approach called mixture theory, or theory of interacting continua, where blood flow is modeled as two superimposed continua, representing the plasma and RBCs.^{13,14} In a recent study, Kim *et al.*¹⁴ used the method to simulate blood flow in a microchannel, and the results compared favorably to experiments. However, it is debated how to correctly calculate the coupling between the two phases, as well as formulate the stress tensor for the solid phase RBCs. This is called the ‘closure problem’ of mixture theory.¹⁵

Another important example is the hydrodynamics of macroscopic suspensions of hard particles, such as in gravity-driven sedimentation. These systems have been described by effective-medium theories of the effective viscosity of the suspension and of the effective single-particle mobility. The textbook by Happel and Brenner¹⁶ summarizes work from 1920 to 1960, in particular unit-cell modeling and infinite-array modeling, both approaches imposing a regular distribution of particles. Later, Batchelor¹⁷ improved the effective-medium models by applying statistical mechanics for irregularly placed particles. In 1982, Mazur and Van Saarloos¹⁸ developed the induced-force method for explicit

Department of Physics, Technical University of Denmark, DTU Physics Building 309, DK-2800 Kongens Lyngby, Denmark. E-mail: mley@fysik.dtu.dk, bruus@fysik.dtu.dk

calculation of the hydrodynamic interactions between many rigid spheres. A few years later, this method was extended by Ladd^{19,20} to allow for a higher number of particles to be considered in an efficient manner. In 1990, Ladd²¹ used the induced-force method in high-concentration suspensions to calculate three central hydrodynamic transport coefficients: the effective suspension viscosity η , the particle diffusivity D , and the particle mobility μ . The obtained results compare well with both experiments and with preceding theoretical work.

While studies of high-density suspensions with active transport are very important in lab-on-a-chip systems, such as in electro-, magneto-, and acoustophoresis,^{1,3,4,22} they have not been treated by the microfluidic DNS-models mentioned above. On the other hand, while the effective-medium theories do treat active transport, they have rarely been used to analyze microfluidic systems. In this work, we present a continuum model of high-density suspensions in microchannels exposed to an external force causing particle migration. Based on the results of Lei *et al.*¹² mentioned above, we are justified to use the computationally less demanding continuum description in not too small microfluidic channels, $a/H \lesssim 0.02$. Moreover, with the hydrodynamic transport coefficients obtained by Ladd,²¹ we can fairly easy write down the governing equations for high-density suspensions following the Nernst–Planck-like approach presented by Mikkelsen and Bruus,²³ but here extended to include the hydrodynamic particle–particle interactions.

We establish a continuum effective-medium theory, in which the hydrodynamic interactions between particles in a high-density suspension flowing through a microchannel are modeled by including the concentration dependency of the effective suspension viscosity, the particle diffusivity and mobility, and the transfer of momentum from the particles to the suspension. We then illustrate the use of the theory by two examples: The first is strongly inspired by the magnetophoretic device studied by Mikkelsen and Bruus.²³ The second is taken from the emerging field of acoustofluidics^{24,25} and involves an acoustophoretic device, for which the dilute limit is well described,^{26–28} but where the behavior in the high-concentration limit is still poorly characterized.

2 Theory

We consider a microchannel at ambient temperature, such as the one sketched in Fig. 1. In a steady-state pressure-driven flow of average inlet velocity v_0 , an aqueous suspension of microparticles, with the homogeneous concentration c_0 (number of particles per volume) at the inlet, is flowing through the microchannel. Only a section of length L is shown. The effects of side-walls, present in actual systems, are negligible for channels with a large width-to-height ratio. Localized in the channel is an active area, where the microparticles are subjected to a transverse single-particle migration force F_{mig} . This force changes the particle distribution, resulting in an inhomogeneous distribution downstream towards the outlet. In this process, the particles are transported by advection, active migration, and diffusion, all of which are

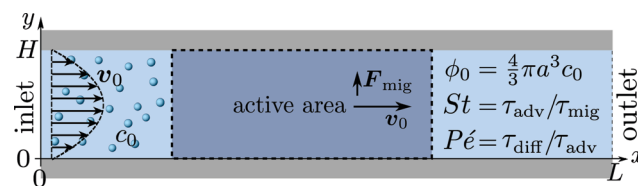


Fig. 1 Sketch of the model system. Spherical microparticles of diameter $2a$ are suspended in a Newtonian fluid with a homogeneous number concentration c_0 , or volume fraction $\phi_0 = \frac{4}{3}\pi a^3 c_0$. The suspension enters from the inlet with velocity v_0 and flows towards the localized active area, where the particles experience a transverse migration force F_{mig} , which redistributes the particles before they leave the channel at the outlet. The resulting particle transport is determined by the relative strength between particle diffusion, advection and migration, which is characterized by three dimensionless numbers: the particle concentration ϕ_0 , the transient Strouhal number St , and the Péclet number Pe .

affected by hydrodynamic particle–particle interactions at high concentrations.

2.1 Model system

As a simple generic model system, we consider a section of length L of a microchannel with constant rectangular cross-section of height H and width W . In specific calculations we take $L = 7H$ and study for simplicity the flat-channel limit $W = 10H$, for which the system, in a large part of the center, is reasonably well approximated by a parallel-plate channel. We take the microparticles to be rigid spheres with diameter $2a$. Their local concentration (number per volume) is described by the continuous field $c(\mathbf{r})$, but often it is practical to work with the dimensionless concentration (particle volume fraction),

$$\phi(\mathbf{r}) = \frac{4}{3}\pi a^3 c(\mathbf{r}). \quad (1)$$

We are particularly interested in high inlet concentrations ϕ_0 between 0.001 and 0.1, and for this range with the typical values $2a = 2\ \mu\text{m}$ and $H = 50\ \mu\text{m}$, the number of particles in the volume $L \times W \times H$ is between 10^4 and 10^6 , which in practice renders direct numerical simulation of the suspension infeasible. We therefore employ continuum modeling in terms of the three continuous fields: the particle concentration $c(\mathbf{r})$, the pressure $p(\mathbf{r})$, and the velocity $\mathbf{v}(\mathbf{r})$ of the suspension.

2.2 Forces and effective particle transport

Our continuum model for the particle current density \mathbf{J} includes diffusion (diff), advection (adv), and migration (mig),²⁹ for which we include hydrodynamic particle–particle interactions through $c(\mathbf{r})$,

$$\mathbf{J} = \mathbf{J}_{\text{diff}} + \mathbf{J}_{\text{adv}} + \mathbf{J}_{\text{mig}} \quad (2a)$$

$$= -D(c)\nabla c + c\mathbf{v} + c\mu(c)\mathbf{F}_{\text{mig}} \quad (2b)$$

$$= -\chi_D(\phi)D_0\nabla c + c\mathbf{v} + c\chi_\mu(\phi)\mu_0\mathbf{F}_{\text{mig}}. \quad (2c)$$

Here,

$$D(c) = \chi_D(\phi)D_0 \quad \text{and} \quad \mu(c) = \chi_\mu(\phi)\mu_0 \quad (2d)$$

is the effective single-particle diffusivity and mobility, respectively, $\chi_D(\phi)$ and $\chi_\mu(\phi)$ are concentration-dependent correction factors described in more detail in section 2.5, while $\mu_0 = (6\pi\eta_0 a)^{-1}$ and $D_0 = k_B T \mu_0$ is the dilute-limit mobility and diffusivity, respectively, where k_B is the Boltzmann constant, T is the temperature, and η_0 is the dilute-limit viscosity of the suspension. We do not in this work consider any effects of van der Waals interactions or steric interactions.²⁹ Due to conservation of particles, the particle current density obeys a steady-state continuity equation,

$$0 = \nabla \cdot \mathbf{j}. \quad (3)$$

2.3 Effective viscosity and flow of the suspension

The flow of the suspension is governed by the continuity equations for momentum and mass. Treating the suspension as an effective continuum medium with the particle concentration $\phi(\mathbf{r})$, its density and viscosity are

$$\rho(\phi) = \chi_\rho(\phi) \rho_0 \quad \text{and} \quad \eta(\phi) = \chi_\eta(\phi)^{-1} \eta_0, \quad (4)$$

with the dimensionless correction factors $\chi_\rho(\phi)$ and $\chi_\eta(\phi)^{-1}$ in front of the density ρ_0 and viscosity η_0 of pure water, respectively. A given particle experiences a drag force, when it is moved relative to the suspension by the migration force \mathbf{F}_{mig} , and in turn, an equal but opposite reaction force is exerted on the suspension. In the continuum limit this is described by the force density $c\mathbf{F}_{\text{mig}}$. In steady state, the momentum continuity equation for an incompressible suspension with the stress tensor $\boldsymbol{\sigma}$ therefore becomes

$$0 = \nabla \cdot [\boldsymbol{\sigma}(\phi) - \rho(\phi)\mathbf{v}\mathbf{v}] + c\mathbf{F}_{\text{mig}}, \quad (5a)$$

$$\boldsymbol{\sigma}(\phi) = -\mathbf{1}p + \chi_\eta(\phi)^{-1}\eta_0[\nabla\mathbf{v} + (\nabla\mathbf{v})^T], \quad (5b)$$

where $\mathbf{1}$ is the unit tensor. Likewise, the steady-state mass continuity equation for an incompressible suspension is written as

$$0 = \nabla \cdot [\chi_\rho(\phi)\rho_0\mathbf{v}]. \quad (6)$$

2.4 Boundary conditions

We assume a concentration $c = c_0$ and a parabolic flow profile

$\mathbf{v} = 6u_0 \frac{y}{H} \left(1 - \frac{y}{H}\right) \mathbf{e}_x$ at the inlet, and vanishing axial gradients

$\partial_x c = 0$ and $\partial_x \mathbf{v} = 0$ at the outlet. At the walls, we assume a no-slip condition $\mathbf{v} = 0$, while the condition for c depends on the specific physical system. Lastly, we fix the pressure level to be zero at the lower corner of the outlet $p(L, 0) = 0$.

2.5 Dimensionless, effective transport coefficients

The dependency of the effective diffusion, mobility, viscosity and density on the particle concentration ϕ is described by the correction factors $\chi_D(\phi)$, $\chi_\mu(\phi)$, $\chi_\eta(\phi)$, and $\chi_\rho(\phi)$, respectively, which can be interpreted as dimensionless effective transport coefficients. The suspension density is a weighted average of the water density ρ_0 and the particle density ρ_p ,

$$\chi_\rho(\phi) = (1 - \phi) + \frac{\rho_p}{\rho_0} \phi. \quad \text{For bio-fluids, particles are often neu-}$$

trally buoyant, so $\rho_p \approx \rho_0$ and $\chi_\rho \approx 1$. In a comprehensive numerical study of finite-sized, hard spheres suspended in an Newtonian fluid at low Reynolds numbers (the Stokes limit), the remaining transport coefficients χ_D , χ_μ , and χ_η were calculated by Ladd²¹ at 14 specific values of ϕ between 0.001 and 0.45. For each of the coefficients χ , we have fitted a fourth-order polynomial to the discrete set of values χ^{-1} , while imposing the condition $\chi(0)^{-1} = 1$ to ensure agreement with the dilute-limit value,

$$\chi_\eta(\phi)^{-1} = 1 + 2.476(7)\phi + 7.53(2)\phi^2 - 16.34(5)\phi^3 + 83.7(3)\phi^4 + \mathcal{O}(\phi^5), \quad (7a)$$

$$\chi_D(\phi)^{-1} = 1 + 1.714(3)\phi + 6.906(13)\phi^2 - 17.05(3)\phi^3 + 61.2(1)\phi^4 + \mathcal{O}(\phi^5), \quad (7b)$$

$$\chi_\mu(\phi)^{-1} = 1 + 5.55(3)\phi + 43.4(3)\phi^2 - 149.6(9)\phi^3 + 562(3)\phi^4 + \mathcal{O}(\phi^5), \quad (7c)$$

where the uncertainty of the last digit is given in the parentheses. To quantify the quality of the fits χ_{fit} compared to the simulated data points χ_{data} , we calculated the relative differ-

ence $\Delta\chi = \frac{\chi_{\text{data}} - \chi_{\text{fit}}}{\chi_{\text{data}}}$. We found the standard deviation of $\Delta\chi$

to be 0.003, 0.0019 and 0.0058 for χ_η , χ_D and χ_μ , respectively. Thus, the fourth-order polynomials describe the data points well. The resulting fits from eqn (7) and the original data points²¹ are plotted in Fig. 2. Note that the mobility χ_μ is the most rapidly decreasing function of concentration ϕ .

We note that the dilute-limit relation $\mu_0 = \frac{1}{6\pi a} \eta_0^{-1}$ and the definitions $\mu = \chi_\mu \mu_0$ and $\eta^{-1} = \chi_\eta \eta_0^{-1}$ do not imply equality of χ_μ and χ_η . In fact, $\chi_\mu < \chi_\eta$, which highlights the complex nature of the interaction problem at high densities.

2.6 Dimensionless parameters

The dynamics of the system can be characterized by three dimensionless numbers. One is the particle concentration ϕ_0 , which is a measure of the magnitude of the hydrodynamic interactions. The other two are related to the relative magnitude of the diffusion, advection and migration current densities in eqn (2), each characterized by the respective time

scales $\tau_{\text{diff}} = \frac{H^2}{8D_0}$, $\tau_{\text{adv}} = \frac{H}{2u_0}$, and $\tau_{\text{mig}} = \frac{H}{2\mu_0 F_{\text{mig}}}$. A small time scale

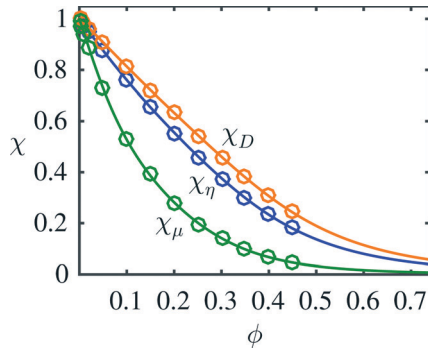


Fig. 2 Plot of the fitted dimensionless effective transport coefficients χ_η , χ_D and χ_μ as a function of concentration ϕ . The full lines represent the fits from eqn (7), while the circles are the original 14 simulation data points by Ladd.²¹

means that the corresponding process is fast and thus dominating. The importance of advection relative to diffusion and of migration relative to advection is characterized by the Péclet number and the transient Strouhal number, respectively,

$$Pe = \frac{\tau_{\text{diff}}}{\tau_{\text{adv}}} = \frac{u_0 H}{4D_0}, \quad (8a)$$

$$St = \frac{\tau_{\text{adv}}}{\tau_{\text{mig}}} = \frac{\mu_0 F_{\text{mig}}}{u_0}, \quad (8b)$$

$$\phi_0 = \frac{4}{3} \pi a^3 c_0. \quad (8c)$$

3 Numerical implementation

Following Nielsen and Bruus,³⁰ we implement the governing eqn (2)–(6) in the general weak-form PDE module of the finite element software COMSOL Multiphysics v. 5.0.³¹ To avoid spurious, numerically induced, negative values of $c(r)$ near vanishing particle concentration, we replace c by the logarithmic variable $s = \log(c/c_0)$. This variable can assume all real numbers, and it ensures that $c = c_0 \exp(s)$ is always positive. We implement the weak form using Lagrangian test functions of first order for p and second order for s , v_x , and v_y .

A particular numerical problem needs to be taken care of in dealing with the advection in our system. The typical average flow speed is $u_0 = 200 \mu\text{m s}^{-1}$ in our channels of height $H = 50 \mu\text{m}$, corresponding to a Péclet number $Pe = 1.7 \times 10^4$. To resolve this flow numerically, a prohibitively fine spatial mesh is needed. However, this problem can be circumvented by artificially increasing the particle diffusivity to $\chi_D = 50$ instead of using eqn (7b). This decreases the Péclet number to $Pe = 2.3 \times 10^2$, but since $Pe \gg 1$ for both the actual and the artificial diffusivity, advection still dominates in both cases, and as discussed in appendix A, the simulation results for the artificial diffusivity are accurate, but a coarser mesh suffices. In this highly advective regime $Pe \gg 1$, the detailed transport in the active area depends on the remaining parameters: the transient Strouhal number St and the inlet concentration ϕ_0 .

More details on the numerical implementation are given in appendix A.

4 Model results and discussion

To exemplify our continuum effective-medium model, we present two examples using the same channel geometry, but different particle migration mechanisms, namely magnetophoresis (MAP) and acoustophoresis (ACP). The magnetophoresis model is the one introduced by Mikkelsen and Bruus,²³ but here extended to include the concentration dependence of the effective transport coefficients χ introduced in section 2.5. This model primarily serves as a model validation. The acoustophoresis model is inspired by the many experimental works reported in Lab on a Chip.^{24,32–35}

4.1 Results for magnetophoresis (MAP)

As in Mikkelsen and Bruus,²³ we consider the parallel-plate system sketched in Fig. 3(a) of height $H = 50 \mu\text{m}$, length $L = 350 \mu\text{m}$, and the boundary conditions of section 2.4. The particles are paramagnetic with magnetic susceptibility $\chi_{\text{mag}} = 1$ and diameter $2a = 2 \mu\text{m}$. A pair of long parallel thin wires is placed perpendicular to the xy -plane with their midpoint at $\mathbf{r}_0 = (x_0, y_0) = (250, 55) \mu\text{m}$, separated by $\mathbf{d} = d\mathbf{e}_x$, and carrying electric currents $\pm I$. The currents lead to a magnetic field, which induces a paramagnetic force \mathbf{F}_{map} on each particle resulting in magnetophoresis. For a particle at position \mathbf{r} , the force is given by²³

$$\mathbf{F}_{\text{map}} = -\frac{2}{\pi} \frac{\chi_{\text{mag}}}{\chi_{\text{mag}} + 3} \mu_0^{\text{em}} a^3 (Id)^2 \frac{\mathbf{r} - \mathbf{r}_0}{|\mathbf{r} - \mathbf{r}_0|^6}, \quad (9)$$

where μ_0^{em} is the vacuum permeability. Note how the rapid fifth-power decrease as a function of the wire distance $|\mathbf{r} - \mathbf{r}_0|$, signals that \mathbf{F}_{map} is a short-ranged local force. Dipole-dipole interactions are neglected. Using the expression for \mathbf{F}_{map} , we can determine the migration time τ_{mig} for a particle

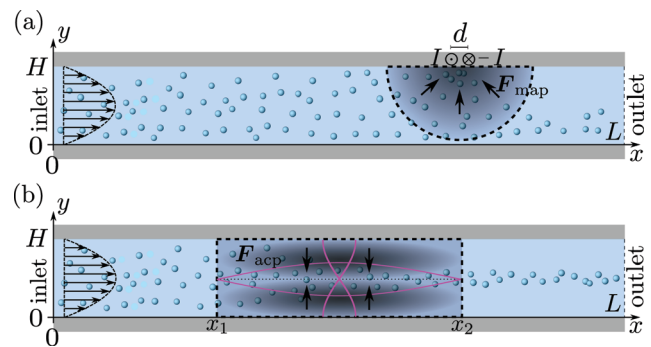


Fig. 3 Specific realizations of the generic system shown in Fig. 1 with height $H = 50 \mu\text{m}$ and length $L = 350 \mu\text{m}$. The microparticles are rigid spheres of diameter $2a = 2 \mu\text{m}$ and a paramagnetic susceptibility $\chi_{\text{mag}} = 1$. A Poiseuille flow with mean velocity u_0 is imposed at the inlet. (a) Magnetophoresis: a pair of thin long wires carrying electrical currents $\pm I$ is placed at the top of the channel $100 \mu\text{m}$ upstream from the outlet. The resulting magnetic force \mathbf{F}_{map} (gray scale) attracts the particles towards the wires. (b) Acoustophoresis: a standing pressure half-wave (magenta) is imposed between x_1 and x_2 . The resulting acoustic force \mathbf{F}_{acp} (gray scale) causes the particles to migrate towards the pressure node at $y = \frac{1}{2}H$.

to migrate vertically from the channel center $(x, y) = \left(x_0, \frac{1}{2}H\right)$, directly below the wires, to the wall $(x, y) = (x_0, H)$. From this we infer the magnetic transient Strouhal number St_{map} ,

$$St_{\text{map}} = \frac{\tau_{\text{adv}}}{\tau_{\text{map}}} = \frac{16}{3\pi^2} \frac{\mu_0^{\text{em}} (Id)^2 a^2}{u_0 \eta_0 H^5}. \quad (10)$$

Wall boundary conditions for the particles. Following the simplifying model of Mikkelsen and Bruus,²³ we assume that once a particle reaches the wall near the wires, it sticks and is thus removed from the suspension. For the upper wall at $y = H$, we therefore set the total particle flux in the y -direction equal to the active migration $J_y = c\mu F_{\text{map},y}$, while at the passive bottom wall at $y = 0$, we choose the standard no-flux condition $J_y = 0$. For short times, this is a good model, but eventually in a real system, the build-up of particles at the wall is likely to occur, which leads to a dynamically change of the channel geometry.

Particle capture as a function of ϕ_0 and St_{map} . In Fig. 4 we have plotted the normalized steady-state particle concentration $\frac{\phi(r)}{\phi_0}$ of the system shown in Fig. 3(a) for the nine combinations of $\phi_0 = 0.001, 0.01, 0.1$ with $St_{\text{map}} = 1, 2, 5$. Firstly,

it is evident from the figure that for a given fixed ϕ_0 and increasing St_{map} , an increasing number of particles are captured by the wire-pair, thus decreasing $\phi(r)$ in a region of increasing size down-stream from the wires. Note also how the slow-moving particles near the bottom wall are pulled upwards by the action of the wires, leaving a decreased particle density there. Secondly, for a fixed St_{map} , the particle capture is non-monotonic as a function of ϕ_0 : it increases going from $\phi_0 = 0$ via 0.001 to 0.01, but then decreases going from 0.01 to 0.1. Thirdly, for the highest concentration $\phi_0 = 0.1$, the morphology of the depleted region has changed markedly: a small region depleted of particles forms around the wires at the top wall together with narrow downstream depletion re-

gions along both the top and bottom wall. All three regions increase somewhat in size for increasing St_{map} .

The normalized capture rate β_{map} . We analyze the particle capture quantitatively in terms of the normalized capture rate β_{map} defined as the ratio between the flux Γ_{topwall} of particles captured on the top wall by the wires, and the flux Γ_{inlet} of particles entering through the inlet,²³

$$\beta_{\text{map}} = \frac{\Gamma_{\text{topwall}}}{\Gamma_{\text{inlet}}}, \quad (11a)$$

$$\Gamma_{\text{surf}} = \left| \int_{\text{surf}} d\ell \mathbf{n} \mathbf{J} \right|, \quad (11b)$$

where \mathbf{n} is the surface normal of a given surface. In Fig. 5(a), we have plotted β_{map} as a function of ϕ_0 for different St_{map} values. All of the curves in this plot show the same qualitative behavior: the capture fraction increases with inlet concentration until a certain point, beyond which it declines.

This general behavior is illustrated by the three specific cases $\phi_0 = 0.02, 0.045$, and 0.1 denoted by the purple bullets A, B and C on the purple “ $St_{\text{map}} = 1$ ”-curve. For these three cases, we have in Fig. 5(b1–d1) plotted the magnetically-induced change $\Delta \mathbf{v} = \mathbf{v} - \mathbf{v}_0$ in the suspension velocity, and in Fig. 5(b2–d2) the magnetic force density $\mathbf{f} = c\mathbf{F}_{\text{map}}$ overlaid by contour lines of c (white). For A in Fig. 5(b1) and (b2) with $\phi_0 = 0.02$, more particles are captured compared to the dilute case, because $c\mathbf{F}_{\text{map}}$ induces a clockwise flow-roll that advects the upstream particles closer to the wires. For B in Fig. 5(c1) and (c2) with $\phi_0 = 0.045$, $c\mathbf{F}_{\text{map}}$ induces two flow rolls, of which the upstream one rotates counter clockwise and advects particles away from the wires, thus lowering the capture compared to A. For C in Fig. 5(d1) and (d2) with $\phi_0 = 0.1$, $c\mathbf{F}_{\text{map}}$ induces a single strong counter-clockwise flow roll that more efficiently advects the upstream particles away from the wires, and β_{map} decreases further.

While the initial increase in β_{map} for ϕ_0 increasing from 0 to 0.03 is in agreement with Mikkelsen and Bruus,²³ black circles in Fig. 5(a), the following decrease in β_{map} for ϕ_0

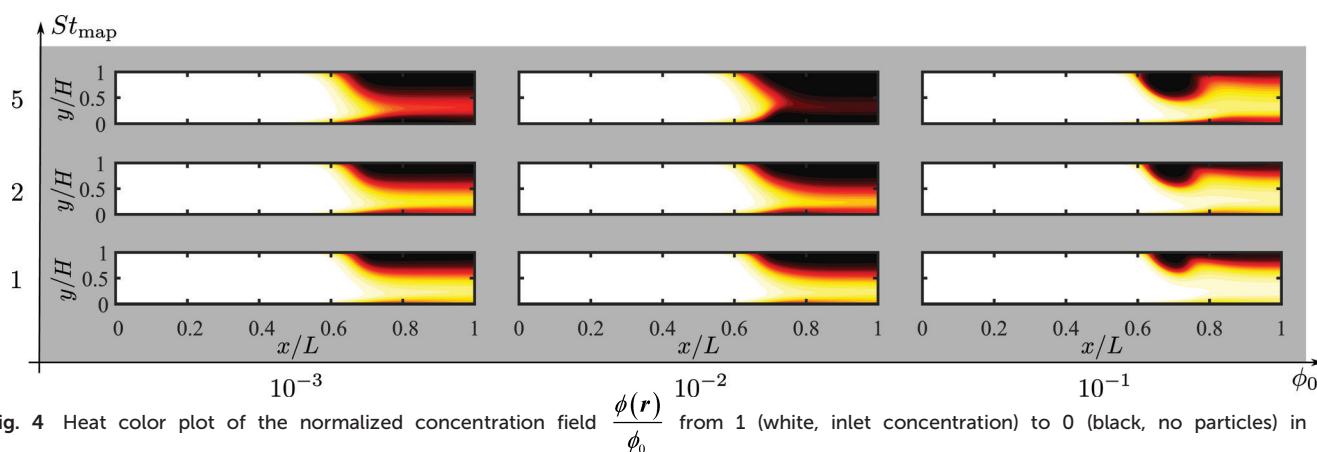


Fig. 4 Heat color plot of the normalized concentration field $\frac{\phi(r)}{\phi_0}$ from 1 (white, inlet concentration) to 0 (black, no particles) in the magnetophoretic system Fig. 3(a), for the nine combinations of $\phi_0 = 0.001, 0.01, 0.1$ with $St_{\text{map}} = 1, 2, 5$.

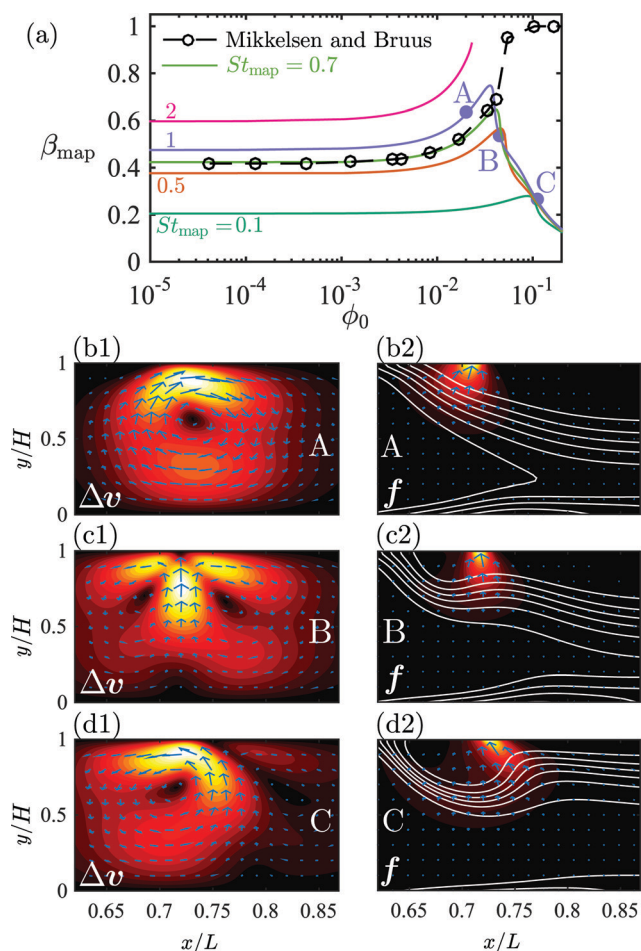


Fig. 5 (a) Lin-log plot of the capture fraction β_{map} as a function of the inlet concentration ϕ_0 for different transient Strouhal numbers St_{map} (full lines). The original results of Mikkelsen and Bruus²³ are plotted as circles connected by a dashed line. The purple bullets on the curve for $St_{\text{map}} = 1$ mark the three situations A, B, and C plotted in (b)–(d) below. (b1), (c1) and (d1) Color plot from 0 (black) to $\{1.0, 1.6, 2.0\}u_0$ (white) and vector plot of the particle-induced velocity $\Delta v = v - v_0$ near the wire-pair for situation A, B and C, respectively. (b2), (c2) and (d2) Color plot from 0 (black) to $2 \times 10^5 \text{ N m}^{-3}$ (white) and vector plot of the external force $f = cF_{\text{map}}$. The white lines are contour lines of the concentration field $\phi(r)$.

increasing beyond 0.03 was not observed by them. The deviation is not due to our inclusion of the effective transport coefficients χ_η and χ_μ , since repeating the simulations²³ with $\chi_\eta = \chi_\mu = 1$ resulted in a curve indistinguishable from the green curve $St_{\text{map}} = 0.7$ in Fig. 5(a). We speculate that this deviation is due to our improved mesh resolution.

4.2 Results for acoustophoresis (ACP)

We consider a system identical to the one described in section 4.1, except that the single-particle migration force F_{mig} now is taken to be the acoustic radiation force F_{acp} arising from the scattering of an imposed standing ultrasound wave on the microparticles. It is given by³⁶

$$F_{\text{acp}} = -\nabla U_{\text{ac}}, \quad (12a)$$

$$U_{\text{ac}} = \frac{4\pi}{3} a^3 \left[\text{Re}[f_0] \frac{1}{2} \kappa_0 \langle p_1^2 \rangle - \text{Re}[f_1] \frac{3}{4} \rho_0 \langle v_1^2 \rangle \right], \quad (12b)$$

where κ_0 and ρ_0 is the compressibility and mass density of the carrier fluid, respectively, f_0 and f_1 are two scattering coefficients, a is the particle radius, and $\langle p_1^2 \rangle$ and $\langle v_1^2 \rangle$ is the time-average of the squared acoustic pressure and velocity fields in the suspension, respectively. Inspired by experimentally observed localized fields,²⁶ we take the acoustic field to be a standing half-wave resonance localized in the dashed

area for x between $x_1 = \frac{2}{7}L$ and $x_2 = \frac{5}{7}L$ as indicated by the magenta curves in Fig. 3(b),

$$p_1 = p_a \sin\left(\pi \frac{7x-2L}{3L}\right) \cos\left(\pi \frac{y}{H}\right) e^{-i\omega t}, \quad \frac{2}{7} \leq \frac{x}{L} \leq \frac{5}{7}, \quad (13a)$$

$$v_1 = -i \frac{1}{\rho_0 \omega} \nabla p_1, \quad \frac{2}{7} \leq \frac{x}{L} \leq \frac{5}{7}. \quad (13b)$$

Here, $\omega = 2\pi f$ is the angular actuation frequency with the frequency f typically in the MHz range, and p_a is the acoustic pressure amplitude typically in the 0.1 MPa range.^{26,32} The acoustophoretic force F_{acp} is obtained by inserting the acoustic fields (13) into eqn (12), and the result is a force, which focuses the particles at the pressure node in the channel center at $y = \frac{1}{2}H$, see appendix B for details.

Given F_{acp} , we then calculate the transient Strouhal number from the acoustic migration time τ_{mig} in the dilute limit ($\chi_\mu = 1$) for a single particle migrating from $(x, y) = \left(\frac{1}{2}L, \frac{1}{8}H\right)$ to $(x, y) = \left(\frac{1}{2}L, \frac{3}{8}H\right)$,²⁶ and from the advection time given by $\tau_{\text{adv}} = \frac{H}{4u_0}$,

$$St_{\text{acp}} = \frac{\tau_{\text{adv}}}{\tau_{\text{mig}}} = \frac{4\pi^2}{\ln\left(\cot\frac{\pi}{8}\right)} \frac{a^2 E_{\text{ac}} \Phi}{\eta_0 H u_0}. \quad (14)$$

Here, $E_{\text{ac}} = p_a^2 / (4\rho_0 c_{\text{liq}}^2)$ is the acoustic energy density (typically $1\text{--}100 \text{ J m}^{-3}$), c_{liq} is the speed of sound in the carrier liquid, and $\Phi = \frac{1}{3}f_0 + \frac{1}{2}f_1$ is the so-called acoustic contrast factor.³⁷

Wall boundary condition for the particles. As the particles in this model enter from the inlet, focus towards the channel center $y = \frac{1}{2}H$, and leave through the outlet, we choose the simple no-flux boundary condition, $n \cdot J|_{y=0,H} = 0$, for the bottom and top walls.

Particle capture as a function of ϕ_0 and St_{acp} . In Fig. 6 is plotted the normalized steady-state particle concentration

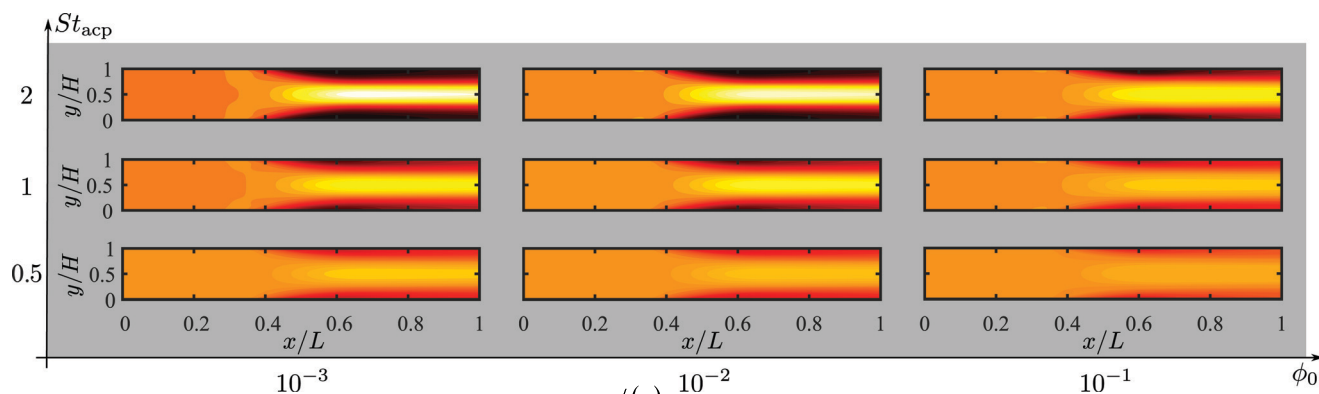


Fig. 6 Heat color plot of the normalized concentration field $\frac{\phi(r)}{\phi_0}$ from 1.73 (white, maximum value) to 0 (black, no particles) in the acoustophoretic system Fig. 3(b), for the nine combinations of $\phi_0 = 0.001, 0.01, 0.1$ with $St_{acp} = 0.5, 1, 2$.

$\frac{\phi(r)}{\phi_0}$ of the system shown in Fig. 3(b) for the nine combinations of $\phi_0 = 0.001, 0.01, 0.1$ to $St_{acp} = 0.5, 1, 2$. Clearly, for a given fixed ϕ_0 and increasing St_{acp} , an increasing number of particles are focused in the center region. This is expected since St_{acp} is proportional to the acoustic energy density E_{ac} . For $\phi_0 = 0.001$, the center-region concentration (white) is 1.73 times the inlet concentration (orange). Secondly, for a fixed St_{acp} , the particle focusing is monotonically decreasing as a function of ϕ_0 as seen from the decrease in both the width of the particle-free black regions and the magnitude of the downstream center-region concentration. See in particular the change from $\phi_0 = 0.01$ to 0.1 .

To quantify the acoustic focusing for a given inlet concentration, we introduce in analogy with eqn (11) the normalized flux β_{acp} of focused particles leaving through the middle 30% of the outlet,

$$\beta_{acp} = \frac{\Gamma_{center}}{\Gamma_{inlet}}, \quad (15a)$$

$$\Gamma_{center} = \left| \int_{0.35W}^{0.65W} dy J_x(L, y) \right|, \quad (15b)$$

In the lin-log plot Fig. 7(a) of β_{acp} versus ϕ_0 for the four Strouhal numbers $St_{acp} = 0.1, 0.5, 1$, and 2 , the above-mentioned monotonic decrease in acoustophoretic focusing is clear. Especially for ϕ_0 exceeding 0.01 a dramatic reduction in focusability sets in.

To determine the dominant hydrodynamic interaction mechanism behind this reduction, we introduce the normalized particle focusing fraction $\Delta\beta_{acp}(\phi_0, St_{acp})$ by the definition,

$$\Delta\beta_{acp}(\phi_0, St_{acp}) = \frac{\beta_{acp}(\phi_0, St_{acp}) - \beta_{acp}(\phi_0, 0)}{\beta_{acp}(0, St_{acp}) - \beta_{acp}(0, 0)}. \quad (16)$$

Here, the difference in normalized center out-flux β_{acp} at an inlet concentration ϕ_0 between “acoustics on” ($St_{acp} > 0$) and “acoustics off” ($St_{acp} = 0$), is calculated relative to the same dif-

ference computed in the dilute limit $cF_{mig} = 0$ and $\chi_\mu = \chi_\eta = 1$, which is written as $\phi_0 = 0$. We notice that $\Delta\beta_{acp}(\phi_0, St_{acp})$ is unity if there is no hydrodynamics interaction effects, and zero if there is no acoustophoretic focusing. In Fig. 7(b), using the full model ($\chi_\mu = \chi_\mu(\phi)$ and $\chi_\eta = \chi_\eta(\phi)$ denoted “all effects”), $\Delta\beta_{acp}$ is plotted versus ϕ_0 (black lines) for the same four St_{acp} values

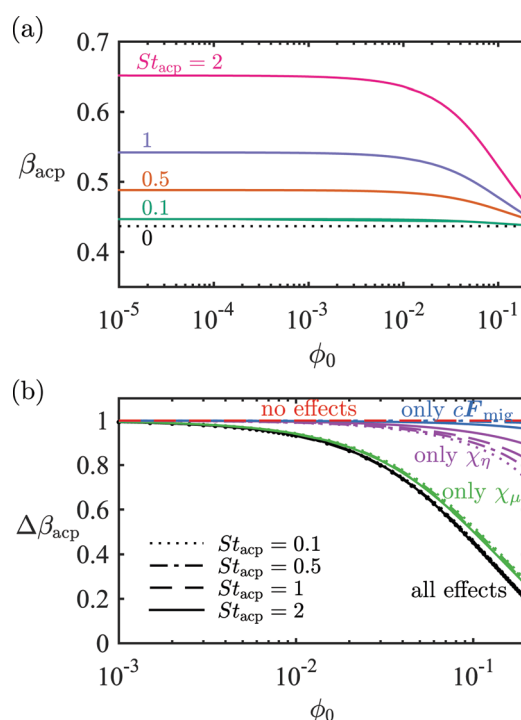


Fig. 7 (a) Lin-log plot of the acoustic particle focusing fraction β_{acp} (given by eqn (15a)) versus the inlet concentration ϕ_0 for four different St_{acp} values. (b) Lin-log plot of the rescaled particle focusing fraction $\Delta\beta_{acp}$, given by eqn (16), as a function of ϕ_0 . The line styles denote different St_{acp} values, and the colors denote the inclusion of one or all hydrodynamic interaction effects, described in section 2. Black: all interaction effects included, green: only effective mobility $\chi_\mu(\phi)$, purple: only effective suspension viscosity $\chi_\eta(\phi)$, blue: only momentum transfer from the particles to the suspension cF_{mig} , and red: no interaction effects included.

as in Fig. 7(a). We note that for the full model (black lines), $\Delta\beta_{\text{acp}}$ is almost independent of the strength St_{acp} of the acoustophoretic force, which makes it ideal for studying the interaction effects through its ϕ_0 dependency.

To elucidate the origin of the observed reduction in focusability, we also plot the following special cases: “no effects” with $\chi_\mu = \chi_\eta = 1$ and $cF_{\text{mig}} = 0$ (red lines), “only cF_{mig} ” with $\chi_\mu = \chi_\eta = 1$ (blue lines), “only χ_η ” with $\chi_\mu = 1$ and $\chi_\eta = \chi_\eta(\phi)$ (purple lines), and “only χ_μ ” with $\chi_\mu = \chi_\mu(\phi)$ and $\chi_\eta = 1$ (green lines). These curves reveal that most of the interaction effect is due to the effective mobility: the green curves “only χ_μ ” are nearly identical to the black curves “all effects”, and both groups of curves show no or little dependence on St_{acp} . The effective suspension viscosity $\chi_\eta(\phi)$ and the particle-induced bulk force cF_{acp} on the suspension only have a minor influence on $\Delta\beta_{\text{acp}}$.

Finally, in Fig. 8 we show the first step towards an experimental validation of our continuum model of hydrodynamic interaction effects. In the figure are seen two micrographs of acoustophoretic focusing of 5.1 μm -diameter polystyrene particles in water in the silicon-glass microchannel setup described in Augustsson *et al.*²⁶ The micrographs are recorded at Lund University by Kevin Cushing and Thomas Laurell under stop-flow conditions $u_0 = 0$ after 0.43 s of acoustophoresis with the acoustic energy $E_{\text{ac}} = 10^2 \text{ J m}^{-3}$. The field of view is near the right edge x_2 of the active region sketched in Fig. 3(b). The good focusing obtained at the low density $\phi_0 = 0.001$ is well reproduced by our model, see Fig. 8(a) and (c). Likewise, the much reduced focusing obtained at the high density $\phi_0 = 0.1$ is also well reproduced by our model, see Fig. 8(b) and (d). Moreover, which is not shown in the figure, the observed transient behavior of the two cases is also reproduced by simulations: For the low concentration $\phi_0 = 0.001$, the particles are migrat-

ing towards to pressure node directly in straight lines, while for the high concentration $\phi_0 = 0.1$, pronounced flow rolls are induced, similar to those shown in Fig. 5.

4.3 Discussion

The results of the continuum effective model simulations of the MAP and the ACP models show that the dominating transport mechanisms differ. For the ACP model, the behavior of a suspension in the high-density regime $\phi_0 \gtrsim 0.01$ is dominated by the strong decrease in the effective single-particle mobility χ_μ shown in Fig. 2. Here, the particle-particle interactions are so strong that the suspension moves as a whole with suppressed relative single-particle motion. The response is a steady degradation of the focusing fraction β_{acp} shown in Fig. 7, as it becomes increasingly difficult for a given particle to migrate towards the center line, where the concentration increases and the mobility consequently decreases. In contrast, for the MAP model, the capture fraction β_{map} increases as ϕ_0 increases from 0 to 0.03, confirming the results of Mikkelsen and Bruus.²³ The reason for the increased capture is that the particle concentration in the near-wire region is low due to the removal of particles, leaving the single-particle mobility unreduced there, while in the region a little farther away, particles attracted by the wires pull along other particles in a positive feedback due to the high-density “stiffening” of the suspension there. Thus, for the MAP system, the dominating interaction effect is through the particle-induced body force cF_{mig} in eqn (5a).

For ϕ_0 increasing beyond 0.03, the observed non-monotonic behavior of β_{map} and continued monotonic behavior of β_{acp} as a function of increasing ϕ_0 , depends on whether or not the specific forces and model geometry lead to the formation of flow rolls, such as shown for the MAP model in Fig. 5. The flow-roll-induced decrease observed in the capture efficiency β_{map} for $\phi_0 \gtrsim 0.03$, see Fig. 7(a), was not observed by Mikkelsen and Bruus,²³ presumably because of their relatively coarse mesh. For the ACP model, no strong influence from induced flow rolls was observed, and the resulting decrease in focus efficiency was monotonic as a function of ϕ_0 . This difference in response is caused by differences in spatial symmetry and in the structure of the two migration forces. The MAP model is asymmetric around the horizontal center line, while the ACP model is symmetric, which accentuates the appearance of flow rolls in the former case. Moreover, the rotation of the body force density cF_{mig} can be calculated as $\nabla \times [cF_{\text{mig}}] = c\nabla \times F_{\text{mig}} - F_{\text{mig}} \times \nabla c$. In the MAP model, both of these rotations are non-zero, while in the ACP model, the first term is zero as F_{acp} is a gradient force, and this feature leads to significant flow rolls in the MAP model and weak ones in the ACP model.

In the above discussion of the results of our model, we have attempted to describe general aspects of hydrodynamic interaction effects, which may be used in future device design considerations. Given the sensitivity on the specific

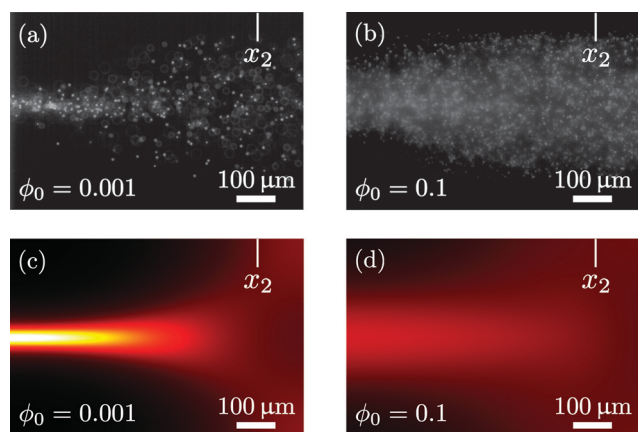


Fig. 8 Topview near the right edge x_2 of the acoustic active region of the particle concentration in a 370 μm -wide microchannel after 0.43 s of acoustophoresis with the acoustic energy $E_{\text{ac}} = 10^2 \text{ J m}^{-3}$ on 5.1 μm -diameter polystyrene particles under stop-flow conditions $u_0 = 0$. (a) Experiment with $\phi_0 = 0.001$. (b) Experiment with $\phi_0 = 0.1$. (c) Continuum modeling with $\phi_0 = 0.001$. (d) Continuum modeling with $\phi_0 = 0.1$. The experimental micrographs courtesy of Kevin Cushing and Thomas Laurell, Lund University.

geometry and on the form of external forces, it is clear that detailed design rules are difficult to establish. However, the simplicity of the model allows for relatively easy implementation in numerical simulations of specific device setups.

5 Conclusion

We have presented a continuum effective medium model including hydrodynamic particle–particle interactions, which requires only modest computational resources and time. The results presented in this paper could be obtained in the order of minutes on an ordinary PC. We have validated the model by comparison to previously published models and found quantitative agreement. Moreover, as a first step towards experimental validation, we have found qualitative agreement with experimental observations of acoustophoretic focusing.

Using our numerical model, we have shown that the response of a suspension to a given external migration force depends on the system geometry, the flow, and the specific form of the migration forces. At high densities $\phi_0 \gtrsim 0.01$ the suspension “stiffens” and relative single-particle motion is suppressed due to a decreasing effective mobility χ_μ . However, the detailed response depends on whether or not particle-induced flow rolls appear with sufficient strength to have an impact.

The continuum effective medium model may prove to be a useful and computationally cheap alternative to the vastly more cumbersome direct numerical simulations in the design of lab-on-a-chip systems involving high-density suspensions, for which hydrodynamic particle–particle interactions are expected to play a dominant role.

Appendix A: Numerical implementation, details

The numerical implementation has been carefully checked and validated. To avoid spurious numerical errors, we have performed a mesh convergence analysis as described in details in Muller *et al.*³⁷ For a continuous field g on a given mesh, we have calculated the relative error

$$C(g) = \sqrt{\int |g - g_{\text{ref}}|^2 da} / \sqrt{\int |g_{\text{ref}}|^2 da}, \text{ where } g_{\text{ref}} \text{ is the solution}$$

obtained for the finest possible mesh. For all fields involved in this study, C falls in the range between 10^{-5} and 10^{-3} , and it has the desired exponential decrease as function of h_{mesh}^{-1} , where h_{mesh} is the mesh element size. The number of mesh points and degrees of freedom used in our final simulations are listed in Table 1.

Table 1 The number of mesh elements N_{mesh} , the degrees of freedom DOF, and the mesh Péclet number $Pé_{\text{mesh}}$ used in the numerical simulations of the MAP and ACP models

Model	N_{mesh}	DOFs	$Pé_{\text{mesh}}$
MAP	70 000–225 000	200 000–2 000 000	5–10
ACP	50 000–200 000	400 000–2 000 000	5–10

We have compared our results with previous work in the literature. Setting $\chi_\mu = \chi_\eta = 1$, our MAP model in section 4.1 is identical to the one by Mikkelsen and Bruus.²³ For this setting, we have calculated the capture fraction β_{map} as a function of the rescaled quantity $(Id)^2/u_0$ (which also appears in the definition (10) for St_{map}), and found exact agreement, including the remarkable data collapse, with the results presented in Fig. 3 of Mikkelsen and Bruus.²³

The numerical stability of the finite-element simulation is controlled by the mesh Péclet number $Pé_{\text{mesh}} = h_{\text{mesh}}u_0/(\chi_D D_0)$ that involves the mesh size h_{mesh} instead of a physical length scale. We found that convergence was ensured for $Pé_{\text{mesh}} \lesssim 10$, which implies the condition $h_{\text{mesh}} \lesssim 10\chi_D D_0/u_0$ for the mesh size. The higher an advection velocity u_0 , the finer a mesh is needed. In order to obtain computation times of the order of minutes per variables ($Pé$, St , ϕ_0) on our standard PC, while still keeping $Pé_{\text{mesh}} \lesssim 10$, we artificially increased χ_D . In Fig. 9 we have plotted the capture fraction β_{map} and the focusing fraction β_{acp} as functions of the transient Strouhal number St for χ_D ranging from 25 to 10 000 in the dilute limit with $\chi_\mu = \chi_\eta = 1$ and $cF_{\text{mig}} = 0$. It is clear from Fig. 9 that the $\beta(St)$ -curves converge for sufficiently small values of χ_D . For $\chi_D \leq 50$, we determine that acceptable convergence is obtained in both models, and we thus fix $\chi_D = 50$ for all calculation performed in this work. This choice of $\chi_D = 50$ allows for acceptable computation times (~ 10 min per variable set). In other words, once the Péclet number is sufficiently high, the convergence is ensured by the dominance of advection over diffusion.

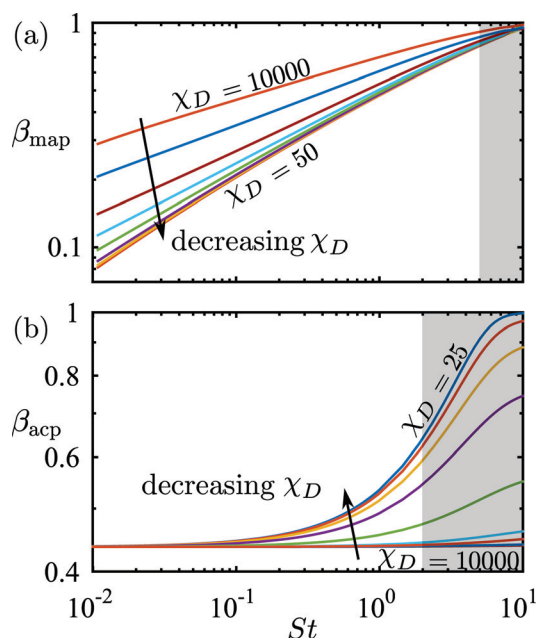


Fig. 9 Log-log plot of (a) the capture fraction β_{map} and (b) the focusing fraction β_{acp} , both as a function of the transient Strouhal number St in the dilute limit ($\chi_\mu = \chi_\eta = 1$ and $cF_{\text{mig}} = 0$) for $\chi_D = 25, 50, 100, 200, 500, 100, 2000, 5000$, and 10 000. Only simulations with St -values outside the gray areas have been included in the analysis of Fig. 4–7.

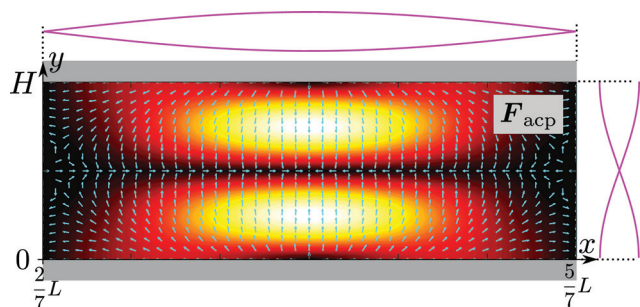


Fig. 10 The magnitude (heat color plot from zero [black] to maximum [white]) and the direction (vector plot) of the acoustophoretic force F_{acp} given in eqn (17a) and (17b).

Appendix B: The acoustophoretic force

The acoustophoretic force F_{acp} is found from the gradient of U_{ac} in eqn (12) using the acoustic fields p_1 and v_1 defined in eqn (13). In Fig. 10 is shown a combined color and vector plot of the resulting force F_{acp} given by the explicit expressions of its components $F_{\text{acp},x}$ and $F_{\text{acp},y}$,

$$F_{\text{acp},x} = \frac{4}{3} \pi a^3 E_{\text{ac}} k_x \sin(2\tilde{x}) \times \left[- \left(f_0 + \frac{3k_x^2}{2k^2} f_1 \right) \cos^2 \tilde{y} + \frac{3k_y^2}{2k^2} f_1 \sin^2 \tilde{y} \right], \quad (17a)$$

$$F_{\text{acp},y} = \frac{4}{3} \pi a^3 E_{\text{ac}} k_y \sin(2\tilde{y}) \times \left[+ \left(f_0 + \frac{3k_y^2}{2k^2} f_1 \right) \sin^2 \tilde{x} - \frac{3k_x^2}{2k^2} f_1 \cos^2 \tilde{y} \right]. \quad (17b)$$

Here, $\tilde{x} = k_x \left(x - \frac{2}{7} L \right)$ and $\tilde{y} = k_y y$ are dimensionless coordinates, and $k_x = 7\pi/(3L)$, $k_y = \pi/H$, and $k^2 = k_x^2 + k_y^2$ are wave numbers. For water-suspended polystyrene spheres with radius $a \geq 1 \mu\text{m}$, we have $f_0 = 0.444$ and $f_1 = 0.034$.³⁷ The acoustic energy density is set to $E_{\text{ac}} = 10^2 \text{ J m}^{-3}$.

Acknowledgements

We thank Kevin Cushing and Thomas Laurell for kindly providing us with the micrographs of Fig. 8(a) and (b). This work was supported by Lund University and the Knut and Alice Wallenberg Foundation (Grant No. KAW 2012.0023).

References

- 1 A. Lenshof, C. Magnusson and T. Laurell, *Lab Chip*, 2012, 12, 1210–1223, DOI: 10.1039/c2lc21256k.
- 2 H. Amini, W. Lee and D. Di Carlo, *Lab Chip*, 2014, 14, 2739–2761, DOI: 10.1039/C4LC00128A.
- 3 T. Z. Jubery, S. K. Srivastava and P. Dutta, *Electrophoresis*, 2014, 35, 691–713, DOI: 10.1039/C4LC01422G.
- 4 M. Hejazian, W. Li and N.-T. Nguyen, *Lab Chip*, 2015, 15, 959–970, DOI: 10.1155/2015/239362.
- 5 W. S. Low and W. A. B. W. Abas, *BioMed Res. Int.*, 2015, 2015, 239362, DOI: 10.1155/2015/239362.
- 6 O. Otto, P. Rosendahl, A. Mietke, S. Golfier, C. Herold, D. Klaue, S. Girardo, S. Pagliara, A. Ekpenyong, A. Jacobi, M. Wobus, N. Topfner, U. F. Keyser, J. Mansfeld, E. Fischer-Friedrich and J. Guck, *Nat. Methods*, 2015, 12, 199–202, DOI: 10.1038/nmeth.3281.
- 7 C. W. Shields, C. D. Reyes and G. P. López, *Lab Chip*, 2015, 15, 1230–1249, DOI: 10.1039/c4lc01246a.
- 8 D. A. Reasor, J. R. Clausen and C. K. Aidun, *Int. J. Numer. Methods Fluids*, 2012, 68, 767–781, DOI: 10.1002/fld.2534.
- 9 J. R. Clausen, D. A. Reasor and C. K. Aidun, *Comput. Phys. Commun.*, 2010, 181, 1013–1020, DOI: 10.1016/j.cpc.2010.02.005.
- 10 M. Mehrabadi, D. N. Ku and C. K. Aidun, *Ann. Biomed. Eng.*, 2015, 43, 1410–1421, DOI: 10.1007/s10439-014-1168-4.
- 11 P. Bagchi, *Biophys. J.*, 2007, 92, 1858–1877, DOI: 10.1529/biophysj.106.095042.
- 12 H. Lei, D. A. Fedosov, B. Caswell and G. E. Karniadakis, *J. Fluid Mech.*, 2013, 722, 214–239, DOI: 10.1017/jfm.2013.91.
- 13 M. Massoudi, J. Kim and J. F. Antaki, *Int. J. Nonlinear Mech.*, 2012, 47, 506–520, DOI: 10.1016/j.ijnonlinmec.2011.09.025.
- 14 J. Kim, J. F. Antaki and M. Massoudi, *J. Comput. Appl. Math.*, 2016, 292, 174–187, DOI: 10.1016/j.cam.2015.06.017.
- 15 M. Massoudi, *Int. J. Eng. Sci.*, 2010, 48, 1440–1461, DOI: 10.1016/j.ijengsci.2010.08.005.
- 16 J. Happel and H. Brenner, *Low Reynolds number hydrodynamics with special applications to particulate media*, Martinus Nijhoff Publishers, The Hague, 1983.
- 17 G. K. Batchelor, *J. Fluid Mech.*, 1972, 52, 245, DOI: 10.1017/S0022112072001399.
- 18 P. Mazur and W. Van Saarloos, *Phys. A*, 1982, 115, 21–57, DOI: 10.1016/0378-4371(82)90127-3.
- 19 A. J. C. Ladd, *J. Chem. Phys.*, 1988, 88, 5051–5063, DOI: 10.1063/1.454658.
- 20 A. J. C. Ladd, *J. Chem. Phys.*, 1989, 90, 1149–1157, DOI: 10.1063/1.456170.
- 21 A. J. C. Ladd, *J. Chem. Phys.*, 1990, 93, 3484–3494, DOI: 10.1063/1.458830.
- 22 B. Cetin, M. B. Ozer and M. E. Solmaz, *Biochem. Eng. J.*, 2014, 92, 63–82, DOI: 10.1016/j.bej.2014.07.013.
- 23 C. Mikkelsen and H. Bruus, *Lab Chip*, 2005, 5, 1293–1297, DOI: 10.1039/b507104f.
- 24 H. Bruus, J. Dual, J. Hawkes, M. Hill, T. Laurell, J. Nilsson, S. Radel, S. Sadhal and M. Wiklund, *Lab Chip*, 2011, 11, 3579–3580, DOI: 10.1039/c1lc90058g.
- 25 T. Laurell and A. Lenshof, *Microscale Acoustofluidics*, Royal Society of Chemistry, 2014.
- 26 P. Augustsson, R. Barnkob, S. T. Wereley, H. Bruus and T. Laurell, *Lab Chip*, 2011, 11, 4152–4164, DOI: 10.1039/c1lc20637k.
- 27 R. Barnkob, P. Augustsson, T. Laurell and H. Bruus, *Phys. Rev. E: Stat., Nonlinear, Soft Matter Phys.*, 2012, 86, 056307, DOI: 10.1103/PhysRevE.86.056307.

- 28 P. B. Muller, M. Rossi, A. G. Marin, R. Barnkob, P. Augustsson, T. Laurell, C. J. Kähler and H. Bruus, *Phys. Rev. E: Stat., Nonlinear, Soft Matter Phys.*, 2013, **88**, 023006, DOI: 10.1103/PhysRevE.88.023006.
- 29 J. K. G. Dhont, *An introduction to dynamics of colloids*, Elsevier, Amsterdam, 1996.
- 30 C. P. Nielsen and H. Bruus, *Phys. Rev. E: Stat., Nonlinear, Soft Matter Phys.*, 2014, **90**, 043020, DOI: 10.1103/PhysRevE.90.043020.
- 31 COMSOL Multiphysics 5.0, www.comsol.com, 2015.
- 32 R. Barnkob, P. Augustsson, T. Laurell and H. Bruus, *Lab Chip*, 2010, **10**, 563–570, DOI: 10.1039/b920376a.
- 33 M. Wiklund, *Lab Chip*, 2012, **12**, 2018–2028, DOI: 10.1039/c2lc40201g.
- 34 M. Nordin and T. Laurell, *Lab Chip*, 2012, **12**, 4610–4616, DOI: 10.1039/c2lc40201g.
- 35 M. Antfolk, P. B. Muller, P. Augustsson, H. Bruus and T. Laurell, *Lab Chip*, 2014, **14**, 2791–2799, DOI: 10.1039/c4lc00202d.
- 36 M. Settnes and H. Bruus, *Phys. Rev. E: Stat., Nonlinear, Soft Matter Phys.*, 2012, **85**, 016327, DOI: 10.1103/PhysRevE.85.016327.
- 37 P. B. Muller, R. Barnkob, M. J. H. Jensen and H. Bruus, *Lab Chip*, 2012, **12**, 4617–4627, DOI: 10.1039/C2LC40612H.

Appendix B

Paper accepted for publication in Physical Review Applied

Title: Three-Dimensional Numerical Modeling of Acoustic Trapping in Glass Capillaries

Authors: Mikkel W. H Ley and Henrik Bruus.

Reference: Paper in print, Physical Review Applied **8**, (2017), (15 pages), proof version attached.

Three-Dimensional Numerical Modeling of Acoustic Trapping in Glass Capillaries

Mikkel W. H. Ley* and Henrik Bruus†

Department of Physics, Technical University of Denmark,
DTU Physics Building 309, DK-2800 Kongens Lyngby, Denmark

(Received 13 April 2017)

Acoustic traps are used to capture and handle suspended microparticles and cells in microfluidic applications. A particular simple and much-used acoustic trap consists of a commercially available, millimeter-sized, liquid-filled straight glass capillary actuated by a piezoelectric transducer. Here, we present a three-dimensional numerical model of the acoustic pressure field in the liquid coupled to the displacement field of the glass wall, taking into account mixed standing and traveling waves as well as absorption. The model explains the dynamical mechanism that leads to the formation of localized acoustic resonance modes in such a straight acoustic waveguide without any geometrical cavities in the axial direction of the capillary. The model further predicts that some of these modes are well suited for acoustic trapping, and it provides estimates for their frequencies and quality factors, the magnitude of the acoustic radiation force on a single test particle as a function of position, and the resulting acoustic retention force of the trap. We show that the model predictions are in agreement with published experimental results, and we discuss how improved and more-stable acoustic-trapping modes might be obtained using the model as a design tool.

DOI:

I. INTRODUCTION

Microscale acoustofluidic devices are used increasingly in biology, the environmental and forensic sciences, and clinical diagnostics [1,2]. Examples include cell synchronization [3], the enrichment of prostate cancer cells in blood [4], the manipulation of *C. elegans* [5], and single-cell patterning [6]. Acoustics can also be used for noncontact microfluidic trapping and particle enrichment [7–9], as well as acoustic tweezing [10–14]. Trapping, an important unit operation in sophisticated cell- and bioparticle-handling systems, can also be obtained using other technologies, such as those in hydrodynamic [15], electro- and dielectrophoretic [16], and optical-trapping systems [17]; see the review by Nilsson *et al.* [18]. However, one of the key parameters for successful commercialization of these technologies is throughput, and here only the hydrodynamic and acoustic systems are competitive [19]. Hydrodynamic systems offer simple device designs and can support high flow rates, as they rely solely on passive transport from inertial migration and drag induced by secondary flows [15]. However, they do not have the capabilities of active transport.

By contrast, acoustofluidics does support active migration, basically due to the acoustic contrast between the suspending medium and the particles [20], and it is therefore an inherently label-free technique. Moreover, it exhibits high cell viability, even over several days [21]. These

aspects and other appealing traits have increased the interest in acoustofluidic systems in recent years [1,2].

A subclass of acoustofluidic devices is based on simple, cheap, and commercially available glass capillaries. Early studies from the 1990s include improving agglutination between erythrocytes [22], simple noncontact particle manipulation in a circular wave tube by acoustic streaming and radiation forces [23], and highly sensitive size-selective particle separation [24]. However, the ultrasound capillary system remains an active research topic, as cell-handling applications have become more numerous and refined over the years. Recent examples include cardiac myoblast viability in ultrasonic fields [25], sonoporation [26], the squeezing of red blood cells [27], and the trapping and retention of particles against an external flow [28].

In this paper, we study specifically a millimeter-sized glass-capillary system used as a versatile acoustic trap in many experimental studies [8,9,26,27,29] and clinical applications, such as the isolation of cell-secreted membrane vesicles [30] and the capture and enrichment of bacteria from blood samples for rapid sepsis diagnostics [31]. A sketch of a generic capillary system is shown in Fig. 1, while typical material parameters are listed in Table I. The capillary is typically actuated locally by a piezoelectric transducer, which is coupled to the capillary either by epoxy glue or by a small drop of glycerol, the latter allowing for the removal and the reuse of both the capillary and the transducer. The device is driven at a resonance frequency to obtain the largest possible acoustic field in the fluid. In the optimal case, the main component of the resonance field is a vertically standing bulk acoustic

*mley@fysik.dtu.dk

†bruus@fysik.dtu.dk

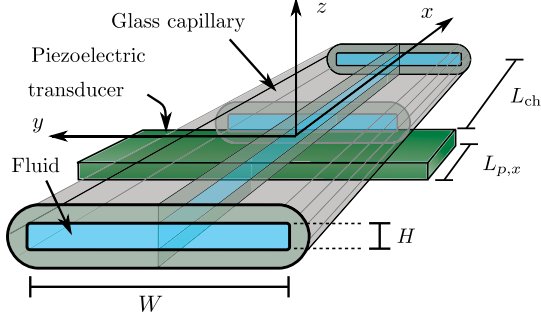


FIG. 1. A sketch of a generic capillary system for acoustic trapping. A millimeter-sized glass capillary (gray) filled with water (blue), is attached to a piezoelectric transducer (green) operated in the megahertz range. At certain frequencies, a resonant acoustic field builds up, in which case the acoustic radiation forces are strong enough to trap suspended microparticles in all spatial directions, and even to retain them against drag from an axial fluid flow through the capillary.

77 wave (SBAW) along the z direction, which unavoidably is
 78 mixed with a traveling bulk acoustic wave (TBAW) in the
 79 axial x direction along the capillary away from the
 80 transducer region.

81 **4** The resulting acoustic radiation forces trap particles
 82 above or near the transducer in all spatial directions and
 83 are often strong enough to retain a single microparticle
 84 against the drag from a fluid flow.

85 In contemporary acoustofluidics, it is a challenge to
 86 model and optimize the design of a given device. Examples
 87 of recent advances in modeling include Lei *et al.* [29], who

modeled the three-dimensional (3D) fluid domain without
 taking the solid domain into account; Muller and Bruus
 [32,39], who made detailed models in 2D of the thermo-
 viscous and transient effects in the fluid domain; Gralinski
et al. [28], who modeled circular capillaries in 3D with fluid
 and glass domains without taking absorption and outgoing
 waves into account; Hahn and Dual [33], who calculated the
 acoustic field in a 3D model for a glass-silicon device (not a
 capillary system) and characterized the various loss mech-
 anisms; and Garofalo *et al.* [40], who studied a coupled
 transducer-silicon-glass-water system in 2D.

In this work, we present a 3D numerical model of the
 capillary acoustic trap of Fig. 1. We model the acoustic
 pressure field in the liquid coupled to the displacement
 field of the glass wall, taking into account mixed standing
 and traveling waves as well as absorption. We model the
 outlets, which, in practice, are connected to long tubes,
 either as being free reflecting surfaces or perfect absorbers
 of outgoing acoustic waves. Our model explains the
 dynamical mechanism that leads to the formation of
 localized acoustic resonance modes in the straight capil-
 laries that are without geometrical cavities in the axial x
 direction. Furthermore, we compare prior experimental
 results from the four devices listed in Table II with
 predictions of our model, particularly the frequency
 response, the levitating resonance modes, and the
 acoustic-trapping forces. For one of the devices, we
 perform two convergence analyses to show to which degree
 numerical convergence is obtained. Lastly, we demonstrate
 how to apply the model as a design tool by studying the
 effects of narrowing the width of a given capillary.

TABLE I. Material parameters at 25°C and 4 MHz used in the numerical modeling of the capillary acoustic trap.

Parameter	Symbol	Value	Unit
Water [32]:			
Mass density	ρ_{fl}	997.05	kg m^{-3}
Compressibility	κ_{fl}	452	TPa^{-1}
Speed of sound	c_{fl}	1496.7	m s^{-1}
Dynamic viscosity	η_{fl}	0.890	mPa s
Damping coefficient [33]	Γ_{fl}	0.004	
Viscous boundary layer	δ	0.27	μm
Pyrex glass [34]:			
Mass density	ρ_{sl}	2230	kg m^{-3}
Young's modulus	E	62.75	GPa
Poisson's ratio	ν	0.2	
Speed of sound, longitudinal	c_{lo}	5592	m s^{-1}
Speed of sound, transverse	c_{tr}	3424	m s^{-1}
Damping coefficient [33]	Γ_{sl}	0.0004	
Polystyrene (ps) for 12-μm-diameter ps particles in water:			
Mass density [35]	ρ_{ps}	1050	kg m^{-3}
Compressibility [36]	κ_{ps}	249	TPa^{-1}
Poisson's ratio [37]	ν_{ps}	0.35	
Speed of sound at 20°C [38]	c_{ps}	2350	m s^{-1}
Monopole coefficient, Eq. (6b)	f_0	0.48	
Dipole coefficient, Eq. (6c)	f_1	0.052–0.003i	

II. THEORY AND NUMERICAL MODEL

We model single-frequency harmonic actuation at fre-
 quency f and angular frequency $\omega = 2\pi f$, such that any
 first-order acoustic field g in the complex-phase represen-
 tation has the time dependence $g(\mathbf{r}, t) = g(\mathbf{r})e^{-i\omega t}$.

Following the thorough analysis by Hahn and Dual [33],
 we introduce effective absorption in our equations by
 modifying the time derivative as $\partial_t \rightarrow -i\omega(1 + i\Gamma)$, where
 $\Gamma \ll 1$ is an effective absorption parameter, with values for
 the respective materials listed in Table I. The remaining
 details of the model are explained in the following
 subsections.

A. Governing equations

The dynamics of the solid (Pyrex) is modeled by the
 elastic displacement \mathbf{u} , the stress $\boldsymbol{\sigma}_{\text{sl}}$, the density ρ_{sl} , and the
 transverse and longitudinal speeds of sound, c_{tr} and c_{lo} ,

$$\nabla \cdot \boldsymbol{\sigma}_{\text{sl}} = -\rho_{\text{sl}}\omega^2(1 + i\Gamma_{\text{sl}})^2\mathbf{u}, \quad (1a)$$

$$\frac{1}{\rho_{\text{sl}}}\boldsymbol{\sigma}_{\text{sl}} = c_{\text{tr}}^2[\nabla\mathbf{u} + (\nabla\mathbf{u})^T] + (c_{\text{lo}}^2 - 2c_{\text{tr}}^2)(\nabla \cdot \mathbf{u})\mathbf{I}, \quad (1b)$$

TABLE II. Capillary geometries modeled in this work: C1 from Hammarström *et al.* [8], C2 from Lei *et al.* [29], C3 from Mishra *et al.* [27], C4 from Gralinski *et al.* [28], and C5 a capillary design proposed in this work. Besides the symbols defined in Fig. 2, R_{cu} is the radius of curvature of the fluid-channel corners, $f_{\text{res}}^{\text{exp}}$ and f_{res} is the experimental and numerical resonance frequencies, respectively, and Q is the numerically calculated quality factor.

Device	L [mm]	W [mm]	H [mm]	H_{gl} [mm]	R_{cu} [μm]	$L_{p,x}$ [mm]	$L_{p,y}$ [mm]	$f_{\text{res}}^{\text{exp}}$ [MHz]	f_{res} [MHz]	Q	d_0 [nm]
C1	2.0	2.0	0.20	0.14	25	1.16	2.0	3.970	3.906	53	0.10
C2	2.0	6.0	0.30	0.30	25	1.0	1.0	2.585	2.495	78	0.10
C3	8.5	0.1	0.10	0.05	19	15	1.0	7.900	6.406	222	0.10
C4	10.0	0.85	0.85	0.225	425	4.0	1.0	1.055	0.981	109	0.10
C5	2.0	0.5	0.20	0.14	25	1.16	0.50	...	4.201	53	0.10

$$c_{\text{tr}}^2 = \frac{1}{2(1+\nu)} \frac{E}{\rho_{\text{sl}}}, \quad c_{\text{lo}}^2 = 2c_{\text{tr}}^2 \frac{1-\nu}{1-2\nu}. \quad (1c)$$

Here, \mathbf{I} is the unit tensor, E is Young's modulus, and ν is Poisson's ratio. The fluid (water) with its acoustic pressure p , velocity \mathbf{v} , density ρ_{fl} , and sound speed c_{fl} is modeled as pressure acoustics with absorption [33],

$$\nabla^2 p = -\frac{\omega^2}{c_{\text{fl}}^2} (1 + i\Gamma_{\text{fl}})^2 p, \quad (2a)$$

$$\mathbf{v} = \frac{-i}{\omega\rho_{\text{fl}}} \nabla p. \quad (2b)$$

B. Boundary conditions

The applied boundary conditions are summarized in Table III and Fig. 2. Because the y - z and x - z planes are mirror planes, we model only a quarter of the system, and symmetry conditions are applied on the two symmetry planes. The stress is zero on all outer boundaries facing the air, and the stress and the velocity fields are continuous across all internal boundaries.

The model of the piezoelectric actuation on the interface $\partial\Omega_{\text{pz}}$ is not straightforward, as neither the excited modes of the piezoelectric transducer nor the coupling layer by which the transducer is attached to the glass capillary have been characterized experimentally in the published studies. We therefore choose to explore the effects of two idealized generic actuation conditions that mimic a simple uniform contraction-expansion mode that pushes and pulls on the

glass-capillary surface through a coupling layer consisting of either a rigid epoxy glue or a fluid glycerol film. From previous work [36], we know that a wall displacement amplitude $d_0 = 0.1$ nm leads to realistic values for experimentally measured pressures [41–43], so we use this value throughout this work. To mimic the rigid epoxy glue, we assume a simple uniform displacement amplitude $u_z = d_0$ in the z direction without transverse motion, Eq. (3a), while, to mimic the fluid glycerol layer with a typical thickness of 10–100 μm that can easily accommodate nanometer-sized fluctuations as well as transverse displacement, we assume that only the area average $\langle u_z \rangle_{\text{pz}}$ of the normal displacement u_z is d_0 , while the shear stress is zero, Eq. (3b),

$$u_z = d_0, \quad u_x = u_y = 0, \quad \text{rigid displacement}, \quad (3a)$$

$$\langle u_z \rangle_{\text{pz}} = d_0, \quad \sigma_{xz} = \sigma_{yz} = 0, \quad \text{average displacement}. \quad (3b)$$

TABLE III. Boundary conditions imposed on the solid and fluid domains in the model shown in Fig. 2.

Domain \leftarrow boundary	Boundary condition
Solid domain \leftarrow air	$\boldsymbol{\sigma}_{\text{sl}} \cdot \mathbf{n} = \mathbf{0}$
Solid domain \leftarrow fluid	$\boldsymbol{\sigma}_{\text{sl}} \cdot \mathbf{n} = -p\mathbf{n}$
Solid domain \leftarrow transducer	Eq. (3a) or Eq. (3b)
Solid domain \leftarrow symmetry	$\mathbf{u} \cdot \mathbf{n} = 0, \mathbf{t} \cdot \boldsymbol{\sigma}_{\text{sl}} \cdot \mathbf{n} = \mathbf{0}$
Fluid domain \leftarrow solid	$\mathbf{v} \cdot \mathbf{n} = -i\omega\mathbf{u} \cdot \mathbf{n}$
Fluid domain \leftarrow air	$p = 0$
Fluid domain \leftarrow symmetry	$\mathbf{n} \cdot \nabla p = 0$

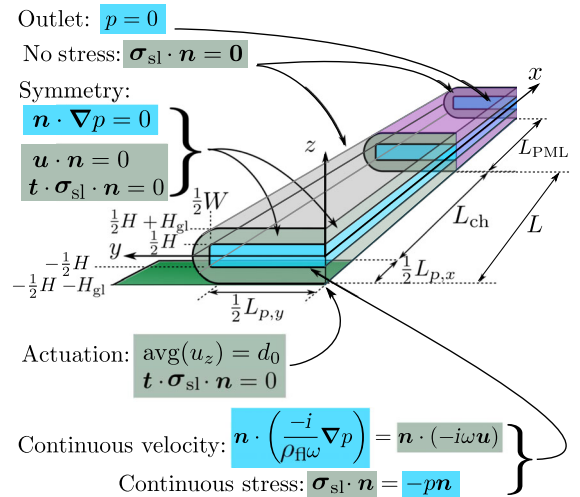


FIG. 2. The computational domain used in the numerical model of Fig. 1 reduced to the quadrant $x > 0$ and $y > 0$ due to symmetry. Shown are the solid wall (gray), the water channel (blue), the actuation plane (green), the perfectly matched layer (PML, purple), and arrows allocating the boundary conditions to their respective boundaries.

C. The outlet and perfectly matched layers

In most setups, the capillary is connected to the micro-fluidic circuit through tubings at the ends. If a large section of the capillary is inserted into a connecting elastic tube [29], this might cause significant absorption. Furthermore, the water domain continues uninterrupted from the capillary into the connecting tube, so an extreme case is that none of the acoustic waves going out from the actuation region are reflected at the ends of the capillary. We model this situation using a perfectly matched layer (PML), which is a domain acting as an artificial perfect absorber of all outgoing TBAWs along the x axis. In our model, the region $x < L$ is normal, while the PML of length L_{PML} is at $L < x < L + L_{\text{PML}}$; see Fig. 2. Following Collino and Monk [44], ideal absorption along the x direction for $x > L$ can be obtained by a complex-valued coordinate stretching of x in the PML domain. This stretching is based on a real-valued function $s(x)$, which is zero in the normal region $x < L$ and increases smoothly from zero in the PML as

$$s(x) = k_{\text{PML}} \left(\frac{x - L}{L_{\text{PML}}} \right)^2, \quad \text{for } L \leq x \leq L + L_{\text{PML}}, \quad (4a)$$

where $k_{\text{PML}} > 0$ is the absorption strength. The coordinate stretching is implemented in the model by changing all occurrences of ∂_x and the integral measure dx as

$$\partial_x \rightarrow \partial_{\tilde{x}} = \frac{1}{1 + is(x)} \partial_x, \quad (4b)$$

$$dx \rightarrow d\tilde{x} = [1 + is(x)]dx, \quad (4c)$$

where the latter appears in the weak-form implementation of the governing equations and boundary conditions; see Sec. II E. The values of L_{PML} and k_{PML} are also discussed in Sec. II E. The coordinate stretching in the PML introduces a positive imaginary part in the wave numbers in the x direction, and it thus dampens the outgoing waves exponentially along the x axis.

The opposite limit of zero absorption is handled by dropping the PML and imposing the no-stress condition at $x = L$.

D. Acoustic energy density and radiation force

Good acoustic trapping in a capillary requires a high acoustic energy density $E_{\text{ac}}^{\text{fl}}$ in the fluid [45] and $E_{\text{ac}}^{\text{sl}}$ in the solid [46], both given by the sum of the space- and time-averaged kinetic and potential energy density, in the respective volumes $V_{\text{act}}^{\text{fl}}$ and $V_{\text{act}}^{\text{sl}}$ above the transducer,

$$E_{\text{ac}}^{\text{fl}} = \int_{V_{\text{act}}^{\text{fl}}} \left(\frac{1}{2} \rho_{\text{fl}} \langle v^2 \rangle + \frac{1}{2} \kappa_{\text{fl}} \langle p^2 \rangle \right) \frac{dV}{V_{\text{act}}^{\text{fl}}}, \quad (5a)$$

$$E_{\text{ac}}^{\text{sl}} = \int_{V_{\text{act}}^{\text{sl}}} \left\{ \frac{1}{2} \rho_{\text{sl}} \omega^2 \langle u^2 \rangle + \frac{1}{4} \langle \boldsymbol{\sigma}_{\text{sl}} : [\nabla \mathbf{u} + (\nabla \mathbf{u})^T] \rangle \right\} \frac{dV}{V_{\text{act}}^{\text{sl}}}, \quad (5b)$$

where each set of angled brackets denotes the time average over one acoustic oscillation period.

The trapping force acting on an elastic particle of radius a_{pa} , density ρ_{pa} , and compressibility κ_{pa} suspended in the fluid is the acoustic radiation force \mathbf{F}^{rad} , which, for mixed standing and traveling waves, is given by [47]

$$\mathbf{F}^{\text{rad}} = -\frac{4}{3} \pi a_{\text{pa}}^3 \left[\kappa_{\text{fl}} \langle (f_0 p) \nabla p \rangle - \frac{3}{2} \rho_{\text{fl}} \langle (f_1 \mathbf{v}) \cdot \nabla \mathbf{v} \rangle \right], \quad (6a)$$

where the monopole and dipole scattering coefficients f_0 and f_1 , respectively, are

$$f_0 = 1 - \frac{\kappa_{\text{pa}}}{\kappa_{\text{fl}}}, \quad (6b)$$

$$f_1 = \frac{2(1-\gamma)(\frac{\rho_{\text{pa}}}{\rho_{\text{fl}}} - 1)}{2\frac{\rho_{\text{pa}}}{\rho_{\text{fl}}} + 1 - 3\gamma}, \quad \gamma = -\frac{3}{2} [1 + i(1 + \tilde{\delta})] \tilde{\delta}, \quad (6c)$$

with $\tilde{\delta} = [1/(a_{\text{pa}})] \sqrt{[(2\eta_{\text{fl}})/\omega\rho_{\text{fl}}]}$ being the viscous boundary-layer thickness normalized by the particle radius a_{pa} .

E. Numerical implementation in weak form

Following Gregersen *et al.* [48], we implement the governing equations and boundary conditions in the weak-form partial-differential-equation module of the finite-element software COMSOL MULTIPHYSICS 5.2 [49]. We use Lagrangian test functions of second order for p , u_x , u_y , and u_z , and we solve for given geometry, materials, actuation frequency ω , and actuation displacement d_0 .

We test the PML for capillary C1 as follows; see Fig. 3. The length L_{PML} of the PML is comparable to the longest wavelength of the system [50], here the longitudinal wavelength $\lambda_{\text{lo}} = 2\pi c_{\text{lo}}/\omega = 1.4$ mm in Pyrex at 4 MHz. By running parametric sweeps in $L_{\text{PML}} \approx \lambda_{\text{lo}}$ and $k_{\text{PML}} > 0$, we find that, for an L_{PML} as short as $0.25\lambda_{\text{lo}}$, the results are independent of the PML strength in the range $10 < k_{\text{PML}} < 10^4$, showing that for this broad parameter range, the outgoing waves are absorbed before reaching the PML back edge at $x = L + L_{\text{PML}}$, and without traces of backscattering from the PML front edge at $x = L$. To further show the independence of the results on the PML, we set $L_{\text{PML}} = 0.25\lambda_{\text{lo}}$ and $k_{\text{PML}} = 10^3$, and we vary the length L_{ch} of the capillary between the piezoelectric transducer and the PML front edge. In Fig. 3, p and u_z are plotted versus x for four fixed (y, z) coordinates, and it is seen that, for $L_{\text{ch}} \gtrsim \lambda_{\text{lo}}$, the resulting fields coincide everywhere outside the PML domain. For smaller values $L_{\text{ch}} \lesssim \lambda_{\text{lo}}$, we do observe deviations in the response, indicating that the outgoing waves are not fully established before they enter the PML and are absorbed. Consequently, in the following, we choose the fixed parameter values $L_{\text{ch}} = 1$ mm, $L_{\text{PML}} = 0.25\lambda_{\text{lo}} = 0.35$ mm, and $k_{\text{PML}} = 10^3$.

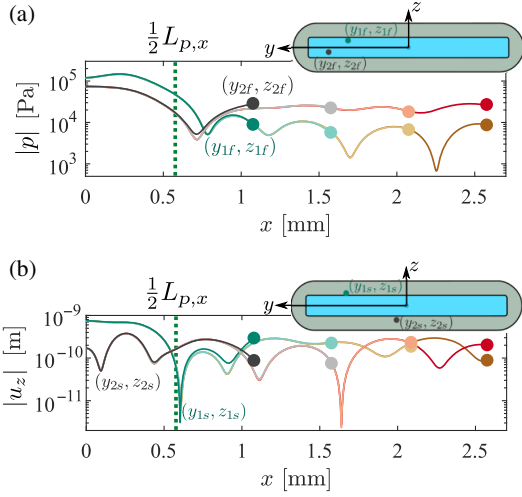


FIG. 3. The acoustic field in capillary C1 as a function of the front-edge position $L = \frac{1}{2}L_{p,x} + L_{ch}$ of the PML domain with fixed $L_{PML} = 0.25\lambda_L$ and $k_{PML} = 10^3$. (a) The pressure amplitude $|p|$ versus x (the colored lines) terminating at L (the colored points) for the two (y, z) positions $(y_{1f}, z_{1f}) = (0.3W, 0.35H)$ and $(y_{2f}, z_{2f}) = (0.4W, -0.25H)$ (the green and black points in the inset). The line colors correspond to $L_{ch} = 0.5, 1.0, 1.5$, and 2.0 mm from green (black) to brown (red). The vertical green dotted line at $x = \frac{1}{2}L_{p,x}$ marks the edge of the actuation region. (b) Similar plot for the vertical displacement amplitude $|u_z|$, but here for the two (y, z) positions $(y_{1s}, z_{1s}) = (0.3W, 0.6H)$, and $(y_{2s}, z_{2s}) = (0.05W, -0.7H)$.

The mesh is generated by first defining a mesh in the y - z plane [see Fig. 4(a)] and then extruding it equidistantly along the x axis using the “swept-mesh” function in COMSOL MULTIPHYSICS; see Fig. 4(b). The size of the mesh elements is controlled by the maximum mesh size d_{mesh} , except for elements on the z axis (the intersection of the two symmetry planes) and on the corner edges of the fluid channel (where the curvature is large), both of which are assigned a smaller maximum mesh size. All mesh sizes used in the model are listed in Table IV. Unless stated otherwise, we have set $d_{\text{mesh}} = H/7$.

For a given field variable g , we perform a mesh-convergence test based on the convergence parameter $C(g)$, which is defined in Ref. [36] as

$$C(g) = \sqrt{\frac{\int_{\Omega} dV |g - g_{\text{ref}}|^2}{\int_{\Omega} dV |g_{\text{ref}}|^2}}, \quad \text{for } 0 \leq x \leq L. \quad (7)$$

Here, the integration volume Ω is the domain in which g is defined but excludes the PML domain. The field g is calculated with the abovementioned characteristic mesh size d_{mesh} , and g_{ref} is the reference field calculated with the finer mesh $d_{\text{mesh}}^{\text{ref}} = 0.9d_{\text{mesh}}$. We cannot use a smaller value of $d_{\text{mesh}}^{\text{ref}}$ because this value, combined with the length $L = 2.5$ mm, results in a memory consumption of 85 gigabytes of RAM out of the 128 gigabytes available on

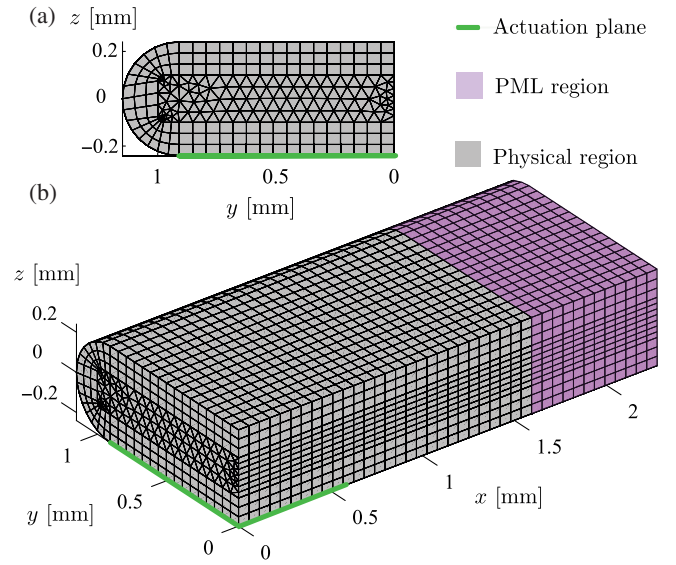


FIG. 4. A coarse version of the mesh at the surface of the computational domain of Fig. 2 for a mesh size of $d_{\text{mesh}} = 57.2 \mu\text{m}$, which is twice the value used in most calculations; see Table IV. (a) The 2D mesh in the y - z plane consisting of a structured mesh in the solid, a free triangular mesh in the fluid, and a refined mesh at the corners of the fluid domain as well as at the vertical symmetry line $y = 0$. (b) The full 3D mesh generated by extruding the 2D mesh shown in (a) along the x direction with equidistant spacing.

our workstation; see Sec. III. With these values, our simulation involves 2×10^6 degrees of freedom and a computation time of around 15 min per parameter set. In Fig. 5, semilog plots of C versus $d_{\text{mesh}}^{\text{ref}}/d_{\text{mesh}}$ for all four fields are shown. The plots exhibit an exponential decrease of C , which indicates good numerical mesh convergence. For the chosen mesh sizes, we obtain $C \approx 0.002$, which is an acceptable level for the present study.

Finally, the area-averaged actuation condition (3b) is imposed on the displacement field u_z on the actuation interface using an envelope function $F(x)$,

TABLE IV. List of the mesh parameters used in the model. The maximum mesh element size is set to $d_{\text{mesh}} = H/7$, with three exceptions: (1) for the reference field g_{ref} of C1 in Eq. (7) and Fig. 5, where $d_{\text{mesh}}^{\text{ref}} = 0.9d_{\text{mesh}}$, (2) for Fig. 6, where $d_{\text{mesh}} = 40.0 \mu\text{m}$, and (3) for C4, where $d_{\text{mesh}} = H/20$.

Location	Linear size	No. of elements	Mesh size
<i>y</i> - <i>z</i> plane:			
Bulk fluid	H	7	d_{mesh}
Bulk solid	H_{gl}	6	d_{mesh}
Corner solid fluid	$\frac{1}{2}\pi R_{\text{cu}}$	10	$0.168 d_{\text{mesh}}$
Fluid symmetry edge	H	15	$0.5d_{\text{mesh}}$
<i>x</i> direction (extruded):			
Bulk fluid	$L + L_{\text{PML}}$	80	d_{mesh}
Bulk solid	$L + L_{\text{PML}}$	80	d_{mesh}

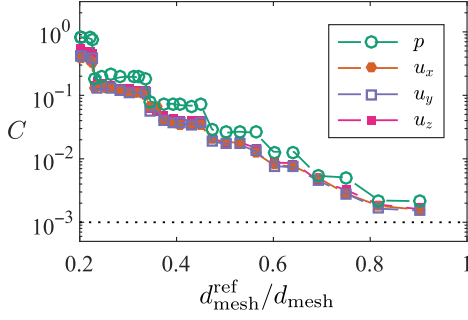


FIG. 5. Semilog plot of the convergence parameter C defined in Eq. (7) versus $d_{\text{mesh}}^{\text{ref}}/d_{\text{mesh}}$, the inverse of the maximum mesh size. The mesh parameter values are listed in Table IV.

$$\int_0^{L_{p,x}/2} \frac{2dx}{L_{p,x}} \int_0^{L_{p,y}/2} \frac{2dy}{L_{p,y}} (u_z - d_0) F(x) = 0, \quad (8a)$$

$$\text{with } F(x) = -\tanh\left(\frac{x - \frac{1}{2}L_p}{\Delta L_p}\right), \quad (8b)$$

where the transition length is set to $\Delta L_p = 100 \mu\text{m}$.

III. RESULTS

We characterize numerically the four different glass capillaries C1, C2, C3, and C4 listed in Table II, for which we find experimental results in the literature: C1 from Hammarström *et al.* [8] (also employed in Refs. [7,9]), C2 from Lei *et al.* [29], C3 from Mishra *et al.* [27], and C4 from Gralinski *et al.* [28]. We also characterize a low-aspect-ratio version of C1 denoted C5. We simulate the acoustic fields for these five capillary systems, each with the two different actuation boundary conditions (3b) and (3a), and each both with and without the absorbing PML region. Supplementally to these studies, we simulate geometrical variations to study the effects of the capillaries' manufacturing tolerances and the length-dependent reflections from the capillary end. Consequently, we study more than 20 different capillary configurations, each swept in frequency using 50 values or more, resulting in over 1000 simulations, all of which show good numerical convergence without spurious effects. We remark that a simulation of a given frequency and geometry takes between 2 and 15 min on our workstation, a Dell Inc Precision T3610 Intel Xeon CPU E5-1650 v2 at 3.50 GHz with 128 gigabytes of RAM and 6 CPU cores. To gain an overall understanding of these systems, we focus in the following subsections on different acoustofluidic aspects for each capillary.

A. Analysis of capillary C1

For capillary C1 [8], we mimic the experimental use of glycerol to attach the transducer by applying the area-averaged condition (3b) for the actuation. Moreover, to avoid the complications arising from reflections at the end

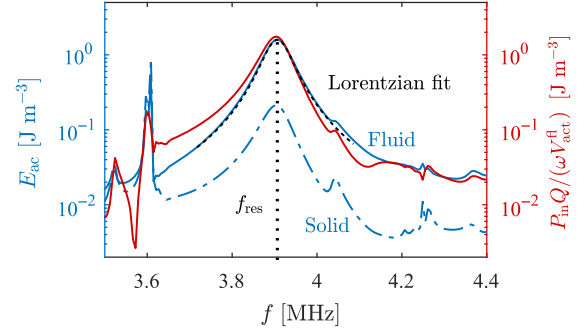


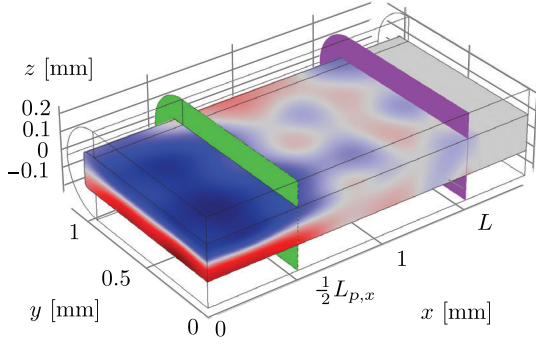
FIG. 6. Semilog plot of simulation results for capillary C1 of the acoustic energy density E_{ac} (the left axis) in the fluid (the blue solid line) and in the solid (the blue dashed line) above the transducer, and the normalized power input $QP_{\text{in}}/(\omega V_{\text{act}}^{\text{fl}})$ (the red line, right axis) from the transducer as a function of the frequency f . E_{ac} is fitted well by a Lorentzian peak (the black dashed line) having a resonance frequency $f_{\text{res}} = 3.906 \text{ MHz}$, a full-width-half-maximum linewidth of $\Delta f = 0.7369 \text{ MHz}$, a quality factor of $Q = 53.0$, and a maximum of $E_{\text{ac}} = 1.60 \text{ J/m}^3$.

of the capillary, we first assume perfect absorption of outgoing waves and thus use the PML.

First, we study the frequency response. In Fig. 6, we show a semilog plot of the volume-averaged acoustic energy density in the fluid volume above the transducer ($0 < x < \frac{1}{2}L_{p,x}$), $E_{\text{ac}}^{\text{fl}}$ for the fluid volume $V_{\text{act}}^{\text{fl}}$, and $E_{\text{ac}}^{\text{sl}}$ for the solid volume $V_{\text{act}}^{\text{sl}}$, as a function of the actuation frequency f . A levitating resonance, strongly dominated by the energy density in the fluid, is identified at $f_{\text{res}} = 3.906 \text{ MHz}$, only 2% lower than the experimental value $f_{\text{res}}^{\text{exp}} = 3.970 \text{ MHz}$ and 4% from the simple half-wave value $c_{\text{fl}}/(2H) = 3.74 \text{ MHz}$. The resonance peak is fitted well by a Lorentzian line shape centered around $f_{\text{res}} = 3.906 \text{ MHz}$ with a quality factor $Q = 53.0$.

We successfully verify that this Q factor is consistent with the relation $E_{\text{ac}}^{\text{tot}} = QP_{\text{in}}/(\omega V_{\text{act}}^{\text{fl}})$, where $P_{\text{in}} = \int_{A_{\text{act}}} \langle (-i\omega \mathbf{u}) \cdot \boldsymbol{\sigma}_{\text{sl}} \cdot \mathbf{n} \rangle da$ is the time-averaged power delivered by the transducer, and $E_{\text{ac}}^{\text{tot}} = E_{\text{ac}}^{\text{fl}} + E_{\text{ac}}^{\text{sl}}$ is the total stored acoustic energy density. Here, we exploit that in a steady state, the input power equals the dissipated power. Besides the main levitating resonance peak, minor resonances without specific structure are also present, reflecting the many complex modes in the coupled fluid-solid system. None of these resonances have particularly good trapping properties, and they would probably not be observed in acoustophoretic experiments.

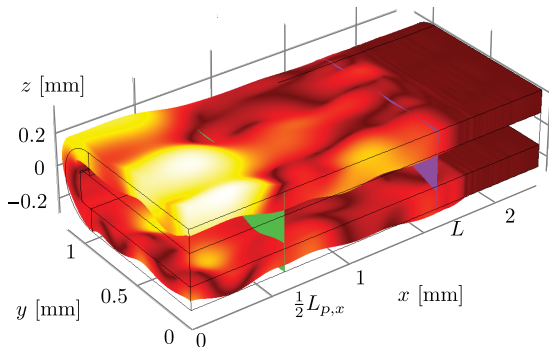
Next, we study the acoustic field. Upon inspection of the pressure and displacement fields at the resonance f_{res} , we find them to be mainly a standing wave above the actuation plane combined with an outgoing traveling wave away from the transducer region for $x > \frac{1}{2}L_{p,x}$; see Videos 1 and 2. An animated Graphics Interchange Format (GIF) version of each video in the paper can be found in the Supplemental Material [51]. The amplitude of the acoustic



F1:1 **VIDEO. 1.** Color plot of the pressure field p in the fluid from
 F1:2 -0.18 MPa (blue) to 0.18 MPa (red) of capillary C1 at the
 F1:3 levitating half-wave resonance $f_{\text{res}} = 3.906$ MHz. The green and
 F1:4 purple planes represent the end of the actuation region and the
 F1:5 beginning of the PML domain, respectively.

368 fields p and u are largest above the transducer. The fluid
 369 pressure p is a nearly perfect vertical half wave with a
 370 horizontal nodal plane near the channel center, which
 371 enables microparticle levitation given its maximum of
 372 0.19 MPa for an actuation amplitude $d_0 = 0.1$ nm.
 373 Because of this feature, we refer to this type of resonance
 374 as levitating half-wave resonance in the following. At the
 375 edge of the transducer, the pressure amplitude drops an
 376 order of magnitude, which, according to Eq. (6a), gives rise
 377 to the lateral forces that constitute the acoustic trap.

378 For the displacement field in the solid, we find its
 379 maximum value to be 1.2 nm, which is an order of
 380 magnitude larger than the average actuation amplitude
 381 $d_0 = 0.1$ nm. Besides the outgoing displacement waves
 382 leaving the capillary in the axial x direction, we also note
 383 the presence of circumferential displacement waves with
 384 short wavelengths around $\frac{1}{4}W$. The glycerol-like, area-
 385 averaged actuation (3b) allows for fluctuations because
 386 it fixes only the mean vertical displacement u_z . At the
 387 resonance f_{res} , we find $u_z = (1.0 \pm 2.8)d_0$ on the actuation
 388 plane. We note that the standard deviation $2.8d_0 = 0.28$ nm

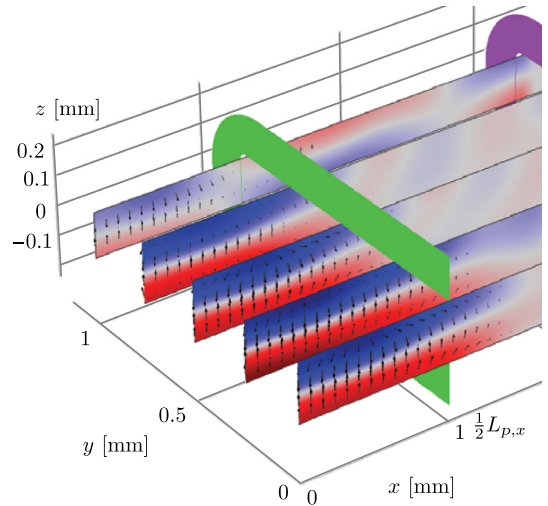


F2:1 **VIDEO. 2.** The displacement field u in the solid (not drawn to
 F2:2 scale) overlaid with a color plot of its magnitude u from 0 nm
 F2:3 (dark red) to 1.2 nm (white) for capillary C1 at the levitating
 F2:4 resonance $f_{\text{res}} = 3.906$ MHz, as in Video 1.

is very small compared to a typical coupling-layer thickness
 of around 0.1 mm.

Despite the absence of a geometrical cavity along the
 capillary, we nevertheless find that a localized SBAW can
 exist in the region above the transducer. This SBAW is
 supported by a dynamically defined cavity that arises at
 resonance because the displacement of the confining glass
 walls becomes an order of magnitude larger in the actuation
 region than elsewhere. Because of its dynamic nature, the
 cavity is leaky: The waves in the axial direction away from
 the actuator region are not evanescent, but they appear as
 TBAWs. The presence of the TBAWs reduces the Q value
 of the resonance state from previously reported values of
 200 – 500 [41] to approximately 50 , a value that, however,
 is large enough to ensure a well-defined resonance. While
 combinations of standing and traveling waves have been
 studied for surface-acoustic-wave systems [52–55], it is
 remarkable that they appear here in a study of bulk-
 acoustic-wave (BAW) systems.

To characterize the trapping capabilities of the device,
 we study the radiation force \mathbf{F}^{rad} , Eq. (6a), acting on a
 12 - μm -diameter polystyrene (ps) test particle suspended in
 the fluid above the transducer. The z component F_z^{rad} of
 \mathbf{F}^{rad} , derived from the nearly perfect standing half wave in
 the vertical direction, levitates the test particle and holds it
 close to the pressure nodal plane. In the actuation region,
 this plane is nearly horizontal, with a vertical position
 between $-0.1H$ and 0 . Away from the actuation region, it
 gradually changes its vertical position and fades away, see
 Video 3. The maximum levitating force on the test particle



F3:1 **VIDEO. 3.** Capillary C1, color plot of the pressure field p from
 F3:2 -0.18 MPa (blue) to 0.18 MPa (red) in vertical planes placed
 F3:3 equidistantly in steps of $\frac{1}{8}W$ starting at $y = 0$, showing the nearly
 F3:4 horizontal nodal plane (gray) wobbling around $z = -0.05H$ at
 F3:5 resonance $f_{\text{res}} = 3.906$ MHz. The acoustic radiation force \mathbf{F}^{rad}
 F3:6 on 12 - μm -diameter polystyrene test particles (black arrows with
 F3:7 logarithmic lengths are used for visual clarity) has a maximum
 F3:8 magnitude of 22 pN.

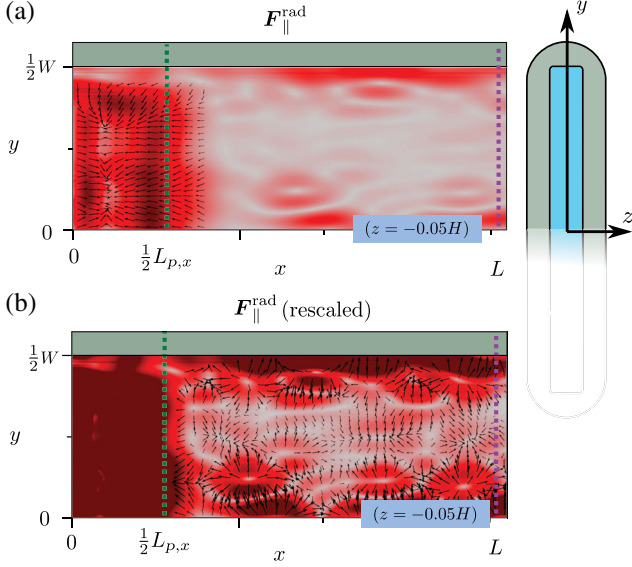


FIG. 7. Capillary C1. (a) The lateral acoustic radiation force $F_{\parallel}^{\text{rad}}$ (the black arrows with logarithmic length) and its magnitude [the color plot from 0 pN (gray) to 0.44 pN (dark red)] acting on 12- μ m-diameter polystyrene beads in the x - y plane at $z = -0.05H$ at resonance $f_{\text{res}} = 3.906$ MHz. (Inset) Cross-section geometry with $W = 2$ mm. (b) Same as (a), but with its maximum color (dark red) decreased to 0.10 pN to emphasize the secondary trapping points.

is $F_z^{\text{rad}} = 22$ pN, which is nearly 50 times larger than the buoyancy-corrected gravitational force $F^{\text{grv}} = 0.44$ pN.

The lateral trapping force $F_{\parallel}^{\text{rad}}$ is given by the x and y components F_x^{rad} and F_y^{rad} of Eq. (6a), and it acts as a retention force when a fluid flow is imposed. In Fig. 7(a) for the C1 capillary at resonance f_{res} , $F_{\parallel}^{\text{rad}}$ is plotted in the plane $z = -0.05H$ (the vector plot) together with its magnitude $F_{\parallel}^{\text{rad}}$ (the color plot). We see two clear trapping points within the actuation region, which are surrounded by strong gradients in the x and y directions, thus enabling lateral particle trapping. The maximum value F_x^{rad} within the actuation region is of particular interest because it serves as a measure for the overall trapping strength of the device. We find $F_x^{\text{rad}} = 0.44$ pN at the position $(x, y, z) = (0.3L_{p,x}, 0, -0.05H)$. Outside the actuation region, a number of weaker, secondary trapping points are observed, as shown in Fig. 7(b). Their presence is emphasized by rescaling the color range, and we note that their positions appear to be random. This finding is in qualitative agreement with experimental observations under flow conditions [56].

We also verify the capability of the device to trap particles by simulating the trajectories of test particles initially placed on a regular grid throughout the trapping region and ending up in the trapping points (not shown).

Finally, we comment on the calibration of the acoustic energy density $E_{\text{ac}}^{\text{fl}}$ in the fluid, which controls the magnitude of the trapping force in the capillary device. Because,

in practice, it is not possible to calculate $E_{\text{ac}}^{\text{fl}}$ in a capillary device for a known ac voltage applied to the piezoelectric transducer, it is important to measure it in any given experiment. The first method is the drop-voltage method [29], where, at first, $E_{\text{ac}}^{\text{fl}}$ is set high enough to levitate a test particle. Then the ac voltage, and thus $E_{\text{ac}}^{\text{fl}}$, is lowered until the particle drops out of the trap, at which point $F_z^{\text{rad}}(E_{\text{ac}}^{\text{fl}}) = \frac{4}{3}\pi a^3(\rho_{\text{pa}} - \rho_{\text{fl}})g$ and $E_{\text{ac}}^{\text{fl}}$ can be found.

The second method is to increase the flow rate, and thus the flow speed v_{flow} , through the device until it reaches critical magnitude, where the maximum lateral retention force $F_{\parallel \text{max}}^{\text{rad}}$ cannot balance the Stokes drag force on the particle any longer. From a scaling argument, and introducing a coefficient α dependent on the device composition and geometry, we can write

$$F_{\parallel \text{max}}^{\text{rad}} = \alpha \frac{4\pi}{3} a^3 E_{\text{ac}}^{\text{fl}} \frac{\omega}{c_{\text{fl}}}, \quad \alpha = 0.0139, \quad (9)$$

where the value for α is found by simulating the C1 capillary. The flow speed at which the Stokes drag exactly balances $F_{\parallel \text{max}}^{\text{rad}}$ is denoted $v_{\text{max}}^{\text{flow}}$, so we can write

$$F_{\parallel \text{max}}^{\text{rad}} = 6\pi\eta_{\text{fl}}\alpha\chi v_{\text{max}}^{\text{flow}}, \quad \chi = \chi_{\text{paral}}^{z=0} = 1.064, \quad (10)$$

where χ is the wall-induced drag enhancement in the center plane of a parallel-plate channel [57], and the value is for the C1 capillary and the given test particle. Approximating the fluid channel to be rectangular, the maximum flow velocity can be related to the maximum flow rate $Q_{\text{max}}^{\text{flow}}$ as $v_{\text{max}}^{\text{flow}} = [\beta/(HW)]Q_{\text{max}}^{\text{flow}}$, where β is an aspect-ratio-dependent constant [58], which, for C1, is $\beta = 1.74$. Combining Eqs. (9) and (10) leads us to

$$E_{\text{ac}}^{\text{fl}} = \frac{9\beta\chi\eta_{\text{fl}}c_{\text{fl}}Q_{\text{max}}^{\text{flow}}}{2\alpha\omega a^2 HW}. \quad (11)$$

With the assumed actuation amplitude $d_0 = 0.1$ nm, we find the maximum acoustic energy density to be 1.60 J/m³, which yields the maximum flow speed and rate of $v_{\text{max}}^{\text{flow}} = 3.1$ μ m/s and $Q_{\text{max}}^{\text{flow}} = 0.043$ μ l/min. We emphasize that this calibration method works only if the in-plane streaming velocity is smaller than the flow velocity.

B. Analysis of capillary C2

In the experiment, capillary C2 is held in place by two rubber sleeves [29], which may justify a generic study using the absorbing PML region. Capillary C2 differs from capillary C1 by being more flat, having a cross-section aspect ratio of 1:20, in contrast to 1:10 for the latter [8]. A more significant difference is that the transducer of C2 is attached by glue and not by glycerol, as with C1. Therefore, we study the differing responses arising from using these two actuation conditions.

Using the glycerol-like area-averaged actuation condition (3b), a strong levitating half-wave resonance resembling the one in C1 and having a quality factor $Q = 78$, is found at $f_{\text{res}}^{\text{avg}} = 2.495$ MHz, equal to the simple half-wave value $c_{\text{fl}}/(2H)$. The maximum levitating force is $F_z^{\text{rad}} = 18$ pN.

Turning to the gluelike rigid actuation condition (3a), the resonance frequency drops slightly to $f_{\text{res}}^{\text{rd}} = 2.345$ MHz, fairly close to the experimentally observed resonance at 2.585 MHz, while the quality factor decreases to $Q = 61$, the acoustic energy density increases by 9%, and the maximum levitating force is nearly doubled to become $F_z^{\text{rad}} = 33$ pN. Qualitatively, the frequency spectrum changes from having an additional resonance peak close to the levitating resonance of $f_{\text{res}} = 2.495$ MHz using the glycerol-like condition to having no extra resonances using the gluelike condition. The spatial structure of the resonance field in the fluid at f_{res} largely remains the same for the two different boundary conditions.

C. Analysis of capillary C3

For the quadratic capillary C3 [27], we use the nominal geometry parameters $W = H = 100$ μm and $H_{\text{gl}} = 50$ μm with PML absorption, and we predict numerically the frequency of the levitating half-wave resonance to be $f_{\text{res}} = 7.35$ MHz, only 2% from the simple half-wave value $c_{\text{fl}}/(2H) = 7.49$ MHz, and 7% lower than the experimental value, $f_{\text{res}}^{\text{exp}} = 7.90$ MHz. This discrepancy leads us to study changes in the predicted acoustic response as a function of geometrical variations within the fabrication uncertainties listed by the producer (VibroCom No. 8510, Mountain Lakes, New Jersey): $\pm 10\%$ for W and H , and $\pm 20\%$ for H_{gl} . Some of the resulting numerical predictions for the resonance frequency f_{res} and Q values, using both the averaged and rigid actuation condition, are listed in Table V.

For these thin-wall capillaries, the levitating half-wave resonance depends strongly on the channel height H and

TABLE V. Simulation results for the quadratic capillary C3: the levitating half-wave resonance frequency f_{res} , the quality factor Q , and the acoustic energy density $E_{\text{ac}}^{\text{fl}}$. The side length $W = H$ and the glass thickness H_{gl} are varied within the fabrication specifications, and we use either the averaged actuation condition A, Eq. (3b), or the rigid condition R, Eq. (3a). The experimental resonance frequency is $f_{\text{res}}^{\text{exp}} = 7.90$ MHz.

$W = H$ [μm]	H_{gl} [μm]	Actuation	f_{res} [MHz]	Q	$E_{\text{ac}}^{\text{fl}}$ [Pa]
90	40	A	8.230	114	67
90	60	A	7.964	60	28
90	60	R	7.950	117	163
100	50	A	7.350	91	40
100	50	R	7.313	157	120
110	40	A	6.670	124	26
110	40	R	6.640	148	84
110	60	A	6.590	79	28

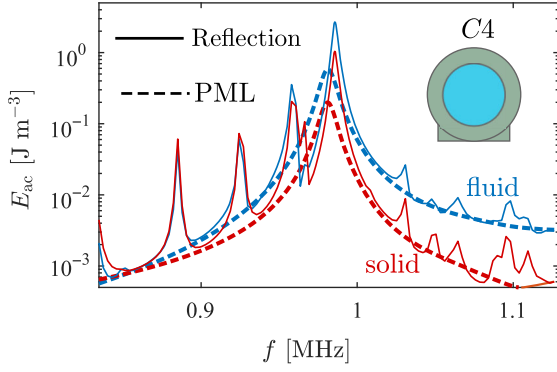
width W , and much less on the glass thickness H_{gl} . The 10% variation $H = W = (100 \pm 10)$ μm leads to a 10% variation in $f_{\text{res}} \approx (7.4 \pm 0.7)$ MHz for a fixed H_{gl} , while the 20% variation in $H_{\text{gl}} = (50 \pm 10)$ μm leads to variations of less than 2% in f_{res} for a fixed H and W . Moreover, in agreement with the results for C2, $E_{\text{ac}}^{\text{fl}}$ and the Q factor for the gluelike rigid actuation condition R are increased by factors of 3–6 and 1.2–3, respectively, compared to those of the glycerol-like averaged condition A. The maximum levitating force with $H = W = 100$ μm for condition R is $F_z^{\text{rad}} = 3690$ pN, while it drops to 1380 pN for condition A. The two actuation types lead to the same levitating resonance frequency within 0.5%.

D. Analysis of capillary C4

In the original work on the circular capillary C4 [28], effects due to reflections at the end of the capillary were discussed. Therefore, we study numerically the frequency response with PML absorption (perfect absorption of all outgoing waves) and without it (reflection of all outgoing waves at the end wall without absorption).

For the case with PML absorption, we find the levitating half-wave resonance to have the following characteristics: $f_{\text{res}} = 0.9753$ MHz, $Q = 109$, $E_{\text{ac}}^{\text{fl}} = 0.96$ Pa, and maximum levitating force $F_z^{\text{rad}} = 1.6$ pN using the glycerol-like condition (3b), and $f_{\text{res}} = 0.9818$ MHz, $Q = 79$, $E_{\text{ac}}^{\text{fl}} = 0.57$ Pa, and the maximum levitating force $F_z^{\text{rad}} = 2.6$ pN using the gluelike condition (3a). These values for f_{res} are close to the experimental value of 0.981 MHz and the theoretical value $\gamma_{11}c_{\text{fl}}/(\pi H) = 1.03$ MHz based on the simple hard-wall cylinder geometry, where $\gamma_{11} = 1.841$ is the first zero of the derivative $J_1'(x)$ of the first Bessel function. As for the other capillaries, the choice of actuation condition leads to no qualitative—and only minor quantitative—differences in the frequency spectrum.

When the PML is removed by imposing the zero-stress condition at $x = L$, the outgoing waves from the transducer region are reflected by the end wall, and complex interference effects arise in the capillary. For a fixed $L_{p,x}$, the channel length L is varied between 1 and 10 mm, and, relative to the PML case, we find that the levitating resonance frequency changes only about 1%, while the Q value and $E_{\text{ac}}^{\text{fl}}$ typically increase by 200%–300% and 400%–600%, respectively. This result illustrates that whether the capillary ends are reflecting or fully absorbing does not affect the frequency of the main levitating mode significantly, while it has a crucial influence on the Q factors and acoustic energies, as well as on the existence of secondary resonance modes. By contrast, the internal attenuation, given by the Γ factors, is unimportant since the associated attenuation lengths $L_{\text{fl}} = [(c_{\text{fl}})/\omega\Gamma_{\text{fl}}] \approx 60$ mm and $L_{\text{sl}} = [(c_{\text{sl}})/\omega\Gamma_{\text{sl}}] \approx 2$ m are longer than the capillary half length $L \approx 20$ mm.



F8:1 FIG. 8. Simulated frequency response of capillary C4 (the
 F8:2 inset shows its cross section), with a total length of $L = 10$ mm
 F8:3 and using the glue-like actuation condition, Eq. (3b). Semilog
 F8:4 plot of the volume-averaged acoustic energy density E_{ac}^{fl} in the
 F8:5 trapping region ($x < \frac{1}{2}L_p$) for the fluid (blue) and the solid (red),
 F8:6 both with PMLs (the thick dashed lines, $k_{\text{PML}} = 10^3$,
 F8:7 $f_{\text{res}}^{\text{PML}} = 0.9812$ MHz) and without (the solid lines, $k_{\text{PML}} =$
 F8:8 0 , $f_{\text{res}}^0 = 0.9856$ MHz).

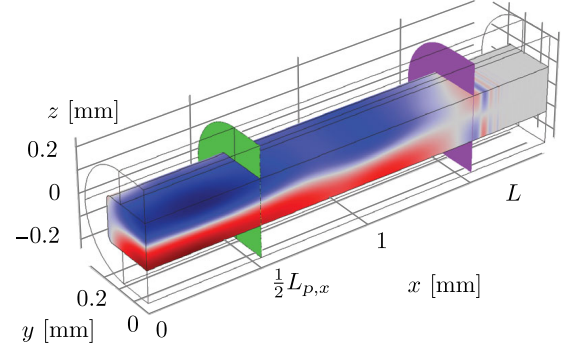
576 For the longest capillary $L = 10$ mm, we plot in Fig. 8
 577 E_{ac} as a function of frequency f near the levitating half-wave
 578 resonance f_{res} with and without PML absorption. First, we
 579 note that f_{res} in the two cases differs by less than 0.4%.
 580 Second, without PML absorption, the energy is not lost
 581 by the outgoing waves and, consequently, the line shape
 582 becomes higher and more narrow. Indeed, the resonance
 583 amplitude E_{ac}^{fl} increases from 0.58 Pa (PML) to 2.69 Pa (no
 584 PML), while the Q factor increases from 109 (PML) to 252
 585 (no PML). Third, without PML, the reflections from the end
 586 wall give rise to a number of additional, nearly equidistant,
 587 smaller resonance peaks, reminiscent of a Fabry-Pérot-like
 588 interference condition for the acoustic wave in the x
 589 direction. Finally, without PML, the reflections lead to a
 590 more irregular spatial pattern of the levitating resonance
 591 mode in the actuation region (not shown) than for that of the
 592 mode with PML absorption and no reflections.

593 Because of the complex nature of the coupling between
 594 pressure waves in the fluid and the compressional and shear
 595 waves in the solid, we have been able to interpret f_{res} only
 596 for the levitating resonance mode—not for other modes—
 597 in simple terms of the three sound speeds of the system,
 598 listed in Table I, combined with the geometrical length
 599 scales of capillary C4, listed in Table II.

E. Analysis of capillary C5

600
 601 We end our numerical modeling of the capillaries by a
 602 study of capillary C5, which is a geometry defined by us
 603 and not studied in the literature. The focus here is to obtain
 604 a more regular spatial pattern of the mode with spatial
 605 variations on the longest possible length scale.

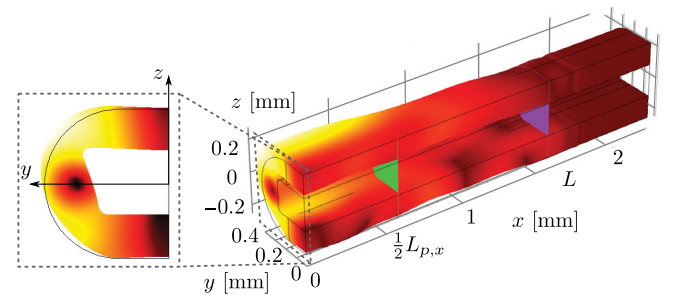
606 The study in Sec. III D of the circular capillary C4
 607 reveals that spatial irregularities in the levitating resonance
 608 mode are reduced when the reflections from the end wall



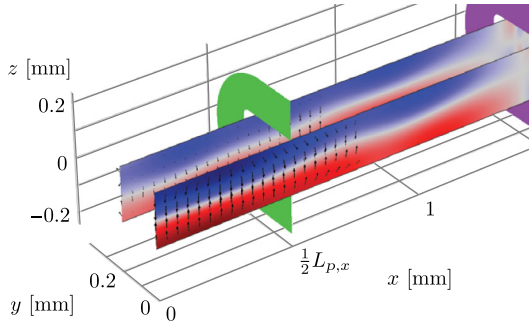
VIDEO. 4. Capillary C5, color plot of the pressure field p in the
 fluid from -0.10 MPa (blue) to 0.10 MPa (red) at the resonance
 frequency $f_{\text{res}} = 4.201$ MHz. The green and purple planes
 represent the end of the actuation region and the beginning of
 the PML domain, respectively.

are absorbed by a PML. We also find this tendency in the
 study in Sec. III A of the wide, flat capillary C1, where,
 even in the presence of a PML, the levitating resonance
 mode has significant spatial variations, see Video 2 and
 Fig. 7(b). These spatial variations are caused by the relative
 high mode numbers in the solid, and therefore we design
 capillary C5 as a version of capillary C1 with its width
 reduced by a factor of 4 to $W = 0.5$ mm, thus reducing the
 cross-section aspect ratio W/H from 10 to 2.5.

The separation of resonance frequencies increases in the
 narrow capillary C5. In the range between 3.5 and 4.4 MHz,
 it contains only two resonance peaks (at 3.572 and
 4.201 MHz), whereas capillary C1 in the same interval
 contains three pronounced peaks and four smaller ones.
 The resonance at $f_{\text{res}} = 4.201$ MHz, with $Q = 53$, is a
 levitating mode well suited for acoustic trapping, and, in
 Videos 4 and 5, we plot the corresponding pressure field p
 and displacement field u . The spatial structure of the
 resonance is more regular, especially in the solid, where
 the displacement in the y - z plane now resembles a simple
 fundamental mode with a pivoting motion around a single
 stationary point away from the symmetry plane (the black
 point on the y axis in the inset of Video 5). Compared to



VIDEO. 5. Capillary C5, the displacement field u in the solid
 (not drawn to scale) overlaid with a color plot of its magnitude u
 from 0 nm (dark red) to 1.2 nm (white) at the resonance frequency
 $f_{\text{res}} = 4.201$ MHz, as in Video 3.



VIDEO. 6. Capillary C5, a color plot of the pressure field p from -0.10 MPa (blue) to 0.10 MPa (red) in vertical planes placed equidistantly in steps of $\frac{3}{8}W$ starting at $y = 0$ showing the nearly horizontal nodal plane (gray) near $z = -0.03H$ at resonance $f_{\text{res}} = 4.201$ MHz. The acoustic radiation force \mathbf{F}^{rad} on $12\text{-}\mu\text{m}$ -diameter polystyrene test particles (black arrows with logarithmic lengths are shown for visual clarity) has a maximum magnitude of 7 pN.

that of capillary C1, the levitating mode of capillary C5 stretches far outside the actuation region and it is more regular in space, but its amplitude is reduced approximately by a factor of 1.8, and the maximum levitating force drops a factor of 3 to $F_z^{\text{rad}} = 7$ pN. The pressure nodal surface of the levitating mode is weakly wobbling around the horizontal plane located at $z = -0.03H$; see Video 6. This wobbling is less pronounced than the one we find in capillary C1, which, moreover, is displaced farther downward—namely, to $z = -0.05H$.

Compared to capillary C1, the reduced pressure amplitude in capillary C5 leads to a corresponding reduction in the lateral radiation force by a factor of $1.8^2 = 3.2$, plotted for $z = -0.03H$ in Fig. 9, and it has a more regular spatial structure compared to that shown in Fig. 7. The main lateral trapping points are now confined to the intersection of the nodal plane and the x - z plane inside the actuation region, although the levitating mode extends far beyond the

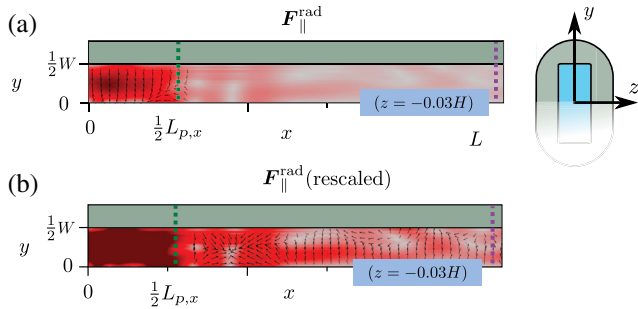


FIG. 9. Capillary C5. (a) The lateral acoustic radiation force $\mathbf{F}_{\parallel}^{\text{rad}}$ (the black arrows) and its magnitude [the color plot from 0 pN (gray) to 0.13 pN (dark red)] acting on $12\text{-}\mu\text{m}$ -diameter polystyrene beads in the x - y plane at $z = -0.03H$ at resonance $f_{\text{res}} = 4.201$ MHz. (Inset) Cross-section geometry with $W = 0.5$ mm. (b) The same as (a), but with its maximum color (dark red) decreased to 0.05 pN (dark red) to emphasize the secondary trapping points.

actuation region; see Video 6. There do exist secondary trapping points outside the actuation region, and compared to those of capillary C1 they are relatively strong, but they are fewer in number and appear in a more regular pattern. This finding is in qualitative agreement with experimental observations on the circular capillary C4 [28].

IV. DISCUSSION

The main outcome of our numerical modeling of glass-capillary devices is that, for each of the five capillaries C1–C5 in our study, we find that a localized acoustic resonance mode, the so-called levitating mode, exists—even though the completely straight capillaries do not contain any geometrical cavities in the axial x direction. This levitating mode is the result of a strong vertical SBAW forming in the region $x < \frac{1}{2}L_p$ of the capillary directly above the transducer. Although the bottom glass wall attached to the transducer is displaced only by $d_0 = 0.1$ nm, the opposite top glass wall above the transducer is displaced an order of magnitude more, approximately $10d_0$. This relatively large displacement results in a dynamically defined cavity that provides sufficient confinement for the vertical SBAW, although acoustic energy is lost by a horizontal TBAW radiating away from the cavity for $x > \frac{1}{2}L_p$. The levitating modes have a relatively high Q value, 50 or higher, and they all exhibit good trapping characteristics: a nearly horizontal pressure nodal plane near the center of the channel (see Videos 3 and 6), with sufficiently strong lateral acoustic forces (see Figs. 7 and 9).

The values of the levitating resonance frequencies f_{res} are in good agreement with the experimental values obtained for capillaries C1–C4 [8,27–29], as listed in Table II. They vary by less than 1% as we change the boundary condition at the outlet from an ideally absorbing PML region to the no-stress condition of a capillary facing air, and as we change the actuation from glycerol-like area-averaged displacement to glue-like rigid displacement. However, we find that varying these idealized generic boundary conditions does result in significant changes of the acoustic energy density $E_{\text{ac}}^{\text{fl}}$ and the acoustic force \mathbf{F}^{rad} on a test particle, as well as the resonance quality factor Q . In general, we find two opposing trends: On the one hand, the absorption of the PML region reduces both the acoustic energy and the trapping forces by a factor of 2–6, which is a drawback for achieving good trapping. On the other hand, the presence of the PML region has three beneficial aspects: It removes the sensitivity to reflections of acoustic waves at the outlet wall, it results in more regular spatial variations, and it makes the trapping strength independent of the position of the transducer relative to the capillary ends.

The submillimeter dimensions of the capillary cross section implies that the levitating resonance frequency f_{res} is sensitive to the exact geometry. We find that, when changing the geometry within the tolerances listed by the manufacturer of the capillaries, the value of the levitating

resonance can vary by as much as 10%, or by up to 0.7 MHz for a 7-MHz resonance. Because the levitating resonance is close to an ideal standing half-wave resonance in the channel of height H , we have $f_{\text{res}} \propto H^{-1}$, and the most critical length parameter therefore becomes H .

Turning to the acoustic radiation force acting on a 12- μm -diameter polystyrene test particle in the device, our model correctly predicts that this force is present in the actuation region with a magnitude large enough to support one or more stable trapping points there. For the assumed actuation amplitude $d_0 = 0.1$ nm, the maximum levitating force F^{rad} ranges from 2 pN (the circular capillary C4) to 3690 pN (the square capillary C3), which is between 5 and 8000 times the buoyancy-corrected gravitational force F^{grv} , depending, of course, on the transducer length $L_{p,x}$. Our model also correctly predicts the existence of weaker, secondary trapping points in the region outside the actuation region, see Figs. 7(b) and 9(b), in agreement with published experiments [28,56]. However, even without the PML absorption, the magnitude of the lateral acoustic force $F_{\parallel}^{\text{rad}}$ is small for most geometries, $F_{\parallel}^{\text{rad}}/F^{\text{grv}} \approx 1$ –10, the exception being capillary C3 with $F_{\parallel}^{\text{rad}}/F^{\text{grv}} > 100$. This small magnitude indicates that the performance of actual acoustic capillary traps may depend on additional forces such as streaming-induced drag forces and particle-particle interactions. For idealized systems with a rectangular cross section and translation invariance in the axial x direction, the critical particle radius a_c , below which streaming drag dominates, can be estimated by $a_c = \delta\sqrt{3\Psi/\Phi}$ [36], where δ is the boundary-layer thickness, Ψ is the streaming coefficient ($= \frac{3}{8}$ for a planar wall), and Φ is the acoustic contrast factor characterizing the strength of the acoustic radiation force. For the levitating mode in 3D, the lateral component of the radiation force is smaller by a factor of α than the levitating vertical one [see Eq. (9)], so, in this case, we estimate $a_c = \delta\sqrt{3\Psi/(\alpha\Phi)}$. Numerically, we find $\alpha \approx 0.01$, see Eq. (9), and this relative weakening of the lateral radiation force indicates that the critical particle radius may be 1 order of magnitude larger than the 1 μm found for typical BAW devices [36,43].

While a wide capillary is good for enhanced throughput, it suffers from the existence of high-mode, short-wavelength elastic waves propagating around the perimeter of the capillary. We find that reducing the aspect ratio removes these perimeter waves while maintaining the good characteristics of the levitating mode. Other irregular spatial patterns in the levitating mode and the acoustic-trapping force are induced by reflections of acoustic waves at the end of the capillary. We find that, by implementing an ideally absorbing PML region, these reflections are removed, and a more regular spatial behavior of the trap is obtained. While the reduction in aspect ratio reduces the throughput and the introduction of absorption reduces the trapping force by a factor of 2–6, the resulting increased regularity in spatial

behavior, the increased separation of modes in frequency implying reduced mixing of unwanted modes, and the decreased sensitivity to the exact location of the transducer relative to the capillary ends may be beneficial design considerations worth taking into account. The redesigned devices may be more robust to small perturbations in the device geometry and mechanical actuation.

Our numerical modeling of the capillary systems for acoustic trapping is in fair agreement with the existing experimental data in the literature. However, to fully establish its capability as a design tool for optimizing acoustic trapping, more experimental data is needed to characterize the acoustic properties more fully. Here, stop-flow experiments as in Ref. [56] would be helpful, as would more systematic reporting of the acoustic energy density present in the devices using, say, the drop-voltage method [29] or the flow versus retention force briefly mentioned in Sec. III A. Also, systematic reporting of the magnitude of the acoustic streaming would be helpful because there might be situations in the capillary systems, where the acoustic streaming is so large that it is comparable to the flow velocities in the channel. If this were the case, our analysis of the lateral acoustic forces must be supplemented by a discussion of the drag forces from acoustic streaming.

V. CONCLUSION

The increased use of acoustic-trapping devices in microfluidic handling of particles allows for the development of alternative functionalities in contemporary biotechnology. In this paper, we develop a three-dimensional numerical model for water-filled glass capillaries, which may be a useful design tool for the future development of acoustic microparticle traps. We validate the model and demonstrate how it captures many of the experimental observations reported in the literature for four different glass-capillary devices, particularly regarding the frequency, the Q factor, as well as the spatial structure and trapping capability of levitating resonance modes. Our model explains the physical mechanism leading to these localized resonance modes in terms of a dynamically defined cavity in the region above the transducer.

We demonstrate the potential of the model as a design tool through an analysis of the sensitivity of the system to changes in the geometry, the specific actuation condition, and the acoustic absorption. We find that, while the existence of a main levitating resonance mode and the value of the resonance frequency are relatively insensitive to these changes, the opposite is true for the magnitude of the trapping force and the lateral spatial structure: The trapping force is strongly increased for rectangular cross sections with a low aspect ratio—the best being the square shape—and the lateral spatial structure of the levitating mode becomes more uniform. For the case without acoustic absorption, reflections at the outlet of the capillary make these responses very sensitive to the length

of the system. The introduction of deliberate absorption of acoustic waves at the outlet would lower this sensitivity and would probably result in more-robust devices. However, this benefit in device operation must be weighed against a decreased magnitude of the acoustic forces.

Our numerical model takes many, but certainly not all, physical relevant aspects into account. The obvious next step, which we are currently working on, is to include the drag force from acoustic streaming, as well as both acoustic and hydrodynamic particle-particle interaction effects. These more elaborate phenomena all involve lateral forces comparable to, or possibly even larger than, the lateral single-particle acoustic radiation force $F_{\parallel}^{\text{rad}}$ calculated in our model. The simulation of these phenomena relies on numerically well-characterized acoustic fields, which, we believe, are provided by the model we present here. Possible model strategies to pursue in such calculations were outlined by Muller and Bruus [32], Muller *et al.* [36] and Lei *et al.* [59] for the case of acoustic streaming, by Silva and Bruus [60] for acoustic particle-particle interactions, and by Ley and Bruus [61] for hydrodynamic particle-particle interactions.

Our numerical model reveals that the acoustic-trapping devices based on simple glass capillaries are perhaps not as simple as they appear at first glance.

ACKNOWLEDGMENTS

We thank our collaborators Carl Johannsson, Mikael Evander, and Thomas Laurell, from Lund University in Sweden, for the valuable discussions related to experimental aspects. This work was supported by Lund University and the Knut and Alice Wallenberg Foundation (Grant No. KAW 2012.0023).

- [1] H. Bruus, J. Dual, J. Hawkes, M. Hill, T. Laurell, J. Nilsson, S. Radel, S. Sadhal, and M. Wiklund, Forthcoming Lab on a Chip tutorial series on acoustofluidics: Acoustofluidics-exploiting ultrasonic standing wave forces and acoustic streaming in microfluidic systems for cell and particle manipulation, *Lab Chip* **11**, 3579 (2011).
- [2] *Microscale Acoustofluidics*, edited by T. Laurell and A. Lenshof (Royal Society of Chemistry, Cambridge, England, 2015).
- [3] P. Thevoz, J. D. Adams, H. Shea, H. Bruus, and H. T. Soh, Acoustophoretic synchronization of mammalian cells in microchannels, *Anal. Chem.* **82**, 3094 (2010).
- [4] P. Augustsson, C. Magnusson, M. Nordin, H. Lilja, and T. Laurell, Microfluidic, label-free enrichment of prostate cancer cells in blood based on acoustophoresis, *Anal. Chem.* **84**, 7954 (2012).
- [5] X. Ding, S.-C. S. Lin, B. Kiraly, H. Yue, S. Li, I.-K. Chiang, J. Shi, S. J. Benkovic, and T. J. Huang, On-chip manipulation of single microparticles, cells, and organisms using surface acoustic waves, *Proc. Natl. Acad. Sci. U.S.A.* **109**, 11105 (2012).
- [6] D. J. Collins, B. Morahan, J. Garcia-Bustos, C. Doerig, M. Plebanski, and A. Neild, Two-dimensional single-cell patterning with one cell per well driven by surface acoustic waves, *Nat. Commun.* **6**, 8686 (2015).
- [7] B. Hammarström, M. Evander, H. Barbeau, M. Bruzelius, J. Larsson, T. Laurell, and J. Nilsson, Non-contact acoustic cell trapping in disposable glass capillaries, *Lab Chip* **10**, 2251 (2010).
- [8] B. Hammarström, T. Laurell, and J. Nilsson, Seed particle enabled acoustic trapping of bacteria and nanoparticles in continuous flow systems, *Lab Chip* **12**, 4296 (2012).
- [9] B. Hammarström, M. Evander, J. Wahlström, and J. Nilsson, Frequency tracking in acoustic trapping for improved performance stability and system surveillance, *Lab Chip* **14**, 1005 (2014).
- [10] B. W. Drinkwater, Dynamic-field devices for the ultrasonic manipulation of microparticles, *Lab Chip* **16**, 2360 (2016).
- [11] D. J. Collins, C. Devendran, Z. Ma, J. W. Ng, A. Neild, and Y. Ai, Acoustic tweezers via sub-time-of-flight regime surface acoustic waves, *Sci. Adv.* **2**, e1600089 (2016).
- [12] H. G. Lim, Y. Li, M.-Y. Lin, C. Yoon, C. Lee, H. Jung, R. H. Chow, and K. K. Shung, Calibration of trapping force on cell-size objects from ultrahigh-frequency single-beam acoustic tweezer, *IEEE Trans. Ultrason. Ferroelectr. Freq. Control* **63**, 1988 (2016).
- [13] D. Baresch, J.-L. Thomas, and R. Marchiano, Observation of a Single-Beam Gradient Force Acoustical Trap for Elastic Particles: Acoustical Tweezers, *Phys. Rev. Lett.* **116**, 024301 (2016).
- [14] A. Riaud, M. Baudoin, O. Bou Matar, L. Becerra, and J.-L. Thomas, Selective Manipulation of Microscopic Particles with Precursor Swirling Rayleigh Waves, *Phys. Rev. Applied* **7**, 024007 (2017).
- [15] J. Zhang, S. Yan, D. Yuan, G. Alici, N.-T. Nguyen, M. E. Warkiani, and W. Li, Fundamentals and applications of inertial microfluidics: A review, *Lab Chip* **16**, 10 (2016).
- [16] J. Voldman, Electrical forces for microscale cell manipulation, *Annu. Rev. Biomed. Eng.* **8**, 425 (2006).
- [17] D. Grier, A revolution in optical manipulation, *Nature (London)* **424**, 810 (2003).
- [18] J. Nilsson, M. Evander, B. Hammarström, and T. Laurell, Review of cell and particle trapping in microfluidic systems, *Anal. Chim. Acta* **649**, 141 (2009).
- [19] B. Cetin, M. B. Ozer, and M. E. Solmaz, Microfluidic bio-particle manipulation for biotechnology, *Biochem. Eng. J.* **92**, 63 (2014).
- [20] J. T. Karlsen and H. Bruus, Forces acting on a small particle in an acoustical field in a thermoviscous fluid, *Phys. Rev. E* **92**, 043010 (2015).
- [21] M. Wiklund, Acoustofluidics 12: Biocompatibility and cell viability in microfluidic acoustic resonators, *Lab Chip* **12**, 2018 (2012).
- [22] M. Grundy, W. Bolek, W. Coakley, and E. Benes, Rapid agglutination testing in an ultrasonic standing wave, *J. Immunol. Methods* **165**, 47 (1993).
- [23] P. Vainshtein, M. Fichman, K. Shuster, and C. Gutfinger, The effect of centreline particle concentration in a wave tube, *J. Fluid Mech.* **306**, 31 (1996).

- [24] M. Wiklund, S. Nilsson, and H. Hertz, Ultrasonic trapping in capillaries for trace-amount biomedical analysis, *J. Appl. Phys.* **90**, 421 (2001).
- [25] D. N. Ankrett, D. Carugo, J. Lei, P. Glynne-Jones, P. A. Townsend, X. Zhang, and M. Hill, The effect of ultrasound-related stimuli on cell viability in microfluidic channels, *J. Nanobiotechnol.* **11**, 20 (2013).
- [26] D. Carugo, D. N. Ankrett, P. Glynne-Jones, L. Capretto, R. J. Boltryk, X. Zhang, P. A. Townsend, and M. Hill, Contrast agent-free sonoporation: The use of an ultrasonic standing wave microfluidic system for the delivery of pharmaceutical agents, *Biomicrofluidics* **5**, 044108 (2011).
- [27] P. Mishra, M. Hill, and P. Glynne-Jones, Deformation of red blood cells using acoustic radiation forces, *Biomicrofluidics* **8**, 034109 (2014).
- [28] I. Gralinski, S. Raymond, T. Alan, and A. Neild, Continuous flow ultrasonic particle trapping in a glass capillary, *J. Appl. Phys.* **115**, 054505 (2014).
- [29] J. Lei, P. Glynne-Jones, and M. Hill, Acoustic streaming in the transducer plane in ultrasonic particle manipulation devices, *Lab Chip* **13**, 2133 (2013).
- [30] M. Evander, O. Gidlöf, B. Olde, D. Erlinge, and T. Laurell, Non-contact acoustic capture of microparticles from small plasma volumes, *Lab Chip* **15**, 2588 (2015).
- [31] P. Ohlsson, M. Evander, K. Petersson, L. Mellhammar, A. Lehmusvuori, U. Karhunen, M. Soikkeli, T. Seppä, E. Tuunainen, A. Spangar, P. von Lode, K. Rantakokko-Jalava, G. Otto, S. Scheduling, T. Soukka, S. Wittfooth, and T. Laurell, Integrated acoustic separation, enrichment, and microchip polymerase chain reaction detection of bacteria from blood for rapid sepsis diagnostics, *Anal. Chem.* **88**, 9403 (2016).
- [32] P. B. Muller and H. Bruus, Numerical study of thermoviscous effects in ultrasound-induced acoustic streaming in microchannels, *Phys. Rev. E* **90**, 043016 (2014).
- [33] P. Hahn and J. Dual, A numerically efficient damping model for acoustic resonances in microfluidic cavities, *Phys. Fluids* **27**, 062005 (2015).
- [34] Corning Inc., “Glass silicon constraint substrates” <http://www.valleydesign.com/Datasheets/Corning%20Pyrex%207740.pdf>.
- [35] *CRC Handbook of Chemistry and Physics*, 95th ed., edited by W. M. Haynes (CRC Press, Boca Raton, FL, 2014).
- [36] P. B. Muller, R. Barnkob, M. J. H. Jensen, and H. Bruus, A numerical study of microparticle acoustophoresis driven by acoustic radiation forces and streaming-induced drag forces, *Lab Chip* **12**, 4617 (2012).
- [37] P. H. Mott, J. R. Dorgan, and C. M. Roland, The bulk modulus and Poisson’s ratio of “incompressible” materials, *J. Sound Vib.* **312**, 572 (2008).
- [38] L. Bergmann, *Der Ultraschall und seine Anwendung in Wissenschaft und Technik*, 6th ed. (S. Hirzel Verlag, Stuttgart, 1954).
- [39] P. B. Muller and H. Bruus, Theoretical study of time-dependent, ultrasound-induced acoustic streaming in microchannels, *Phys. Rev. E* **92**, 063018 (2015).
- [40] F. Garofalo, T. Laurell, and H. Bruus, Performance Study of Acoustophoretic Microfluidic Silicon-Glass Devices by Characterization of Material- and Geometry-Dependent Frequency Spectra, *Phys. Rev. Applied* **7**, 054026 (2017).
- [41] R. Barnkob, P. Augustsson, T. Laurell, and H. Bruus, Measuring the local pressure amplitude in microchannel acoustophoresis, *Lab Chip* **10**, 563 (2010).
- [42] P. Augustsson, R. Barnkob, S. T. Wereley, H. Bruus, and T. Laurell, Automated and temperature-controlled micro-PIV measurements enabling long-term-stable microchannel acoustophoresis characterization, *Lab Chip* **11**, 4152 (2011).
- [43] P. B. Muller, M. Rossi, A. G. Marin, R. Barnkob, P. Augustsson, T. Laurell, C. J. Kähler, and H. Bruus, Ultrasound-induced acoustophoretic motion of microparticles in three dimensions, *Phys. Rev. E* **88**, 023006 (2013).
- [44] F. Collino and P. B. Monk, Optimizing the perfectly matched layer, *Comput. Methods Appl. Mech. Eng.* **164**, 157 (1998).
- [45] A. D. Pierce, *Acoustics* (Acoustical Society of America, Woodbury, NY, 1991).
- [46] L. D. Landau and E. M. Lifshitz, *Theory of Elasticity*, 3rd ed., Course of Theoretical Physics Vol. 7 (Pergamon Press, Oxford, 1986).
- [47] M. Settles and H. Bruus, Forces acting on a small particle in an acoustical field in a viscous fluid, *Phys. Rev. E* **85**, 016327 (2012).
- [48] M. M. Gregersen, M. B. Andersen, G. Soni, C. Meinhardt, and H. Bruus, Numerical analysis of finite Debye-length effects in induced-charge electro-osmosis, *Phys. Rev. E* **79**, 066316 (2009).
- [49] COMSOL MULTIPHYSICS 5.2a, <http://www.comsol.com> (2016).
- [50] A. F. Oskooi, L. Zhang, Y. Avniel, and S. G. Johnson, The failure of perfectly matched layers, and towards their redemption by adiabatic absorbers, *Opt. Express* **16**, 11376 (2008).
- [51] See Supplemental Material at <http://link.aps.org/supplemental/10.1103/PhysRevApplied.000.000000> for animated GIF versions of Videos 1–6.
- [52] N. Nama, R. Barnkob, Z. Mao, C. J. Kähler, F. Costanzo, and T. J. Huang, Numerical study of acoustophoretic motion of particles in a PDMS microchannel driven by surface acoustic waves, *Lab Chip* **15**, 2700 (2015).
- [53] C. Devendran, N. R. Gunasekara, D. J. Collins, and A. Neild, Batch process particle separation using surface acoustic waves (SAW): Integration of travelling and standing SAW, *RSC Adv.* **6**, 5856 (2016).
- [54] C. Devendran, T. Albrecht, J. Brenker, T. Alan, and A. Neild, The importance of travelling wave components in standing surface acoustic wave (SSAW) systems, *Lab Chip* **16**, 3756 (2016).
- [55] J. W. Ng, D. J. Collins, C. Devendran, Y. Ai, and A. Neild, Flow-rate-insensitive deterministic particle sorting using a combination of travelling and standing surface acoustic waves, *Microfluid. Nanofluid.* **20**, 151 (2016).
- [56] M. W. H. Ley, C. Johannesson, M. Evander, T. Laurell, and H. Bruus, in *Proceedings of the 20th International Conference on Miniaturized Systems for Chemistry and Life Sciences (MicroTAS 2016)*, Dublin, 2016 (Chemical and Biological Microsystems Society, Washington, DC, 2016), p. 711.
- [57] J. Happel and H. Brenner, *Low Reynolds Number Hydrodynamics with Special Applications to Particulate Media* (Martinus Nijhoff Publishers, The Hague, 1983).

- [58] H. Bruus, *Theoretical Microfluidics* (Oxford University Press, Oxford, 2008).
- [59] J. Lei, P. Glynne-Jones, and M. Hill, Comparing methods for the modelling of boundary-driven streaming in acoustofluidic devices, *Microfluid. Nanofluid.* **21**, 23 (2017).
- [60] G.T. Silva and H. Bruus, Acoustic interaction forces between small particles in an ideal fluid, *Phys. Rev. E* **90**, 063007 (2014).
- [61] M.W.H. Ley and H. Bruus, Continuum modeling of hydrodynamic particle-particle interactions in microfluidic high-concentration suspensions, *Lab Chip* **16**, 1178 (2016).

1050
1051
1052
1053
1054
1055
1056

Bibliography

- [1] P. B. Muller and H. Bruus. *Numerical study of thermoviscous effects in ultrasound-induced acoustic streaming in microchannels*. Phys Rev E **90**, 043016 (2014).
- [2] M. J. Holmes, N. G. Parker, and M. J. W. Povey. *Temperature dependence of bulk viscosity in water using acoustic spectroscopy*. J Phys Conf Ser **269**, 012011 (2011).
- [3] P. Hahn and J. Dual. *A numerically efficient damping model for acoustic resonances in microfluidic cavities*. Physics of Fluids **27**, 062005 (2015).
- [4] CORNING, Houghton Park C-8, Corning, NY 14831, USA. *Glass Silicon Constraint Substrates*.
- [5] *CRC Handbook of Chemistry and Physics*, 95th ed., (CRC Press, Boca Raton, FL, 2014).
- [6] P. B. Muller, R. Barnkob, M. J. H. Jensen, and H. Bruus. *A numerical study of microparticle acoustophoresis driven by acoustic radiation forces and streaming-induced drag forces*. Lab Chip **12**, 4617–4627 (2012).
- [7] P. H. Mott, J. R. Dorgan, and C. M. Roland. *The bulk modulus and poisson’s ratio of “incompressible” materials*. J Sound Vibr **312**, 572–575 (2008).
- [8] L. Bergmann, *Der Ultraschall und seine Anwendung in Wissenschaft und Technik*, 6th ed., (S. Hirzel Verlag, Stuttgart, 1954).
- [9] A. Lenshof, C. Magnusson, and T. Laurell. *Acoustofluidics 8: Applications in acoustophoresis in continuous flow microsystems*. Lab Chip **12**, 1210–1223 (2012).
- [10] H. Amini, W. Lee, and D. Di Carlo. *Inertial microfluidic physics*. Lab Chip **14**, 2739–2761 (2014).
- [11] T. Z. Jubery, S. K. Srivastava, and P. Dutta. *Dielectrophoretic separation of bioparticles in microdevices: A review*. Electrophoresis **35**, 691–713 (2014).
- [12] M. Hejazian, W. Li, and N.-T. Nguyen. *Lab on a chip for continuous-flow magnetic cell separation*. Lab Chip **15**, 959–970 (2015).
- [13] W. S. Low and W. A. B. W. Abas. *Benchtop technologies for circulating tumor cells separation based on biophysical properties*. Biomed Res Int **2015**, 239362 (2015).

- [14] O. Otto, P. Rosendahl, A. Mietke, S. Golfier, C. Herold, D. Klaue, S. Girardo, S. Pagliara, A. Ekpenyong, A. Jacobi, M. Wobus, N. Topfner, U. F. Keyser, J. Mansfeld, E. Fischer-Friedrich, and J. Guck. *Real-time deformability cytometry: on-the-fly cell mechanical phenotyping*. Nat Meth **12**, 199–202 (2015).
- [15] C. W. Shields, C. D. Reyes, and G. P. López. *Microfluidic cell sorting: A review of the advances in the separation of cells from debulking to rare cell isolation*. Lab Chip **15**, 1230–1249 (2015).
- [16] P. Ohlsson, M. Evander, K. Petersson, L. Mellhammar, A. Lehmusvuori, U. Karhunen, M. Soikkeli, T. Seppa, E. Tuunainen, A. Spangar, P. von Lode, K. Rantakokko-Jalava, G. Otto, S. Scheduling, T. Soukka, S. Wittfooth, and T. Laurell. *Integrated acoustic separation, enrichment, and microchip polymerase chain reaction detection of bacteria from blood for rapid sepsis diagnostics*. Analytical Chemistry **88**, 9403–9411 (2016).
- [17] D. J. Collins, B. Morahan, J. Garcia-Bustos, C. Doerig, M. Plebanski, and A. Neild. *Two-dimensional single-cell patterning with one cell per well driven by surface acoustic waves*. Nat Commun **6**, 8686 (2015).
- [18] S. Goodwin, J. D. McPherson, and W. R. McCombie. *Coming of age: ten years of next-generation sequencing technologies*. Nature Reviews Genetics **17**, 333–351 (2016).
- [19] B. Cetin, M. B. Ozer, and M. E. Solmaz. *Microfluidic bio-particle manipulation for biotechnology*. Biochem Eng J **92**, 63–82 (2014).
- [20] J. Zhang, S. Yan, D. Yuan, G. Alici, N.-T. Nguyen, M. E. Warkiani, and W. Li. *Fundamentals and applications of inertial microfluidics: a review*. Lab Chip **16**, 10–34 (2016).
- [21] J. T. Karlsen and H. Bruus. *Forces acting on a small particle in an acoustical field in a thermoviscous fluid*. Phys Rev E **92**, 043010 (2015).
- [22] M. Wiklund. *Acoustofluidics 12: Acoustofluidics 12: Biocompatibility and cell viability in microfluidic acoustic resonators*. Lab Chip **12**, 2018–28 (2012).
- [23] H. Bruus, J. Dual, J. Hawkes, M. Hill, T. Laurell, J. Nilsson, S. Radel, S. Sadhal, and M. Wiklund. *Forthcoming lab on a chip tutorial series on acoustofluidics: Acoustofluidics-exploiting ultrasonic standing wave forces and acoustic streaming in microfluidic systems for cell and particle manipulation*. Lab Chip **11**, 3579–3580 (2011).
- [24] T. Laurell and A. Lenshof (eds.), *Microscale Acoustofluidics*, (Royal Society of Chemistry, Cambridge, 2015).
- [25] W. Coakley, D. Bardsley, M. Grundy, F. Zamani, and D. Clarke. *Cell manipulation in ultrasonic standing wave fields*. Journal of Chemical Technology and Biotechnology **44**, 43–62 (1989).

- [26] P. Thevoz, J. D. Adams, H. Shea, H. Bruus, and H. T. Soh. *Acoustophoretic synchronization of mammalian cells in microchannels*. Anal Chem **82**, 3094–3098 (2010).
- [27] P. Augustsson, C. Magnusson, M. Nordin, H. Lilja, and T. Laurell. *Microfluidic, label-free enrichment of prostate cancer cells in blood based on acoustophoresis*. Anal Chem **84**, 7954–7962 (2012).
- [28] X. Ding, S.-C. S. Lin, B. Kiraly, H. Yue, S. Li, I.-K. Chiang, J. Shi, S. J. Benkovic, and T. J. Huang. *On-chip manipulation of single microparticles, cells, and organisms using surface acoustic waves*. PNAS **109**, 11105–11109 (2012).
- [29] B. Hammarström, M. Evander, H. Barbeau, M. Bruzelius, J. Larsson, T. Laurell, and J. Nilsson. *Non-contact acoustic cell trapping in disposable glass capillaries*. Lab Chip **10**, 2251–2257 (2010).
- [30] B. Hammarström, T. Laurell, and J. Nilsson. *Seed particle enabled acoustic trapping of bacteria and nanoparticles in continuous flow systems*. Lab Chip **12**, 4296–4304 (2012).
- [31] B. Hammarström, M. Evander, J. Wahlström, and J. Nilsson. *Frequency tracking in acoustic trapping for improved performance stability and system surveillance*. Lab Chip **14**, 1005–1013 (2014).
- [32] B. W. Drinkwater. *Dynamic-field devices for the ultrasonic manipulation of microparticles*. Lab Chip **16**, 2360–2375 (2016).
- [33] D. J. Collins, C. Devendran, Z. Ma, J. W. Ng, A. Neild, and Y. Ai. *Acoustic tweezers via sub-time-of-flight regime surface acoustic waves*. Science Advances **2**, e1600089 (2016).
- [34] H. G. Lim, Y. Li, M.-Y. Lin, C. Yoon, C. Lee, H. Jung, R. H. Chow, and K. K. Shung. *Calibration of trapping force on cell-size objects from ultrahigh-frequency single-beam acoustic tweezer*. IEEE Transactions on Ultrasonics Ferroelectrics and Frequency Control **63**, 1988–1995 (2016).
- [35] D. Baresch, J.-L. Thomas, and R. Marchiano. *Observation of a single-beam gradient force acoustical trap for elastic particles: Acoustical tweezers*. Phys Rev Lett **116**, 024301 (2016).
- [36] A. Riaud, M. Baudoin, O. B. Matar, J. L. Thomas, and P. Brunet. *On the influence of viscosity and caustics on acoustic streaming in sessile droplets: an experimental and a numerical study with a cost-effective method*. Journal of Fluid Mechanics **821**, 384–420 (2017).
- [37] R. Barnkob. *Physics of microparticle acoustophoresis*. Ph.D. thesis, Technical University of Denmark, www.fysik.dtu.dk/microfluidics (2012).

- [38] P. Augustsson, R. Barnkob, S. T. Wereley, H. Bruus, and T. Laurell. *Automated and temperature-controlled micro-piv measurements enabling long-term-stable microchannel acoustophoresis characterization*. Lab Chip **11**, 4152–4164 (2011).
- [39] R. Barnkob, P. Augustsson, T. Laurell, and H. Bruus. *Measuring the local pressure amplitude in microchannel acoustophoresis*. Lab Chip **10**, 563–570 (2010).
- [40] N. Nama, R. Barnkob, Z. Mao, C. J. Kähler, F. Costanzo, and T. J. Huang. *Numerical study of acoustophoretic motion of particles in a PDMS microchannel driven by surface acoustic waves*. Lab Chip **15**, 2700–2709 (2015).
- [41] L. D. Landau and E. M. Lifshitz, *Fluid Mechanics*, vol. 6, 2nd ed., (Pergamon Press, Oxford, 1993).
- [42] L. D. Landau and E. M. Lifshitz, *Theory of Elasticity. Course of Theoretical Physics*, vol. 7, 3rd ed., (Pergamon Press, Oxford, 1986).
- [43] J. Happel and H. Brenner, *Low Reynolds number hydrodynamics with special applications to particulate media*, (Martinus Nijhoff Publishers, The Hague, 1983).
- [44] L. G. Leal. *Advanced transport phenomena: Fluid mechanics and convective transport processes*. Advanced Transport Phenomena: Fluid Mechanics and Convective Transport Processes **9780521849104**, 1–912 (2007).
- [45] H. Bruus, *Theoretical Microfluidics*, (Oxford University Press, Oxford, 2008).
- [46] M. Settnes and H. Bruus. *Forces acting on a small particle in an acoustical field in a viscous fluid*. Phys Rev E **85**, 016327 (2012).
- [47] COMSOL Multiphysics 5.2a. <http://www.comsol.com> (2016).
- [48] L. H. Olesen. *Computational Fluid Dynamics in Microfluidic Systems*. Master’s thesis, Technical University of Denmark, www.fysik.dtu.dk/microfluidics (2003). Supervised by Professor Henrik Bruus.
- [49] C. P. Nielsen. *Introduction to weak form modeling in comsol* (2013). Note on weak form and COMSOL implementation. version 1.3.
- [50] M. M. Gregersen, M. B. Andersen, G. Soni, C. Meinhart, and H. Bruus. *Numerical analysis of finite debye-length effects in induced-charge electro-osmosis*. Phys Rev E **79**, 066316 (2009).
- [51] D. A. Reasor, J. R. Clausen, and C. K. Aidun. *Coupling the lattice-boltzmann and spectrin-link methods for the direct numerical simulation of cellular blood flow*. Int J Numer Methods Fluids **68**, 767–781 (2012).
- [52] J. R. Clausen, D. A. Reasor, and C. K. Aidun. *Parallel performance of a lattice-boltzmann/finite element cellular blood flow solver on the ibm blue gene/p architecture*. Comput Phys Comm **181**, 1013–1020 (2010).

- [53] M. Mehrabadi, D. N. Ku, and C. K. Aidun. *A continuum model for platelet transport in flowing blood based on direct numerical simulations of cellular blood flow*. Ann Biomed Eng **43**, 1410–1421 (2015).
- [54] P. Bagchi. *Mesoscale simulation of blood flow in small vessels*. Biophys J **92**, 1858–1877 (2007).
- [55] H. Lei, D. A. Fedosov, B. Caswell, and G. E. Karniadakis. *Blood flow in small tubes: quantifying the transition to the non-continuum regime*. J Fluid Mech **722**, 214–239 (2013).
- [56] M. Massoudi, J. Kim, and J. F. Antaki. *Modeling and numerical simulation of blood flow using the theory of interacting continua*. Int J Non-linear Mech **47**, 506–520 (2012).
- [57] J. Kim, J. F. Antaki, and M. Massoudi. *Computational study of blood flow in microchannels*. J Comput Appl Math **292**, 174–187 (2016).
- [58] M. Massoudi. *A mixture theory formulation for hydraulic or pneumatic transport of solid particles*. Int J Eng Sci **48**, 1440–1461 (2010).
- [59] G. K. Batchelor. *Sedimentation of a dilute suspension of spheres*. J Fluid Mech **52**, 245 (1972).
- [60] P. Mazur and W. Van Saarloos. *Many-sphere hydrodynamic interactions and mobilities in a suspension*. Physica A **115A**, 21–57 (1982).
- [61] A. J. C. Ladd. *Hydrodynamic interactions in a suspension of spherical particles*. J Chem Phys **88**, 5051–5063 (1988).
- [62] A. J. C. Ladd. *Hydrodynamic interactions and the viscosity of suspensions of freely moving spheres*. J Chem Phys **90**, 1149–1157 (1989).
- [63] A. J. C. Ladd. *Hydrodynamic transport coefficients of random dispersions of hard spheres*. J Chem Phys **93**, 3484–3494 (1990).
- [64] C. Mikkelsen and H. Bruus. *Microfluidic capturing-dynamics of paramagnetic bead suspensions*. Lab Chip **5**, 1293–1297 (2005).
- [65] R. Barnkob, P. Augustsson, T. Laurell, and H. Bruus. *Acoustic radiation- and streaming-induced microparticle velocities determined by microparticle image velocimetry in an ultrasound symmetry plane*. Phys Rev E **86**, 056307 (2012).
- [66] P. B. Muller, M. Rossi, A. G. Marin, R. Barnkob, P. Augustsson, T. Laurell, C. J. Kähler, and H. Bruus. *Ultrasound-induced acoustophoretic motion of microparticles in three dimensions*. Phys Rev E **88**, 023006 (2013).
- [67] J. K. G. Dhont, *An introduction to dynamics of colloids*, (Elsevier, 1996).

- [68] M. Nordin and T. Laurell. *Two-hundredfold volume concentration of dilute cell and particle suspensions using chip integrated multistage acoustophoresis*. Lab Chip **12**, 4610–4616 (2012).
- [69] M. Antfolk, P. B. Muller, P. Augustsson, H. Bruus, and T. Laurell. *Focusing of sub-micrometer particles and bacteria enabled by two-dimensional acoustophoresis*. Lab Chip **14**, 2791–2799 (2014).
- [70] D. Carugo, D. N. Ankrett, P. Glynne-Jones, L. Capretto, R. J. Boltryk, X. Zhang, P. A. Townsend, and M. Hill. *Contrast agent-free sonoporation: The use of an ultrasonic standing wave microfluidic system for the delivery of pharmaceutical agents*. Biomicrofluidics **5**, 044108 (2011).
- [71] P. Mishra, M. Hill, and P. Glynne-Jones. *Deformation of red blood cells using acoustic radiation forces*. Biomicrofluidics **8**, 034109 (2014).
- [72] J. Lei, P. Glynne-Jones, and M. Hill. *Acoustic streaming in the transducer plane in ultrasonic particle manipulation devices*. Lab Chip **13**, 2133–2143 (2013).
- [73] M. Evander, O. Gidlöf, B. Olde, D. Erlinge, and T. Laurell. *Non-contact acoustic capture of microparticles from small plasma volumes*. Lab Chip **15**, 2588–2596 (2015).
- [74] I. Gralinski, S. Raymond, T. Alan, and A. Neild. *Continuous flow ultrasonic particle trapping in a glass capillary*. Journal of Applied Physics **115**, 054505 (2014).
- [75] P. B. Muller and H. Bruus. *Theoretical study of time-dependent, ultrasound-induced acoustic streaming in microchannels*. Phys Rev E **92**, 063018 (2015).
- [76] F. Garofalo, T. Laurell, and H. Bruus. *Performance Study of Acoustophoretic Microfluidic Silicon-Glass Devices by Characterization of Material- and Geometry-Dependent Frequency Spectra*. Phys Rev Applied **7**, 054026 (2017).
- [77] F. Collino and P. B. Monk. *Optimizing the perfectly matched layer*. Comput Methods Appl Mech Eng **164**, 157–171 (1998).
- [78] A. F. Oskooi, L. Zhang, Y. Avniel, and S. G. Johnson. *The failure of perfectly matched layers, and towards their redemption by adiabatic absorbers*. Optics Express **16**, 11376–11392 (2008).
- [79] C. Devendran, N. R. Gunasekara, D. J. Collins, and A. Neild. *Batch process particle separation using surface acoustic waves (SAW): integration of travelling and standing saw*. RSC Adv **6**, 5856–5864 (2016).
- [80] C. Devendran, T. Albrecht, J. Brenker, T. Alan, and A. Neild. *The importance of travelling wave components in standing surface acoustic wave (SSAW) systems*. Lab Chip **16**, 3756–3766 (2016).

- [81] J. W. Ng, D. J. Collins, C. Devendran, Y. Ai, and A. Neild. *Flow-rate-insensitive deterministic particle sorting using a combination of travelling and standing surface acoustic waves*. *Microfluidics and Nanofluidics* **20**, 151 (2016).
- [82] M. W. H. Ley, C. Johannesson, M. Evander, T. Laurell, and H. Bruus. *Modeling and experiments of acoustic trapping forces in a small glass capillary*. Proc 20th MicroTAS, 9 - 13 October 2016, Dublin, Ireland 711–712 (2016).
- [83] A. Y. Rednikov and S. S. Sadhal. *Acoustic/steady streaming from a motionless boundary and related phenomena: generalized treatment of the inner streaming and examples*. *J Fluid Mech* **667**, 426–462 (2011).
- [84] P. Hahn, A. Lamprecht, and J. Dual. *Numerical simulation of micro-particle rotation by the acoustic viscous torque*. *Lab on a Chip* **16**, 4581–4594 (2016).
- [85] J. S. Bach. *Theory and simulation of microscale acoustic streaming in 3 dimensions*. Master’s thesis, Technical University of Denmark, www.fysik.dtu.dk/microfluidics (2017).
- [86] J. Lei, M. Hill, and P. Glynne-Jones. *Transducer-plane streaming patterns in thin-layer acoustofluidic devices*. *Physical Review Applied* **8**, 014018 (7 pp.), 014018 (7 pp.) (2017).
- [87] J. S. Bach and H. Bruus. *Acoustic fields and streaming near a curved oscillating boundary*. *The Journal of the Acoustical Society of America* In preparation (2017).
- [88] W. L. Nyborg. *Acoustic streaming near a boundary*. *J Acoust Soc Am* **30**, 329–339 (1958).
- [89] M. Longuet-Higgins. *On the transport of mass by time-varying ocean currents*. *Deep-Sea Research* **16**, 431–447 (1969).
- [90] J. Vanneste and O. Bühler. *Streaming by leaky surface acoustic waves*. *Proc R Soc a* **467**, 1779–1800 (2011).
- [91] J. Lei, P. Glynne-Jones, and M. Hill. *Comparing methods for the modelling of boundary-driven streaming in acoustofluidic devices*. *Microfluidics and Nanofluidics* **21**, 23 (2017).
- [92] G. T. Silva and H. Bruus. *Acoustic interaction forces between small particles in an ideal fluid*. *Phys Rev E* **90**, 063007 (2014).
- [93] T. Baasch, I. Leibacher, and J. Dual. *Multibody dynamics in acoustophoresis*. *Journal of the Acoustical Society of America* **141**, 1664–1674 (2017).
- [94] J. T. Karlsen, P. Augustsson, and H. Bruus. *Acoustic force density acting on inhomogeneous fluids in acoustic fields*. *Phys Rev Lett* **117**, 114504 (2016).